

Reactivity in the Single Molecule Junction

Rachel L. Starr

Submitted in partial fulfillment of the
requirements for the degree of
Doctor of Philosophy
under the Executive Committee
of the Graduate School of Arts and Sciences

COLUMBIA UNIVERSITY

2021

© 2021

Rachel L. Starr

All Rights Reserved

Abstract

Reactivity in the Single Molecule Junction

Rachel L. Starr

In the last two decades, significant strides have been made towards utilizing the scanning tunneling microscope (STM) as a reaction chemistry tool, in addition to its primary use as an imaging instrument. Built off the STM, the STM-break junction (STM-BJ) technique was developed specifically for the reliable and reproducible measurement of properties of a single molecule suspended between two electrodes. These advances are crucial to the fields of molecular electronics and single-molecule reactivity, the latter also relating back to traditional bulk chemistry. By intelligently designing experiments and systems to probe with the STM and STM-BJ, we can begin to understand chemical processes on a deeper level than ever before.

Chapter 1 provides an overview of the recent work using the STM and STM-BJ to effect chemical transformations which involve the making and breaking of bonds. We contextualize this progress in terms of single-molecule manipulation and synthetic chemistry, to understand the implications and outlook of this field of study. Seminal surface-based reactions are discussed, in addition to reactions that occur in both solution and within the single molecule junction. Differences between STM and STM-BJ capabilities and limitations are detailed, and the challenges of translating these fundamental experiments into functional reactions are addressed.

Chapter 2 describes using the STM-BJ to study the binding of aryl iodides between gold electrodes. Important details regarding these binding modes, which were previously incompletely understood, are revealed via concrete experimental evidence. Our data suggests that this system, which is synthetically accessible, holds promise for forming the sought-after and highly conducting covalent gold-carbon bonds *in situ* and can be modulated with applied bias.

Chapter 3 builds upon the knowledge gained in Chapter 2, and focuses on the reactivity of aryl iodides in the junction. We demonstrate a new *in situ* reaction of an Ullmann coupling, or dimerization, of various biphenyl iodides. By strategically designing the molecules studied, we are also able to gain mechanistic insight into this process, which in the bulk still remains debated, as well as demonstrate a cross-coupling reaction. This project is ongoing as of the submission of this dissertation, so other findings and continuing experiments are included.

Chapter 4 transitions towards a different type of binder to gold, the cyclopropenylidene-based carbene. These amino-functionalized carbenes prove to be stronger linkers than N-heterocyclic carbenes, which are known binders to gold. Using a variety of surface analysis, imaging, and computational techniques, we explore the binding geometries and energies of cyclopropenylidenes, expanding the scope of carbene surface modifiers.

Chapter 5 summarizes this body of PhD research, suggests directions for future work, and concludes the dissertation. These works explore the binding and reactivity of molecules on gold surfaces and within the single molecule junction, improving upon the understanding of this newly burgeoning field. This thesis seeks to encourage future work on these and related systems, to continue refining our comprehension of both junction and bulk reaction chemistry processes.

Table of Contents

List of Figures.....	iv
Acknowledgements	vii
Chapter 1: A Single Molecule Blueprint for Synthesis.....	1
1.1 Preface.....	1
1.2 Introduction.....	1
1.3 STM-Driven Surface Chemistry	4
1.4 Nanoscale Electrode-Driven Reactions	14
1.5 Probing Single-Molecule Reactions	28
1.6 Conclusion and Outlook	33
1.7 References.....	35
Chapter 2: Gold-Carbon Contacts from Oxidative Addition of Aryl Iodides	52
2.1 Preface.....	52
2.2 Introduction.....	52
2.3 Aryl Iodide Single Molecule Junctions: Two Binding Modes	54
2.4 Elucidating Binding Modes	56
2.5 Computational Studies	58
2.6 Bias Dependent Behavior	60
2.7 Conclusion and Outlook	62
2.8 Synthetic Details	62
2.9 DFT Calculations	73

2.10 STM-BJ Method	74
2.11 Additional Data.....	75
2.12 References.....	79
Chapter 3: Harnessing Aryl Iodide Reactivity Towards an <i>In Situ</i> Ullmann Coupling	84
3.1 Preface.....	84
3.2 Introduction.....	84
3.3 Evidence and Scope of the <i>In Situ</i> Ullmann Coupling Reaction	86
3.4 Probing the Mechanism	90
3.5 The Fate of the Iodide	93
3.6 Other Reaction Criteria	94
3.7 Conclusion and Outlook	99
3.8 Synthetic Details	100
3.9 STM-BJ Method	120
3.10 SEM and EDX	120
3.11 Additional Data.....	121
3.12 NMR Spectra	131
3.13 References.....	146
Chapter 4: Cyclopropenylidenes as Strong Carbene Anchoring Groups on Au Surfaces	151
4.1 Preface.....	151
4.2 Introduction.....	151
4.3 Computational Studies of BAC Surface Binding	153
4.4 Spectroscopic Analysis of Surface-Bound BACs.....	155

4.5 Imaging of Surface-Bound BACs	158
4.6 Conclusion and Outlook	160
4.7 Synthetic Details	160
4.8 Computational Details	161
4.9 Details of XPS and NEXAFS Measurements	164
4.10 Details of DFT Calculations of X-ray Photoemission and Absorption Spectra	167
4.11 Scanning probe microscopy experiments	173
4.12 References.....	174
Chapter 5: Conclusions and Outlook.....	179
5.1 Summary	179
5.2 Future Work.....	181
5.3 Concluding Remarks.....	182

List of Figures

Figure 1.1 STM-driven reactions.	5
Figure 1.2 Visualizing reaction intermediates with the STM.	9
Figure 1.3 Triggering reactions in junctions.	14
Figure 1.4 In situ formation of covalent Au contacts from different leaving groups.	16
Figure 1.5 Electrochemically gated switches in the STM-BJ.	19
Figure 1.6 Electric field driven reactions in an STM.	25
Figure 1.7 Key transition states for electric field catalyzed reactions in the STM-BJ.	26
Figure 1.8 Inducing reactivity one molecule at a time.	30
Figure 2.1 Schematic of aryl iodide junction and the two visible conductance peaks.	55
Figure 2.2 <i>In situ</i> oxidative addition schematic and corroboratioin with gold analogs.	57
Figure 2.3 Calculated transmission functions and β plot.	59
Figure 2.4 Bias dependent behavior in an ionic environment.	61
Figure 2.5 Synthetic scheme for the synthesis of asymmetrical iodides and gold analogs.	64
Figure 2.6 Additioinal conductance data for the iodide series.	75
Figure 2.7 Oxidative addition of a symmetric diiodobiphenyl.	76
Figure 2.8 Additional conductance data for the gold series.	77
Figure 2.9 Additional computational data for junction geometry and transmission.	78
Figure 2.10 Additional bias dependent data.	78
Figure 2.11 Cyclic voltammogram demonstrating no electrochemistry.	79
Figure 3.1 A schematic of the <i>in situ</i> Ullmann coupling and structures of the aryl iodides.	87
Figure 3.2 1D and 2D histograms demonstrating dimerization.	88
Figure 3.3 Cross-coupling schematic and 1D histograms.	90

Figure 3.4 Cartoon representations of oxidative addition and coupling.....	92
Figure 3.5 Tip cleaning data and cartoon representation.....	93
Figure 3.6 Solvent and bias effects.....	95
Figure 3.7 Surfance roughness and electrolyte effects.....	97
Figure 3.8 Conductance data for other aryl iodides studied.....	122
Figure 3.9 Mass spectrometry data for anthracenes.....	123
Figure 3.10 Mass spectrometry data for the thiomethyl analyte.....	124
Figure 3.11 Mass spectrometry data for the amine analyte.....	125
Figure 3.12 Mass spectrometry data for the pyridine analyte.....	126
Figure 3.13 Au analog measured in PC and TCB.....	126
Figure 3.14 Additional cross-coupling data.....	127
Figure 3.15 Additional tip cleaning data.....	128
Figure 3.16 Cartoon representation of oxidative addition in different solvents.....	129
Figure 3.17 Substrate surface analysis data.....	129
Figure 3.18 Dimerization without electrolyte.....	130
Figure 3.19 NMR spectra of compound 5.....	131
Figure 3.20 NMR spectra of compound I4.....	132
Figure 3.21 NMR Spectra of compound D4.....	133
Figure 3.22 NMR spectra of compound 7.....	134
Figure 3.23 NMR spectra of compound 8.....	135
Figure 3.24 NMR spectra of compound 9.....	136
Figure 3.25 NMR spectra of compound 11.....	137
Figure 3.26 NMR spectra of compound Br1.....	138

Figure 3.27 NMR spectrum of compound 12.....	139
Figure 3.28 NMR spectra of compound 13.....	140
Figure 3.29 NMR spectra of compound OTf1.....	141
Figure 3.30 NMR spectra of compound 15.....	142
Figure 3.31 NMR spectra of compound 16.....	143
Figure 3.32 NMR spectra of compound 17.....	144
Figure 3.33 NMR spectra of compound C1.....	145
Figure 4.1 BAC structure and calculated binding energies.	155
Figure 4.2 BAC synthesis and NEXAFS structure.....	156
Figure 4.3 Experimental and simulated STM and AFM images of BAC on Au(111).	159
Figure 4.4 Unit cell used in the DFT calculations of the adsorbed molecule.....	162
Figure 4.5 DAC structure and energy as a function of tilt angle.	163
Figure 4.6 Electrostatic potential representations of DAC and NHC.	164
Figure 4.7 XPS measurement of the as-deposited BAC film.	165
Figure 4.8 N1s and C1s XPS data of BAC film deposited on Au(111).....	166
Figure 4.9 Comparison of Au 4f intensity attenuation.....	167
Figure 4.10 Optimized geometry of the BAC molecule with a gold dimer.....	168
Figure 4.11 Comparison of the experimental XPS data with calculated CEBEs.	169
Figure 4.12 Polarization dependent carbon K-edge magic angle NEXAFS.....	170
Figure 4.13 Experimental vs. calculated NEXAFS and calculated orbitals.	173

Acknowledgements

I could fill an additional dissertation with my gratitude for the many wonderful people who have impacted my life. It takes a village to raise a grad student, and I was no exception.

First, I thank my advisors, Latha Venkataraman and Xavier Roy, for affording me the opportunity to join their labs out of the blue and without experience in their fields. I can't begin to guess why they decided to take a chance on me, but I am eternally grateful. They were extremely patient with me as I dove headfirst into two steep learning curves and attempted to fit a full PhD into half the time. Working between two PIs with complementary skill sets provided us with a unique lens for problem solving, and I benefitted greatly from the time that Xav and Latha dedicated to my projects every week. I deeply appreciate their support, scientifically and beyond, and I credit so much of this PhD to them. It has been an absolute pleasure to work under an inspirational woman in STEM such as Latha; I have learned so much from her intellect, management style, and professionalism. In Xav's lab, where I had my desk, it was reassuring to know that he was just a few steps away (if not already in my office) to answer my never-ending questions, give me ideas, or come into the lab with me. Thank you both for making me feel like my thoughts were valuable, and for helping me make the most of my PhD.

I thank Laura Kaufman and Allie Obermeyer for sitting on my committee since my second year. They both helped me navigate the difficult decision to switch labs, and their advice and listening ears were truly invaluable and deeply appreciated. I also had the opportunity to collaborate with Allie prior to switching labs, which, although short-lived, was a highlight of my PhD. Thank you to Mike Steigerwald for joining my committee recently, and for his continued scientific input. His pure love for science, paired with his creative ideas and encouragement, is unmatched, and it has been a delight being the beneficiary of his brain and positive attitude.

Transitioning to two new groups brought many challenges alongside the rewards, and I am grateful to the students in the Roy and Venkataraman labs who were so welcoming. In the Roy Lab, I especially thank Evan for being an extraordinarily nonjudgmental, patient, and kind teacher, while making me smile between my blunders. I also thank Ilana, who quickly became my close collaborator, for her patience and scientific input. Although our project took us in some wacky directions, her curiosity and methodical problem solving kept me motivated. It has been a joy to work together in the lab, over Zoom, and writing manuscripts. I thank Jake for being my desk- and lunch-mate for two years and friend for five. Since day one of grad school he's been there to lend an ear, share a joke, support my networking efforts, or suggest a new adventure (from camping, to graveyards, to cooking). I can't wait to embark on our next chapters together in DC. Lastly, thank you to every Roy lab member who helped me in all ways big and small, from using the glovebox to running CV to crystallography, I am grateful for your generosity with your time and knowledge.

In the Venkataraman lab, I thank every single lab member for helping me with some form of troubleshooting. I especially thank Julia, Suman, and E-Dean for their perpetual willingness to answer my continual stream of questions. Julia and E-Dean taught me everything about STM-BJ when I joined the lab, and Julia continues to be a constant (basically daily) source of assistance, without whom I would be very inefficient. I also thank Tianren for his computational contribution to one of my projects, and for subsequently teaching me how to do some basic computational work.

Before I joined these labs, I had the privilege of working with another set of very talented, driven, and all-around fun scientists, who became some of my closest friends. I thank Luis for my time in his lab surrounded by such wonderful people. I extend an enormous thank you to Spencer, my first grad school mentor, who taught me so much about what it means to be a PhD researcher. He was unbelievably patient with me, and we had a blast collaborating on projects and sharing

hood space. I was also extremely lucky to work alongside Jess, who quickly became a role model. She has been an incredible resource and personal cheerleader for my professional development, and I cannot express my gratitude for the doors she has opened for me. Thank you to Andrew, Sam, and JLow, who made the lab such a lively place to be every day, and gave me the education I didn't know I needed on sports, music, lifting, sandwiches, and more. I lived for our daily group lunches and weekend outings, and I am so lucky to call you all my friends.

Science can be frustrating, but being surrounded by some really amazing, smart, fun, and caring people more than makes up for it. I thank everyone who made grad school some of my best years so far. When I look back on my PhD, it's our escapades from climbing, to karaoke, to Yuca, that I will remember the most. I can't wait to continue making memories together and watching you all succeed. For maintaining my sanity, I thank: Jake, Lindsey, Andrew, Jess, JLow, Scott, Spencer, Sam, Anouck, Makeda, Pinkard, Drew, and Michael.

My journey to grad school started with some amazing high school chemistry teachers, and continued with my incredible Barnard chemistry professors and research advisor, Christian Rojas. I thank you all for instilling in me an excitement about chemistry, and the confidence to pursue it. The Barnard chemistry department is truly unique, and I am so grateful to have spent four years in a home away from home, with a supportive, nurturing, and bold chemistry family.

Outside of the chemistry world, I am eternally grateful for my pre-grad school friends who stuck with me all this time. Your support means the world to me, and your friendships were essential to surviving my PhD. Special thanks to: Dani, Melissa, Elli, Lida, Dan (x2), Peter, Alex, Bryan, and SO many more that I don't have the space to list.

Lastly, the biggest thank you goes to my family. Living close to home for the last nine years, I've had the privilege of frequently seeing my and Ben's families, which has been such a

joy and a comfort. I thank my grandparents for being my biggest and most enthusiastic fans. I cherish our time together and our weekly phone conversations. I thank my parents, Gail and Michael, for their unwavering encouragement, interest, enthusiasm, and support. They are there for me in every way imaginable, be it weighing difficult decisions, dog sitting, or understanding my taxes. Thank you for consoling me during stressful times, and for celebrating every accomplishment, no matter how small. I know I can count on you always, and for that I consider myself extremely lucky.

An even bigger, final thank you goes to Ben. I'm sure I've been insufferable at times over the last almost 8 years, but especially throughout my PhD, and especially during the pandemic. Although I'm the one receiving a degree, Ben deserves an award for still loving me after the highest highs and lowest lows of the PhD, many of which were experienced 200 miles apart. His level-headedness has always been an essential balance to my personality, and I wouldn't have made it through a single day of this journey without him as a stabilizing force. His support of my goals, interests, and career means the world to me, especially with his recent encouragement to accept a once-in-a-lifetime job opportunity in DC, even though it threw a wrench into our plans. Although this pandemic deserves no credit for anything, I'm very grateful for the silver linings of living together for my last year of school, and of course adopting Daphne who has enriched our lives so much. I love you both to the moon and back.

For the women in STEM who paved the way

Chapter 1: A Single Molecule Blueprint for Synthesis

1.1 Preface

Significant portions of this chapter are adapted from a review that has been accepted for publication in *Nature Reviews Chemistry* as of the writing of this dissertation entitled “A Single Molecule Blueprint for Synthesis” by Ilana Stone, Rachel L. Starr, Yaping Zang, Colin Nuckolls, Michael L. Steigerwald, Tristan H. Lambert, Xavier Roy, and Latha Venkataraman.

1.2 Introduction

Over the past 20 years, the scanning tunneling microscope (STM) has been transformed from an imaging instrument to a device capable of manipulating single atoms and molecules to drive chemical reactions. These reactions establish the foundation of single-molecule reaction chemistry and reveal how chemistry can be reimaged outside of conventional synthetic conditions. Reactions that require ultra-high vacuum and surface binding strategies are limited, however, in scale, scope, and device complexity, making them inapplicable as a general solution for synthetic chemistry. With the STM-break junction (BJ) technique, methods have been developed to reliably and reproducibly measure the conductance of single molecules in solution attached to metal electrodes. Probing these transformations in solution-based environments and developing a molecular-level understanding of these solution processes is paving the way for the design of chemical reactions with novel reaction kinetics and modulated thermodynamics. The STM has the unique ability to apply a strong directional field to a reaction system. Combining this

capability with the different external catalytic stimuli such as light and pH, further widens the scope of possible reactions in an ambient STM setup. The tools that enable these processes and our understanding of the processes are just now converging. Most of the work that is detailed in this section has only been realized in the last five to ten years. As this explosive field reaches a tipping point, here we provide a summary of this recent work and contextualize it within both the realms of single-molecule manipulation and synthetic chemistry in order to provide insight into the accomplishments and outlook of this chemistry.

Although some of the work examined here is better known for its implications in the field of molecular electronics, the focus of this section is the chemical transformations that have been discovered as part of those efforts. While they are ancillary to the functionality of the molecular devices, these reactions are in and of themselves groundbreaking transformations, occurring in environments that were never intended for chemical reactions. Described within are the implications of these transformations for synthetic chemistry. We focus less on the structure-function relationships and the nanotechnological considerations that typically contextualize this work, and instead highlight reaction discoveries and the fundamental properties of chemical transformations that are subsequently revealed.

The focus of this section is on reactions in which bond breakage or formation within molecules anchored to nanoelectrodes is driven by a local potential. We will 1) provide an overview of how the STM can be used as a tool for reaction chemistry, 2) outline reactions that occur in solution, categorized by their mechanisms and implications for specific fields of chemical catalysis, and 3) discuss reactions that are monitored at the single-molecule level and can only occur in a single-molecule junction. We begin with the first reactions that were catalyzed and controlled using the STM. The first reactions discussed occur on surfaces and are distinguished

from solution-based reactions in an STM. Reactions induced by the STM tip and thermal reactions that are monitored via STM imaging are considered separately, and the latter are used to illustrate the capabilities of the STM that cannot be accomplished using break junction techniques. The challenges and limitations of these surface reactions are also considered, and more recent examples of STM induced reactions are discussed to illustrate the evolution of STM surface chemistry and its scope. These recent studies show that there are inherent limitations to surface reactions, and in order to surpass these limits, a new tool such as the break junction is an essential and complementary development.

The remainder and majority of the section focuses on reactions that occur in break junctions and are triggered by the local potential of the electrodes. Recent examples are used to illustrate how this technique accesses new reactivity that is unattainable by either traditional solution-based chemistry or the manipulation of specific surface adsorbates. Reactions in this section are categorized by their mechanisms and implications for specific fields of chemical catalysis. The *in situ* formation of Au–C and mixed metal covalent bonds are considered from the perspective of organometallic chemistry. Electrochemically gated reactions are distinguished from electrostatic reactions to differentiate between those that are more relevant to electrochemical versus electric field-driven catalysis. Reactions that integrate other modes of catalysis by working in concert with external stimuli such as the application of light and mechanical force are briefly discussed, as they are especially relevant to dual catalysis strategies involving photoredox^{1,2} and the emerging field of electrophotocatalysis.^{3–5}

The last reactions detailed are those in which junction-based techniques impart precisely controlled and unique redox activity to one molecule at a time. These reactions are monitored at the single-molecule level and can only occur in a single-molecule junction. The transformation of

each molecule in solution can be probed in real time using the STM break junction, as only molecules held between the electrodes undergo the transformation. Although these reactions are synthetically less viable for scalable processes, they demonstrate a level of precision that is unachievable by any other means. Finally, we address the challenges of translating fundamental experiments into functional reactions with an eye towards developing these powerful analytical tools into a template for nanoscale materials synthesis.

1.3 STM-Driven Surface Chemistry

Although it was not originally intended as such, the STM can be used as a tool for reaction chemistry (Figure 1.1a). In each of the reactions outlined here, the STM can be used to control the formation and cleavage of chemical bonds, resulting in new chemical species^{6–17} or molecular conformations.^{18–27} The groundbreaking work that established the STM tip as a nanocatalyst for chemical reactions involved molecules adsorbed on surfaces under ultrahigh vacuum (UHV). These seminal studies combined the ability of the STM to control mechanical motions, such as lateral movement and vertical transfer,^{28–37} with the ability to manipulate molecules electronically, either by stimulating adsorbed molecules through the tunneling current^{6,7,10–12,16,20,24}, the applied electric field between the tip and the molecule^{18,19,25–27}, or a combination of both mechanisms.

In this section, we describe some of the fundamental achievements that redefined the STM as a tool to control chemistry at the spatial limit of individual atoms and molecules adsorbed on surfaces and to probe the properties of individual molecules while simultaneously manipulating their chemical connectivity. The STM is used to induce bond formation one atom at a time, observe individual steps in a chemical reaction, and characterize product formation. More recent examples

of surface reactions are discussed to illustrate the versatility of the STM to induce and probe reactivity, and to show how mechanisms have been elucidated over the last twenty years.

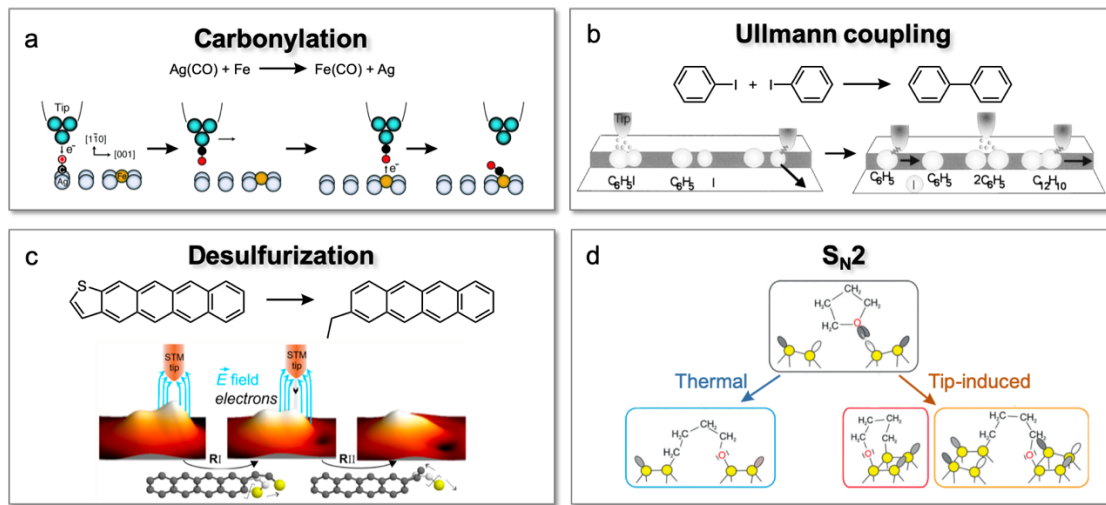


Figure 1.1 *STM-driven reactions*. Reactions on surfaces rely on the mechanical precision of the STM nanoelectrode to pick out individual adsorbed molecules and induce reactivity with an applied bias. (a) The STM is used to control the step-by-step formation of individual $\text{Fe}(\text{CO})$ molecules from adsorbed Fe atoms and CO molecules.⁶ The tunneling current can be used to locate and move CO molecules onto available Fe atoms. Bond formation is only achieved in the presence of a tunneling current. (b) An Ullmann homocoupling of iodobenzene on a $\text{Cu}(111)$ surface⁷ is controlled by the STM tip. The bimolecular reaction is induced by injection of electrons into single molecules. (c) The STM locally triggers desulfurization of a thiophene subunit of a tetracenothiophene molecule on a $\text{Cu}(111)$ surface⁹ via two distinct reaction pathways: An applied bias may induce desulfurization via an electric field or via a direct current with a sufficiently high injection of electrons. (d) An $\text{S}_{\text{N}}2$ reaction on a $\text{Si}(001)$ surface is demonstrated via ether cleavage of tetrahydrofuran (THF). The STM tip induces one of two mechanisms depending on the applied bias, either electron transfer or vibrational excitation. The mechanisms yield distinct products from each other and from those of the thermally induced reaction.³⁸

Foundational reactions

The STM was first introduced as a nanocatalyst for bond formation with the controlled, step-by-step formation of individual $\text{Fe}(\text{CO})$ molecules from adsorbed Fe atoms and CO molecules⁶ (Figure 1.1a). This work capitalized on the mechanical precision of the STM tip to

locate and translate individual CO molecules and the tunable tunneling current in the STM junction to induce attachment of CO ligands to Fe metal atoms co-adsorbed on a Ag(110) surface. The reaction proceeded in a series of mechanical and electrical steps, in which the tunneling current was used to locate and move CO molecules, transferring them to available Fe atoms. Without the tunneling current, bond formation was not achieved even at close proximities, demonstrating that the electrical environment of the STM junction was driving the reaction. The conformation of the newly formed Fe–CO bonds was studied via imaging and inelastic electron tunneling spectroscopy (IETS), demonstrating the multidimensional use of the STM to control and observe a stepwise reaction at the single-molecule level.

Shortly after, the first organic reaction was controlled by the STM via an Ullmann homocoupling of iodobenzene on a Cu(111) surface⁷ (Figure 1.1b). The Ullmann coupling is a ubiquitous chemical transformation used widely in organic syntheses to couple aryl unites together and form new C–C bonds starting with simple and readily available aryl halide precursors.^{39,40} The Ullmann coupling has been an especially attractive strategy for the synthesis of graphene nanoribbons (GNRs).⁴¹ Here, the STM tip was used to control each step of the bimolecular reaction: dehalogenation of iodobenzene, diffusion of the newly formed reactive phenyl species, and finally formation of new C–C bond. By injecting electrons into single molecules and monitoring changes in the conductance corresponding to a dehalogenation event, the authors observed a linear dependence of the dissociation rate on the tunneling current and hypothesized that a single electron causes the C–I bond to break. They then used the tip-adsorbate forces^{32,33} to move the resulting reactive phenyl species to meet a second dehalogenated molecule and release the molecule from the tip. An inelastic tunneling bias excited the molecules and initiated formation of a new C–C bond, completing the homocoupling.

Both of these fundamental reactions relied on the mechanical precision of the STM nanoelectrode to pick out individual absorbed molecules and the electrical environment around the tip under an applied bias to induce reactivity, demonstrating the unique capability of this instrument to control chemistry. The Ullmann reaction especially revealed that common and practical synthetic reactions could be studied at the single-molecule level. The original Ullmann reaction, discovered over a century ago, required super-stoichiometric copper and refluxing in high boiling solvents such as DMSO or DMF. Tremendous efforts are still underway to find milder and greener conditions and catalysts.⁴⁰ Controlling this reaction in the STM is an innovative approach to catalysis.

Surface experiments, however, suffer from several challenges and do not offer a viable approach to large-scale synthesis. These experiments discussed above are all conducted under UHV and the mechanical manipulation of single atoms requires very low temperatures. These requirements are restrictive, impractical, and not scalable, and the products of these reactions are bound to the substrates. Furthermore, it can be difficult to determine whether the driving force of the reaction is the tunneling current or the electric field. In the next section, more recent reactions are discussed in which these mechanistic differences are considered, and some practical applications of this groundbreaking approach to controlling reactivity are demonstrated.

Recent STM-Driven Surface Reactions

The proliferation of chemical transformations controllable by the STM largely correlates with a growing interest in single-molecule electronics and device miniaturization, which has brought the study of charge transport behavior in molecular junctions to the forefront of chemical and physical research. As this body of work expanded, multiple reaction mechanisms emerged in

the STM. The differences between these mechanisms are often quite subtle, as can be seen with the use of the STM to locally trigger desulfurization of a thiophene subunit of a tetracenothiophene molecule on a Cu(111) surface⁹ (Figure 1.1c). Two distinct reaction pathways were observed: a direct desulfurization, and a two-step reaction in which each C–S bond was broken in a stepwise fashion. Reactivity in both pathways was induced by applying a positive bias, but the mechanisms could be controlled by altering the bias regime and the distance between the tip and the substrate. At a larger distance, only the first C–S cleavage event occurred, with the second event requiring closer contact. The dominant stimulus of the first step was assumed to be the electric field, but a combination of the electric field and a direct current controlled the second event, which required a sufficiently high injection of electrons.

Another study demonstrated an STM tip-induced S_N2-like ether cleavage of tetrahydrofuran (THF) on a Si(001) surface, which proceeded via two mechanisms depending on the applied bias (Figure 1.1d).³⁸ Similarly, one mechanism involved a one-electron transfer from the STM tip to the molecule, while the other involved inelastic tunneling and vibrational excitations. The products of the two reaction pathways were distinct from each other and from those of the thermally induced reaction. Products bound to the Si surface could be distinguished through STM imaging. These results demonstrated that typical S_N2 limitations, such as steric constraints, can be overcome by using the STM on an inert surface to induce and study unconventional reaction mechanisms.

These recent examples are demonstrative of the multiple mechanistic pathways that can emerge in the STM junction, and as the scope of these reactions continues to broaden, it is evident that more investigation into these mechanisms is required. This work also foreshadows how selectivity will become equally important to designing chemistry in a junction as it is in synthetic

chemistry. Either direct injection of electrons or the application of an electric field could manipulate a molecule with multiple reactive sites. By altering the bias regime such that only one of multiple mechanistic pathways is active, one could selectively control the behavior of just one moiety of a molecule.

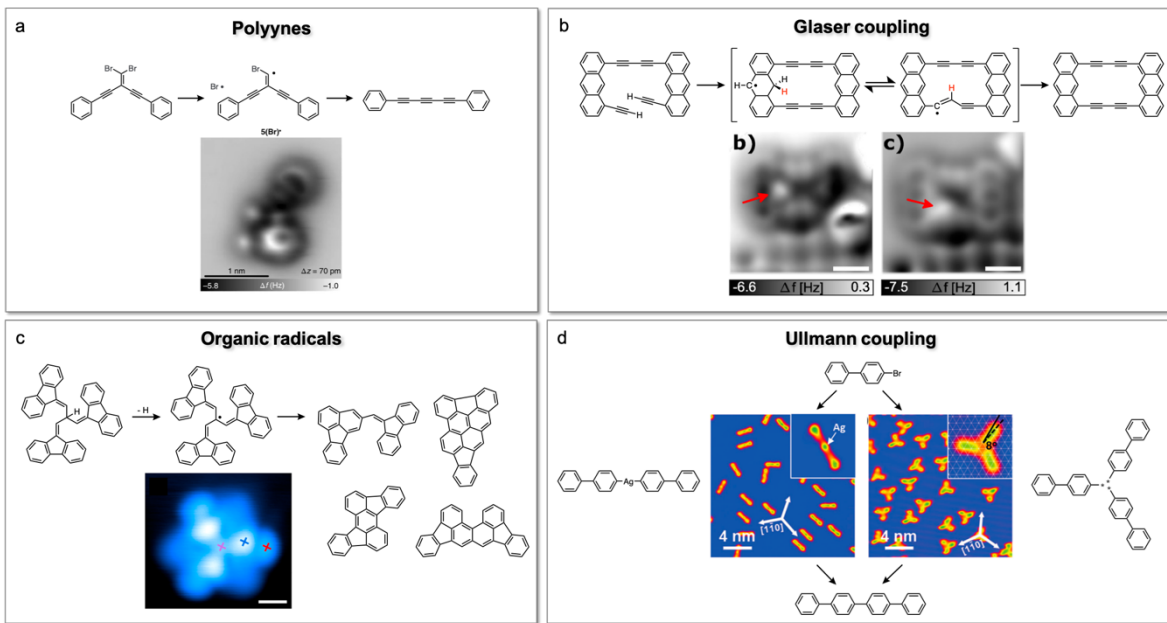


Figure 1.2 *Visualizing reaction intermediates with the STM.* The STM uniquely allows for visualization of reaction intermediates that are otherwise inaccessible and/or short lived, leading to important mechanistic insights. (a) The formation of polyynes is triggered by STM current.⁴² Inducing this reaction on an inert surface allows for the first visualization of a vinyl radical intermediate. (b) An intramolecular Glaser coupling is also induced by the STM tip on an inert surface to observe partially dehydrogenated intermediates.⁴³ Stepwise manipulation of this reaction lends new mechanistic information. (c) Bond resolved STM (BRSTM) allows for imaging of a monoradical resulting from the removal of a hydrogen atom from an sp^3 hybridized carbon, before the formation of four distinct products.⁴⁴ Isolating and studying organic radical structures is notably difficult by traditional methods. (d) The STM elucidates two reaction pathways that lead to identical Ullmann coupling products.⁴⁵ Reaction pathways are controlled by manipulating the concentration of reactants and confining the reaction area, and STM imaging offers access to the surface stabilized carbon-metal-carbon intermediates.

Another important feature of the STM is the ability to study molecules on inert surfaces, which has afforded the observation of otherwise-inaccessible intermediates. Thin layers of inert material like NaCl have been utilized to gain mechanistic insight into a variety of reactions. For example, the STM current was used to induce the formation of polyynes, and imaging on an inert NaCl surface revealed mechanistic insight into the reductive rearrangement of a 1,1-dibromoolefin to an alkyne.⁴² This study demonstrated that electrons from the probe tip reduced and cleaved C–Br bonds individually, triggering a 1,2-shift by atomic manipulation on the surface. Visualization of the geometry of a vinyl radical intermediate (Figure 1.2a) was possible for the first time because of the persistence of the intermediates on the inert surface. Another STM-induced reaction studied on an inert surface was that of bianthracene molecules with two terminal alkynes, which underwent an intramolecular Glaser-like coupling.⁴³ Reaction intermediates remained on the NaCl surface long enough to allow for orbital density mapping and observation of partially dehydrogenated intermediates (Figure 1.2b). Manipulation on an inert surface allows for each step of a reaction to be induced and studied individually, and does not require catalytic activity or binding of the analyte to an electrode. Without these restrictions, more complex structures can be fabricated and studied in the future.

Thermally Induced Reactions on Surfaces

Studying reactions with the STM enables real-space imaging of molecules at the single bond level. Novel techniques such as bond resolved STM (BRSTM) have enabled imaging of such elusive intermediates as organic radicals. Other advantages include a wider scope of molecules that can be studied, such as the products of polymerization reactions,⁴⁶ and most notably polycyclic aromatic hydrocarbons (PAHs) in addition to molecular wires. This latter class of molecules is

difficult to study in the STM due to both a lack of linkers and the large size of the molecules. Novel PAHs that have not been produced via conventional organic syntheses have been studied using STM imaging capabilities⁴⁷. Many of these reactions have been reviewed previously.⁴⁸ Here we detail some recent work that highlights the capabilities of the STM that are thus far unachievable using the break junction technique.

Imaging Reaction Intermediates with BRSTM. The advent of BRSTM, in which the STM tip is functionalized with a molecule, has enabled resolution imaging of the internal bond structures of individual molecules. Studying reactions with this technique enables the visualization of elusive intermediates. The first example of covalent C–N bond formation in an extended PAH via surface catalyzed cyclodehydrogenation was recently observed.⁴⁹ Using BRSTM the chair-like conformation of the reaction intermediates could be seen adsorbed on the metal substrates. BRSTM has also been used to observe organic radicals. For example, the removal of a hydrogen atom from an sp^3 hybridized carbon on Au (111)⁴⁴ resulted in monoradical that could be imaged before forming four distinct products (Figure 1.2c). Organic radicals are important both for studying reaction mechanisms and as well as applications to molecular spintronics.⁵⁰ Isolating these radicals and identifying their chemical structures via conventional means, however, presents a tremendous challenge because of their short lifetime under ambient conditions. Imaging via STM offers unprecedented access to these ubiquitous reaction intermediates

Ullmann Coupling. Surface assisted dehalogenative coupling is a stalwart reaction in surface chemistry. The thermally induced Ullmann coupling on Au, Cu or Ag has been heavily relied upon in the synthesis of 2D materials. Precise control over the reaction dynamics is crucial for designing complex molecular architectures and relies on a detailed understanding of the mechanistic processes involved in Ullmann coupling reactions. The mechanistic details and

consequent selectivity of these reactions, however, can be widely manipulated via subtle changes in reactants, surface topology and conditions. By imaging the surface stabilized carbon-metal-carbon complexes formed from the initial dehalogenation, the STM offers unrivaled access to these reaction dynamics.

A recent STM study of the coupling of 4-bromobiphenyl on various surfaces showed that two pathways led to identical coupling products, one that preceded through a linear intermediate and one through a three-armed clover shaped intermediate (Figure 1.2d).⁴⁵ The pathways could be controlled by a surface molecular assembly strategy analogous to the cage-effect of solution chemistry; by manipulating the concentration of reactants and confining the reaction area, the reaction dynamics could be controlled. Further experiments revealed that depending on the metal surface employed, four-armed clover formations were observed as well. Importantly all pathways led to formation of a linear product. This work demonstrates how access to the carbon-metal-carbon intermediates reveals reaction dynamics that are impossible to differentiate by analyzing the products alone.

From Surfaces to Solution

The reactions discussed in the preceding sections rely on functionality specific to the STM and unavailable to the STM-BJ to characterize intermediates and products. STM imaging can distinguish between products that differ in their surface binding, providing a level of detail that may be lost using the STM-BJ technique. Various products of different excitation mechanisms could yield similar conductance traces in the STM-BJ, despite their unique binding to the surface. The break junction technique is also not suitable for investigations relying on inert surfaces, as conductive, non-inert surfaces are required for electrodes. These materials often prevent

intermediates from lingering on surfaces or may interfere with the reaction pathway as active catalysts. The STM, however, can image on conductive surfaces covered by a thin layer of inert material, broadening the scope of possible mechanisms and intermediates studied. Additionally, since molecules are not required to bind to electrodes for STM imaging, a wider range of reaction intermediates can be observed than with the STM-BJ. Therefore, molecules including those that are without linkers to the electrodes, low- or non-conducting, and large or bulky are accessible.

While the work highlighted in this section demonstrates the unique ability of the STM to catalyze reactions on the atomic level and provide images of intermediates and products, even recent examples present a slew of challenges inhibiting the synthetic utility of this chemistry. Single-molecule surface chemistry still requires stringent conditions, and surface-bound products do not offer the same practicality or ease in processing as solution-based synthetic chemistry does. The following sections focus on the recent work that has begun to bridge the gap between these seminal experiments and the utilization of this technique for practical syntheses. These works establish the break junction as an important tool for probing reactivity and mechanisms of single molecules in solution that are fundamental to practical synthetic chemistry.

1.4 Nanoscale Electrode-Driven Reactions

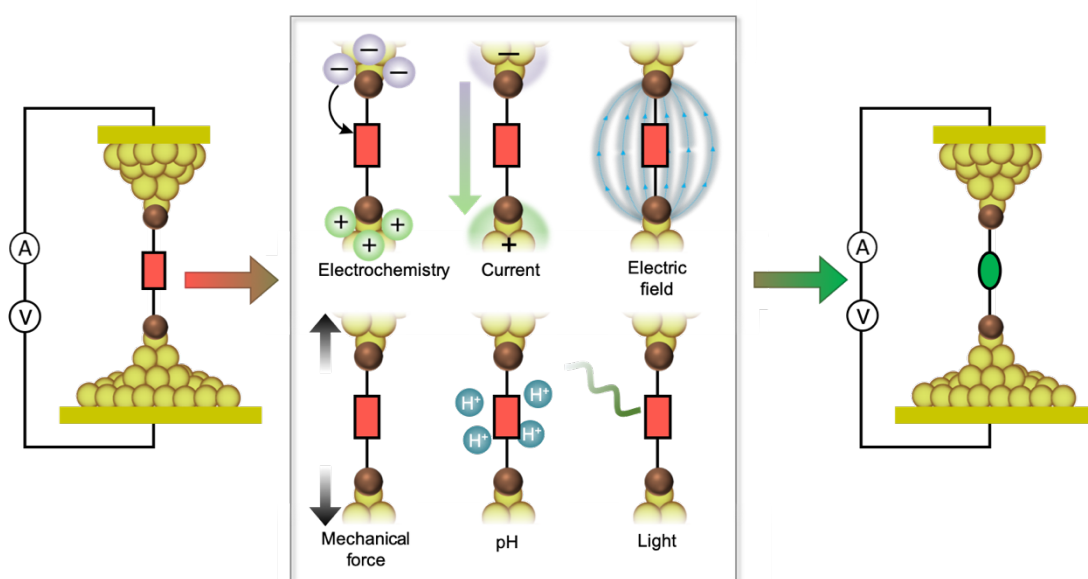


Figure 1.3 *Triggering reactions in junctions.* Within the framework of an STM, myriad chemical stimuli can be exerted to induce reactivity. The electrodes can be considered chemical reagents by providing an electric current, an electric field, a mechanical force or acting as an electrochemical redox agent. The red rectangle and green oval represent the reactant and product, respectively, stressing that the applied stimulus induces a chemical transformation and directly involves the formation or breakage of bonds, resulting in a new molecule. In an electrochemically gated junction, a redox active molecule can gain or lose a single electron. Redox-driven reactions require a polar solvent and a supporting electrolyte, with the formation of a dense double layer of ions around the nanostructured tip. The small exposed area of the tip and highly concentrated electric potential provides an asymmetric field distribution that allows reactions directly at the tip. Reactions can also be activated by a current-driven excitation of vibrational modes that can cause bond rupture.

The electrode environment can also induce an electric field with variable magnitude and orientation, stabilizing charge-separated transition states, minor resonance contributors, and reaction intermediates. The lower energy barrier to these otherwise less available and less stable conformations provides an accessible reaction pathway. Additionally, the electrodes can mechanically trigger reactions by repeatedly forming and breaking contacts between the tip and the substrate. Molecules caught in the junction can be stretched until a single bond is broken by mechanical force. This solution-based application of mechanical force is distinct from the mechanical manipulations of earlier STM-controlled reactions, in which individual atoms are relocated on a surface (Figure 1.1).

Because these junction-based reactions occur in solution, other catalytic stimuli, such as acid-base or photocatalysis, can be employed. Protonation can affect the molecular backbone by inducing

reversible ring closure or isomerization, or the linker by altering the coupling of the molecule to the electrode. Irradiation can also excite electrons in photochromic molecules in the metal. In the former, the molecule must be decoupled from metal electrodes so excited photons are not quenched. Moreover, these external stimuli can be combined to create finely tuned, dual-control systems.

***In situ* Au Contacts**

When constructing organic single-molecule junctions, charge transport across the metal–molecule interface⁵¹ is dictated by the coupling of the linkers’ discrete molecular orbitals to the electronic bands of the electrodes. Therefore, molecules must be thoughtfully designed with highly-coupling linkers in mind, but the organometallic synthesis of such molecules is often quite challenging and inaccessible. Yet, direct Au–C linkages are particularly attractive⁵² because they lead to a remarkable increase in conductance. Creating a robust, low-resistance contact to Au within the junction starting from more synthetically accessible molecules is an elegant alternative. Such a solution not only introduces a new level of convenience and simplicity, but also yields valuable information about metal–C bonds that might be applicable to organometallic reaction chemistry.

Organostannanes. Noncovalent Au–C linkages have been achieved through C₆₀, benzene and π-stacked benzene^{53–56}, but to achieve more robust, low resistance contact the carbon backbone of the molecule should be covalently bonded to the electrode. This linkage has been achieved *in situ* using trimethyl tin (SnMe₃)-terminated molecules that were cleaved in the junction to yield direct Au–C linkages (Figure 1.4a).⁵² STM-BJ measurements performed on SnMe₃-terminated alkanes⁵⁷ revealed that across the series of alkanes, the direct Au–C junctions showed a 100-fold increase in conductance compared to analogous junctions with other linkers.^{58–62} A mechanism

similar to a reductive elimination was proposed for the deprotection.⁶³ This study successfully demonstrated a reproducible method for *in situ* formation of highly conducting metal-organic contacts. A follow-up study⁶⁴ demonstrated that slightly altering the molecular design and placing the SnMe₃ at the benzylic position enhanced the coupling of the electrode into the π system of the conjugated molecule, leading to an even higher conductance.

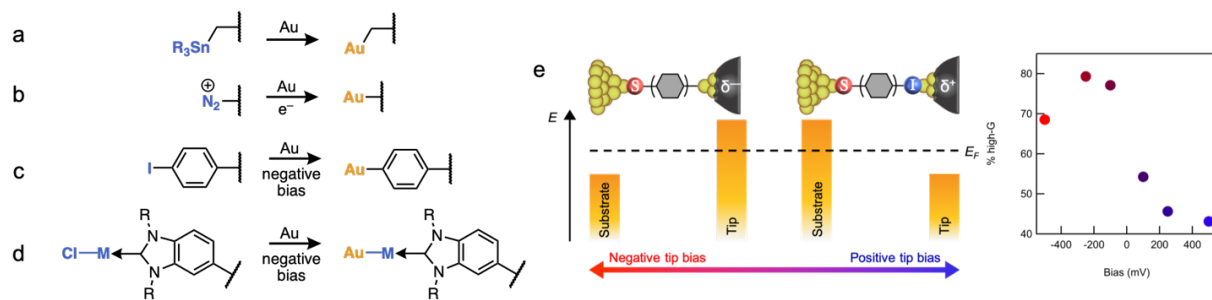


Figure 1.4 *In situ* formation of covalent Au contacts from different leaving groups. Molecules with labile groups that can be easily cleaved in the junction provide a convenient strategy for the formation of Au covalent bonds. A variety of functional groups have been employed: (a) Trimethyl tin (SnMe₃)-terminated molecules are cleaved in the junction to yield direct Au–C linkages^{52,57} with a 100-fold increase in conductance compared to analogous junctions. (b) Aryldiazonium salts undergo *in situ* cathodic electrochemical reduction to form single-molecule junctions with strong covalent Au–C bonds that are stable over a long junction distance.^{65,66} (c) Aryl iodides in the STM-BJ demonstrate both dative Au–I and covalent Au–C linkages that result from the dissociation of the halide linker. (d) Air stable NHC-metal chloride complexes are electrochemically reduced *in situ* to form Au–M–C bonds under ambient junction conditions.⁶⁷ (e) Aryl iodides exhibit a bias dependent oxidative addition process in the junction. At more negative bias, the reaction is promoted, and the percent of Au–C bonds present increases with the dissociation of the labile iodide linker.

Diazonium salts. The cathodic electrochemical reduction of aryldiazonium salts can also be used to form single-molecule junctions with strong covalent Au–C bonds (Figure 1.4b).⁶⁵ These direct Au–C bonds are exceptionally stable over a long junction distance. In one study, molecular films terminated with diazonium salts at both ends underwent a radical reduction reaction,

followed by release of N₂, to form covalent metal-single molecule-semiconductor junctions between Au and Si.⁶⁶ The electron-poor diazonium spontaneously attached to both electrodes. These junctions showed a comparatively long junction lifetime of ~1 second⁶⁸, attributed to the robustness of the covalent Si–C and Au–C linkages.

Aryl iodides. Perhaps the most practical and economical approach to creating *in situ* Au–C contacts is the use of aryl iodides⁶⁹, which are common functional groups in organic chemistry. STM-BJ measurements performed on a series of asymmetric aryl iodides elucidated the binding modes (Figure 1.4c) of iodides to gold, demonstrating that both dative Au–I and covalent Au–C linkages were formed. Covalent linkages were formed from the dissociation of the iodide linker, the extent of which was mediated by the bias in an electrochemical environment. This relationship suggested an oxidative addition at the Au surface, as was demonstrated by experiments in a polar solvent that yielded Au–C bond formation (Figure 1.4e). More broadly, this dependence demonstrates the remarkable control of chemical reactivity in the junction through facile bias modulation. This work further opened the door to manipulating chemical transformations using the electric field generated in the molecular junction.

Carbenes. A less ubiquitous but no less versatile class of functional groups that readily link to metals are carbenes, neutral molecules comprising a divalent carbon atom with a six-electron valence shell.⁷⁰ Carbene anchors have been used to form trifunctional primed contacts that create a reactive site for the *in situ* growth of molecular wires.⁷¹ The metal–carbon π bond not only creates an efficient conduit for charge carriers, but was also active in olefin metathesis, and was further developed for catalytic polymer growth on functionalized ruthenium nanoparticles.⁷² This work laid the foundation for forming stable monolayers between carbenes and metals using solution phase chemistry. Carbenes can also be implemented as highly coupled linkers in single-molecule

devices. The rich chemistry and strong σ -donating ability of N-heterocyclic carbenes (NHCs) offer unique prospects for applications in nanoelectronics, sensing, and electrochemistry.^{73–78} Notably, however, direct linkage to Au could not be achieved with free NHCs in solution or via vapor phase NHC-CO₂.^{79,80} Therefore, in order to study the electron transport across single NHC-bound molecules with STM-BJ,⁶⁷ air stable NHC–metal chloride (NHC–M–Cl) complexes⁸¹ with M = Au, Ag, or Cu were synthesized. These NHC metal complexes were electrochemically reduced *in situ*^{82,83} to form NHC–M–electrode contacts under ambient conditions (Figure 1.4d). We note that this *in situ* electrochemical approach yielded not Au–C bonds, but Au–M–C bonds. The carbene delivered an additional metal atom to the Au electrode, forming mixed metal contact points (Figure 1.4d), which would normally be very synthetically challenging. By performing this chemistry *in situ*, the conductance properties through multiple metal contact points could be studied using only one set of electrodes.

The examples above show how simple chemical reactions in the junction have enabled great progress towards enhancing the conductance of single-molecule devices. Not all of these methods are suitable for scalable processes, as many require toxic and synthetically challenging molecules and present practical challenges. Nonetheless, these advancements as a whole represent a powerful new approach to Au–C bond formation, and moving towards ubiquitous functional groups like iodides demonstrates the growing potential of these systems. Furthermore, the oxidative addition and reductive elimination steps involved in these reactions are fundamental steps in organometallic catalysis and may be implemented in other junction reactions beyond the formation of Au–C contacts. The STM-BJ will undoubtedly uncover further methods of integrating common chemicals into robust circuits.

Electrochemically Gated Reactions

Controlling the switching between charge-transport states of a molecule in a metal-molecule junction remains one of the most challenging aspects of molecular electronics.⁸⁴ Electrochemical gating with the STM-BJ (Figure 1.5a) is an attractive method for controlling and studying bias-induced conductance switching, and it also presents an appealing way to discover and study nanoscale electrochemical catalysis. It obviates the need for exogenous chemicals or stimuli to induce reversible bond breakage and formation in molecular junctions. Using only the potential difference between the electrodes or the current through the molecule the connectivity of the molecule is altered to access large on/off conductance ratios. This section reviews some of the notable electrochemical gate-driven STM-BJ switches with a focus on the chemical reactions that drive the switching behavior

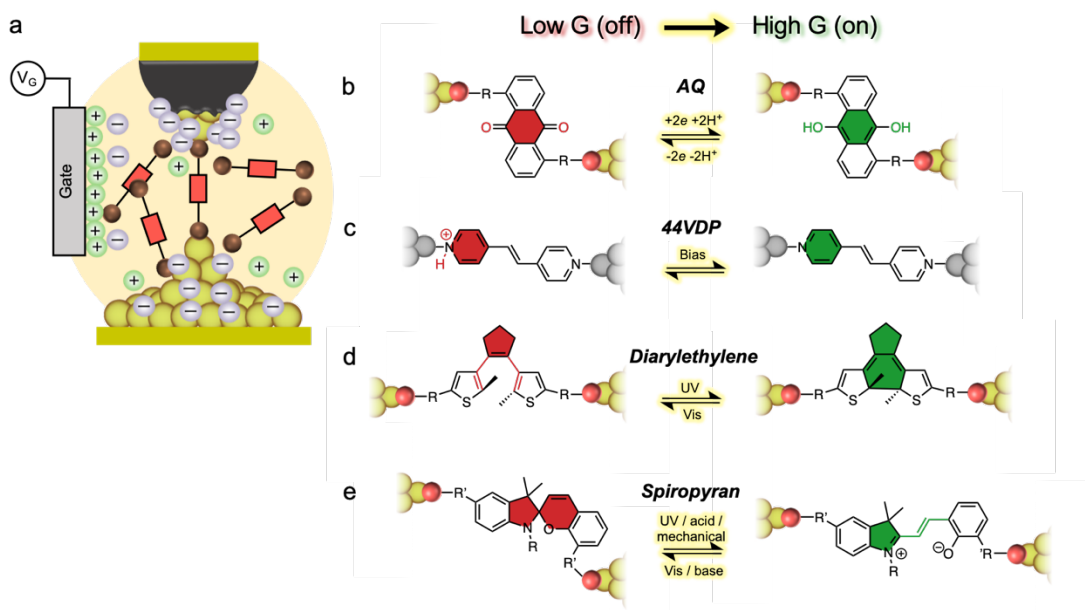


Figure 1.5 Electrochemically gated switches in the STM-BJ. (a) Schematic of a three-electrode electrochemically gated junction. The bias voltage between the two working electrodes and the

gate voltage can be controlled simultaneously. The tip is coated with a chemically inert wax such that the area of Au exposed to solution is drastically reduced compared to the substrate. A dense double layer of ions promotes electrochemical transformations via electron transfer. (b) Anthraquinones undergo electrochemical gating-induced reversible switching to hydroquinones, resulting in conductance changes greater than one order of magnitude.⁸⁴ (c) An applied potential is used in tandem with pH changes to induce switching in junctions comprising 4,4'-vinylenedipyridine between Ni electrodes (illustrated as grey spheres).⁸⁵ (d) Photochromic dithienylcyclopentenes exhibit optoelectronic switching upon irradiation resulting in a change of the conjugation and conductance of the molecule.^{86,87} (e) Spiropyrans respond to numerous orthogonal stimuli including light, pH and mechanical force to switch between and open and closed form.⁸⁸

Redox switches. Redox-active molecules are perfect candidates for reversible junction reactions. Anthraquinones are particularly attractive for facile systems to study switchable electrical properties, lending insight into redox and quantum interference behavior.⁸⁹ The reversible conductance tuning of two isomeric anthraquinone (AQ) derivatives (Figure 1.5b) was demonstrated using electrochemical gating-induced switching.⁸⁴ A reductive potential reversibly reduced the AQ derivatives to their hydroquinone analogs, and an oxidative bias reformed the original AQ, resulting in conductance changes greater than one order of magnitude. Notably, the change in the redox state of these molecules involves both breakage and formation of new C-H and O-H bonds. The on/off ratio was stable throughout cycling, demonstrating a highly reversible process.

An applied potential can also be used in tandem with pH changes to induce switching in junctions comprising 4,4'-vinylenedipyridine (44VDP) between nickel electrodes (Figure 1.5c)⁸⁵. Two distinct conductance states were observed upon varying the pH, and the pH at which switching was observed could be varied using the electrochemical gate potential. Protonation/deprotonation of the pyridine anchors caused the conductance switching, which could be seen within a single trace, suggesting the switching is stochastic and chemically (as opposed to

structurally) driven. This simultaneous control of pH and gate potential demonstrated how the STM-BJ technique can be used to study acid-base equilibria of single molecules, including the observation of discrete proton transfers to and from a single molecule within metal–molecule–metal junctions. In principle, this sensor could be used to detect pH changes as well as to measure the local pH. These studies demonstrate how the STM-BJ allows for facile, controlled switching of a single redox molecule, and detecting such processes at the single-molecule level provides insight into controlled transformations that are typically inaccessible through conventional ensemble techniques.^{90,91}

Externally Modulated Switches. In addition to chemical reactions in the STM-BJ induced by junction-based mechanisms, reactions can also be controlled in the junction using external stimuli. These stimuli replace exogenous chemicals or chemical catalysts that are used in prototypical synthetic reactions. The reactions discussed in this section involve two of the more commonly applied stimuli, light^{86,87,92–98}, and mechanical force^{99,100}, but are by no means an exhaustive list, as many other modes of catalysis can be incorporated (Box 1). External stimuli compatible with the junction range from light, mechanical force, protons,¹⁰¹ voltage,^{102–109} stereoelectronic effects,¹¹⁰ electric field,^{111–113} or magnetic field.^{114–116} Although these reactions are not strictly controlled by the junction, they are frequently incorporated into on/off switches that are essential to the field of nanoelectronics. Many of the observations regarding fundamental processes made at the single-molecule level cannot be gleaned from bulk chemistry, and inform our broader understanding of these chemical processes.

Optical switches have garnered widespread interest for their application to molecular electronics¹¹⁷ and many other emerging fields such as biomimetic catalysis¹¹⁸ and photopharmacology.¹¹⁹ Photochromic dithienylcyclopentenes have been used to achieve

optoelectronic switching⁸⁶ both in and out of the junction (Figure 1.5d). Outside of the junction, upon irradiation the covalent C–C bonds in the switchable moiety can be selectively broken or formed based on the wavelength of the light, resulting in a change of the conjugation and conductance of the molecule. In the junction, however, only an irreversible on-to-off switch is observed. The Au electrodes quench the first excited state of the open (off) form, preventing the reversal back to the closed (on) form. The quenching of a molecule by metal electrodes presents a general challenge to translating bulk chemistry to single-molecule behavior. Quenching can be avoided by decoupling the active site of a molecule from the electrodes, and diarylethylenes have become a common moiety in molecular switches. A modified diarylethylene covalently linked between graphene electrodes was also shown to reversibly photoswitch at room temperature.⁸⁷ The altered structure of the molecule decreased the coupling with the electrode to prevent problematic quenching. The switching ratio was greater than 100 and stable over many cycles. This adjustment highlights the importance of chemical design and the structure-function relationship between molecules, enhancing their utility in electronics as well as for adapting bulk chemistry to the single-molecule junction.

Switches in the junction can also be manipulated with orthogonal external stimuli to form logic gates,¹²⁰ by selectively stimulating a pH-sensitive moiety and a photochromic moiety to obtain four possible conductance states. Additionally, stimuli-specific spiropyran (SP) devices⁸⁸ were fabricated, in which both mechanical and chemical stimuli were used to probe bond strength. Spiropyran is a particularly prominent moiety due to the stark contrast between the closed form SP and open form merocyanine (MC) properties (Figure 1.5e), which can be harnessed in a single-molecule device for switching applications. These studies demonstrate the utility of the STM-BJ for finely investigating reactions at the single-molecule level by breaking and reforming junctions.

They also highlight the fundamental ease of using the STM-BJ to monitor reaction activity. Furthermore, they highlight some of the challenges that arise in *in situ* reactions that don't occur in the bulk, such as the quenching of molecules by electrodes the short lifetime of junctions formed in the STM-BJ. These challenges are important to identify so that they can be tackled as the field advances.

Electrostatic reactions

One of the most promising and practical aspects of break junction chemistry is the ability to catalyze reactions using an electric field. Catalyzing reactions involving non-redox active molecules using an electric field has long been theorized¹²¹, but has only recently been realized^{121–127}. Solution-based electric field catalysis offers an economic, environmentally friendly, and synthetically straightforward alternative to conventional methods that use exogenous chemical catalysts. Electric fields facilitate reactions of non-redox molecules by stabilizing transition states or minor charge separated resonance contributors^{91,128–130}. These otherwise less accessible transition states can potentially alter or tune selectivity,^{124,130–133} and depending on their alignment with respect to the field, can manipulate the kinetics and thermodynamics of non-redox processes. As such, electric field catalysis is potentially applicable to a wide scope of reactions, yet it remains incompletely understood^{127,134} and underdeveloped.

Two major challenges in expanding the applicability of this chemistry are precisely orienting the direction of the electric field with the reaction axis of a molecule, and applying such a highly oriented and intense field. STM-BJ offers a viable route to access this emerging field, since the solution around the nanoelectrodes is continuously exposed to a high electric field (Figure 1.6a). Over time, all of the molecules in a solution can be exposed to the field via diffusion and

local turbulence created by the moving tip. In this section, we focus on three examples that demonstrate how the electric field catalyzes an isomerization, a bimolecular reaction, and an intramolecular aromatization of non-redox active molecules.

Bimolecular reactions. A bimolecular, non-redox, bond forming process accelerated by an external electric field was exhibited for the first time using a Diels Alder cyclization of a surface tethered furan and a thiol-anchored norbornene derivative dienophile (Figure 1.6b).⁹¹ The preassembled layer of dienophile on the substrate allowed for unambiguous orientation of the double bond, whereas the tip-tethered diene was free to rotate and approach the dienophile in any of four possible orientations. The preassembled substrate layer was aligned with the field such that formation of only one low-energy product was sensitive to the field. The STM-BJ was used to supply the electric field and monitor the reaction *in situ*. A fivefold increase in the frequency of the reaction was observed when a large negative bias was applied, suggesting that the field facilitates electron flow from dienophile to diene, stabilizing an otherwise minor resonance contributor (Figure 1.7a). Although this Diels Alder reaction occurred on a preassembled surface, it could not be replicated in solution and suffered from an ultra-low conversion rate of a few molecules per hour. Furthermore, the results were never verified via comparison to products formed *ex situ*. This work, however, importantly demonstrated that the scope of electric field catalysis includes non-redox processes, vastly expanding the applicability of electrostatically catalyzed reactions.

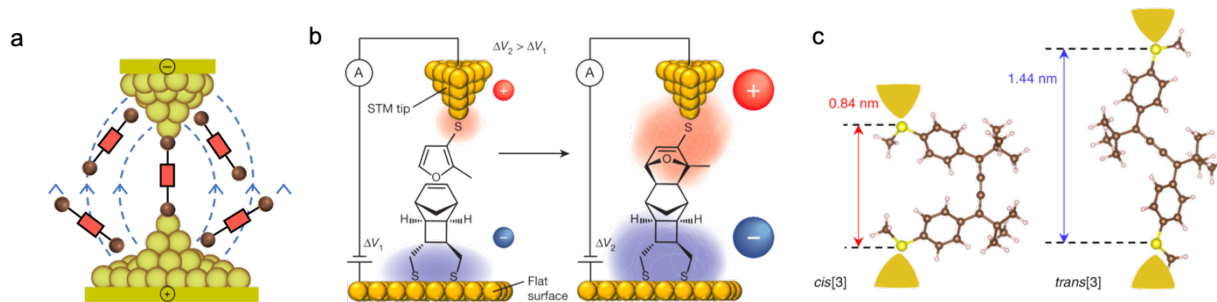


Figure 1.6 Electric field driven reactions in an STM. (a) Schematic of an electric field between an STM tip and substrate that is also present across the single-molecule junction. (b) A bimolecular, non-redox, bond forming process accelerated by an external electric field is demonstrated with the Diels Alder cyclization of a surface tethered furan and a thiol-anchored norbornene derivative dienophile.⁹¹ The STM-BJ is used to supply the electric field and monitor the reaction *in situ*. Reactants and products can be differentiated by characteristic conductance values and molecular plateau lengths. (c) Cumulenes undergo *cis-trans* isomerization in the presence of an electric field with an increased conversion rate compared to thermally controlled solutions. The reaction occurs throughout the solution near the junction. The dramatic difference in molecular conductance plateau length allows for *in situ* monitoring of the reaction.

Isomerization. Recently, the local electric field in the STM-BJ was used to catalyze the *cis-trans* isomerization of cumulenes (Figure 1.6c).¹³⁵ The external electric field increased the rate of isomerization and changed the distribution of *cis* and *trans* products. Because the conductance signatures of the *trans* and *cis* isomers are distinct due to the large difference in the displacement of the electrodes (Figure 1.6c), the reactants and products could be easily monitored *in situ* by STM-BJ. The quantitative distribution of *cis* and *trans* products revealed that at a positive bias, a solution of *cis* cumulene in the STM-BJ was converted to predominantly *trans*. Furthermore, by increasing the reaction time, enough *trans* product was generated for the sample to be analyzed by HPLC. The number of converted molecules far exceeds the number of single-molecule junctions formed, indicating that the reaction is catalyzed by the electric field and occurs throughout the solution near the tip.

The mechanistic rationale for this reaction illustrates the simple yet elegant way that an electric field can alter the selectivity and feasibility of a non-redox process. Using DFT to explore how the electrostatic field might alter reaction kinetics and thermodynamics to favor the *trans* isomer, the authors proposed that the rotational barrier to isomerization is energetically more accessible with an electric field. The electric field stabilized the otherwise less prominent polar zwitterionic resonance structure (Figure 1.7b), which enabled relatively free rotation around the terminal C–C bonds. This work demonstrates solution based, electric field-driven isomerization in a non-polar solvent that affords thermodynamic and kinetic control of product distribution, opening the door for more electrostatically controlled solution chemistry.

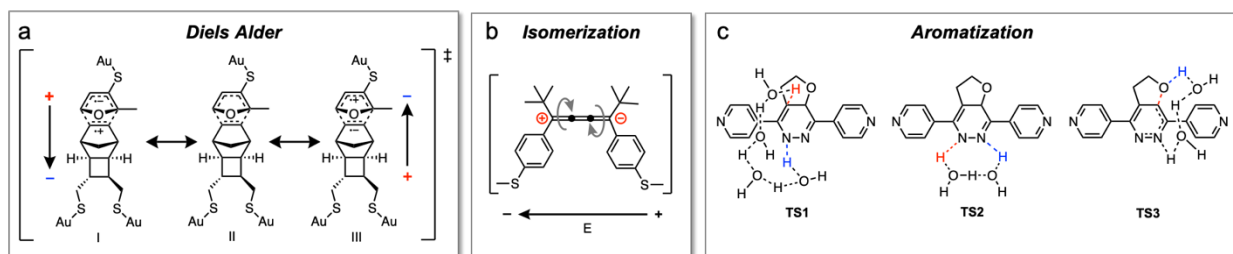


Figure 1.7 Key transition states for electric field catalyzed reactions in the STM-BJ. Non-redox processes are stabilized by the directional electric field, allowing for unique reactivity in the junction. (a) The electric field between the tip and substrate facilitates electron flow from dienophile to diene in a Diels-Alder cyclization, stabilizing an otherwise minor resonance contributor.⁹¹ (b) The electric field stabilizes the non-canonical zwitterionic resonance structure to facilitate the cis-trans isomerization of cumulenes.¹³⁵ (c) The second step in a cascade reaction involving an inverse electron demand Diels-Alder and subsequent aromatization is catalyzed in the junction by an electric field.¹³⁶ The field aligns only with the aromatization process and stabilizes the key transition states in the second step of a two-step reaction.

Aromatization. Tuning the orientation between an external electric field and the reaction axis can selectively catalyze an individual step of a cascade reaction. Figure 1.7c shows the key transition state for an inverse electron demand Diels-Alder reaction followed by an aromatization

reaction to form a fully conjugated, conducting final product.¹³⁶ Using a mechanically controlled break junction (MCBJ) in the presence of an electric field, only the second step of the two-step cascade is accelerated. The reaction axis of the Diels-Alder is orthogonal to that of the field, but the aromatization is aligned. Thus, the field catalyzes the aromatization step and accelerates it by an order of magnitude with applied bias, but the rate of cyclization remains unaffected. The ability to accelerate selected steps in a multistep process could be used to manipulate or even toggle between the kinetically or thermodynamically favored distribution of products in a multistep process.

The Future of Electric Field Catalysis. As a whole, these reactions highlight the scalable applications of solution-based electric field catalysis and the possible synthetic applications of chemistry discovered in the break junction. Reactions proceed under ambient conditions, and the local potential that drives them obviates the need for exogenous chemicals. These reactions are the closest facsimile to practical bulk chemistry as they occur in the solution around the tip and do not require junction formation. This mechanistic observation further widens the scope of these reactions to substrates without aurophilic linkers.¹³⁵ Simultaneously, the reactions also benefit from the ability to study them one molecule at a time, as the break junction allows for the monitoring of reaction kinetics.

Developing electric field catalysis as a practical synthetic tool still faces many challenges. Multiple experiments are required to glean mechanistic information, and often need to be supplemented by non-junction experiments. The technique also needs to be validated by *ex situ* formation of products. Because the distance between electrodes changes during the STM-BJ measurements, the magnitude of the field cannot be precisely determined and a quantitative measurement of field dependence is unavailable. These hurdles may be overcome by controlling

nanoenvironments surrounding reaction centers, employing microfluidic techniques, and architecting devices that allow for the application of an electric field in a confined nanoenvironment. These fundamental experiments, however, have cemented the STM-BJ as a critical tool to explore the burgeoning field of electrostatic catalysis.

1.5 Probing Single-Molecule Reactions

The advents of both STM and atomic force microscopy (AFM)¹³⁷ have enabled atomic scale resolution for imaging reactants and products, and have opened the door to both monitor and control reactions at the single-molecule level. Capitalizing on the foundational work discussed in section 2.1 and using the seminal reactions as a springboard, more recent work has focused on applying these techniques to control reaction chemistry in more complex systems. For example, ligand functionalization of metals has been expanded beyond the deposition of CO to complexation of larger, more intricate organic molecules,^{11,138} and tip-induced radical formation and dehalogenation have been used to induce intramolecular rearrangements and ring formation in polycyclic aromatic systems.^{139,140} Importantly, these reactions are tip-induced and not thermally induced, contrasting with single-molecule surface reactions that are achieved through annealing. STM-AFM has been used to resolve thermal assisted reactions such as complex cyclization cascades¹⁴¹ and many rearrangements and couplings.^{47,48} Much of this work has been reviewed previously.¹⁴² In this section, we highlight some of the most recent achievements in single-molecule reactions and discuss the evolution of the field to new techniques like the break junction that allow us to control not only surface reactions at the single-molecule level but solution-based chemistry as well.

Recently, low temperature STM-AFM was used to synthesize the highly elusive carbon allotrope, cylco[18]carbon (C-18), on a Cu(111) surface.¹⁴³ Starting with C₂₄O₆, voltage pulses were applied for a few seconds at a time, resulting in the decarbonylation of two, four or six CO moieties and a 13% yield of the fully decarbonylated product, C-18 (Figure 1.8a). This molecule could be deliberately reversibly switched between its two charge states, resulting in different geometries imaged by STM and AFM. Furthermore, by applying an elevated bias, two partially decarbonylated molecules could be fused together resulting in a covalent coupling reaction of neighboring molecules. This work represents a milestone in the applicability of tip-induced chemistry to achieve elusive reactivity and capture molecules that cannot be studied using more conventional synthetic techniques, though the constraints of on-surface reactions still apply. The reaction requires an inert surface and low temperature (5 K), and sublimation of the material onto the Cu surface induced partial decarbonylation and dissociation of CO molecules prior to tip modulation.

One of the unique aspects of the break junction technique is the ability to effect and observe reactions in a solution that occur one molecule at a time.^{6,7,141} In contrast to previous approaches to single-molecule reactivity that require pre-assembled molecules on a surface, the works highlighted in the rest of this section are the first observations of controlled single-molecule bond formation between molecules dispersed in solution. We stress that these solution-based reactions much more closely resemble conventional reactions, which will ultimately prove critical for gaining insight into real-world applications and phenomena. These proof-of-principle studies offer a new model for interrogating chemical reactions at the single-molecule level and for the precise construction of molecular nanostructures that are otherwise challenging to create via conventional macroscopic methods.

The first demonstration of a truly single-molecule bond formation process in solution was the electrochemical manipulation of a Au–N contact to modify charge transport across the interface (Figure 1.8b).¹⁴⁴ Using a series of oligophenylenediamine wires, the authors demonstrated that an oxidizing bias led to *in situ* formation of a new type of Au–N bond in the break junction. Normally, amines bind selectively to undercoordinated Au atoms through dative interactions^{145,146}, but by changing the magnitude of the positive bias in the STM-BJ, the anilines showed three discrete conducting states. The higher conductance states represented newly formed covalent bonds between the Au and N, analogous to the self-assembly of thiolate monolayers on a Au surface.^{147–150} The ultra-high conductance state delivered the highest reported conductance values for all known oligophenylen contacts,^{56,151,152} achieving better electronic coupling *in situ* than covalent Au–S or Au–C bonds.¹⁵²

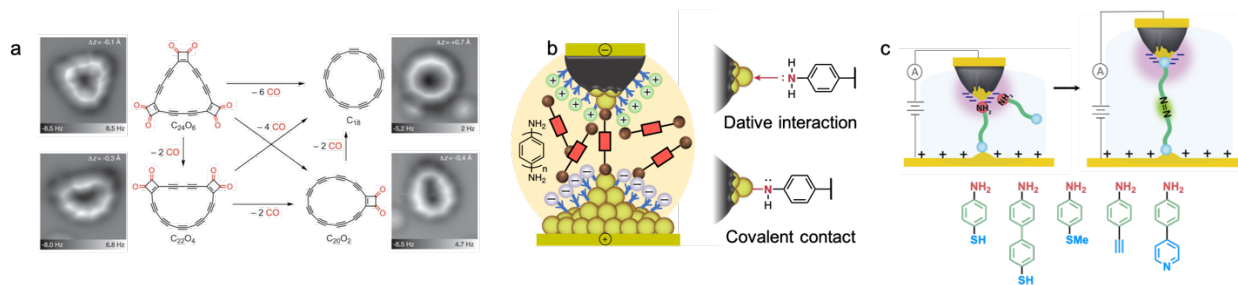


Figure 1.8 *Inducing reactivity one molecule at a time.* (a) Synthesis of the carbon allotrope cyclo[18]carbon (C-18) on a Cu(111) surface, using voltage pulses to induce decarbonylation.¹⁴³ AFM images in the right- and left-most columns show the molecule at each stage of decarbonylation. (b) Schematic of the oligophenylenediamine junction, and distinct binding modes of the amine linker. The electrochemical manipulation of the Au–N contact modifies the charge transport across the interface, resulting in oligophenylenediamine wires with low, high and ultra-high conductance states.¹⁴⁴ The difference in conductance is attributed to the increasingly covalent nature of the Au–N bond under an oxidative bias. (c) Schematic of *in situ* azobenzene formation with applied bias and substrate. The electrooxidative homocoupling of a various anilines in the STM-BJ leads to formation of azobenzenes showing the versatility of this reaction mechanism.¹⁵³

A subsequent study showed that a series of asymmetric anilines could undergo *in situ* electrooxidative homocoupling in the STM-BJ to form azobzenenes¹⁵³ (Figure 1.8c). Oxidative coupling reactions are important for chemical synthesis and bioconjugation¹⁵⁴ as an alternative to traditional cross-coupling strategies,¹⁵⁵ and the development of nanocatalysts and electrosynthetic techniques to effect such transformations offer a versatile and environmentally friendly synthetic alternative.^{156–158} In the STM-BJ, anilines underwent a “one-pot” selective oxidative coupling to form azobzenenes on the nanostructured Au STM tip under oxidative bias. The *in situ* coupling reaction was robust, with a variety of anilines comprising different aurophilic linkers and backbone lengths reacting quickly and reproducibly under an oxidative bias (Figure 1.8c). The selective synthesis of geometric isomers depending on the linker was also demonstrated. Notably, in the case of the pyridine linked aniline, the *cis* isomer is formed and not the more energetically stable *trans* isomer that is formed in bulk synthesis. This unexpected conformation demonstrated how the junction can impart new selectivity to a reaction. Furthermore, sequential coupling of complementary anilines could be achieved in the junction, resulting in complex molecular architectures that are more synthetically onerous. Thus, chemicals that were not formed *ex situ* could still be accessed and probed.

Together, these reactions stress the unique characteristics of reactions in the junction which are enumerated using the *in situ* formation of azobzenenes as a demonstrative example. First, the necessary voltage to trigger the electrooxidation at the tip was lower than the oxidation potential of aniline and its derivatives,^{159,160} suggesting that the redox transformation in the junction was facilitated by the attachment of the anilines to undercoordinated Au atoms (active sites). This low voltage contrasts with homogeneous bulk syntheses requiring strong oxidants, often in stoichiometric quantities.¹⁶¹ Second, the immediate formation of the longer molecule, as evidenced

by a characteristic conductance signature, is significant, demonstrating that an individual aniline caught in the single-molecule junction underwent a one-electron oxidation by the Au tip to initiate the reaction. After the observation of the longer azobenzene, if the bias was subsequently decreased, only the shorter anilines were observed, reinforcing that only the molecules caught in the junction underwent transformation. A low percentage of longer molecules in solution led to a small probability of measuring them, once the bias was decreased. This behavior further contrasts these reactions with those discussed earlier, such as the isomerization of cumulenes, where the bulk of the solution is converted.

These solution-based single-molecule reactions demonstrate the unprecedented and exquisitely precise control of bond formation that the STM-BJ offers. These reactions are performed under ambient conditions and require no exogenous chemicals or preassembled molecular layers. Observing and controlling these fundamentally nanoscale processes in individual molecules promises levels of precision beyond those achieved through traditional ensemble techniques. The experimental implementation of such concepts, however, remains a major challenge. Although the single-molecule reactions are not yet practical for large-scale synthesis, the control over single-molecule bond formation may inform the mechanistic reaction pathways of synthetic redox reactions and illuminate new avenues for molecular design. For instance, the STM-BJ can be used to apply a large, directional electric field across a molecule to investigate its effect on the reactivity of the system. This strategy is a relatively easy approach to testing a number of reactions, and the understanding gathered through these measurements could be used to develop new catalysts *de novo* with built-in electric fields. These studies and similar ongoing efforts will drive forward the fundamental understanding of nanoscale chemical and physical phenomena.

1.6 Conclusion and Outlook

The reactions detailed in this chapter have opened the door for more detailed interrogation into reaction chemistry. Instruments originally built for imaging and molecular interrogation have become powerful reaction tools. Manipulations of single-molecules bound to metal surfaces have demonstrated exquisite control over chemical processes. Break junction techniques have expanded these capabilities to include reactions in solutions, obviating the need for stringent conditions such as UHV and low temperatures or additional steps such as chemical deposition and extraction of products. Solution-based techniques can accommodate not only organometallic reactions but purely organic reactions as well where products are free floating in solution, away from the electrodes. The STM enhances utility where the break junction lacks, permitting larger molecules, intermediates, and reactions on inert surfaces to be studied in more detail than ever before. These reactions span a wide range of transformations including bimolecular reactions as well as isomerizations and rearrangements that involve breakage and formation of new chemical bonds.

Synthesizing and probing single-molecules with the STM tip in solution offers a deeper understanding of single-molecule processes and may lead to new discoveries in bulk solution-based chemistry. By highlighting and categorizing these achievements, one can see how close examination of the chemistry that occurs in the STM informs a variety of reaction types and modes of catalysis, including photochemistry, electrochemical and electric field catalysis, organometallic chemistry, and more. Together, chemists and physicists are now presented with the challenge of developing these reactions in a practical and scalable way that bears on both synthetic chemistry and molecular electronic design. A crucial area of exploration will be designing versions of junctions that accommodate bulk transformations. Another important capability will be integrating

the ability of the STM to monitor reactions *in situ* with more conventional techniques for analyzing products like nuclear magnetic resonance spectroscopy or mass spectrometry. These developments may also preclude the need for multiple experimental conditions or supplementing junction studies with non-junction experiments that are currently required in order to glean mechanistic insight and validate some results. Furthermore, each niche area of catalysis will encounter its own challenges: Electrostatic reactions would benefit from a method to quantify the magnitude of the electric field dependence. The performance and endurance of molecular switches that incorporate orthogonal stimuli such as photo-excitation would benefit from new methods to prevent quenching by the electrodes. Finally, reactions that occur only when molecules are held between the electrodes are the furthest from being developed for large-scale synthesis yet offer the most precise control over reactivity. These experiments, however, could be used now as testbeds for catalytic systems, providing a rapid and robust approach to probing the effect of directional electric fields on molecules and reactions.

In order to approach these practical hurdles, however, questions about the rules that govern chemistry in the junction need to be addressed. It is imperative that these reactions be interrogated in the same way that bulk synthetic chemistry is assessed with the familiar chemistry vernacular: What kind of selectivity can be achieved with these reactions? What energy barriers can be overcome by using the junction to catalyze reactions? Can the kinetic and thermodynamic forces of the junction be bridled in a way that we achieve the requisite control over chemical behavior? As junction reactions are incorporated into the canon of chemical synthesis, answers to these questions will emerge, unveiling a roadmap for future application and expansion.

In the following chapters, reactivity in the single molecule junction is explored via aryl halides. First, the dehalogenation and resulting binding modes of aryl iodides are elucidated and

discussed. Subsequently, *in situ* reactions of aryl iodides are investigated, including dimerization (Ullmann coupling) and cross-coupling processes. Important mechanistic insight is gleaned from required reaction conditions and observed reactivity, relating single molecule chemistry back to bulk chemistry. Lastly, the binding energetics and geometry of a different class of linkers, cyclopropenylidenes, to metal surfaces is interrogated via surface analysis. Taken together, these studies at the single molecule level bring us closer to answering fundamental questions regarding the rules governing chemistry, both in the junction and in the bulk.

1.7 References

- (1) Skubi, K. L.; Blum, T. R.; Yoon, T. P. Dual Catalysis Strategies in Photochemical Synthesis. *Chem. Rev.* **2016**, *116*, 10035–10074.
- (2) Twilton, J.; Le, C. C.; Zhang, P.; Shaw, M. H.; Evans, R. W.; Macmillan, D. W. C. The Merger of Transition Metal and Photocatalysis. *Nat. Rev. Chem.* **2017**, *1*, 0052.
- (3) Wang, F.; Stahl, S. S. Merging Photochemistry with Electrochemistry: Functional-Group Tolerant Electrochemical Amination of C(Sp₃)-H Bonds. *Angew. Chem. Int. Ed.* **2019**, *58*, 6385–6390.
- (4) Zhang, W.; Carpenter, K. L.; Lin, S. Electrochemistry Broadens the Scope of Flavin Photocatalysis: Photoelectrocatalytic Oxidation of Unactivated Alcohols. *Angew. Chem. Int. Ed.* **2020**, *59*, 409–417.
- (5) Kim, H.; Kim, H.; Lambert, T. H.; Lin, S. Reductive Electrophotocatalysis: Merging Electricity and Light To Achieve Extreme Reduction Potentials. *J Am Chem Soc* **2020**, *142*, 2087–2092.
- (6) Lee, H. J.; Ho, W. Single-Bond Formation and Characterization with a Scanning Tunneling Microscope. *Science*. **1999**, *286*, 1719–1723.
- (7) Hla, S.; Bartels, L.; Meyer, G.; Rieder, K. Inducing All Steps of a Chemical Reaction with

the Scanning Tunneling Microscope Tip: Towards Single Molecule Engineering. *Phys. Rev. Lett.* **2000**, *85* (13), 2777–2780.

- (8) Minato, T.; Kajita, S.; Pang, C. L.; Asao, N.; Yamamoto, Y.; Nakayama, T.; Kawai, M.; Kim, Y. Tunneling Desorption of Single Hydrogen on the Surface of Titanium Dioxide. *ACS Nano* **2015**, *9* (7), 6837–6842.
- (9) Borca, B.; Michnowicz, T.; Pétuya, R.; Pristl, M.; Schendel, V.; Pentegov, I.; Kraft, U.; Klauk, H.; Wahl, P.; Gutzler, R.; et al. Electric-Field-Driven Direct Desulfurization. *ACS Nano* **2017**, *11*, 4703–4709.
- (10) Ohmann, R.; Vitali, L.; Kern, K. Actuated Transitory Metal-Ligand Bond as Tunable Electromechanical Switch. *Nano Lett.* **2010**, *10* (8), 2995–3000.
- (11) Mohn, F.; Repp, J.; Gross, L.; Meyer, G.; Dyer, M. S.; Persson, M. Reversible Bond Formation in a Gold-Atom-Organic-Molecule Complex as a Molecular Switch. *Phys. Rev. Lett.* **2010**, *105* (26), 1–4.
- (12) Liljeroth, P.; Repp, J.; Meyer, G. Current-Induced Hydrogen Tautomerization and Conductance Switching of Naphthalocyanine Molecules. *Science*. **2007**, *317*, 1203–1206.
- (13) Simic-Milosevic, V.; Mehlhorn, M.; Rieder, K. H.; Meyer, J.; Morgenstern, K. Electron Induced Ortho-Meta Isomerization of Single Molecules. *Phys. Rev. Lett.* **2007**, *98* (11), 1–4.
- (14) Maksymovych, P.; Sorescu, D. C.; Jordan, K. D.; Yates, J. T. Collective Reactivity of Molecular Chains Self-Assembled on a Surface. *Science*. **2008**, *322* (5908), 1664–1667.
- (15) Neél, N.; Lattelais, M.; Bocquet, M. L.; Kröger, J. Depopulation of Single-Phthalocyanine Molecular Orbitals upon Pyrrolic-Hydrogen Abstraction on Graphene. *ACS Nano* **2016**, *10* (2), 2010–2016.
- (16) Shen, T. C.; Wang, C.; Abeln, G. C.; Tucker, J. R.; Lyding, J. W.; Avouris, P.; Walkup, R. E. Atomic-Scale Desorption through Electronic and Vibrational Excitation Mechanisms. *Science*. **1995**, *268* (5217), 1590–1592.
- (17) Serrate, D.; Moro-Lagares, M.; Piantek, M.; Pascual, J. I.; Ibarra, M. R. Enhanced Hydrogen Dissociation by Individual Co Atoms Supported on Ag(111). *J. Phys. Chem. C* **2014**, *118*

(11), 5827–5832.

- (18) Qiu, X. H.; Nazin, G. V.; Ho, W. Mechanisms of Reversible Conformational Transitions in a Single Molecule. *Phys. Rev. Lett.* **2004**, *93* (19), 1–4.
- (19) Alemani, M.; Peters, M. V.; Hecht, S.; Rieder, K.; Moresco, F.; Grill, L. Electric Field-Induced Isomerization of Azobenzene by STM. *J. Am. Chem. Soc.* **2006**, *128*, 14446–14447.
- (20) Lastapis, M.; Martin, M.; Riedel, D.; Hellner, L.; Comtet, G.; Dujardin, G. Picometer-Scale Electronic Control of Molecular Dynamics inside a Single Molecule. *Science*. **2005**, *308* (5724), 1000–1003.
- (21) Iancu, V.; Deshpande, A.; Hla, S. W. Manipulating Kondo Temperature via Single Molecule Switching. *Nano Lett.* **2006**, *6* (4), 820–823.
- (22) Henningsen, N.; Franke, K. J.; Torrente, I. F.; Schulze, G.; Priewisch, B.; Rück-Braun, K.; Dokić, J.; Klamroth, T.; Saalfrank, P.; Pascual, J. I. Inducing the Rotation of a Single Phenyl Ring with Tunneling Electrons. *J. Phys. Chem. C* **2007**, *111* (40), 14843–14848.
- (23) Simic-Milosevic, V.; Morgenstern, K. Bending a Bond within an Individual Adsorbed Molecule. *J. Am. Chem. Soc.* **2009**, *131* (2), 416–417.
- (24) Yongfeng, W.; Kröger, J.; Berndt, R.; Hofer, W. A. Pushing and Pulling a Sn Ion through an Adsorbed Phthalocyanine Molecule. *J. Am. Chem. Soc.* **2009**, *131* (10), 3639–3643.
- (25) Grill, L.; Rieder, K. H.; Moresco, F. Exploring the Interatomic Forces between Tip and Single Molecules during STM Manipulation. *Nano Lett.* **2006**, *6* (12), 2685–2689.
- (26) Grill, L.; Rieder, K. H.; Moresco, F.; Rapenne, G.; Stojkovic, S.; Bouju, X.; Joachim, C. Rolling a Single Molecular Wheel at the Atomic Scale. *Nat. Nanotechnol.* **2007**, *2* (2), 95–98.
- (27) Kudernac, T.; Ruangsrapichat, N.; Parschau, M.; MacIá, B.; Katsonis, N.; Harutyunyan, S. R.; Ernst, K. H.; Feringa, B. L. Electrically Driven Directional Motion of a Four-Wheeled Molecule on a Metal Surface. *Nature* **2011**, *479* (7372), 208–211.

- (28) Gimzewski, J. K.; Joachim, C. Nanoscale Science of Single Molecules Using Local Probes. *Science*. **1999**, *283* (5408), 1683–1688.
- (29) Jung, T. A.; Schlittler, R. R.; Gimzewski, J. K.; Tang, H.; Joachim, C. Controlled Room-Temperature Positioning of Individual Molecules: Molecular Flexure and Motion. *Science*. **1996**, *271* (5246), 181–184.
- (30) Eigler, D. M.; Schweizer, E. K. Positioning Single Atoms with Scanning Tunnelling Microscope. *Nature* **1990**, *344* (April), 524.
- (31) Dujardin, G.; Walkup, R. E.; Avouris, P. Dissociation of Individual Molecules with Electrons from the Tip of a Scanning Tunneling Microscope. *Science*. **1992**, *255* (5049), 1232–1235.
- (32) Meyer, G.; Bartels, L.; Zöphel, S.; Henze, E.; Rieder, K. H. Controlled Atom by Atom Restructuring of a Metal Surface with the Scanning Tunneling Microscope. *Phys. Rev. Lett.* **1997**, *78* (8), 1512–1515.
- (33) Bartels, L.; Meyer, G.; Rieder, K. H. Basic Steps of Lateral Manipulation of Single Atoms and Diatomic Clusters with a Scanning Tunneling Microscope Tip. *Phys. Rev. Lett.* **1997**, *79* (4), 697–700.
- (34) Bartels, L.; Meyer, G.; Rieder, K. H. Dynamics of Electron-Induced Manipulation of Individual CO Molecules on Cu(111). *Phys. Rev. Lett.* **1998**, *80* (9), 2004–2007.
- (35) Stipe, B. C.; Rezaei, M. A.; Ho, W.; Gao, S.; Persson, M.; Lundqvist, B. I. Single-Molecule Dissociation by Tunneling Electrons. *Phys. Rev. Lett.* **1997**, *78* (23), 4410–4413.
- (36) Lauhon, L. J.; Ho, W. Single-Molecule Chemistry and Vibrational Spectroscopy: Pyridine and Benzene on Cu(001). *J. Phys. Chem. A* **2000**, *104* (11), 2463–2467.
- (37) Crommie, M. F.; Lutz, C. P.; Eigler, D. M. Confinement of Electrons to Quantum Corrals on a Metal Surface. *Science*. **1993**, *262* (5131), 218–220.
- (38) Mette, G.; Adamkiewicz, A.; Reutzel, M.; Koert, U.; Dürr, M.; Höfer, U. Controlling an SN₂ Reaction by Electronic and Vibrational Excitation: Tip-Induced Ether Cleavage on Si(001). *Angew. Chemie - Int. Ed.* **2019**, *58* (11), 3417–3420.

- (39) Ullman, F.; Bielecki, J. Ueber Synthesen in Der Biphenylreihe. *J. Ber. Dtsch. Chem. Ges.* **1901**, *34*, 2174–2185.
- (40) Mondal, S. Recent Advancement of Ullmann-Type Coupling Reactions in the Formation of C–C Bond. *ChemTexts* **2016**, *2*, 17.
- (41) Cai, J.; Ruffieux, P.; Jaafar, R.; Bieri, M.; Braun, T.; Blankenburg, S.; Muoth, M.; Seitsonen, A. P.; Saleh, M.; Feng, X.; et al. Atomically Precise Bottom-up Fabrication of Graphene Nanoribbons. *Nat. Lett.* **2010**, *466*, 470–473.
- (42) Pavliček, N.; Gawel, P.; Kohn, D. R.; Majzik, Z.; Xiong, Y.; Meyer, G.; Anderson, H. L.; Gross, L. Polyyne Formation via Skeletal Rearrangement Induced by Atomic Manipulation. *Nat. Chem.* **2018**, *10*, 853–858.
- (43) Albrecht, F.; Rey, D.; Fatayer, S.; Schulz, F.; Pérez, D.; Peña, D.; Gross, L. Intramolecular Coupling of Terminal Alkynes by Atom Manipulation. *Angew. Chemie - Int. Ed.* **2020**, *59* (51), 22989–22993.
- (44) Song, S.; Guo, N.; Li, X.; Li, G.; Haketa, Y.; Telychko, M.; Su, J.; Lyu, P.; Qiu, Z.; Fang, H.; et al. Real-Space Imaging of a Single-Molecule Monoradical Reaction. *J. Am. Chem. Soc.* **2020**, *142* (31), 13550–13557.
- (45) Zhou, X.; Wang, C.; Zhang, Y.; Cheng, F.; He, Y.; Shen, Q.; Shang, J.; Shao, X.; Ji, W.; Chen, W.; et al. Steering Surface Reaction Dynamics with a Self-Assembly Strategy: Ullmann Coupling on Metal Surfaces. *Angew. Chemie - Int. Ed.* **2017**, *56* (42), 12852–12856.
- (46) Geagea, E.; Jeannoutot, J.; Féron, M.; Palmino, F.; Thomas, C. M.; Rochefort, A.; Chérioux, F. Collective Radical Oligomerisation Induced by an STM Tip on a Silicon Surface. *Nanoscale* **2021**, *13* (1), 349–354.
- (47) Kawai, S.; Haapasilta, V.; Lindner, B. D.; Tahara, K.; Spijker, P.; Buitendijk, J. A.; Pawlak, R.; Meier, T.; Tobe, Y.; Foster, A. S.; et al. Thermal Control of Sequential On-Surface Transformation of a Hydrocarbon Molecule on a Copper Surface. *Nat. Commun.* **2016**, *7*, 12711.
- (48) Clair, S.; De Oteyza, D. G. Controlling a Chemical Coupling Reaction on a Surface: Tools and Strategies for On-Surface Synthesis. *Chem. Rev.* **2019**, *119* (7), 4717–4776.

- (49) Piskun, I.; Blackwell, R.; Jornet-Somoza, J.; Zhao, F.; Rubio, A.; Louie, S. G.; Fischer, F. R. Covalent C-N Bond Formation through a Surface Catalyzed Thermal Cyclodehydrogenation. *J. Am. Chem. Soc.* **2020**, *142* (8), 3696–3700.
- (50) Ratera, I.; Veciana, J. Playing with Organic Radicals as Building Blocks for Functional Molecular Materials. *Chem. Soc. Rev.* **2012**, *41* (1), 303–349.
- (51) Nitzan, A.; Ratner, M. A. Electron Transport in Molecular Wire Junctions. *Science*. **2003**, *300*, 1384–1389.
- (52) Cheng, Z.; Skouta, R.; Vazquez, H.; Widawsky, J. R.; Schneebeli, S.; Chen, W.; Hybertsen, M. S.; Breslow, R.; Venkataraman, L. In Situ Formation of Highly Conducting Covalent Au–C Contacts for Single-Molecule Junctions. *Nat. Nanotechnol.* **2011**, *6* (6), 353–357.
- (53) Kiguchi, M.; Tal, O.; Wohlthat, S.; Pauly, F.; Krieger, M.; Djukic, D.; Cuevas, J. C.; Ruitenbeek, J. M. Van. Highly Conductive Molecular Junctions Based on Direct Binding of Benzene to Platinum Electrodes. *Phys. Rev. Lett.* **2008**, *101*, 046801.
- (54) Kaneko, S.; Nakazumi, T.; Kiguchi, M. Fabrication of a Well-Defined Single Benzene Molecule Junction Using Ag Electrodes. *J. Phys. Chem. Lett.* **2010**, *1* (24), 3520–3523.
- (55) Schneebeli, S. T.; Kamenetska, M.; Cheng, Z.; Skouta, R.; Friesner, R. A.; Venkataraman, L.; Breslow, R. Single-Molecule Conductance through Multiple π - π -Stacked Benzene Rings Determined with Direct Electrode-to-Benzene Ring Connections. *J. Am. Chem. Soc.* **2011**, *133*, 2136–2139.
- (56) Martin, C. A.; Ding, D.; Sørensen, J. K.; Bjørnholm, T.; Ruitenbeek, J. M. Van; van der Zant, H. S. J. Fullerene-Based Anchoring Groups for Molecular Electronics. *J. Am. Chem. Soc.* **2008**, *130*, 13198–13199.
- (57) Bulten, E. J.; Budding, H. A. The Synthesis of Small-Ring Monostannacycloalkanes. *J. Organomet. Chem.* **1976**, *110*, 167–174.
- (58) Xu, B.; Tao, N. J. Measurement of Single-Molecule Resistance by Repeated Formation of Molecular Junctions. *Science*. **2003**, *301*, 1221–1223.
- (59) Venkataraman, L.; Klare, J. E.; Tam, I. W.; Nuckolls, C.; Hybertsen, M. S.; Steigerwald, M. L. Single-Molecule Circuits with Well-Defined Molecular Conductance. *Nano Lett.*

2006, 6 (3), 458–462.

- (60) Hybertsen, M. S.; Venkataraman, L.; Klare, J. E.; Whalley, A. C.; Steigerwald, M. L.; Nuckolls, C. Amine-Linked Single-Molecule Circuits: Systematic Trends across Molecular. *J. Phys. Condens. Matter* **2008**, *20*, 374115.
- (61) Olavarria-Contreras, I. J.; Perrin, M. L.; Chen, Z.; Klyatskaya, S.; Ruben, M.; Van Der Zant, H. S. J. C-Au Covalently Bonded Molecular Junctions Using Nonprotected Alkynyl Anchoring Groups. *J. Am. Chem. Soc.* **2016**, *138* (27), 8465–8469.
- (62) Hong, W.; Li, H.; Liu, S.; Fu, Y.; Li, J.; Kaliginedi, V.; Decurtins, S.; Wandlowski, T. Trimethylsilyl-Terminated Oligo(Phenylene Ethynylene)s: An Approach to Single-Molecule Junctions with Covalent Au–C Σ -Bonds. *J. Am. Chem. Soc.* **2012**, *134* (47), 19425–19431.
- (63) Bennett, M. A.; Bhargava, S. K.; Hockless, D. C. R.; Welling, L. L.; Willis, A. C. Dinuclear Cycloaurated Complexes Containing Bridging (2-Diphenylphosphino)Phenylphosphine and (2-Diethylphosphino)Phenylphosphine, C₆H₄PR₂ (R = Ph, Et). Carbon-Carbon Bond Formation by Reductive Elimination at a Gold(II)-Gold(II) Center. *J. Am. Chem. Soc.* **1996**, *118* (43), 10469–10478.
- (64) Chen, W.; Widawsky, J. R. Highly Conducting π -Conjugated Molecular Junctions Covalently Bonded to Gold Electrodes. *J. Am. Chem. Soc.* **2011**, *133* (43), 17160–17163.
- (65) Hines, T.; Díez-Pérez, I.; Nakamura, H.; Shimazaki, T.; Asai, Y.; Tao. Controlling Formation of Single-Molecule Junctions by Electrochemical Reduction of Diazonium Terminal Groups. *J. Am. Chem. Soc.* **2013**, *135*, 3319–3322.
- (66) Peiris, C. R.; Vogel, Y. B.; Brun, A. P. Le; Aragone, A. C.; Coote, M. L.; Ismael, D.; Ciampi, S.; Darwish, N. Metal – Single-Molecule – Semiconductor Junctions Formed by a Radical Reaction Bridging Gold and Silicon Electrodes. *J. Am. Chem. Soc.* **2019**, *141*, 14788–14797.
- (67) Doud, E. A.; Inkpen, M. S.; Lovat, G.; Montes, E.; Paley, D. W.; Steigerwald, M. L.; Vázquez, H.; Venkataraman, L.; Roy, X. In Situ Formation of N-Heterocyclic Carbene-Bound Single-Molecule Junctions. *J. Am. Chem. Soc.* **2018**, *140* (28), 8944–8949.
- (68) Pla-Vilanova, P.; Aragonès, A. C.; Ciampi, S.; Sanz, F.; Darwish, N.; Diez-Perez, I. The

Spontaneous Formation of Single-Molecule Junctions via Terminal Alkynes. *Nanotechnology* **2015**, *26*, 381001.

- (69) Starr, R. L.; Fu, T.; Doud, E. A.; Stone, I.; Roy, X.; Venkataraman, L. Gold–Carbon Contacts from Oxidative Addition of Aryl Iodides. *J. Am. Chem. Soc.* **2020**, *142* (15), 7128–7133.
- (70) Bourissou, D.; Guerret, O.; Gabbaï, F. P.; Bertrand, G. Stable Carbenes. *Chem. Rev.* **2000**, *100* (1), 39–91.
- (71) Tulevski, G. S.; Myers, M. B.; Hybertsen, M. S.; Steigerwald, M. L.; Nuckolls, C. Formation of Catalytic Metal-Molecule Contacts. *Science* **2005**, *309* (5734), 591–594.
- (72) Ren, F.; Feldman, A. K.; Carnes, M.; Steigerwald, M.; Nuckolls, C. Polymer Growth by Functionalized Ruthenium Nanoparticles. *Macromolecules* **2007**, *40* (23), 8151–8155.
- (73) Zhukhovitskiy, A. V.; MacLeod, M. J.; Johnson, J. A. Carbene Ligands in Surface Chemistry: From Stabilization of Discrete Elemental Allotropes to Modification of Nanoscale and Bulk Substrates. *Chem. Rev.* **2015**, *115* (20), 11503–11532.
- (74) Zhukhovitskiy, A. V.; Mavros, M. G.; Van Voorhis, T.; Johnson, J. A. Addressable Carbene Anchors for Gold Surfaces. *J. Am. Chem. Soc.* **2013**, *135* (20), 7418–7421.
- (75) Crudden, C. M.; Horton, J. H.; Narouz, M. R.; Li, Z.; Smith, C. A.; Munro, K.; Baddeley, C. J.; Larrea, C. R.; Drevniok, B.; Thanabalasingam, B.; et al. Simple Direct Formation of Self-Assembled N-Heterocyclic Carbene Monolayers on Gold and Their Application in Biosensing. *Nat. Commun.* **2016**, *7*, 12654.
- (76) Ott, L. S.; Cline, M. L.; Deetlefs, M.; Seddon, K. R.; Finke, R. G. Nanoclusters in Ionic Liquids: Evidence for N-Heterocyclic Carbene Formation from Imidazolium-Based Ionic Liquids Detected by ^2H NMR. *J. Am. Chem. Soc.* **2005**, *127* (16), 5758–5759.
- (77) Hurst, E. C.; Wilson, K.; Fairlamb, I. J. S.; Chechik, V. N-Heterocyclic Carbene Coated Metal Nanoparticles. *New J. Chem.* **2009**, *33* (9), 1837–1840.
- (78) Weidner, T.; Baio, J. E.; Mundstock, A.; Große, C.; Karthäuser, Si.; Bruhn, C.; Siemeling, U. NHC-Based Self-Assembled Monolayers on Solid Gold Substrates. *Aust. J. Chem.* **2011**, *64*, 1177–1179.

- (79) Crudden, C. M.; Horton, J. H.; Ebralidze, I. I.; Zenkina, O. V.; McLean, A. B.; Drevniok, B.; She, Z.; Kraatz, H. B.; Mosey, N. J.; Seki, T.; et al. Ultra Stable Self-Assembled Monolayers of N-Heterocyclic Carbenes on Gold. *Nat. Chem.* **2014**, *6* (5), 409–414.
- (80) Wang, G.; Rühling, A.; Amirjalayer, S.; Knor, M.; Ernst, J. B.; Richter, C.; Gao, H. J.; Timmer, A.; Gao, H. Y.; Doltsinis, N. L.; et al. Ballbot-Type Motion of N-Heterocyclic Carbenes on Gold Surfaces. *Nat. Chem.* **2017**, *9*, 152–156.
- (81) Gonell, S.; Poyatos, M.; Peris, E. Triphenylene-Based Tris(N-Heterocyclic Carbene) Ligand: Unexpected Catalytic Benefits. *Angew. Chemie - Int. Ed.* **2013**, *52* (27), 7009–7013.
- (82) Capozzi, B.; Xia, J.; Adak, O.; Dell, E. J.; Liu, Z.; Taylor, J. C.; Neaton, J. B.; Campos, L. M.; Venkataraman, L. Single-Molecule Diodes with High Rectification Ratios through Environmental Control. *Nat. Nanotechnol.* **2015**, *10*, 522–527.
- (83) Lovat, G.; Choi, B.; Paley, D. W.; Steigerwald, M. L.; Venkataraman, L.; Roy, X. Room-Temperature Current Blockade in Atomically Defined Single-Cluster Junctions. *Nat. Nanotechnol.* **2017**, *12* (11), 1050–1054.
- (84) Baghernejad, M.; Zhao, X.; Ørnso, K. B.; Füeg, M.; Moreno-García, P.; Rudnev, A. V.; Kaliginedi, V.; Vesztergom, S.; Huang, C.; Hong, W.; et al. Electrochemical Control of Single-Molecule Conductance by Fermi- Level Tuning and Conjugation Switching. *J. Am. Chem. Soc.* **2014**, *136*, 17922–17925.
- (85) Brooke, R. J.; Jin, C.; Szumski, D. S.; Nichols, R. J.; Mao, B.-W.; Thygesen, K. S.; Schwarzacher, W. Single-Molecule Transistor Utilizing a Nickel-Pyridyl Spinterface. *Nano Lett.* **2015**, *15*, 275–280.
- (86) Dulić, D.; van der Molen, S. J.; Kidernac, T.; Jonkman, H. T.; de Jong, J. J. D.; Bowden, T. N.; van Esch, J.; Feringa, B. L.; van Wees, B. J. One-Way Optoelectronic Switching of Photochromic Molecules on Gold. *Phys. Rev. Lett.* **2003**, *91* (20), 207402.
- (87) Jia, C.; Migliore, A.; Xin, N.; Huang, S.; Wang, J.; Yang, Q.; Wang, S.; Chen, H.; Wang, D.; Feng, B.; et al. Covalently Bonded Single-Molecule Junctions with Stable and Reversible Photoswitched Conductivity. *Science*. **2016**, *352* (6292), 1443–1446.
- (88) Walkey, M. C.; Peiris, C. R.; Ciampi, S.; Aragone, A. C.; Domínguez-Espíndola, R. B.; Jago, D.; Pulbrook, T.; Skelton, B. W.; Sobolev, A. N.; Díez-Pérez, I.; et al. Chemically and

Mechanically Controlled Single-Molecule Switches Using Spiropyrans. *ACS Appl. Mater. Interfaces* **2019**, *11*, 36886–36894.

- (89) Darwish, N.; Díez-Pérez, I.; Da Silva, P.; Tao, N.; Gooding, J. J.; Paddon-Row, M. N. Observation of Electrochemically Controlled Quantum Interference in a Single Anthraquinone-Based Norbornylogous Bridge Molecule. *Angew. Chemie - Int. Ed.* **2012**, *51* (13), 3203–3206.
- (90) Mattei, M.; Kang, G.; Goubert, G.; Chulhai, D. V.; Schatz, G. C.; Jensen, L.; Van Duyne, R. P. Tip-Enhanced Raman Voltammetry: Coverage Dependence and Quantitative Modeling. *Nano Lett.* **2017**, *17* (1), 590–596.
- (91) Aragonès, A. C.; Haworth, N. L.; Darwish, N.; Ciampi, S.; Bloomfield, N. J.; Wallace, G. G.; Diez-perez, I.; Coote, M. L. Electrostatic Catalysis of a Diels – Alder Reaction. *Nature* **2016**, *531*, 88–91.
- (92) Broman, S. L.; Lara-Avila, S.; Thisted, C. L.; Bond, A. D.; Kubatkin, S.; Danilov, A.; Nielsen, M. B. Dihydroazulene Photoswitch Operating in Sequential Tunneling Regime: Synthesis and Single-Molecule Junction Studies. *Adv. Funct. Mater.* **2012**, *22*, 4249–4258.
- (93) Whalley, A. C.; Steigerwald, M. L.; Guo, X.; Nuckolls, C. Reversible Switching in Molecular Electronic Devices. *J. Am. Chem. Soc.* **2007**, *129*, 12590–12591.
- (94) Kronemeijer, A. J.; Akkerman, H. B.; Kudernac, T.; van Wees, B. J.; Feringa, B. L.; Blom, P. W. M.; de Boer, B. Reversible Conductance Switching in Molecular Devices. *Adv. Mater.* **2008**, *20*, 1467–1473.
- (95) Uchida, K.; Yamanoi, Y.; Yonezawa, T.; Nishihara, H. Reversible On / Off Conductance Switching of Single Diarylethene Immobilized on a Silicon Surface. *J. Am. Chem. Soc.* **2011**, *133*, 9239–9241.
- (96) Tam, E. S.; Parks, J. J.; Shum, W. W.; Zhong, Y.-W.; Santiago-Berrios, M. B.; Zheng, X.; Yang, W.; Chang, G. K.-L.; Abruna, H. D.; Ralph, D. C. Single-Molecule Conductance of Pyridine-Terminated Dithienylethene Switch Molecules. *ACS Nano* **2011**, *5* (6), 5115–5123.
- (97) Aradhya, S. V; Meisner, J. S.; Krikorian, M.; Ahn, S.; Parameswaran, R.; Steigerwald, M. L.; Nuckolls, C.; Venkataraman, L. Dissecting Contact Mechanics from Quantum

Interference in Single- Molecule Junctions of Stilbene Derivatives. *Nano Lett.* **2012**, *12*, 1643–1647.

- (98) Ikeda, M.; Tanifuji, N.; Yamaguchi, H.; Matsuda, K. Photoswitching of Conductance of Diarylethene-Au Nanoparticle Network. *Chem. Commun.* **2007**, 1355–1357.
- (99) Li, C.; Pobelov, I.; Wandlowski, T.; Bagrets, A.; Arnold, A.; Evers, F. Charge Transport in Single Au | Alkanedithiol | Au Junctions : Coordination Geometries and Conformational Degrees of Freedom. *J Am Chem Soc.* **2008**, *130*, 318–326.
- (100) Kim, Y.; Song, H.; Strigl, F.; Pernau, H.; Lee, T.; Scheer, E. Conductance and Vibrational States of Single-Molecule Junctions Controlled by Mechanical Stretching and Material Variation. *Phys. Rev. Lett.* **2011**, *106*, 196804.
- (101) Li, L.; Lo, W.-Y.; Cai, Z.; Zhang, N.; Yu, L. Proton-Triggered Switch Based on a Molecular Transistor with Edge-on Gate. *Chem. Sci.* **2016**, *7*, 3137–3141.
- (102) Meng, F.; Hervault, Y.; Shao, Q.; Hu, B.; Norel, L.; Riguat, S.; Chen, X. Orthogonally Modulated Molecular Transport Junctions for Resettable Electronic Logic Gates. *Nat. Commun.* **2014**, *5*, 3023.
- (103) Green, J. E.; Choi, J. W.; Boukai, A.; Bunimovich, Y.; Johnston-Halperin, E.; Deionno, E.; Luo, Y.; Sheriff, B. A.; Xu, K.; Shin, Y. S.; et al. A 160-Kilobit Molecular Electronic Memory Patterned at 10^{11} Bits per Square Centimetre. *Nature* **2007**, *445*, 414–417.
- (104) Xu, B. Q.; Li, X. L.; Xiao, X. Y.; Sakaguchi, H.; Tao, N. J. Electromechanical and Conductance Switching Properties of Single Oligothiophene Molecules. *Nano Lett.* **2005**, *5* (7), 1491–1495.
- (105) Díez-Pérez, I.; Li, Z.; Guo, S.; Madden, C.; Huang, H.; Che, Y.; Yang, X.; Zang, L.; Tao, N. Ambipolar Transport in an Electrochemically Gated Single-Molecule Field-Effect Transistor. *ACS Nano* **2012**, *6* (8), 7044–7052.
- (106) He, J.; Fu, Q.; Lindsay, S.; Ciszek, J. W.; Tour, J. M. Electrochemical Origin of Voltage-Controlled Molecular Conductance Switching. *J. Am. Chem. Soc.* **2006**, *128*, 14828–14835.
- (107) Li, Z.; Liu, Y.; Mertens, S. F. L.; Pobelov, I. V.; Wandlowski, T. From Redox Gating to Quantized Charging. *J. Am. Chem. Soc.* **2010**, *132*, 8187–8193.

- (108) Janin, M.; Ghilane, J.; Lacroix, J.-C. When Electron Transfer Meets Electron Transport in Redox-Active Molecular Nanojunctions. *J. Am. Chem. Soc.* **2013**, *135*, 2108–2111.
- (109) Yin, X.; Zang, Y.; Zhu, L.; Low, J. Z.; Liu, Z.; Cui, J.; Neaton, J. B.; Venkataraman, L.; Campos, L. M. A Reversible Single-Molecule Switch Based on Activated Antiaromaticity. **2017**, 1–6.
- (110) Su, T. A.; Li, H.; Steigerwald, M. L.; Venkataraman, L.; Nuckolls, C. Stereoelectronic Switching in Single-Molecule Junctions. *Nat. Chem.* **2015**, *7*, 215–220.
- (111) Collier, C. P.; Mattersteig, G.; Wong, E. W.; Luo, Y.; Beverly, K.; Sampaio, J.; Raymo, F. M.; Stoddart, J. F.; Heath, J. R. A [2] Catenane-Based Solid State Electronically Reconfigurable Switch. *Science*. **2000**, *289*, 1172–1175.
- (112) Kubatkin, S.; Danilov, A.; Hjort, M.; Cornil, J.; Brédas, J.-L.; Stuhr-hansen, N.; Hedegård, P.; Bjørnholm, T. Single-Electron Transistor of a Single Organic Molecule with Access to Several Redox States. *Nature* **2003**, *425*, 698–701.
- (113) Miyamachi, T.; Gruber, M.; Davesne, V.; Bowen, M.; Boukari, S.; Joly, L.; Scheurer, F.; Rogez, G.; Yamada, T. K.; Ohresser, P.; et al. Robust Spin Crossover and Memristance across a Single Molecule. *Nat. Commun.* **2012**, *3*, 938.
- (114) Aragonès, A. C.; Aravena, D.; Cerdá, J. I.; Acís-Castillo, Z.; Li, H.; Real, J. A.; Sanz, F.; Hihath, J.; Ruiz, E.; Díez-Pérez, I. Large Conductance Switching in a Single-Molecule Device through Room Temperature Spin-Dependent Transport. *Nano Lett.* **2016**, *16*, 218–226.
- (115) Pasupathy, A. N.; Bialczak, R. C.; Martinek, J.; Grose, J. E.; Donev, L. A. K.; McEuen, P. L.; Ralph, D. C. The Kondo Effect in the Presence of Ferromagnetism. *Science*. **2004**, *306*, 86–89.
- (116) Cho, W. J.; Cho, Y.; Min, S. K.; Kim, W. Y.; Kim, K. S. Chromium Porphyrin Arrays As Spintronic Devices. *J. Am. Chem. Soc.* **2011**, *133*, 9364–9369.
- (117) Feringa, B. L.; Van Delden, R. A.; Koumura, N.; Geertsema, E. M. Chiroptical Molecular Switches. *Chem. Rev.* **2000**, *100* (5), 1789–1816.
- (118) Choudhury, J.; Semwal, S. Emergence of Stimuli-Controlled Switchable Bifunctional

Catalysts. *Synlett* **2018**, *29* (2), 141–147.

- (119) Broichhagen, J.; Frank, J. A.; Trauner, D. A Roadmap to Success in Photopharmacology. *Acc. Chem. Res.* **2015**, *48* (7), 1947–1960.
- (120) Zhang, N.; Lo, W.; Jose, A.; Cai, Z.; Li, L.; Yu, L. A Single-Molecular AND Gate Operated with Two Orthogonal Switching Mechanisms. *Adv. Mater.* **2017**, *29*, 1701248.
- (121) Xu, L.; Izgorodina, E. I.; Coote, M. L. Ordered Solvents and Ionic Liquids Can Be Harnessed for Electrostatic Catalysis. *J. Am. Chem. Soc.* **2020**, *142* (29), 12826–12833.
- (122) Rogers, F. J. M.; Noble, B. B.; Coote, M. L. Computational Optimization of Alkoxyamine-Based Electrochemical Methylation. *J. Phys. Chem. A* **2020**, *124* (29), 6104–6110.
- (123) Dutta Dubey, K.; Stuyver, T.; Stuyver, T.; Kalita, S.; Shaik, S. Solvent Organization and Rate Regulation of a Menshutkin Reaction by Oriented External Electric Fields Are Revealed by Combined MD and QM/MM Calculations. *J. Am. Chem. Soc.* **2020**, *142* (22), 9955–9965.
- (124) Meir, R.; Chen, H.; Lai, W.; Shaik, S. Oriented Electric Fields Accelerate Diels – Alder Reactions and Control the Endo / Exo Selectivity. *ChemPhysChem* **2010**, *11*, 301–310.
- (125) Gryn'ova, G.; Marshall, D. L.; Blanksby, S. J.; Coote, M. L. Switching Radical Stability by PH-Induced Orbital Conversion. *Nat. Chem.* **2013**, *5*, 474–481.
- (126) Gryn'ova, G.; Coote, M. L. Origin and Scope of Long-Range Stabilizing Interactions and Associated SOMO – HOMO Conversion in Distonic Radical Anions. *J. Am. Chem. Soc.* **2013**, *135*, 15392–15403.
- (127) Shaik, S.; de Visser, S. P.; Kumar, D. External Electric Field Will Control the Selectivity of Enzymatic-Like Bond Activations. *J. Am. Chem. Soc.* **2004**, *126*, 11746–11749.
- (128) Fried, S. D.; Bagchi, S.; Boxer; Steven G. Extreme Electric Fields Power Catalysis in the Active Site of Ketosteroid Isomerase. *Science*. **2014**, *346* (6216), 1510–1514.
- (129) Welborn, V. V.; Pestana, L. R.; Head-Gordon, T. Computational Optimization of Electric Fields for Better Catalysis Design. *Nat. Catal.* **2018**, *1*, 649–655.

- (130) Che, F.; Gray, J. T.; Ha, S.; Kruse, N.; Scott, S. L.; McEwen, J.-S. Elucidating the Roles of Electric Fields in Catalysis : A Perspective. *ACS Catal.* **2018**, *8*, 5153–5174.
- (131) Ciampi, S.; Darwish, N.; Aitken, H. M.; Díez-Pérez, I.; Coote, M. L. Harnessing Electrostatic Catalysis in Single Molecule, Electrochemical and Chemical Systems: A Rapidly Growing Experimental Tool Box. *Chem. Soc. Rev.* **2018**, *47*, 5146–5164.
- (132) Foroutan-Nejad, C.; Marek, R. Potential Energy Surface and Binding Energy in the Presence of an External Electric Field : Modulation of Anion – π Interactions for Graphene-Based Receptors. *Phys. Chem. Chem. Phys.* **2014**, *16*, 2508–2514.
- (133) Lau, V. M.; Pfalzgra, W. C.; Markland, T. E.; Kanan, M. W. Electrostatic Control of Regioselectivity in Au(I)-Catalyzed Hydroarylation. *J. Am. Chem. Soc.* **2017**, *139*, 4035–4041.
- (134) Meyers, F.; Marder, S. R.; Pierce, B. M.; Brédas, J. L. Electric Field Modulated Nonlinear Optical Properties of Donor-Acceptor Polyenes: Sum-Over-States Investigation of the Relationship between Molecular Polarizabilities (α , β , and γ) and Bond Length Alternation. *J. Am. Chem. Soc.* **1994**, *116* (23), 10703–10714.
- (135) Zang, Y.; Zou, Q.; Fu, T.; Ng, F.; Fowler, B.; Yang, J.; Li, H.; Steigerwald, M. L.; Nuckolls, C.; Venkataraman, L. Directing Isomerization Reactions of Cumulenes with Electric Field. *Nat. Commun.* **2019**, *10*, 4482.
- (136) Huang, X.; Tang, C.; Li, J.; Chen, L.; Zheng, J.; Zhang, P.; Le, J.; Li, R.; Li, X.; Liu, J.; et al. Electric Field – Induced Selective Catalysis of Single-Molecule Reaction. *Sci. Adv.* **2019**, *5* (6), eaaw3072.
- (137) Gross, L.; Mohn, F.; Moll, N.; Liljeroth, P.; Meyer, G. The Chemical Structure of a Molecule Resolved by Atomic Force Microscopy. *Science*. **2009**, *325* (5944), 1110–1114.
- (138) Albrecht, F.; Neu, M.; Quest, C.; Swart, I.; Repp, J. Formation and Characterization of a Molecule-Metal-Molecule Bridge in Real Space. *J. Am. Chem. Soc.* **2013**, *135* (24), 9200–9203.
- (139) Pavliček, N.; Schuler, B.; Collazos, S.; Moll, N.; Pérez, D.; Gutián, E.; Meyer, G.; Peña, D.; Gross, L. On-Surface Generation and Imaging of Arynes by Atomic Force Microscopy. *Nat. Chem.* **2015**, *7*, 623–628.

- (140) Schuler, B.; Fatayer, S.; Mohn, F.; Moll, N.; Pavlieèk, N.; Meyer, G.; Penã, D.; Gross, L. Reversible Bergman Cyclization by Atomic Manipulation. *Nat. Chem.* **2016**, *8*, 220–224.
- (141) de Oteyza, D. G.; Gorman, P.; Chen, Y.-C.; Wickenburg, S.; Riss, A.; Mowbray, D.; Etkin, G.; Pedramrazi, Z.; Tsai, H.-Z.; Rubio, A.; et al. Direct Imaging of Covalent Bond Structure in Single-Molecule Chemical Reactions. *Science*. **2013**, *340*, 1434–1438.
- (142) Pavlicek, N.; Gross, L. Generation, Manipulation and Characterization of Molecules by Atomic Force Microscopy. *Nat. Rev. Chem.* **2017**, *1*, 0005.
- (143) Kaiser, K.; Scriven, L. M.; Schulz, F.; Gawel, P.; Gross, L.; Anderson, H. L. An Sp-Hybridized Molecular Carbon Allotrope, Cyclo[18]Carbon. *Science*. **2019**, *365* (6459), 1299–1301.
- (144) Zang, Y.; Pinkard, A.; Liu, Z.; Neaton, B.; Steigerwald, M. L.; Roy, X.; Venkataraman, L. Electronically Transparent Au – N Bonds for Molecular Junctions. *J. Am. Chem. Soc.* **2017**, *139*, 14845–14848.
- (145) Harun, M. K.; Lyon, S. B.; Marsh, J. Formation and Characterisation of Thin Phenolic Amine-Functional Electropolymers on a Mild Steel Substrate. *Prog. Org. Coatings* **2005**, *52* (3), 246–252.
- (146) Leff, D. V.; Brandt, L.; Heath, J. R. Synthesis and Characterization of Hydrophobic, Organically-Soluble Gold Nanocrystals Functionalized with Primary Amines. *Langmuir* **1996**, *12* (20), 4723–4730.
- (147) Adenier, A.; Chehimi, M. M.; Gallardo, I.; Pinson, J.; Vilà, N. Electrochemical Oxidation of Aliphatic Amines and Their Attachment to Carbon and Metal Surfaces. *Langmuir* **2004**, *20* (19), 8243–8253.
- (148) Bélanger, D.; Pinson, J. Electrografting: A Powerful Method for Surface Modification. *Chem. Soc. Rev.* **2011**, *40* (7), 3995–4048.
- (149) Gallardo, I.; Pinson, J.; Vilà, N. Spontaneous Attachment of Amines to Carbon and Metallic Surfaces. *J. Phys. Chem. B* **2006**, *110* (39), 19521–19529.
- (150) Xu, B.; Zhou, L.; Madix, R. J.; Friend, C. M. Highly Selective Acylation of Dimethylamine Mediated by Oxygen Atoms on Metallic Gold Surfaces. *Angew. Chemie - Int. Ed.* **2010**, *49*

(2), 394–398.

- (151) Venkataraman, L.; Klare, J. E.; Nuckolls, C.; Hybertsen, M. S.; Steigerwald, M. L. Dependence of Single-Molecule Junction Conductance on Molecular Conformation. *Nature* **2006**, *442*, 904–907.
- (152) Mishchenko, A.; Vonlanthen, D.; Meded, V.; Bürkle, M.; Li, C.; Pobelov, I. V.; Bagrets, A.; Viljas, J. K.; Pauly, F.; Evers, F.; et al. Influence of Conformation on Conductance of Biphenyl-Dithiol Single-Molecule Contacts. *Nano Lett.* **2010**, *10* (1), 156–163.
- (153) Zang, Y.; Stone, I.; Inkpen, M. S.; Ng, F.; Lambert, T. H.; Nuckolls, C.; Steigerwald, M. L.; Roy, X.; Venkataraman, L. In Situ Coupling of Single Molecules Driven by Gold-Catalyzed Electrooxidation. *Angew. Chem., Int. Ed.* **2019**, *58*, 16008–16012.
- (154) Funes-Ardoiz, I.; Maseras, F. Oxidative Coupling Mechanisms: Current State of Understanding. *ACS Catal.* **2018**, *8* (2), 1161–1172.
- (155) Liu, C.; Zhang, H.; Shi, W.; Lei, A. Bond Formations between Two Nucleophiles: Transition Metal Catalyzed Oxidative Cross-Coupling Reactions. *Chem. Rev.* **2011**, *111* (3), 1780–1824.
- (156) Yan, M.; Kawamata, Y.; Baran, P. S. Synthetic Organic Electrochemical Methods since 2000: On the Verge of a Renaissance. *Chem. Rev.* **2017**, *117* (21), 13230–13319.
- (157) Stamenkovic, V. R.; Strmcnik, D.; Lopes, P. P.; Markovic, N. M. Energy and Fuels from Electrochemical Interfaces. *Nat. Mater.* **2016**, *16* (1), 57–69.
- (158) She, Z. W.; Kibsgaard, J.; Dickens, C. F.; Chorkendorff, I.; Nørskov, J. K.; Jaramillo, T. F. Combining Theory and Experiment in Electrocatalysis: Insights into Materials Design. *Science*. **2017**, *355* (6321).
- (159) Jonsson, M.; Lind, J.; Eriksen, T. E.; Merényi, G. Redox and Acidity Properties of 4-Substituted Aniline Radical Cations in Water. *J. Am. Chem. Soc.* **1994**, *116* (4), 1423–1427.
- (160) Pavitt, A. S.; Bylaska, E. J.; Tratnyek, P. G. Oxidation Potentials of Phenols and Anilines: Correlation Analysis of Electrochemical and Theoretical Values. *Environ. Sci. Process. Impacts* **2017**, *19* (3), 339–349.

- (161) Merino, E. Synthesis of Azobenzenes: The Coloured Pieces of Molecular Materials. *Chem. Soc. Rev.* **2011**, *40* (7), 3835–3853.

Chapter 2: Gold-Carbon Contacts from Oxidative Addition of Aryl Iodides

2.1 Preface

This chapter is based on a manuscript entitled “Gold-Carbon Contacts from Oxidative Addition of Aryl Iodides” by Rachel L. Starr, Tianren Fu, Evan A. Doud, Ilana Stone, Latha Venkataraman, and Xavier Roy published in Journal of the American Chemical Society, 2020, 142 (15), 7128-7133.¹ I authored this work in which we sought to explore the binding modes of aryl iodides in single molecule junctions. I synthesized and characterized the compounds used in this study with essential help from Evan Doud and Ilana Stone from the Roy group, and I performed the scanning tunneling microscope-based break-junction (STM-BJ) measurements. Tianren Fu from the Venkataraman and Nuckolls groups performed theoretical calculations on the iodine and gold complexes in the single molecule junction.

2.2 Introduction

Chapter 1 describes the types of molecules and reactivity that the STM-BJ has been used to study. For this to be possible, analyte molecules must be designed such that they bind to the electrodes. In many cases, this means incorporating aurophilic linkers, therefore it remains crucial to continue improving the nature of the contact between the linkers and the electrodes. This chapter describes how aryl iodides can be utilized to access a highly conducting single-molecule linkage, and also elucidates the reactivity of these molecules towards dehalogenation.

The controlled binding of single molecules between nanoscopic metal electrodes is a critical step in the design and assembly of molecular electronic devices. The specific binding

groups, or linkers, on the molecule establish the mechanical connections to the electrodes and couple the discrete molecular orbitals to the electronic bands of the electrodes. Studying charge transport across the resulting metal-organic interfaces provides fundamental understanding of the nature of these contacts. Typical linkers used to bind organic molecules to metal electrodes include thiols,^{2,3} thioethers,⁴ and amines.⁵ Aryl halide are ubiquitous functional groups in organic chemistry, yet despite their obvious appeal as surface-binding linkers and as precursors for controlled graphene nanoribbon synthesis, they have seldom been used as such in molecular electronics. As a result, the binding motifs and electronic coupling strength of aryl halides are poorly understood and ambiguously reported. For example, some prior work with aryl iodides have reported dative Au–I contacts,^{6,7} while others have suggested without substantial evidence that the iodide dissociates from the molecule, yielding a direct Au–C bond.⁸ Such linkages are particularly attractive for single molecule electronics, as covalent interactions generally lead to an increase in conductance.⁹ Junctions with Au–C linkages have been achieved using alkyne linkers^{10,11,12} and trimethyl tin-functionalized precursors,^{9,13,14} however these methods typically involve intensive syntheses, toxic chemicals, and are typically limited to select organic backbones. Aryl halides have also been used as precursors for the synthesis of graphene nanoribbons, an important component of next generation nanoscale electronic devices.¹⁵ The dissociation of aryl halides is the first mechanistic step of this reaction, however the process only occurs under ultra-high vacuum and at high temperatures.¹⁶

In this work, we measure the single-molecule conductance of a series of oligophenylene molecular wires terminated asymmetrically with iodine and thiomethyl. We demonstrate that the aryl iodide moiety undergoes a voltage-induced oxidative addition reaction on the Au surface to form a single molecule junction connected through a covalent Au–C bond. The formation of the

Au–C bond is validated by measuring the conductance of the molecules *in situ* and comparing these values to analogous control compounds prepared *ex situ* with the complex Au^I(PPh₃) in place of the iodide. Density functional theory-based transport calculations support our experimental observations and reveal that Au–C linkages display an increased conductance when compared to junctions formed through a dative Au–I interaction. Moreover, we show that the proposed surface-based oxidative addition mechanism can be modulated by controlling the bias applied across the junction, wherein one electrode is polarized to increase its chemical potential, selectively promoting the reaction. In addition to establishing the different binding modes of aryl iodides, our results chart a path to actively controlling oxidative addition on an Au surface using an applied bias.

2.3 Aryl Iodide Single Molecule Junctions: Two Binding Modes

Conductance measurements were carried out using the scanning tunneling microscope-based break junction (STM-BJ) technique^{3,5} using solutions of the molecules in 1,2,4-trichlorobenzene (TCB, a non-polar solvent) or propylene carbonate (PC, a polar solvent). For the PC measurements, the Au tip was coated with an insulating layer to suppress background ionic current.¹⁷ One dimensional (1D) conductance histograms and two-dimensional (2D) conductance-displacement histograms are constructed by compiling thousands of traces into logarithmic (conductance) and linear (displacement) bins without any data selection (see S for details).

We first examine molecules in the series **1-4** comprising 1-4 phenylene units with asymmetric thiomethyl and iodide linkers (Figure 2.1a). These molecules were synthesized using an iterative Suzuki cross-coupling strategy followed by functional group modification (see Section

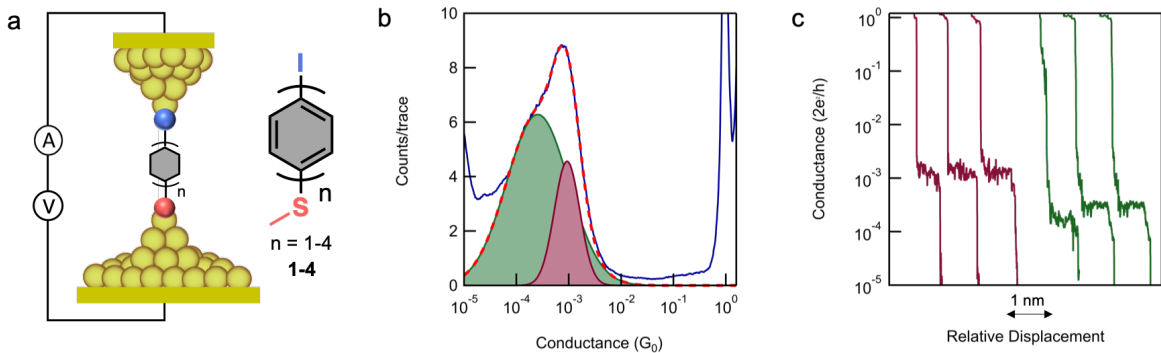


Figure 2.1 (a) Schematic of a single molecule junction and structure of **3**. (b) Logarithm-binned 1D histogram of **3** showing two peaks (taken at 100 mV in TCB). The histogram is fit with a double Gaussian (red), which is divided into high-G (magenta) and low-G (green) constituents. (c) Individual traces demonstrating the different conductance values corresponding to the high-G and low-G peaks.

2.10 for details). The asymmetry of the linkers allows us to specifically probe the behavior of the iodide. Figure 2.1b highlights conductance data taken in TCB at 100 mV for **3** (see Figure 2.6 for the complete series). At all biases, there are two conductance states, suggesting the presence of two binding modes. The distinct conductance signatures are evidenced by a double peak in the 1D histogram (Figure 2.1b), and two plateaus of similar lengths in the individual traces (Figure 2.1c). The high- and low-conductance values (high- and low-G, respectively), extracted from the 1D histogram by fitting with a double Gaussian to these data, are 2.5×10^{-4} and $1.0 \times 10^{-3} G_0$ for **3**. Analogous analyses for **1**, **2** and **4** are in Figure 2.6.

These two different conductance states are remarkable, and cannot be attributed to two molecules in parallel given the factor of ~ 4 difference in conductance. Since we predominantly see either the high-G or the low-G, we can also rule out a simple junction conformational change that occurs upon elongation seen for analogous backbones with pyridine terminations.¹⁸ We therefore hypothesize that the two conductance states arise from two distinct binding modes of the

molecule in the junction: the low-G peak corresponds to molecules binding through a dative Au–I bond, and the high-G peak to molecules binding through a covalent Au–C bond, which forms through an oxidative addition of the aryl iodide to an undercoordinated Au atom at the electrode surface (Figure 2.2a). This hypothesis also rationalizes our observation that for each molecule, the length of the plateaus is consistent with the molecular length. We ascribe the low-G component of the double Gaussian fit to the Au–I interaction (Figure 2.1b, green) and the high-G component to the Au–C interaction (magenta). The dative Au–I interaction leads to a wider distribution of conductance values due to the many possible binding geometries and increased degrees of freedom of the aryl–I–Au contact. Symmetric molecules with two iodide linkers were also studied (Figure 2.7), but these yield more complicated data due to the multiple possible combinations of iodide dissociation.

2.4 Elucidating Binding Modes

To substantiate this hypothesis, we synthesized a new series of molecules (see Section 2.8 for synthetic details) with an intrinsic Au–C bond in which the iodide linker present in **1-3** is replaced by a Au^I(PPh₃) complex (Figure 2.2b, **Au1-Au3**).^{12,19} Based on the propensity of the PPh₃ ligand to dissociate from the Au atom in the junction,⁹ we conclude that **Au1-Au3** form molecular junctions analogous to those created with **1-3** upon Au–C bond formation. We first discuss **Au3** in relation to **3** (Figure 2.2c-e), and note that our observations apply to the complete series (Figure 2.8). Conductance measurements on **Au3**, performed under the same conditions as **3**, reveal only one conductance state whose position aligns with the high-G peak of **3**. The conductance value for **Au3**, obtained from a Gaussian fit of the peak, is in good agreement with the high-G of **3** (Figure

2.2c). Moreover, the conductance plateau of **Au3** in the 2D histogram (Figure 2.2e) has essentially the same shape and position as the high-G plateau of **3** (Figure 2.2d). We note that the plateau length of **Au3** is slightly longer than that of **3**, likely due to the extra Au atom (Figure 2.8 for entire series), as has been previously observed in analogous measurements.²⁰ These observations strongly support that **Au3** and the high-G conductance state of **3** are the same molecule in the junction.

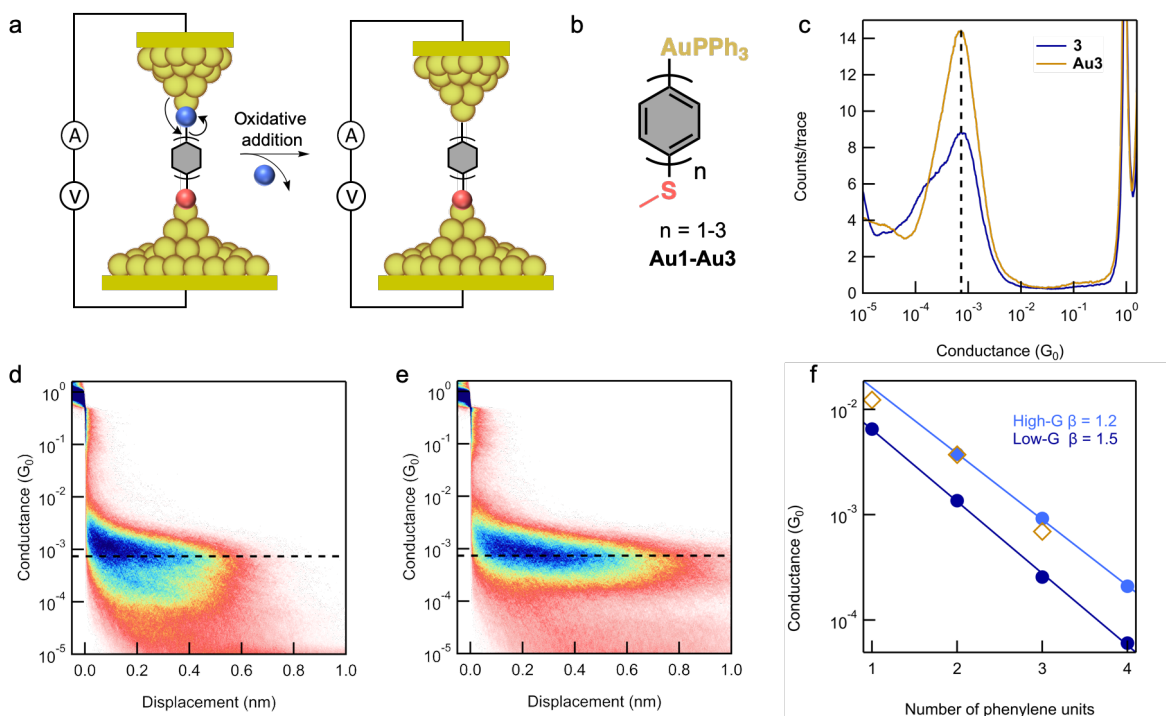


Figure 2.2 (a) Schematic of oxidative addition in the junction. (b) Structure of **Au1-Au3**. (c) 1D histograms of **3** (blue) and **Au3** (yellow). The black dashed line is a guide for the eye denoting the high-G conductance value of **3**, and aligning with the peak conductance value for **Au3**. (d) 2D histogram of **3** (TCB, 100 mV), with the black dashed line denoting the high-G conductance value. (e) 2D histogram of **Au3** (TCB, 100 mV), with the same black dashed line denoting the **3** high-G conductance value aligning with the **Au3** peak conductance. The longer plateau is consistent with an extra Au atom in the junction. (f) Semi-logarithmic plot of the conductance histogram peak value as a function of the number of phenylene units in the backbone of **1-4** (filled circles) and **Au1-Au3** (unfilled diamonds). The **Au1-Au3** peak values align with the high-G values of **1-4**. β values are calculated from the linear fit.

The conductance values determined from both series, **1-4** and **Au1-Au3**, are plotted as a function of the molecular length (expressed as the number of phenylene units) on a semi-logarithmic scale (Figure 2.2f.). From a linear fit of this data, we obtain the slope β , where $G \sim e^{-\beta n}$ describing the exponential decay of conductance with increasing number of phenylene units. The low-G state of **1-4** has a β value of 1.5 per phenylene unit, in good agreement with oligophenylene systems with dative linkers^{21,22}. The β value for the high-G state of **1-4** is close to that of the **Au1-Au3** series and is smaller (1.2 per phenylene unit). This reinforces our conclusion that two distinct types of binding are occurring. Together, these observations confirm our hypothesis that the iodide dissociates in the junction, and a higher-conducting covalent Au–C linkage forms via oxidative addition. We theorize that the undercoordinated Au atoms at the junction, which are electron rich and reactive, promote the dissociation of the iodide by transferring electron density to the aryl carbon, enabling the formation the Au–C bond.

2.5 Computational Studies

To understand these results, we turn to DFT to model the transmission across the molecular junctions using the FHI-aims package^{23,24} and the AITRANSS code.^{25,26} The modeled molecule in the junction is bound to the apex atoms of two 60-atom tetrahedral Au clusters that represent the electrodes. The transmission functions for **1-4** and **Au1-Au4** are calculated using the non-equilibrium Green's function formalism^{25,26} starting from junction geometries optimized using the PBE exchange-correlation functional²⁷ (Figure 2.3a). The calculated molecular junction conductance of **2-4**, which is proportional to the transmission at the Fermi level (E_F), is lower than

that of **Au2-Au4**, with the difference in conductance increasing with molecular length. This trend reproduces the experimental results shown in Figure 2.2f. Figure 2.3b shows the transmission at E_F of **1-4** and **Au1-Au4** plotted against molecule length. This data is fit to an exponential function $T = Ae^{-\beta n}$ to obtain the conductance decay for the series. The β value obtained from the fit of the **1-4** series (0.69 per phenylene unit) is larger than that of the **Au1-Au4** series (0.58 per phenylene unit), also in agreement with the experimental observations (Figure 2.3b). These calculations provide further support to our hypothesis that the iodide dissociates during junction formation resulting in an Au–aryl linkage.

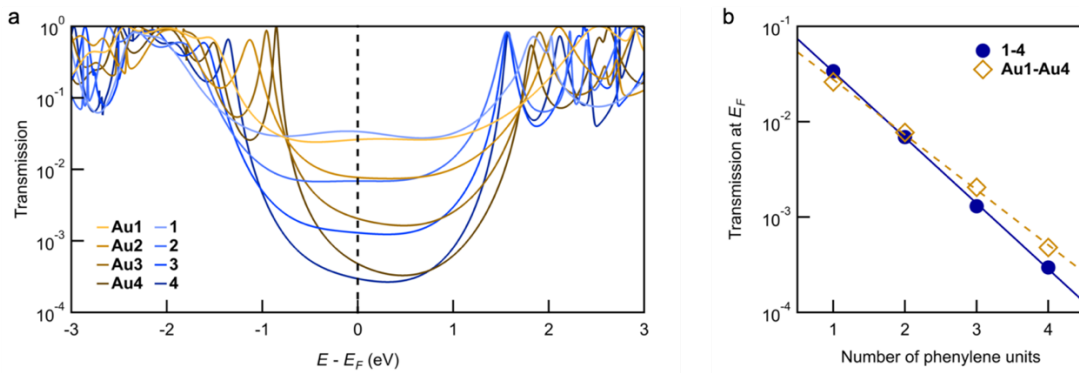


Figure 2.3 (a) Calculated transmission functions of **1-4** and **Au1-Au4**. (b) Calculated transmission at E_F plotted against molecule length, demonstrating the decay is different for each series (**1-4**: $\beta = 0.69$ per phenylene unit; **Au1-Au4**: $\beta = 0.58$ per phenylene unit).

The DFT-based calculations discussed above overestimate the conductance²⁸ because the PBE exchange-correlation functional underestimates the molecular HOMO-LUMO gaps. To examine this limitation, we repeated the calculation using B3LYP functional, which yields more accurate HOMO-LUMO gaps but is computationally expensive. We modeled **2** and **Au2** attached to 18 Au atom clusters as model electrodes and find that for both junctions, the HOMO-LUMO

gap is larger and the transmission at E_F calculated using the B3LYP functional is lower than those calculated using PBE (Figure 2.9).^{29–31} Note that DFT does not include the polarizability of metal in response to charge transfer, implying that B3LYP overestimates the energy separation between the HOMO and LUMO resonances in the transmission function.³² We may thus regard the PBE and B3LYP results as upper and lower bounds of the transmission function, respectively. The transmission of **Au2** is about two-fold higher than **2** at E_F according to PBE and ten-fold according to B3LYP. This again fits the experimental trends.

2.6 Bias Dependent Behavior

When measured in TCB, the 1D and 2D histograms of **1-4** consistently show conductance features indicative of both dative Au–I and covalent Au–C linkages. We now demonstrate that the formation of the Au–C linkage can be actively favored by using an electrical bias to modulate the chemical potential of the electrode. These measurements are performed with a wax-coated tip in the polar solvent PC with tetrabutylammonium hexafluorophosphate (TBAPF₆, 100 mM concentration) as a supporting electrolyte. This setup allows us to polarize the tip electrode through the formation of a dense double layer of charge at the small exposed area.³³ Figure 2.4a illustrates how the application of a negative bias increases the chemical potential of the tip, making it electron rich, therefore promoting the oxidative addition reaction that leads to the Au–C bond formation.

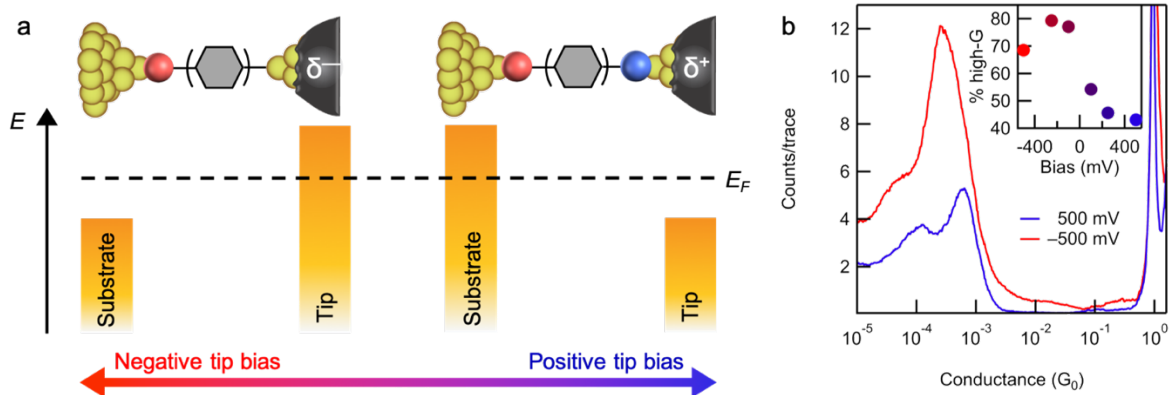


Figure 2.4 (a) Schematic of a single-molecule junction created in an ionic environment, using a wax-coated tip. When a positive tip bias is applied (right, denoted by δ^+), Au–I linkages are favored. When a negative tip bias is applied (left, denoted by δ^-), electron density at the tip can be donated to the aryl carbon, favoring the direct Au–C linkage. (b) 1D histograms taken in PC at \pm 500 mV, demonstrating preferential Au–C junction formation at negative bias. Inset: percentage of junctions that are Au–C compared to Au–I.

To examine this possibility, we measured **3** at various applied tip biases between −500 and 500 mV. All 1D histograms show both low-G and high-G peaks (Figure 2.10), indicating that both Au–I and Au–C bound junctions form. The relative height of these two peaks, however, changes dramatically with bias. This is illustrated in Figure 2.4b for tip biases of −500 and 500 mV. Note that the peaks shift as a result of the applied bias due to a gating effect.³⁴ At 500 mV, the height of the two peaks is similar, signifying that both Au–I and Au–C bound junctions are equally probable. At −500 mV the high-G peak is much more prominent, demonstrating that Au–C bound junctions form much more frequently than Au–I bound ones at negative bias.

To quantify the effect of the applied bias, we analyze our traces to determine the percentage of high-G traces in a given data set (Figure 2.10). The average percentage of high-G at each bias is shown in the inset of Figure 2.4b. The percentage of high-G traces gradually increases as the bias changes from 500 to −500 mV, essentially doubling from around 40% to 80% within this bias

range. At positive bias, the tip is electron deficient, and both Au–I and Au–C interactions are present while at negative bias, the tip is electron rich and thus more prone to undergo oxidative addition with the aryl iodide moiety to form the Au–C bond.

2.7 Conclusion and Outlook

By studying a series of asymmetric oligophenylene compounds, we have established two different binding modes of aryl iodide linkers to Au electrodes in single-molecule junctions. We observe both a lower-conducting, dative Au–I contact and a higher-conducting, covalent Au–C bond. Our data indicate that the Au–C bond forms through an oxidative addition process, in which the electron rich Au electrode enables iodide dissociation. Remarkably, this reaction can be controlled by the applied tip bias. This leads to desirable, higher-conducting covalent Au–C linkages that were previously accessible only through complicated methods. This work opens the door to manipulating chemical transformations using the electric field generated in the molecular junction.

2.8 Synthetic Details

All reactions were performed open to atmosphere with magnetic stirring, unless otherwise noted. All commercial reagents and solvents were used as provided. All final products were dried *in vacuo* prior to reporting yields. 4-bromothioanisole was purchased from Acros Organics. Trifluoroacetic acid (TFA), benzene, and chloro(triphenylphosphine)gold(I) were obtained from Alfa Aesar. Triisopropyl borate was purchased from Strem Chemicals. CDCl₃, CD₂Cl₂, and DMSO-d₆ were purchased from Cambridge Isotope Laboratories. Dichloromethane (DCM), ethyl

acetate, ethanol, hexanes, acetonitrile, tetrahydrofuran (THF), and toluene were obtained from Fisher Scientific. Dry and deoxygenated solvents were prepared by elution through a dual-column solvent system (MBraun SPS). Silica gel was obtained from Silicycle. All other reagents were purchased from Sigma-Aldrich.

¹H and ¹³C NMR spectra were recorded on Bruker DRX300, DRX400 and DMX500 spectrometers in solvents as specified and at frequencies as noted. Data for ¹H NMR are reported as follows: chemical shift (δ , in ppm), multiplicity (s = singlet, d = doublet, t = triplet, q = quartet, m = multiplet), coupling constant (J , in Hz), and integration (b = broad). Data for ¹³C and ³¹P NMR are reported in terms of chemical shift. Accurate mass measurements/high resolution mass spectra (HRMS) were obtained from the Columbia University Chemistry Department Mass Spectrometry Facility on a Waters XEVO G2-XS QToF mass spectrometer equipped with UPLC inlet and a LockSpray source with one of three probes: electrospray ionization (ESI) probe, atmospheric pressure chemical ionization (APCI) probe, or atmospheric pressure solids analysis probe (ASAP). Electrochemical measurements were performed on a Bio-Logic VMP-3 potentiostat/galvanostat.

An overall synthetic scheme is given in Figure 2.5.

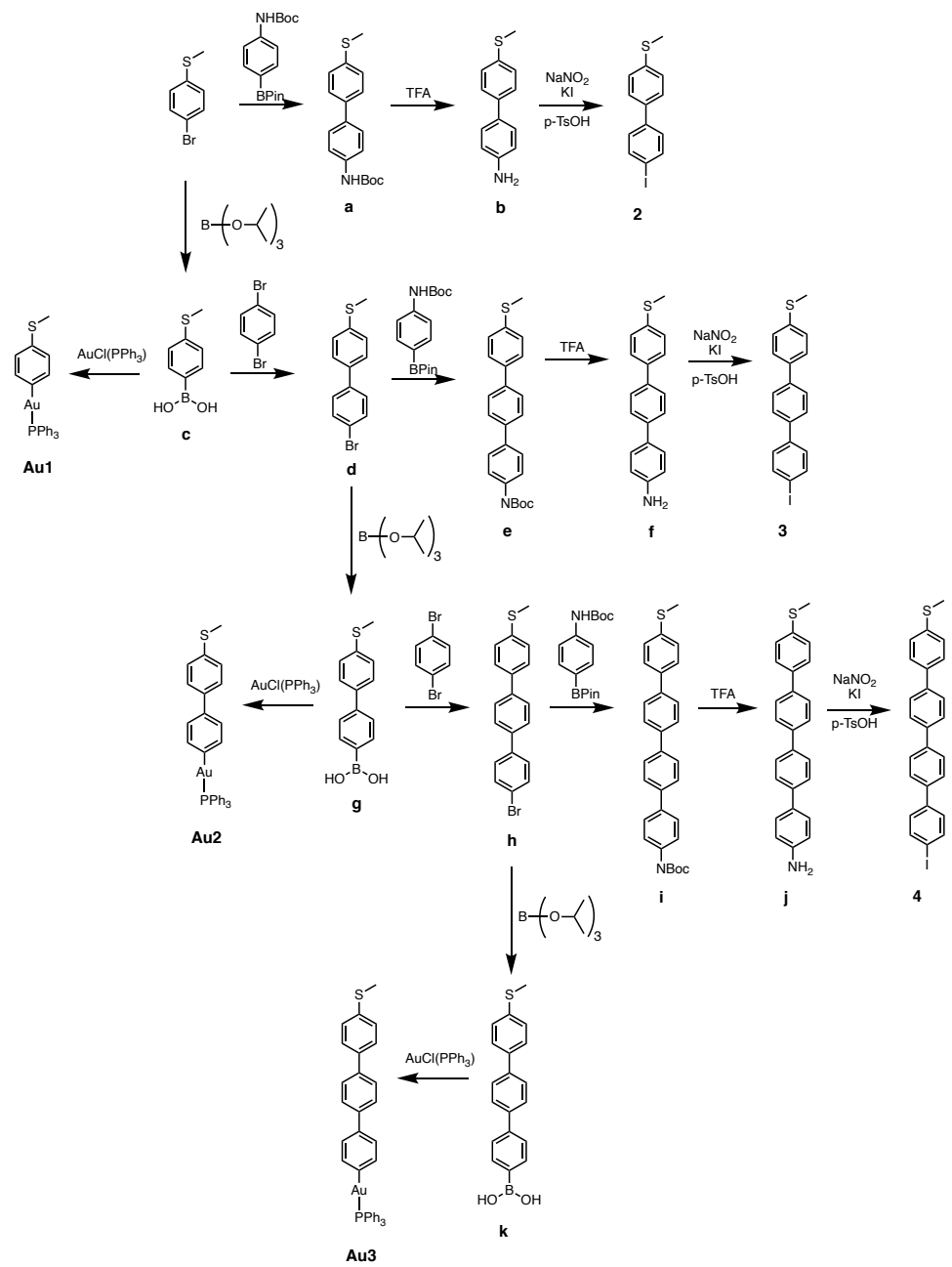
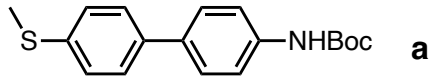
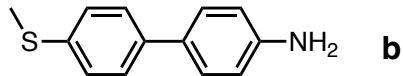


Figure 2.5 Synthetic scheme for the synthesis of asymmetrical iodides (**2-4**) and gold analogs (**Au1-Au3**).



a. Synthesized following a modified literature procedure.³⁵ A 250 mL three-necked round bottom flask fitted with a reflux condenser and equipped with a Teflon coated stir bar under N₂ atmosphere was charged with 4-bromothioanisole (500 mg, 2.46 mmol), 4-(N-boc-amino)phenyl boronic acid pinacol ester (864 mg, 2.71 mmol) and tetrakis(triphenylphosphine)palladium(0) (228 mg, 0.197 mmol). A separate 100 mL round bottom flask equipped with a Teflon stir bar under N₂ atmosphere was charged with potassium bicarbonate (1700 mg, 12.3 mmol), toluene (60 mL), ethanol (9 mL) and water (6 mL) and sparged with N₂ for 20 minutes. The basic solution was then added to the solids resulting in a bright yellow cloudy solution. The reaction mixture was refluxed at 110 °C for 24 h. After cooling to room temperature, the solvent was removed via rotary evaporation. The solid residue was dissolved in DCM (50 mL), washed with water (2 x 50 mL) and brine (1 x 50 mL), dried with Na₂SO₄, and the solvent was removed via rotary evaporation. The crude brown solid was purified using silica gel flash column chromatography, eluting with 5% ethyl acetate in hexanes to afford **1** as a white solid. Yield: 488 mg, 63%.

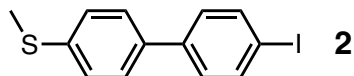
The characterization data is consistent with what has been previously reported.³⁵ ¹H NMR (300 MHz, CDCl₃) δ 7.49 (ddt, *J* = 6.7, 4.3, 2.2 Hz, 4H), 7.42 (d, *J* = 8.6 Hz, 2H), 7.34 – 7.29 (m, 2H), 6.49 (s, 1H), 2.51 (s, 3H), 1.54 (s, 9H).



b. A vial containing protected amine **a** (163 mg, 0.517 mmol) was equipped with a Teflon coated stir bar and charged with TFA (4.0 mL, 51.7 mmol) and stirred for 30 minutes. The reaction mixture was diluted with DCM (10 mL) and washed with 1M NaOH (3 x 10 mL). The aqueous

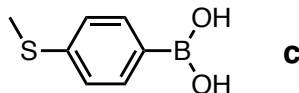
layers were combined and extracted further with DCM (2 x 10 mL). All organic layers were combined and dried with Na₂SO₄, and the solvent was removed via rotary evaporation to afford the deprotected amine. Yield: 97 mg, 87%.

¹H NMR (300 MHz, DMSO-d₆) δ 7.50 (d, *J* = 8.5 Hz, 2H), 7.39 (d, *J* = 8.5 Hz, 2H), 7.28 (d, *J* = 8.5 Hz, 2H), 6.74 (d, *J* = 8.5 Hz, 2H), 2.48 (s, 3H).



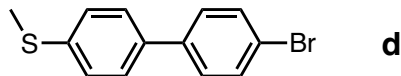
2. A vial containing the deprotected amine **b** (157 mg, 0.729 mmol) was equipped with a Teflon coated stir bar and charged with p-toluenesulfonic acid (377 mg, 2.19 mmol). The solids were dissolved in 10 mL MeCN and the mixture was cooled to 0 °C. In a separate vial, potassium iodide (303 mg, 1.82 mmol) and sodium nitrite (101 mg, 1.46 mmol) were dissolved in 0.3 mL water. The aqueous solution was slowly added dropwise to the organic solution (immediate color change to brown). The reaction was left to stir overnight and warm to room temperature. After 18 h, the reaction mixture was diluted with water (20 mL) and basified (pH 9) with sodium bicarbonate. Sodium thiosulfate (2 mL) was added. The mixture was extracted with ethyl acetate (3 x 30 mL). The organic layers were combined and dried with Na₂SO₄, and the solvent was removed via rotary evaporation. The crude material was purified using silica gel flash column chromatography, eluting with 5% ethyl acetate in hexanes to afford **2** as a light yellow solid. Yield: 154 mg, 65%.

The characterization data is consistent with what has been previously reported.³⁶ ¹H NMR (300 MHz, CDCl₃) δ 7.75 (d, *J* = 8.5 Hz, 2H), 7.48 (d, *J* = 8.5 Hz, 2H), 7.35 – 7.27 (m, 4H), 2.52 (s, 3H); ¹³C NMR (126 MHz, CDCl₃) δ 138.14, 137.89, 128.97, 128.62, 127.81, 127.17, 124.28, 90.83, 15.87. HRMS (ASAP+) calculated for C₁₃H₁₁SI⁺ [M+H]⁺ 325.9626, observed 325.9629 [M+H]⁺.



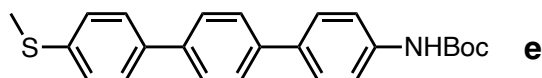
c. Boronic acids were synthesized following a modified literature procedure.³⁵ An oven-dried 2-neck 250 mL round bottom flask equipped with a Teflon coated stir bar, 60 mL addition funnel with a rubber septum, gas inlet adapter, and rubber septum was charged with 50 mL of THF under N₂ atmosphere. The flask was cooled to -78 °C in a dry ice/acetone bath, and *n*-BuLi (2.5 M in hexanes, 9.63 mL, 24.1 mmol) was added to the cooled THF and allowed to stir for 10 minutes. A solution of 4-bromothioanisole (3.00 g, 14.8 mmol) in 50 mL of THF was added to the addition funnel via a N₂ flushed syringe. The 4-bromothioanisole solution was then added dropwise to the *n*-BuLi solution and the reaction was stirred for 1 h, forming a white slurry. A solution of triisopropyl borate (3.78 g, 20.1 mmol) in 20 mL of THF was then added to the addition funnel using a N₂ flushed syringe. The triisopropyl borate solution was added dropwise; the reaction was warmed to room temperature after the addition finished and was stirred for an additional 3 h. The reaction was then opened to air, 100 mL of water was added dropwise through the addition funnel, and allowed to stir for an additional 30 min. 1M aqueous HCl was slowly added until a pH of 1 was obtained, and the mixture was stirred for 30 min. THF was then removed in vacuo. The resulting solid was then filtered and washed with water (3 x 50 mL), hexanes (3 X 50 mL), and dried overnight in vacuo to yield 3 as a white fluffy powder. Yield: 1.53 g, 62%.

The characterization data is consistent with what has been previously reported.³⁵ ¹H NMR (300 MHz, DMSO-d₆): δ 7.94 (s, 2H), 7.71 (d, *J* = 8.3 Hz, 2H), 7.20 (d, *J* = 8.3 Hz, 2H), 2.47 (s, 3H).



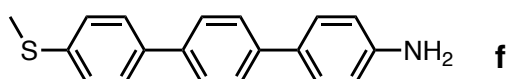
d. Synthesized following a modified literature procedure.³⁵ A 250 mL three-necked round bottom flask fitted with a reflux condenser and equipped with a Teflon coated stir bar under N₂ atmosphere was charged with **c** (1500 mg, 8.93 mmol), 1,4-dibromobenzene (4630 mg, 19.6 mmol) and tetrakis(triphenylphosphine)palladium(0) (310 mg, 0.268 mmol). A separate 250 mL round bottom flask equipped with a Teflon stir bar under N₂ atmosphere was charged with potassium bicarbonate (6170 mg, 44.6 mmol), dioxane (60 mL), and water (30 mL) and sparged for 20 minutes. The basic solution was then added to the solid resulting in a yellow solution. The reaction mixture was refluxed at 95 °C for 24 hours. After cooling to room temperature, the solvent was removed via rotary evaporation. The solid residue was dissolved in ethyl acetate (50 mL), washed with water (3 x 50 mL) and brine (2 x 50 mL), dried with Na₂SO₄, and the solvent was removed via rotary evaporation. The light yellow solid was purified using silica gel flash column chromatography, eluting with hexanes to afford **d** as an off-white solid. Yield: 1555 mg, 62%.

The characterization data is consistent with what has been previously reported.³⁵ ¹H NMR (300 MHz, CDCl₃) δ 7.55 (d, *J* = 8.9 Hz, 2H), 7.51 – 7.39 (m, 4H), 7.32 (d, *J* = 8.0 Hz, 2H), 2.52 (s, 3H).



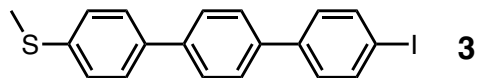
e. Prepared by the same procedure as **a**, but using **d** (140 mg, 0.501 mmol) as the starting bromide. Yield: 133 g, 68%.

¹H NMR (400 MHz, CDCl₃) δ 7.63 (s, 4H), 7.57 (dd, *J* = 8.5, 3.6 Hz, 4H), 7.45 (d, *J* = 8.5 Hz, 2H), 7.35 (d, *J* = 8.4 Hz, 2H), 6.51 (s, 1H), 2.53 (s, 3H), 1.54 (s, 9H).



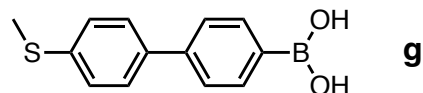
f. Prepared by the same procedure as **b**, but using **e** (133 mg, 0.341 mmol) as the starting protected amine. Yield: 79 mg, 79%.

^1H NMR (300 MHz, DMSO-d₆) δ 7.70 – 7.58 (m, 6H), 7.38 (dd, J = 18.2, 8.5 Hz, 4H), 6.65 (d, J = 8.5 Hz, 2H), 5.23 (s, 2H), 2.51 (s, 3H).



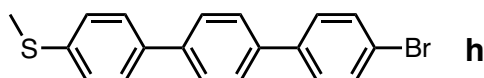
3. Prepared by the same procedure as **2**, but using **f** (79 mg, 0.269 mmol) as the deprotected amine. Yield: 13 mg, 12%.

^1H NMR (400 MHz, DMSO-d₆) δ 7.83 (d, J = 8.4 Hz, 1H), 7.76 (s, 4H), 7.70 (ddd, J = 13.4, 8.6, 1.3 Hz, 3H), 7.55 – 7.46 (m, 2H), 7.38 – 7.36 (m, 2H), 2.52 (s, 3H). Insolubility of the compound precluded ^{13}C NMR characterization. HRMS (ASAP+) calculated for C₁₉H₁₅SI⁺ [M+H]⁺ 401.9939, observed 401.9954 [M+H]⁺.



g. Prepared via the same procedure as **c**, but using **d** (1.00 g, 3.58 mmol) as the starting bromide. Yield: 720 mg, 82%.

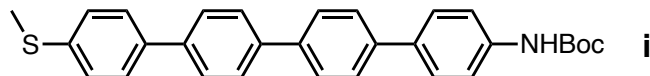
The characterization data is consistent with what has been previously reported.³⁵ ^1H NMR (300 MHz, DMSO-d₆) δ 8.03 (s, 2H), 7.86 (d, J = 8.2 Hz, 2H), 7.63 (t, J = 8.4 Hz, 4H), 7.35 (d, J = 8.5 Hz, 2H), 2.51 (s, 3H).



h. Prepared in a similar manner to **d**, with some modifications. **c** (1.0 g, 5.95 mmol) was used as the starting boronic acid, and 4,4'-dibromobiphenyl (2.3 g, 7.37 mmol) was used as the starting

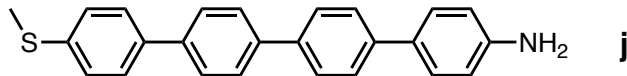
bromide. The reaction was run in a 1:4 H₂O/THF solvent mixture at 85 °C for 2 days. The product was obtained as a white powder. Yield: 1.58 g, 75%.

The characterization data is consistent with what has been previously reported.³⁷ ¹H NMR (400 MHz, CDCl₃) δ 7.64 (d, *J* = 4.6 Hz, 4H), 7.60 – 7.48 (m, 6H), 7.35 (d, *J* = 8.5 Hz, 2H), 2.54 (s, 3H).



i. Synthesized following a modified literature procedure.³⁸ A 3-necked round bottom flask was charged with **h** (150 mg, 0.422 mmol), 4-(N-boc-amino)phenyl boronic acid pinacol ester (142 mg, 0.443 mmol), tetrakis(triphenylphosphine)palladium(0) (15 mg, 0.0127 mmol), and CsF (192 mg, 1.27 mmol) under N₂ atmosphere. The solids were dissolved in anhydrous THF (12.5 mL) and refluxed for 3 days. The reaction mixture was cooled to room temperature, and the Boc-protected product precipitated from the reaction mixture and was collected by filtration. The solid was washed repeatedly with THF and H₂O to give a gray solid. Yield: 70 mg, 35%.

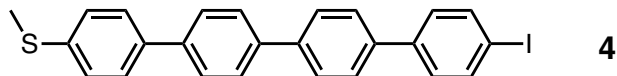
¹H NMR (300 MHz, CDCl₃) δ 7.83 – 7.67 (m, 12H), 7.59 (d, *J* = 8.5 Hz, 2H), 7.46 (d, *J* = 8.5 Hz, 2H), 6.56 (s, 1H), 2.52 (s, 3H), 1.54 (s, 9H). Insolubility of the compound precluded ¹³C NMR characterization.



j. Synthesized following a modified literature procedure.³⁸ Protected amine **i** (70 mg, 0.150 mmol) was suspended in 0.5 mL DCM and cooled to 0 °C. TFA (1.0 mL) was added dropwise and the resulting solution was stirred for 24 h. Upon treatment with aqueous NaOH (2 M, ~1.5 mL) the

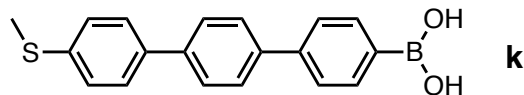
product precipitated from the solution and was collected by filtration. Repeated washing with H₂O and DCM gave **j**. Yield: 19 mg, 34%.

¹H NMR (300 MHz, DMSO-d₆): δ 7.82 – 7.62 (m, 10H), 7.44 (d, *J* = 7.8 Hz, 2H), 7.37 (d, *J* = 8.1 Hz, 2H), 6.69 (d, *J* = 7.6 Hz, 2H), 5.15 (s, 1H), 4.75 (s, 1H), 2.52 (s, 3H). Insolubility of the compound precluded ¹³C NMR characterization.



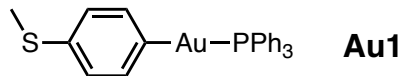
4. Prepared by the same procedure as **2** and **3**, but using **j** (19 mg, 0.0517 mmol) as the deprotected amine. Yield: 6 mg, 24%.

¹H NMR (300 MHz, DMSO-d₆) δ 7.72 (d, *J* = 30.4 Hz, 8H), 7.37 (d, *J* = 8.0 Hz, 3H), 6.68 (m, 1H), 5.07 (d, *J* = 4.8 Hz, 2H), 4.95 (s, 2H), 2.52 (s, 3H). Insolubility of the compound precluded ¹³C NMR characterization. HRMS (ASAP+) calculated for C₂₅H₂₀Si⁺ [M+H]⁺ 479.0330, observed 479.0327 [M+H]⁺.



k. Prepared via the same procedure as **c** and **g**, but using **h** (1.0 g, 2.81 mmol) as the starting bromide. Isolated as a light tan powder. Yield: 800 mg, 89%.

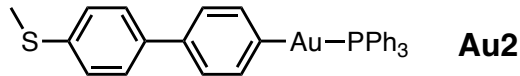
¹H NMR (300 MHz, DMSO-d₆) δ 8.06 (s, 2H), 7.89 (d, *J* = 7.9 Hz, 1H), 7.76 (dd, *J* = 3.5, 1.9 Hz, 4H), 7.69 (d, *J* = 8.1 Hz, 5H), 7.38 (s, 2H), 2.52 (s, 3H).



Au1. Synthesized following a modified literature procedure.³⁹ An oven-dried round bottom flask was charged with boronic acid **c** (50 mg, 0.298 mmol) and cesium carbonate (88.1 mg, 0.271

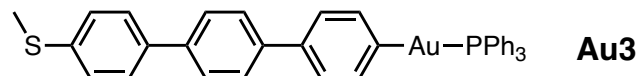
mmol) under a N₂ atmosphere. The solids were dissolved in 5 mL of isopropanol. Chloro(triphenylphosphine)gold(I) (66.9 mg, 0.135 mmol) was added and the reaction mixture was sparged with N₂ for 20 minutes. The reaction was then stirred at 50 °C for 24 h. After cooling to room temperature, the solvent was removed via rotary evaporation. The solid residue was dissolved in benzene, filtered through celite, and concentrated again to yield a white solid. To recrystallize, a solution of **Au1** in benzene was layered with an equal volume of hexanes and placed in a 5 °C refrigerator overnight. Yield: 31 mg, 18%.

The characterization data is consistent with what has been previously reported.⁴⁰ ¹H NMR (500 MHz, CD₂Cl₂) δ 7.64 – 7.58 (m, 6H), 7.51 (ddd, *J* = 14.4, 7.4, 2.1 Hz, 9H), 7.46 – 7.43 (m, 2H), 7.19 – 7.15 (m, 2H), 2.44 (s, 3H); ¹³C NMR (126 MHz, CD₂Cl₂) δ 139.64, 134.37, 134.26, 131.19, 131.17, 129.09, 129.00, 126.08, 126.03, 16.08; ³¹P NMR (202 MHz, CD₂Cl₂) δ 43.55. HRMS (ESI+) calculated for C₂₅H₂₃AuPS⁺ [M+H]⁺ 583.0924, observed 583.0933 [M+H]⁺.



Au2. Prepared via the same procedure as **Au1**, but using **g** (22 mg, 0.0950 mmol) as the starting boronic acid. Isolated as a white solid. Yield: 15 mg, 25%.

¹H NMR (300 MHz, CD₂Cl₂) δ 7.68 – 7.46 (m, 22H), 7.31 (d, *J* = 8.4 Hz, 2H), 2.51 (s, 3H); ¹³C NMR (126 MHz, CD₂Cl₂) δ 140.05, 134.78, 134.67, 131.60, 131.58, 129.50, 129.41, 126.49, 126.44, 16.49.; ³¹P NMR (121 MHz, CD₂Cl₂) δ 43.47. HRMS (ESI+) calculated for C₃₁H₂₇AuPS⁺ [M+H]⁺ 659.1237, observed 659.1246 [M+H]⁺.



Au3. Prepared via the same procedure as **Au1** and **Au2**, but using **k** (50 mg, 0.156 mmol) as the starting boronic acid. Isolated as a light brown solid. Yield: 27 mg, 24%.

¹H NMR (300 MHz, CD₂Cl₂) δ 7.73 – 7.44 (m, 26H), 7.33 (d, *J* = 1.9 Hz, 1H), 2.53 (s, 3H); ¹³C NMR (126 MHz, CD₂Cl₂) δ 140.37, 134.99, 134.89, 132.55, 132.47, 132.31, 131.74, 129.66, 129.58, 129.05, 128.95, 127.74, 127.68, 127.60, 127.43, 54.27, 54.06, 53.84, 53.62, 53.41, 16.30; ³¹P NMR (121 MHz, CD₂Cl₂) δ 43.47. HRMS (ESI+) calculated for C₃₇H₃₁AuPS⁺ [M+H]⁺ 735.1550, observed 735.1559 [M+H]⁺.

2.9 DFT Calculations

For transmission function calculations, the relaxed geometry of each molecule in the junction is found using density functional theory (DFT). The target molecule is first relaxed with Au atoms bound to each linker. For **Au1-Au4**, two Au atoms are placed on the Au linker, and one Au atom on the S linker. For **1-4**, one Au atom is placed on the S linker, but a Au₁₉ cluster is put on the I linker, to better simulate the Au–I bond. The geometry is relaxed until the maximum residue force component per atom is below 10⁻² eV·Å⁻¹. Once the geometry is optimized, two Au₆₀ tetrahedral clusters are appended to each linker, replacing the Au atoms used during the geometry optimization. For B3LYP calculations, smaller Au₁₈ clusters are used to decrease the time of each calculation. Within the clusters, the neighboring Au–Au distance is 2.88 Å. The clusters represent the (111) lattice surface of gold. Figure 2.9 demonstrates the geometry of Au₆₀-species-Au₆₀ cluster used in the calculation for **Au2** and **2**, respectively. The structures are illustrated using VESTA 3.⁴¹

2.10 STM-BJ Method

Conductance measurements were made using a custom-built scanning tunneling microscope that has been described in detail before.⁵ Conductance measurements were performed in dilute solutions (100 μM) of the molecules in either 1,2,4-trichlorobenzene (TCB), or propylene carbonate (PC) with 0.1 M tetrabutylammonium perchlorate (TBAPF₆) as a supporting electrolyte.¹⁷ The insulated tips used with PC were created by driving a mechanically cut gold tip through Apiezon wax.¹⁷ One-dimensional (1D) conductance histograms are constructed using logarithmic bins (100/decade), and two-dimensional (2D) histograms use logarithmic bins along the conductance axis (100/decade) and linear bins (1000/nm) along the displacement axis. The junction length is determined by displacement profiling of the molecular conductance feature in the two-dimensional histograms.

2.11 Additional Data

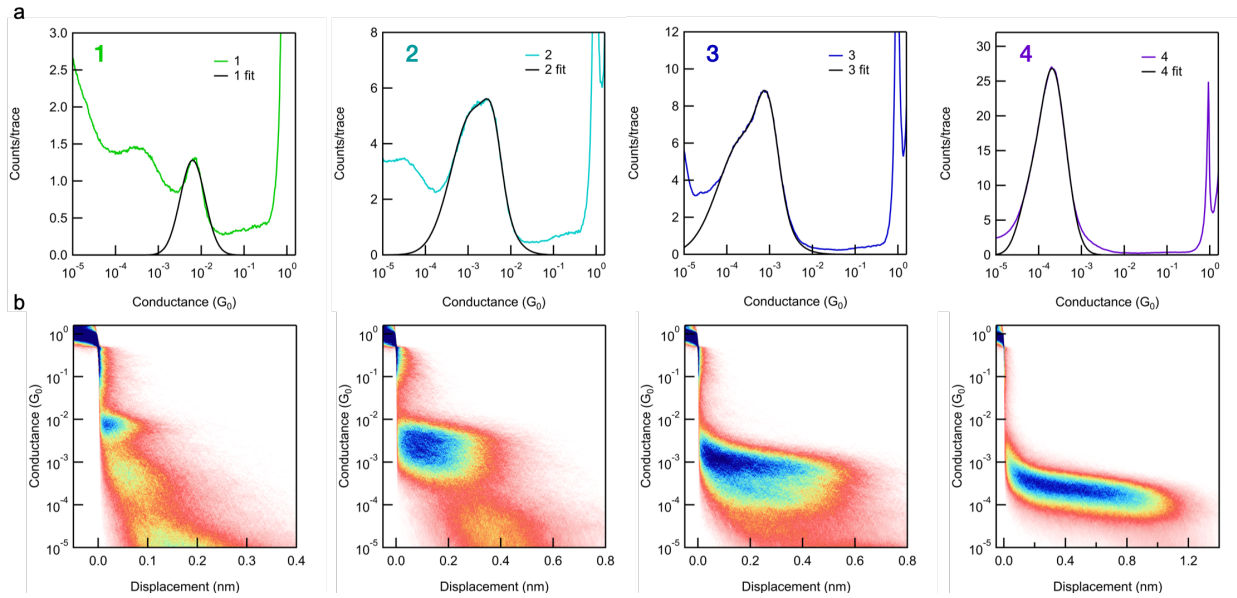


Figure 2.6 (a) Logarithm-binned 1D and (b) and (b) 2D conductance-displacement histograms of 1-4 measured in TCB at 100 mV. Double Gaussian fits in (a) are shown in black. Peak splitting is most clearly observed in 2 and 3.

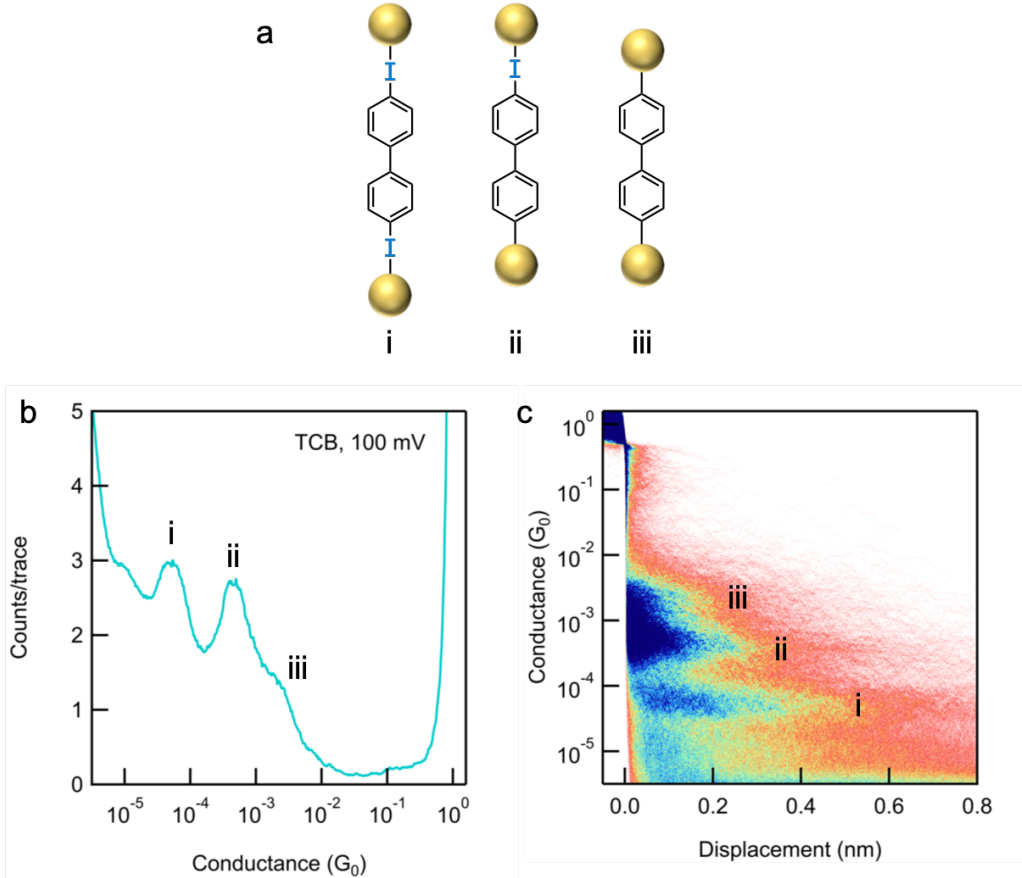


Figure 2.7 Oxidative addition via iodide linker is observed for the symmetric molecule diiodobiphenyl. (a) Schematic of diiodobiphenyl in the junction showing the three expected binding modes: two Au–I contacts, one Au–I and one Au–C contact, and two Au–C contacts. (b) Logarithm-binned 1D histograms of diiodobiphenyl measured in TCB at 100 mV. Three peaks are visible; we assign the highest peak to junction type iii and the lowest one type i. (c) 2D conductance-displacement histogram generated from the data used to create the 1D histogram. Three distinct peaks are clearly visible, with the length increasing as conductance decreases. This is consistent with our hypothesis; the shortest junction has two Au–C contacts while the longest one has two Au–I contacts.

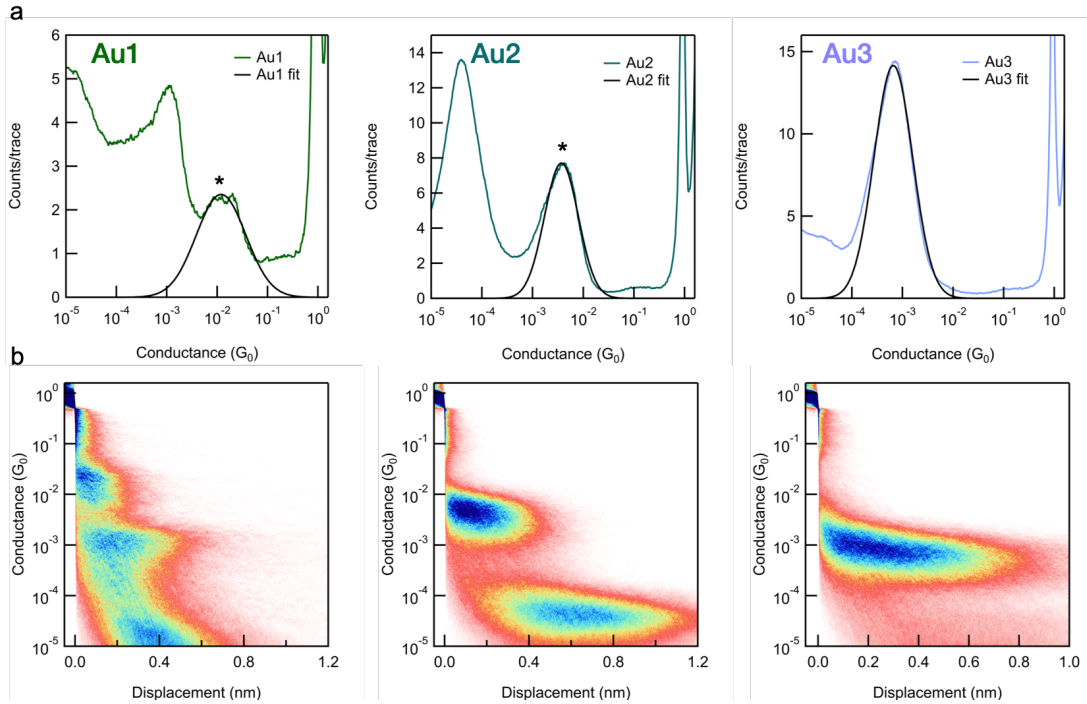


Figure 2.8 (a) Logarithm-binned 1D and (b) 2D conductance-displacement histograms of **Au1-3** measured in TCB at 100 mV. Gaussian fits in (a) are shown in black. Note that the higher conducting junction corresponds to the $\text{Au}-(\text{Ph})_n-\text{SMe}-\text{Au}$ junction. The lower conducting peaks with longer plateaus are due to $\text{Au}-\text{SMe}-(\text{Ph})_{2n}-\text{SMe}-\text{Au}$ dimers formed in situ.

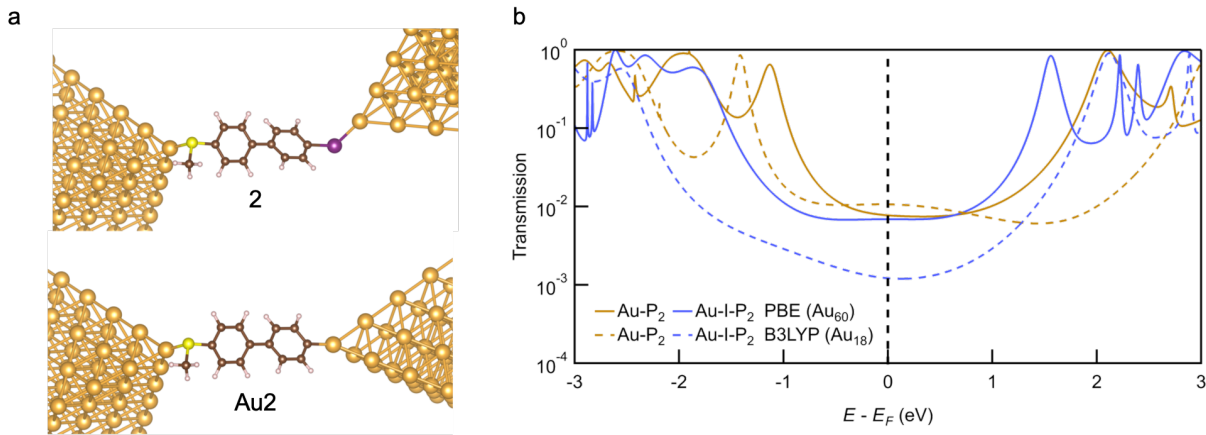


Figure 2.9 (a) Relaxed junction geometries of **2** and **Au2** attached to Au_{60} clusters. (b) Comparison of the transmission functions of **2** and **Au2** calculated using PBE (solid) and B3LYP (dashed). The PBE and B3LYP results provide upper and lower bounds of the transmission at Fermi.

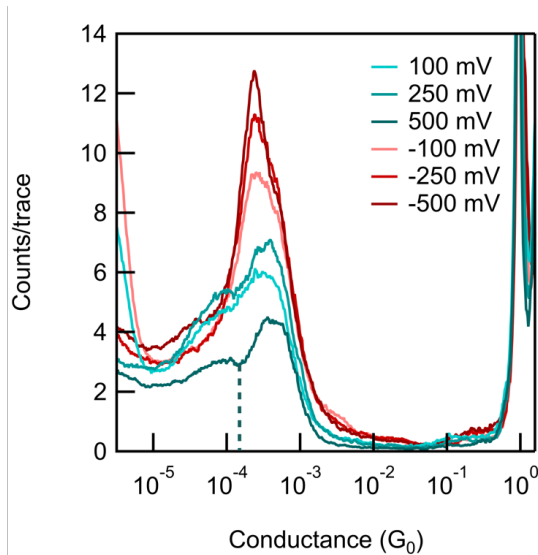


Figure 2.10 Logarithm-binned 1D histograms of **3** measured in PC at different biases. To quantify the effect of the applied bias, we divided the 1D histograms at every bias into a high-G and low-G window (dotted line represents an example cutoff for the +500 mV data). The number of data points within each window was counted to obtain the percentage of points per the trace corresponding to the high-G peak. This was iterated over thousands of traces at each bias. The analysis was repeated with multiple data sets.

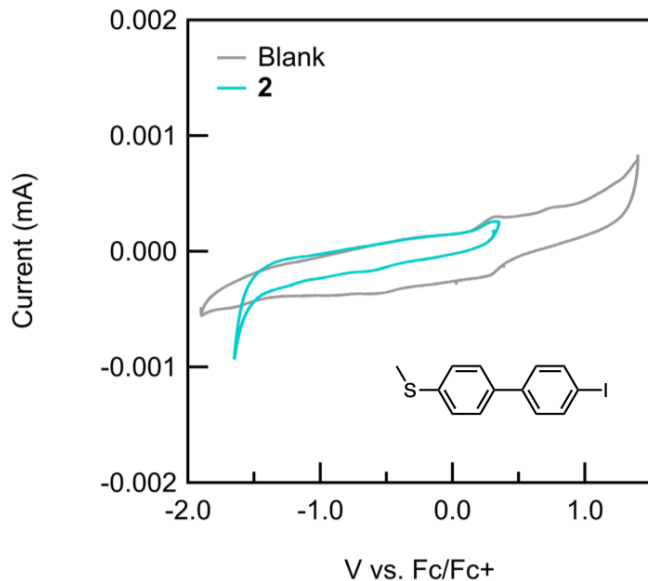


Figure 2.11 Cyclic voltammogram of **2**. No reductive peak is visible. CVs were taken in PC with TBAPF₆ as a supporting electrolyte, using a gold electrode and a scan rate of 50 mV/s.

2.12 References

- (1) Starr, R. L.; Fu, T.; Doud, E. A.; Stone, I.; Roy, X.; Venkataraman, L. Gold–Carbon Contacts from Oxidative Addition of Aryl Iodides. *J. Am. Chem. Soc.* **2020**.
- (2) Reed, M. A.; Zhou, C.; Muller, C. J.; Burgin, T. P.; Tour, J. M. Conductance of a Molecular Junction. *Science*. **1997**, *278*, 252–254.
- (3) Xu, B.; Tao, N. J. Measurement of Single-Molecule Resistance by Repeated Formation of Molecular Junctions. *Science*. **2003**, *301*, 1221–1223.
- (4) Park, Y. S.; Whalley, A. C.; Kamenetska, M.; Steigerwald, M. L.; Hybertsen, M. S.; Nuckolls, C.; Venkataraman, L. Contact Chemistry and Single-Molecule Conductance : A Comparison of Phosphines , Methyl Sulfides , and Amines. *J. Am. Chem. Soc.* **2007**, *129*, 15768–15769.
- (5) Venkataraman, L.; Klare, J. E.; Nuckolls, C.; Hybertsen, M. S.; Steigerwald, M. L. Dependence of Single-Molecule Junction Conductance on Molecular Conformation. *Nature* **2006**, *442*, 904–907.

- (6) Komoto, Y.; Fujii, S.; Hara, K.; Kiguchi, M. Single Molecular Bridging of Au Nanogap Using Aryl Halide Molecules. *J. Phys. Chem. C* **2013**, *117*, 24277–24282.
- (7) Peng, L.; Huang, B.; Zou, Q.; Hong, Z.; Zheng, J.; Shao, Y.; Niu, Z.; Zhou, X.; Xie, H.; Chen, W. Low Tunneling Decay of Iodine-Terminated Alkane Single-Molecule Junctions. *Nanoscale Res. Lett.* **2018**, *13*, 121–126.
- (8) Bürkle, M.; Xiang, L.; Li, G.; Rostamian, A.; Hines, T.; Guo, S.; Zhou, G.; Tao, N.; Asai, Y. The Orbital Selection Rule for Molecular Conductance as Manifested in Tetraphenyl-Based Molecular Junctions. *J. Am. Chem. Soc.* **2017**, *139*, 2989–2993.
- (9) Cheng, Z.; Skouta, R.; Vazquez, H.; Widawsky, J. R.; Schneebeli, S.; Chen, W.; Hybertsen, M. S.; Breslow, R.; Venkataraman, L. In Situ Formation of Highly Conducting Covalent Au–C Contacts for Single-Molecule Junctions. *Nat. Nanotechnol.* **2011**, *6* (6), 353–357.
- (10) Hong, W.; Li, H.; Liu, S.; Fu, Y.; Li, J.; Kaliginedi, V.; Decurtins, S.; Wandlowski, T. Trimethylsilyl-Terminated Oligo(Phenylene Ethynylene)s: An Approach to Single-Molecule Junctions with Covalent Au–C Σ -Bonds. *J. Am. Chem. Soc.* **2012**, *134* (47), 19425–19431.
- (11) Bejarano, F.; Olavarria-contreras, I. J.; Droghetti, A.; Rungger, I.; Rudnev, A.; Gutiérrez, D.; Mas-torrent, M.; Veciana, J.; van der Zant, H. S. J.; Rovira, C.; et al. Robust Organic Radical Molecular Junctions Using Acetylene Terminated Groups for C–Au Bond Formation. *J. Am. Chem. Soc.* **2018**, *140*, 1691–1696.
- (12) Millar, D.; Venkataraman, L.; Doerrer, L. H. Efficacy of Au - Au Contacts for Scanning Tunneling Microscopy Molecular Conductance Measurements. *J. Phys. Chem. C* **2007**, *111* (47), 17635–17639.
- (13) Batra, A.; Kladnik, G.; Gorjizadeh, N.; Steigerwald, M.; Nuckolls, C.; Quek, S. Y.; Cvetko, D.; Morgante, A.; Venkataraman, L. Trimethyltin-Mediated Covalent Gold – Carbon Bond Formation. *J. Am. Chem. Soc.* **2014**, *136* (36), 12556–12559.
- (14) Chen, W.; Widawsky, J. R. Highly Conducting π -Conjugated Molecular Junctions Covalently Bonded to Gold Electrodes. *J. Am. Chem. Soc.* **2011**, *133* (43), 17160–17163.
- (15) Cai, J.; Ruffieux, P.; Jaafar, R.; Bieri, M.; Braun, T.; Blankenburg, S.; Muoth, M.; Seitsonen, A. P.; Saleh, M.; Feng, X.; et al. Atomically Precise Bottom-up Fabrication of

Graphene Nanoribbons. *Nat. Lett.* **2010**, *466*, 470–473.

- (16) Batra, A.; Cvetko, D.; Kladnik, G.; Adak, O.; Cardoso, C.; Ferretti, A.; Prezzi, D.; Molinari, E.; Morgante, A.; Venkataraman, L. Probing the Mechanism for Graphene Nanoribbon Formation on Gold Surfaces through X-Ray Spectroscopy. *Chem. Sci.* **2014**, *5*, 4419–4423.
- (17) Nagahara, L. A.; Thundat, T.; Lindsay, S. M. Preparation and Characterization of STM Tips for Electrochemical Studies. *Rev. Sci. Instrum.* **1989**, *60* (10), 3128–3130.
- (18) Quek, S. Y.; Kamenetska, M.; Steigerwald, M. L.; Choi, H. J.; Louie, S. G.; Hybertsen, M. S.; Neaton, J. B.; Venkataraman, L. Mechanically Controlled Binary Conductance Switching of a Single-Molecule Junction. *Nat. Nanotechnol.* **2009**, *4*, 230–234.
- (19) Pankajakshan, S.; Loh, T. Base-Free Palladium-Catalyzed Sonogashira Coupling Using Organogold Complexes. *Chem. Asian J.* **2011**, *6*, 2291–2295.
- (20) Inkpen, M. S.; Liu, Z. F.; Li, H.; Campos, L. M.; Neaton, J. B.; Venkataraman, L. Non-Chemisorbed Gold–Sulfur Binding Prevails in Self-Assembled Monolayers. *Nat. Chem.* **2019**, *11*, 351–358.
- (21) Zang, Y.; Pinkard, A.; Liu, Z.; Neaton, B.; Steigerwald, M. L.; Roy, X.; Venkataraman, L. Electronically Transparent Au – N Bonds for Molecular Junctions. *J. Am. Chem. Soc.* **2017**, *139*, 14845–14848.
- (22) Hsu, L.; Wu, N.; Rabitz, H. Conductance and Activation Energy for Electron Transport in Series and Parallel Intramolecular Circuits. *Phys. Chem. Chem. Phys.* **2016**, *18*, 32087–32095.
- (23) Blum, V.; Gehrke, R.; Hanke, F.; Havu, P.; Havu, V.; Ren, X.; Reuter, K.; Scheffler, M. Ab Initio Molecular Simulations with Numeric Atom-Centered Orbitals. *Comput. Phys. Commun.* **2009**, *180* (11), 2175–2196.
- (24) Havu, V.; Blum, V.; Havu, P.; Scheffler, M. Efficient O(N) Integration for All-Electron Electronic Structure Calculation Using Numeric Basis Functions. *J. Comput. Phys.* **2009**, *228* (22), 8367–8379.
- (25) Arnold, A.; Weigend, F.; Evers, F. Quantum Chemistry Calculations for Molecules Coupled to Reservoirs : Formalism , Implementation , and Application to Benzenedithiol Formalism

, Implementation , and Application to Benzenedithiol. *J. Chem. Phys.* **2007**, *126*, 174101.

- (26) Bagrets, A. Spin-Polarized Electron Transport Across Metal–Organic Molecules: A Density Functional Theory Approach. *J. Chem. Theory Comput.* **2013**, *9*, 2801–2815.
- (27) Perdew, J. P.; Burke, K.; Ernzerhof, M. Generalized Gradient Approximation Made Simple. *Phys. Rev. Lett.* **1996**, *77* (18), 3865–3868.
- (28) Koentopp, M.; Burke, K.; Evers, F. Zero-Bias Molecular Electronics : Exchange-Correlation Corrections to Landauer’s Formula. *Phys. Rev. B* **2006**, *73*, 121403.
- (29) Vosko, S.; Wilk, L.; Nusair, M. Accurate Spin-Dependent Electron Liquid Correlation Energies for Local Spin Density Calculations: A Critical Analysis1. *Can. J. Phys.* **1980**, *58*, 1200.
- (30) Lee, C.; Yang, W.; Parr, R. G. Development of the Colle-Salvetti Correlation-Energy Formula into a Functional of the Electron Density. *Phys. Rev. B* **1988**, *37* (2), 785–789.
- (31) Becke, A. D. A New Mixing of Hartree–Fock and Local Density-Functional Theories. *J. Chem. Phys.* **1993**, *98*, 1372.
- (32) Egger, D. A.; Liu, Z.; Kronik, L. Reliable Energy Level Alignment at Physisorbed Molecule – Metal Interfaces from Density Functional Theory. *Nano Lett.* **2015**, *15*, 2448–2455.
- (33) Capozzi, B.; Xia, J.; Adak, O.; Dell, E. J.; Liu, Z.; Taylor, J. C.; Neaton, J. B.; Campos, L. M.; Venkataraman, L. Single-Molecule Diodes with High Rectification Ratios through Environmental Control. *Nat. Nanotechnol.* **2015**, *10*, 522–527.
- (34) Capozzi, B.; Low, J. Z.; Xia, J.; Liu, Z.-F.; Neaton, J. B.; Campos, L. M.; Venkataraman, L. Mapping the Transmission Functions of Single-Molecule Junctions. *Nano Lett.* **2016**, *16* (6), 3949–3954.
- (35) Doud, E. A.; Inkpen, M. S.; Lovat, G.; Montes, E.; Paley, D. W.; Steigerwald, M. L.; Vázquez, H.; Venkataraman, L.; Roy, X. In Situ Formation of N-Heterocyclic Carbene-Bound Single-Molecule Junctions. *J. Am. Chem. Soc.* **2018**, *140* (28), 8944–8949.
- (36) Hiremath, R.; Varney, S. W.; Swift, J. A. Oriented Crystal Growth of 4-Iodo-4'-

Nitrobiphenyl on Polar Self-Assembled Monolayer Templates: A Case for “Chemical Epitaxy.” *Chem. Mater.* **2004**, *16* (24), 4948–4954.

- (37) Stefani, D.; Perrin, M.; Gutiérrez-Cerón, C.; Aragonès, A. C.; Labra-Muñoz, J.; Carrasco, R. D. C.; Matsushita, Y.; Futera, Z.; Labuta, J.; Ngo, Th. H.; et al. Mechanical Tuning of Through-Molecule Conductance in a Conjugated Calix [4] Pyrrole. *Chem. Sel.* **2018**, *3* (23), 6473–6478.
- (38) Al-shamery, K. Synthesis of Symmetrically and Unsymmetrically Para -Functionalized p - Quaterphenylenes. *Synthesis (Stuttg)*. **2007**, No. 4, 613–621.
- (39) Pankajakshan, S.; Loh, T.-P. Base-Free Palladium-Catalyzed Sonogashira Coupling Using Organogold Complexes SI. *Chem. Asian J.* **2011**, *6*, 2291–2295.
- (40) Weber, D.; Jones, T. D.; Adduci, L. L.; Gagnø, M. R. Strong Electronic and Counterion Effects on Geminal Digold Formation and Reactivity as Revealed by Gold (I)–Aryl Model Complexes. *Angew. Chemie Int. Ed.* **2012**, *51* (10), 2452–2456.
- (41) Momma, K.; Izumi, F. VESTA 3 for Three-Dimensional Visualization of Crystal , Volumetric and Morphology Data. *J. Appl. Crystallogr.* **2011**, *44*, 1272–1276.

Chapter 3: Harnessing Aryl Iodide Reactivity Towards an *In Situ* Ullmann Coupling

3.1 Preface

This chapter is based on a project that is ongoing as of the writing of this dissertation. Ilana Stone from the Roy group and I have been collaborating to explore the Ullmann coupling-like reactivity of aryl iodides in the single molecule junction. Ilana synthesized and characterized the compounds used in this study, and I performed the scanning tunneling microscope-based break-junction (STM-BJ) measurements and data analysis. Brandon Fowler and Fereshteh Zandkarimi obtained and analyzed the mass spectra. Ren Wiscons performed the SEM and EDX surface analysis. Michael Steigerwald provided essential insight into our experiments and results, which proved critical to our mechanistic understanding. Xavier Roy and Latha Venkataraman continue to oversee and advise on this project. We also thank the NSF CCI Center for Chemistry with Electric Fields for sparking thought-provoking conversation and bringing many new and interesting ideas to the table, as well as continued funding for this and other related projects.

3.2 Introduction

We expanded upon our understanding of the behavior of aryl iodides in the single molecule junction, detailed in Chapter 2, by next exploring their reactivity. Under the influence of a strong electric field, we can both observe and manipulate their chemical transformations. This chapter describes the dimerization of a collection of aryl iodides in an Ullmann coupling reaction, as well as a selective cross-coupling. These studies provide insight into the mechanism of the

dehalogenation and Ullmann coupling processes, which although studied widely on surfaces and in bulk, are still debated.

The Ullmann coupling is a century-old reaction¹ that persists as a ubiquitous reaction in synthetic chemistry for the coupling of aryl halides. The traditional Ullmann reaction employs stoichiometric Cu and requires high temperatures. A number of recent advances have enabled the use of milder conditions involving alternative Cu catalysts,² greener synthetic methods,^{3,4} microwave-^{5–7} and ultrasound-assisted^{8,9} syntheses, and reactions supported by nanoparticles.^{10,11} Ullmann couplings are commonly used in many natural product syntheses,¹² and for the bottom-up synthesis of graphene nanoribbons,¹³ a cutting-edge process in nanotechnology development. The Ullmann coupling is a particularly attractive strategy for the synthesis of covalent 2D networks, since the topology of scaffolds can be easily tuned by changing the position and reactivity of the halogen atoms. Despite this substantial utility and the fact that this reaction is widely employed in a variety of applications, the mechanism of the Ullmann reaction remains incompletely understood. Thus, a facile and precise technique that enables experiments to probe deeper into an atomistic understanding of the mechanism and kinetics of the elementary reaction steps is desirable.

Among the many ways to interrogate chemical mechanisms, selective control of reactions at the single molecule level holds the potential to resolve reaction properties and mechanisms, though robust techniques remain elusive. In 2000, Hla et al.¹⁴ established what remains the predominant method to effect these transformations via a surface-assisted Ullmann coupling; however, the coupling needed to be manually executed, using the STM tip to move, separate, and combine molecules on the surface. Although great strides have been made utilizing “on-surface” synthetic techniques to probe reactions at the single-molecule level,^{15–19} these approaches are

restricted to ultra-high vacuum or low temperature conditions, preclude the diversification of reactions, and thus limit the range of accessible chemical reactions and substrates that can be probed. The Ullmann coupling remains the prototypical reaction for further refining on-surface techniques, but many fundamental and mechanistic aspects have yet to be revealed. Scanning tunneling microscopy (STM)-based techniques offer a precise technique to achieve atomic-level studies under facile conditions, yet few reactions have been proven to be controlled in the STM-break junction (STM-BJ).²⁰⁻²⁶ Here, we demonstrate an Ullmann coupling reaction under ambient conditions, using the nanostructured Au STM tip as catalyst.

3.3 Evidence and Scope of the *In Situ* Ullmann Coupling Reaction

Experimental details for the modified STM technique have been described previously.²⁷ Briefly, break junction measurements are performed in an ionic environment using an insulated Au STM tip with an exposed area of $\sim 1 \mu\text{m}^2$ and an Au substrate with an area larger than 0.5 cm^2 (Figure 3.1a). When a potential bias is applied to the tip, a dense electric double layer builds up around the small tip area, facilitating charge transfer. Using this approach, we measured the single-molecule conductance of a series of aryl iodides (Figure 3.1b) in propylene carbonate (PC) with tetrabutylammonium hexafluorophosphate (TBAPF₆) or tetrabutylammonium perchlorate (TBAP) as supporting electrolyte. Because the electrolyte concentration (0.1 M) is much higher than that of the iodide (10-100 μM), a large concentration of ions exists around the junction. To produce statistically reproducible data, the measurement is repeated thousands of times, and the traces are compiled into one-dimensional (1D) logarithmically-binned conductance histograms and two-dimensional (2D) conductance-displacement histograms without any data selection. This analysis

provides two molecule-specific signatures: the most probable molecular conductance from the 1D histogram and the junction elongation (molecular plateau length), which relates to the molecular backbone length, from the 2D histogram.²⁸

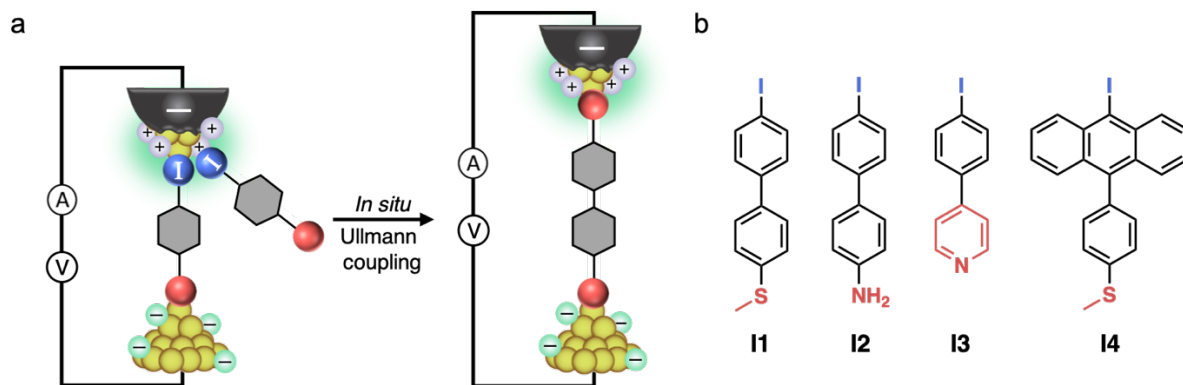


Figure 3.1 (a) A schematic of the *in situ* Ullmann coupling. The measurements are performed in a polar solvent with a wax coated tip, allowing a dense double layer of charge to build up, facilitating reactivity. Note that the molecules drawn are cartoon representations, not the molecules used in this study. (b) The scope of aryl iodides tested, **I1**-**I4**, which successfully undergo an Ullmann coupling under our standard ambient conditions. Linkers are denoted in red, as in panel (a), and iodides in blue.

Figure 3.2a-b highlights conductance data of **I1** in PC (see Figure 3.8 and Figure 3.9 for data of the full series of aryl iodides, and Section 3.8 for synthetic details). Consistent with previously reported data,²⁶ the two peaks corresponding to the two binding modes of **I1** are present in both the 1D and 2D histograms. However, a new, lower G peak at $2.2 \times 10^{-5} G_0$ (where $G_0 = 2e^2/h$ is the conductance quantum) emerges. The corresponding 2D histogram (Figure 3.2b) shows a markedly longer molecular plateau of about 1.0 nm. Together, these distinct features signify the formation of a new type of junction with a molecule that is longer than **I1** and displays a correspondingly lower conductance. We hypothesize that **I1** undergoes an oxidative addition with

the Au tip, as previously described.²⁶ This results in dehalogenation and subsequent C–C bond formation with a second nearby dehalogenated molecule to form the longer homocoupled molecule **D1** (Figure 3.2a,d dark red structure). In short, **I1** undergoes an *in situ* Ullmann coupling.

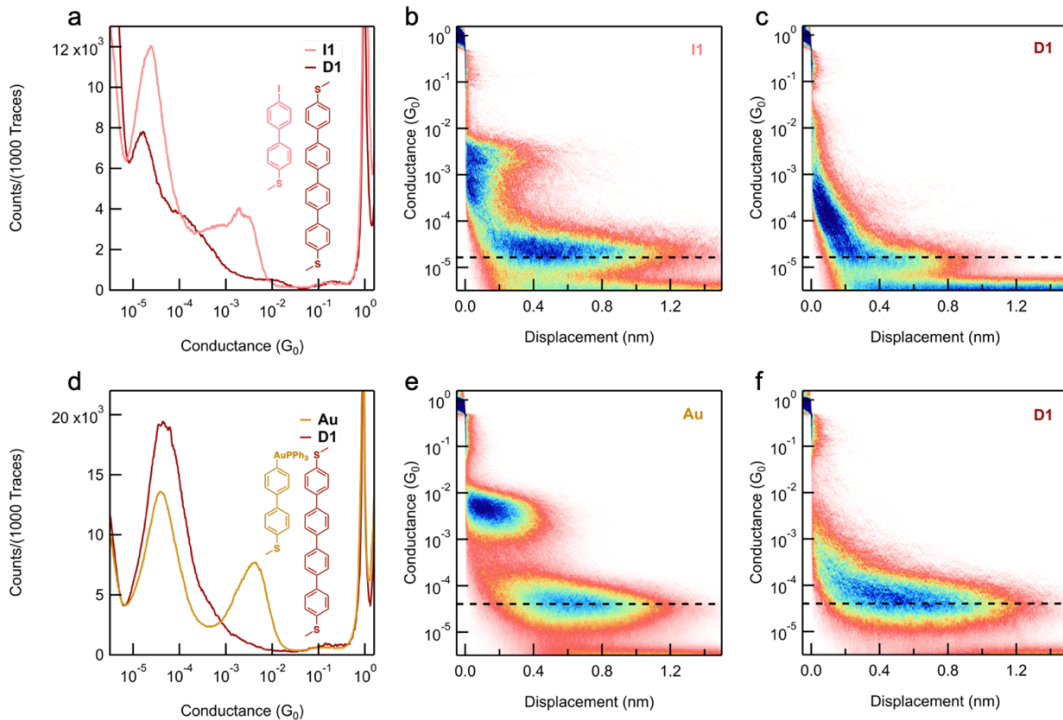


Figure 3.2 (a) Logarithm-binned 1D histograms of **I1** and **D1** in PC (polar solvent). The low-G peak of **I1** aligns with the **D1** peak, confirming dimerization of **I1**. (b-c) 2D histogram of **I1** and **D1** in PC, with the black dashed line denoting the dimer conductance value. (d) 1D histograms of Au and **D1** in 1,2,4-trichlorobenzene (TCB, nonpolar solvent). The low-G peak of Au aligns with the **D1** peak, confirming dimerization of Au in TCB. (e-f) 2D histogram of Au and **D1** in TCB, with the black dashed line denoting the dimer conductance value.

To verify this hypothesis, we synthesized **D1** *ex situ* (see Section 3.8 for synthetic details) and compared its molecular conductance and junction elongation to those for the *in situ* coupling of **I1** (Figure 3.2a,c). The 1D histogram for **D1** prepared *ex situ* shows a clear conductance peak (Figure 3.2a) at the same value as that for the *in situ* coupling product of **I1**. Moreover, the junction

elongation displayed in the 2D histogram for **D1** prepared *ex situ* (Figure 3.2c) is essentially the same as that for **D1** formed *in situ* (Figure 3.2b). Additionally, mass spectrometry (MS) confirms the presence of the coupling product (Figure 3.10, Figure 3.11, Figure 3.12). These results imply that the new molecule created in the junction is the Ullmann coupling product **D1** produced from the *in situ* homocoupling, or dimerization, of **I1**.

Interestingly, when measuring the AuPPh₃ analog of **I1**,²⁶ denoted as **Au** (Figure 3.2d, yellow structure), we observe two prominent conductance peaks (Figure 3.2d-e), one at 3.8×10^{-3} G₀ that matches the high-G state of **I1**,²⁶ and one at 4.0×10^{-5} G₀ that matches the peak of **D1** formed *ex situ* (Figure 3.2d, f). These peaks arise in both PC (Figure 3.13a) and TCB (Figure 3.2d-e). Because the dehalogenation is the rate limiting step in the on-surface Ullmann coupling,^{15,29} it is reasonable to assume that the *in situ* Ullmann coupling would proceed from the pre-dehalogenated Au complexes in TCB, without the presence of an ionic double layer and the resulting strong electric field. The dimerization of **Au** proceeds at all biases in TCB (Figure 3.13b), whereas the dimerization of **I1** never proceeds in TCB (Figure 3.7a), despite undergoing oxidative addition.

This facile dimerization further supports our hypothesis that the first mechanistic step of an Ullmann coupling in the junction is dehalogenation. It also suggests that both molecules undergoing the Ullmann coupling must separately undergo oxidative addition before reacting with each other. Because this is so facile with the pre-dehalogenated complexes, they always dimerize. However, although the aryl iodides undergo enough oxidative addition in TCB to visualize the high-G, dehalogenated linkage, it is not frequent enough for them to react with one another. Performing the experiments in PC allows for a stronger electric field and more oxidative addition occurring within a smaller area, therefore enabling coupling.

3.4 Probing the Mechanism

As previously described,²⁶ we believe the dehalogenation step to be occurring via an oxidative addition of the aryl molecule to the Au surface. Since a reductive bias promotes iodide dissociation, we hypothesize that the extra electron density at the tip can donate to the aryl carbon, displacing the iodide. To further probe this suggestion, we studied the reactivity of aryl molecules with various end groups in place of the iodide (Figure 3.3a). Iodides are known to be reactive towards oxidative addition, whereas bromides are less so, and triflates even less so.^{30–32} Therefore, we examine a series of molecules based on the amine-linker aryl iodide **I2**. The diamine Ullmann product **D2** (Figure 3.3a, dark blue structure) yields a very sharp and distinctive conductance feature (Figure 3.3b,c, dark blue traces), making it easy to observe and differentiate from other possible products. We synthesized analogous aryl amines with a bromide (**Br1**, see Section 3.8 for synthetic details) and a triflate (**OTf1**, Section 3.8), both methylated to yield a cross-coupling product that would be distinct from the homocoupling product. In these mixed end group experiments, we added an excess of the less reactive species compared to **I2**, to increase the likelihood of any possible oxidative addition of the former, and subsequent cross-coupling.

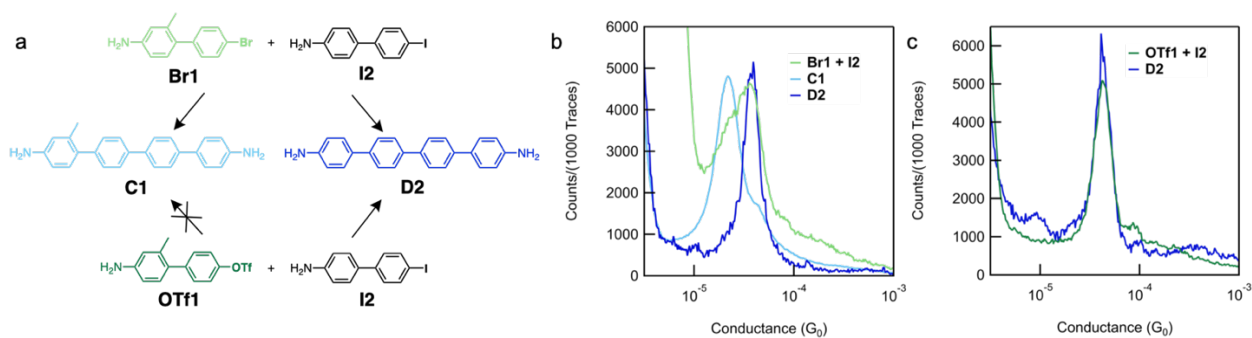


Figure 3.3 (a) When an aryl bromide **Br1** and an aryl iodide **I2** are measured together in the STM-BJ, both the iodide homocoupling product **D2** and the cross-coupled product **C1** are observed.

However, when an aryl triflate **OTf1** and an aryl iodide **I2** are measured together, only the iodide homocoupling product **D2** is observed, and no cross-coupling takes place. This is further evidence towards an oxidative addition-like mechanism, as opposed to alternatives like S_N2 . (b) The 1D histogram of the mixed **Br1 + I2** solution (light green trace) clearly demonstrates a low-G shoulder that is not seen in the 1D histogram of **D2** (dark blue), but matches the conductance of **C1** (light blue) synthesized *ex situ*. This indicates successful cross-coupling. (c) The 1D histogram of the mixed **OTf1 + I2** solution matches that of **D2**, indicating only homocoupling is taking place.

Upon measuring these mixtures in PC at a negative tip bias, we observed that in the case of the **Br1 + I2** experiment (Figure 3.3b, light green trace), a peak that matches the homocoupling product **D2** (Figure 3.3b, dark blue trace) is present. Additionally, there is a low-G shoulder which does not correlate to **D2** or to **Br1** homocoupling (Figure 3.14a). As such, we hypothesize that the low-G shoulder is the cross-coupling product of **Br1** and **I2** (see Figure 3.14c, d for additional data). To verify our theory, the methylated dimer **C1** was synthesized *ex situ* (see Section 3.8 for details), and is a match (Figure 3.3b, light blue trace) for the low-G shoulder. When measuring the **OTf1 + I2** mixture, no such low-G shoulder is observed (Figure 3.3c), only a peak which correlates with **D2** is present. **OTf1** was also confirmed not to homocouple (Figure 3.14b). These observations indicate that oxidative addition is happening frequently enough with the bromide, but not with the triflate, for cross-coupling to occur (Figure 3.4a). This follows the trend of reactivity towards oxidative addition, further supporting our mechanistic hypothesis.

As stated above, **Br1** does not homocouple, however it participates in cross-coupling. This is further experimental evidence of oxidative addition reactivity trends. We postulate that aryl bromides, which are only somewhat reactive towards oxidative addition, will not undergo oxidative addition efficiently enough for homocoupling to occur (Figure 3.4a). However, when an aryl bromide is mixed with an aryl iodide, which will undergo oxidative addition more readily,

any dehalogenated aryl bromides are surrounded by dehalogenated aryl iodides (Figure 3.4b), and can therefore react in a cross-coupling.

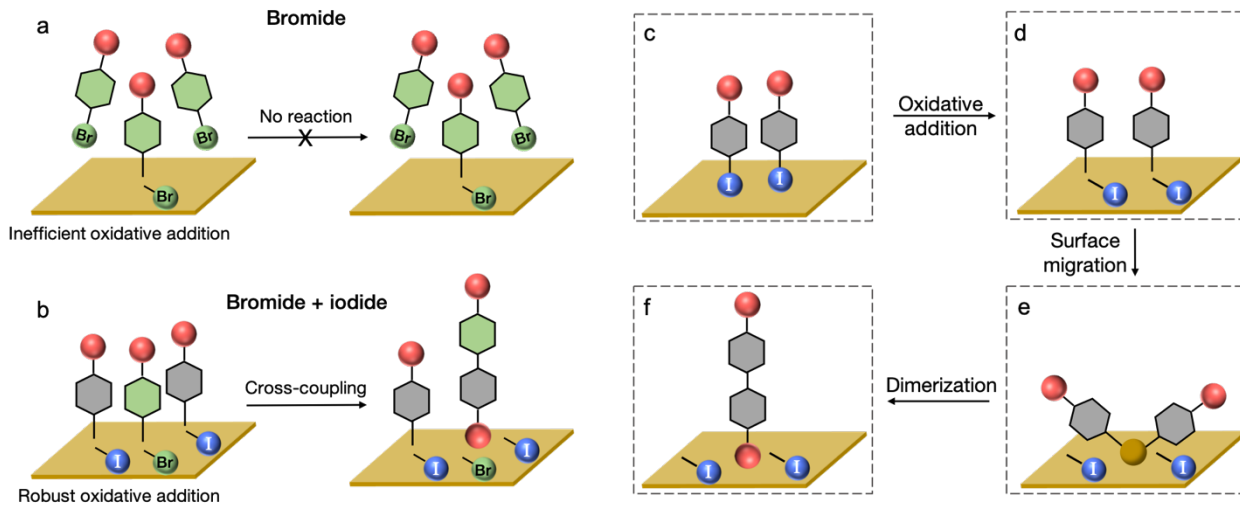


Figure 3.4 Note: in these cartoons, Au is depicted as a flat surface for simplicity. (a) Aryl bromides (green) do not undergo enough oxidative addition to homocouple. (b) When aryl bromides and iodides (gray) are mixed, cross-coupling can occur due to the robust oxidative addition of iodides. (c-f) The proposed mechanism, as follows: each aryl halide undergoes oxidative addition to become dehalogenated (c to d); the dehalogenated aryl groups migrate towards each other (d to e); they either arrive near each other both on the surface or attached to an adatom (adatom scenario depicted in e); they couple and form a new C–C bond (e to f).

Taken together, we believe the mechanism is roughly as follows (Figure 3.4c-f): each aryl halide undergoes oxidative addition, attaching itself to the Au surface with the detached halogen possibly somewhere else on the surface. Then, if the aryl groups are not already near each other, they migrate on the surface until they are in the vicinity to react. They might remain attached to the surface in a tilted configuration,^{33,34} or they could be bound to an adatom or some other surface structure.³⁵ Finally, they come together to form a new C–C bond to make the dimer.

3.5 The Fate of the Iodide

With this understanding of the dehalogenation and oxidative addition mechanistic details, we sought to clarify the fate of the iodide after dehalogenation. When measurements of I₂ were run for a long time (~12 h), a pattern in the height of the homocoupling product peak arose: first the counts increase, indicating more dimer is forming over time, but then the counts begin decrease. This is visualized in Figure 3.5a-b following the rainbow ordering of the traces on the 1D histogram (Figure 3.5a) and points on the counts versus trace number plot (Figure 3.5b). We hypothesize that this could be a result of a deceleration in dimer formation, or a decrease in dimer pickup rate, both of which could stem from the tip being “dirty.”

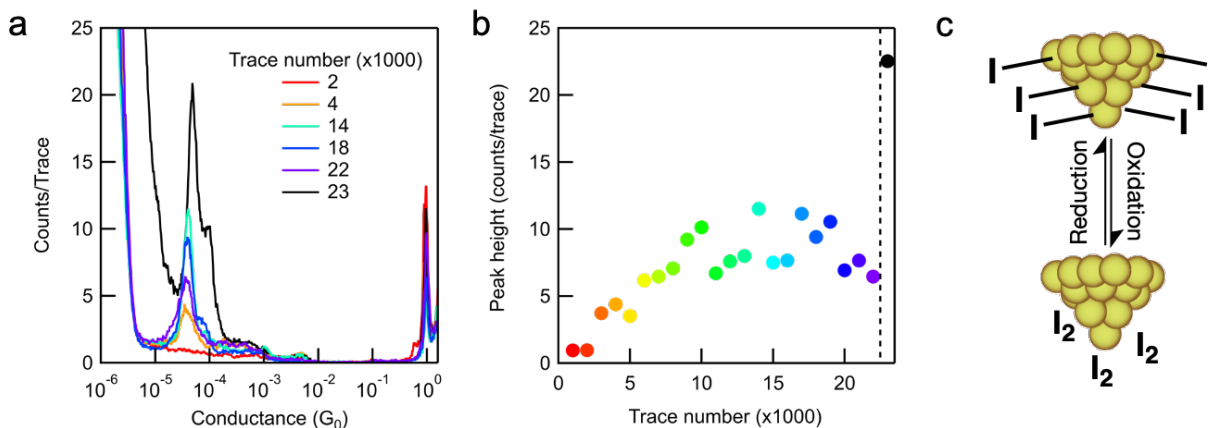


Figure 3.5 (a) 1D histograms of I₂ taken every 1000 traces demonstrate the trend in dimer counts over time. Certain traces are selected for clarity. The rainbow order of the colors follows trace progression (red = early traces, purple = late traces). Counts first increase, and then fall. The trace in black was taken after a high bias pulse, with the counts increasing by almost a factor of 4. (b) A different representation of the dimer counts over time, demonstrating the same rise and fall of counts as in (a). Again, the black marker after the dotted line demonstrates the ~4-fold increase in counts after a high bias pulse. (c) Cartoon representation of the fate of the iodide. The detached iodide sticks to the tip after dehalogenation, and is released by application of a large bias to the tip, “cleaning” the tip. The state of the released iodide is unknown; it is drawn as a I₂ in the case of applying a large oxidative tip bias.

We propose that after the oxidative addition step, the newly detached iodide is sticking to the Au tip and either blocking reactive sites or crowding it, hindering pickup of the dimer, or both. Two pieces of evidence support this hypothesis: if the tip is replaced with a clean tip, the counts will increase (Figure 3.15), and if a high tip bias is applied for a few seconds (Figure 3.5a,b black trace and point) the counts will also increase. In the latter case, it is possible that the iodide is being oxidized off the Au surface (see Figure 3.5c for a cartoon representation), although the exact mechanism and state of the freed iodide remains elusive.

3.6 Other Reaction Criteria

Over the course of studying this reaction in the single molecule junction, we collected many other observations and data about reactivity. It is not entirely clear yet how they all fit together, but the parameters outlined below seem to be critical to the success of the reaction. I will now describe what we have discovered so far and our leading hypotheses, in addition to suggested experiments for future work.

Polar solvent. As previously described, Ullmann coupling measurements are carried out in a polar solvent (PC), and although oxidative addition is observed in nonpolar solvents like TCB, homocoupling is never observed. Figure 3.6a demonstrates that across a series of nonpolar solvents (TCB in black, bromonaphthalene (BNP) in green, and tetradecane (TD) in blue), no dimer is observed when measuring **I1**, compared to PC (red) where there is clear dimer formation. This could be attributed to infrequent oxidative addition, as mentioned above, or in the case of aromatic solvents there is the potential for them to stack between the aromatic analyte and block surface migration (see Figure 3.16 for cartoon representation). Moreover, the polar solvent with supporting

electrolyte creates the aforementioned concentrated electric field, which could also promote the oxidative addition and homocoupling. Further experiments to better understand the solvent effects could involve a wider range of solvents, mixtures of solvents, different concentrations of supporting electrolyte, adding electrolyte to a nonpolar solvent (as long as the solvent does not dissolve the wax used for coating tips), or increasing the concentration of analyte relative to the solvent.

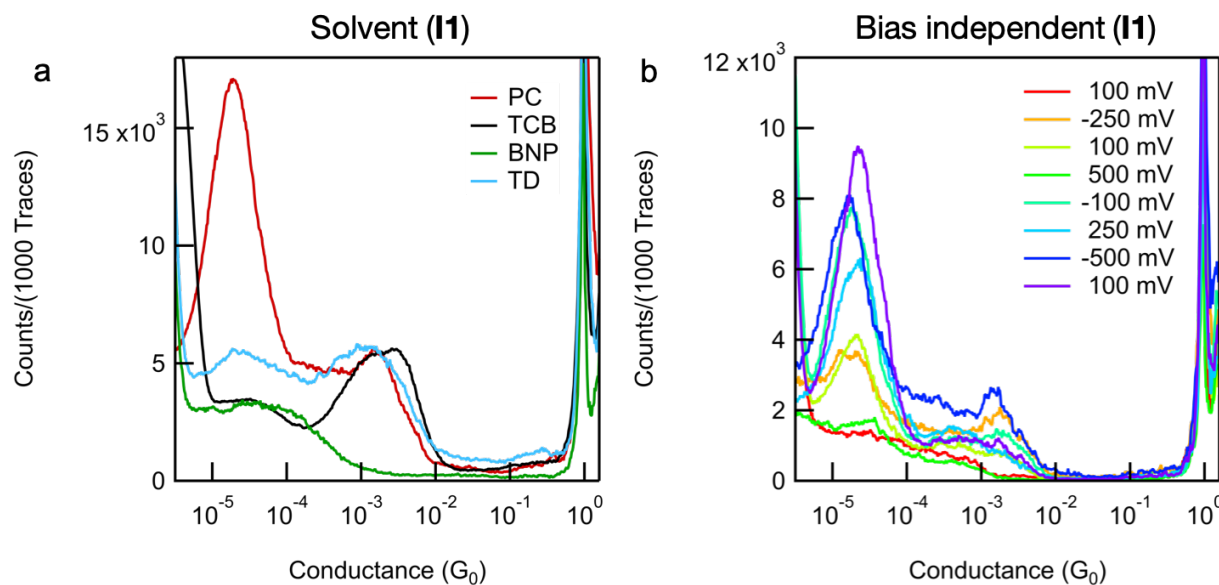


Figure 3.6 (a) **I1** measured in different solvents. The Ullmann coupling product peak is only visible in PC (polar solvent), and not in any of the other (nonpolar) solvents tested. (b) **I1** measured at a variety of biases in a random order, demonstrating that time is the overriding factor in dimer formation as opposed to bias.

Bias independence. Our original hypothesis stemmed from the knowledge that oxidative addition of aryl iodides can be promoted by applying a negative tip bias,²⁶ so we figured the same would apply to dimer formation. However, we find that bias alone does not dictate the amount of dimer formed (visualized by counts for short duration experiments). This can be demonstrated by applying different biases in a random order when measuring **I1** (Figure 3.6b): although the

magnitude and polarity of the bias is changed at random, the dimer counts consistently increase over time (from red to purple). Other observations are also inconsistent with the original bias-driven theory. For example, measuring at the same bias on different days can lead to drastically different counts. Additionally, we have observed instances where smaller magnitude biases yield higher counts than larger magnitude biases. Altogether, this leads us to believe that bias alone is not the strongest driving force of this reaction.

These new observations could be further supported with a robust dimer quantification method. We have investigated using NMR, MS, and high-performance liquid chromatography (HPLC) for both detection and quantification of homocoupling product with a variety of analytes, however so far none of these methods have panned out. The insolubility of multi-phenyl analytes is often a limiting factor. Recently, we began to explore fluorescence as a mode of quantification, as many of the analytes in this study fluoresce strongly. Additionally, the starting materials and their corresponding products are well separated in both their ideal excitation and emission wavelengths, which is promising for optimizing a protocol to quantify dimer formation. Fluorescence is sensitive to much lower concentrations, requires smaller volumes, and tolerates solvents that more readily solubilize our analytes, so we are hopeful that this method will be more conducive to our system. These experiments are currently underway.

Surface roughness. The roughness of the Au surface seems to play a critical role in reactivity. We observed that when **I2** is measured on rough substrates, dimer readily forms, but when measured on smooth surfaces, there is little to no reaction. We have also observed on rough surfaces, through a lateral motion experiment in which the tip is moved to various spots on the substrate, that different areas of the same substrate can lead to vastly different amounts of dimer. Rough surfaces include Au coated glass (Figure 3.7a, pink), or polished stainless steel pucks

(Figure 3.7a, yellow, which is the type of substrate used throughout this Ullmann study unless otherwise noted) which become rough upon polishing (see Figure 3.7b for an SEM image). The comparison smooth surfaces are Au-coated mica (Figure 3.7a, green), and any substrate coated with a thick layer (>130 nm) of Au. If oxidative addition is occurring on the surface, and a rougher surface with more active sites might promote reactivity. So far, we only examined the surfaces visually by SEM and elementally by EDX (Figure 3.17), so future experiments could include further probing the surface composition and topology, both before and after measuring in the STM-BJ. This could include using different surface characterization techniques, examining what remains on the surface after an experiment, or developing a method to fabricate surfaces with a controlled roughness to determine the effects more precisely.

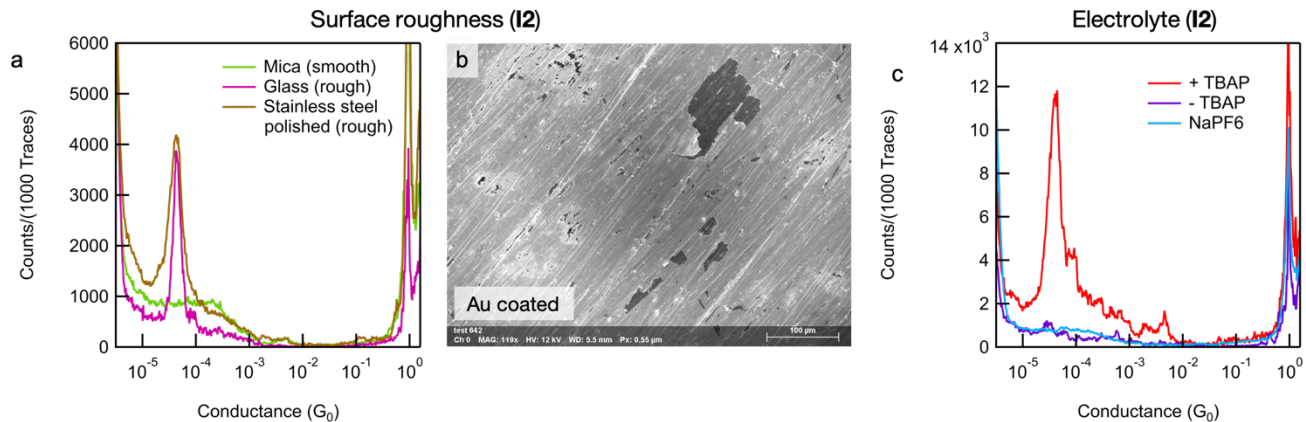


Figure 3.7 (a) I2 measured on three types of substrates: mica (smooth, green), glass (rough, pink) and stainless steel polished (rough, yellow). Homocoupling is not observed on smooth surfaces, but proceeds on rough surfaces. (b) SEM image of a polished and Au coated stainless steel puck. Clear striations are seen post-polishing, indicating a high degree of surface roughness. (c) The presence of electrolyte affects the reactivity of I2. Lacking electrolyte (purple) and using a smaller cation (blue) both hinder homocoupling as compared to using TBAP (red).

Electrolyte: presence and cation size. When measuring in a polar solvent, a large concentration of supporting electrolyte is typically added to facilitate formation of the ionic double layer. To probe the role of the electrolyte we conducted a number of different experiments, which yielded mixed results. The plots shown in Figure 3.7c correspond to an experiment in which solutions of **I2** were made with TBAP, without TBAP, and with NaPF₆. These solutions were left on Au substrates that were not subjected to any bias or electric field. After 4 hours, they were each put onto the STM-BJ setup and a small number (200) of traces was taken at a low bias (+100 mV). In the case of the solution with TBAP (red), there is clear dimer formation, however in the cases of solution without TBAP (purple) and with NaPF₆ (blue), no dimer is formed.

From this and other experiments not shown, we draw two conclusions: that supporting electrolyte is necessary for observable reactivity, and the size of the cation affects reactivity. We theorize that these observations are a result of a change in the ionic double layer. It is remarkable that at ambient conditions on a Au surface any dimer is forming, and we attribute this to the strong electric field created within the double layer. Therefore, if the double layer is removed by taking away supporting electrolyte, or modified by changing the size of the ions, it somehow disrupts the electric field in a way that hinders reactivity. It is also worth noting that when taking typical STM-BJ measurements and applying any bias, homocoupling will proceed with or without a supporting electrolyte (Figure 3.18).

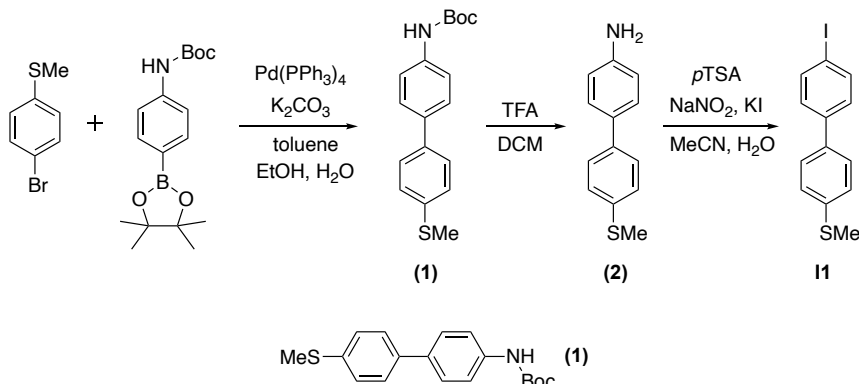
We do not yet have a comprehensive understanding of the effect of the electrolyte and the resulting electric field, and there are many possible directions to explore. A systematic electrolyte study could clarify its role, including varying the identities of the cation and the anion, changing the concentration, applying different biases, and (if possible) quantifying the resulting homocoupling. Additionally, computations could aid in the understanding of the electric field

arising from the presence of the supporting electrolyte, on the molecules and on the reaction. Because we cannot yet quantify the electric field in the junction, the exact differences between the fields present with and without electrolyte remains unknown. It could be useful to understand generally how an electric field impacts reactivity. Turning towards computations might provide information about transition states, dipole moments, or reaction energies, which could inform our understanding of field and electrolyte effects. Some preliminary work in this realm is underway in collaboration with the Berkelbach group.

3.7 Conclusion and Outlook

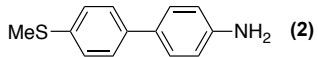
We have demonstrated the successful Ullmann coupling reaction in the STM-BJ across a range of aryl iodides, under ambient conditions and without exogenous chemicals or stimuli. The reaction consistently proceeds in PC, verified by measuring the coupling product prepared *ex situ*, as well as by MS. Some initial mechanistic insights can be gleaned, notably that the dehalogenation step is likely the rate limiting step in our system, akin to other surface Ullmann chemistry. Moreover, we believe this process follows an oxidative addition-like mechanism, based both on previous evidence and on preliminary cross-coupling data. By examining the reactivity of iodides versus bromides versus triflates, we have shown that only those groups more prone to oxidative addition will participate in coupling. There are a number of interesting threads that remain incomplete, but when further explored, will clarify the full picture of this junction reaction. These include the effects of the solvent, bias, electrolyte, and surface topology. This project is ongoing, and although we have gained a lot of insight into the *in situ* Ullmann coupling, there is clearly still much to be discovered.

3.8 Synthetic Details



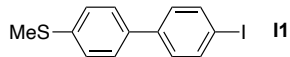
1. A 100 mL three-necked round bottom flask fitted with a reflux condenser and equipped with a Teflon coated stir bar under N₂ atmosphere was charged with 4-bromothioanisole (215 mg, 1.04 mmol), (4-tert-butoxycarbonylaminophenyl)boronic acid pinacol ester (360 mg, 1.13 mmol), K₂CO₃ (690 mg, 5 mmol), and Pd(PPh₃)₄ (30 mg, 0.03 mmol). A separate 50 mL round bottom flask equipped with a Teflon stir bar under N₂ atmosphere was charged with toluene (24 mL), ethanol (5 mL) and water (2.5 mL) and sparged with N₂ for 20 min. The solution was then added to the mixture of solids resulting in a bright yellow cloudy solution. The reaction mixture was refluxed for 36 h. After cooling to room temperature, the solvent was removed via rotary evaporation. The solid residue was extracted with ethyl acetate (2 x 50 mL), washed with water (50 mL) and brine (50 mL), dried with Na₂SO₄ and the solvent was removed via rotary evaporation. The residue was purified using silica gel flash column chromatography, eluting with EtOAc/hexanes to afford a beige solid. Yield: 196 mg, 60%.

This compound has been reported previously. ¹H NMR (400 MHz, CDCl₃) δ 7.61 – 7.46 (m, 4H), 7.42 (d, *J* = 8.3 Hz, 2H), 7.31 (d, *J* = 8.3 Hz, 2H), 6.49 (s, 1H), 2.52 (s, 3H), 1.54 (s, 9H).



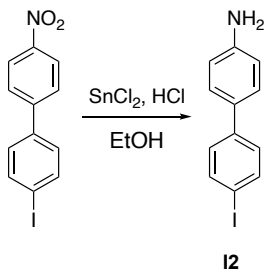
2. A 25 mL round bottom flask equipped with a Teflon coated stir bar was charged with **1** (120 mg, 0.56 mmol) and dissolved in DCM (4 mL). Trifluoroacetic acid (0.5 mL) was added, and the solution turned orange upon addition. The reaction was stirred at room temperature for one hour, then diluted with DCM (50 mL) and washed with 1 M aqueous NaOH (50 mL), brine (50 mL) and dried with Na₂SO₄. The solvent was removed via rotary evaporation to afford a beige solid. Yield: 80 mg, 97%.

This compound has been reported previously.²⁶ ¹H NMR (400 MHz, DMSO) δ 7.48 (d, *J* = 8.6 Hz, 2H), 7.33 (d, *J* = 8.6 Hz, 2H), 7.26 (d, *J* = 8.5 Hz, 2H), 6.62 (d, *J* = 8.6 Hz, 2H), 5.18 (s, 2H), 2.47 (s, 3H).



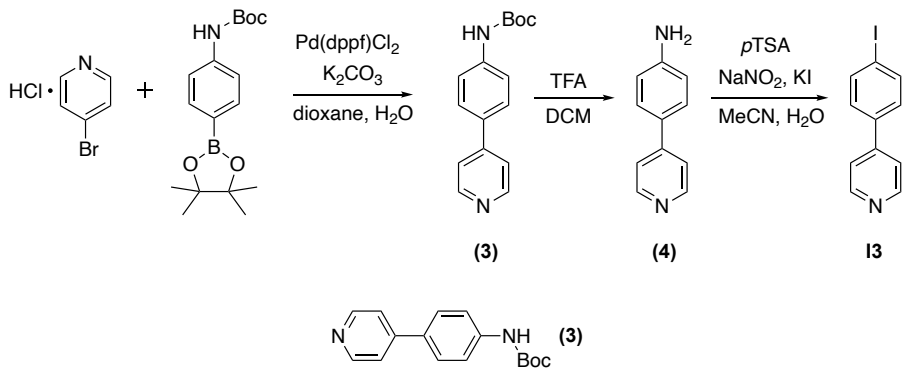
11. A 25 mL round bottom flask equipped with a Teflon coated stir bar was charged with **2** (70 mg, .33 mmol) and dissolved in acetonitrile (4 mL) and water (0.2 mL). *p*-Toluenesulfonic acid monohydrate (190 mg, 1 mmol) was added and the resulting suspension was allowed to stir for 5 minutes and placed in a room temperature water bath. A separate solution of NaNO₂ (46 mg, 0.67 mmol) and potassium iodide (138 mg, 0.83 mmol) in water (1.3 mL) was added slowly, resulting in a viscous, dark brown mixture. The reaction was stirred overnight then quenched with saturated NaHCO₃, extracted into DCM (3 x 30 mL), washed with brine (50 mL) and dried with Na₂SO₄. The solvent was removed via rotary evaporation and the residue was purified using silica gel flash column chromatography, eluting with DCM/hexanes to afford a white solid. Yield: 72 mg, 68%.

This compound has been reported previously.²⁶ ¹H NMR (400 MHz, CDCl₃) δ 7.75 (d, *J* = 8.4 Hz, 2H), 7.48 (d, *J* = 8.4 Hz, 2H), 7.31 (dd, *J* = 8.5, 6.8 Hz, 4H), 2.52 (s, 3H).



I2. An oven-dried 50 mL three-neck round bottom flask fitted with a reflux condenser and equipped with a Teflon coated stir bar under N₂ atmosphere was charged with 4-iodo-4'-nitrobiphenyl (310 mg, 0.95 mmol), SnCl₂•2H₂O (1.27 g, 5.6 mmol) and ethanol (8 mL). The solution was sparged with N₂ for 20 minutes. Concentrated aqueous HCl (1 mL) was then added and the solution was refluxed overnight. The mixture was cooled to room temperature and then poured into 10 mL of ice cold water. The solution was basified by careful addition of 2 M aqueous NaOH until the pH reached ~10. The aqueous solution was then extracted with DCM (3 x 25 mL), washed with brine (50 mL) and dried with Na₂SO₄. The solvent was removed via rotary evaporation, and the crude mixture was recrystallized in hot ethanol to afford a white powder. Yield: 155 mg, 55%.

This compound has been reported previously.³⁶ ¹H NMR (400 MHz, DMSO) δ 7.69 (d, *J* = 8.5 Hz, 2H), 7.64 – 7.00 (m, 4H), 6.63 (d, *J* = 8.5 Hz, 2H), 5.27 (s, 2H).



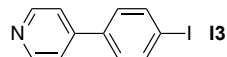
3. A 100 mL three-necked round bottom flask fitted with a reflux condenser and equipped with a Teflon coated stir bar under N₂ atmosphere was charged with 4-bromopyridine hydrochloride salt (307 mg, 1.58 mmol), (4-tert-butoxycarbonylaminophenyl)boronic acid pinacol ester (557 mg, 1.74 mmol), K₂CO₃ (815 mg, 5.8 mmol), and Pd(dppf)Cl₂ DCM adduct (53 mg, 0.07 mmol). A separate 50 mL round bottom flask equipped with a Teflon stir bar under N₂ atmosphere was charged with dioxane (9 mL) and water (1 mL) and sparged with N₂ for 20 min. The solution was then added to the mixture of solids resulting in a bright yellow cloudy solution. The reaction mixture was refluxed for 36 h. After cooling to room temperature, the solvent was removed via rotary evaporation. The solid residue was extracted with ethyl acetate (2 x 50 mL), washed with water (50 mL) and brine (50 mL), dried with Na₂SO₄ and the solvent was removed via rotary evaporation. The residue was purified using basified silica gel flash column chromatography, eluting with EtOAc/hexanes buffered with Et₃N to afford a white crystalline solid. Yield: 370 mg, 87%.

This compound has been reported previously.³⁷ ¹H NMR (400 MHz, DMSO) δ 9.54 (s, 1H), 8.58 (d, *J* = 6.2 Hz, 2H), 7.74 (d, *J* = 8.7 Hz, 2H), 7.66 (d, *J* = 6.2 Hz, 2H), 7.60 (d, *J* = 8.7 Hz, 2H), 1.49 (s, 9H).



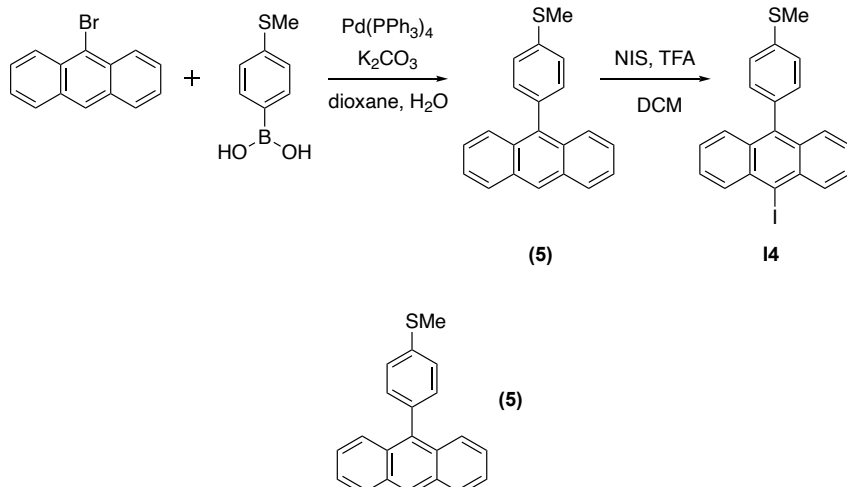
4. A 25 mL round bottom flask equipped with a Teflon coated stir bar was charged with **4** (360 mg, 1.33 mmol) and dissolved in DCM (10 mL). Trifluoroacetic acid (3 mL) was added, and the was stirred at room temperature for one hour, then diluted with DCM (50 mL) and washed with 1 M aqueous NaOH (50 mL), brine (50 mL) and dried with Na₂SO₄. The solvent was removed via rotary evaporation to afford a pale yellow solid. Yield: 210 mg, 93%.

This compound has been reported previously.³⁷ ¹H NMR (400 MHz, DMSO) δ 8.48 (d, *J* = 5.1 Hz, 2H), 7.76 – 7.16 (m, 4H), 6.67 (d, *J* = 8.5 Hz, 2H), 5.61 (s, 2H).

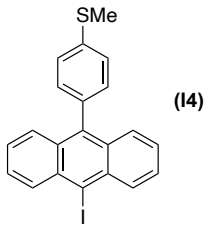


I3. A 25 mL round bottom flask equipped with a Teflon coated stir bar was charged with **4** (112 mg, .66 mmol) and dissolved in acetonitrile (8 mL) and water (0.5 mL). *p*-Toluenesulfonic acid monohydrate (380 mg, 2 mmol) was added and the resulting suspension was allowed to stir for 5 minutes and placed in a room temperature water bath. A separate solution of NaNO₂ (92 mg, 1.33 mmol) and potassium iodide (276 mg, 1.66 mmol) in water (3 mL) was added slowly, resulting in a viscous, dark brown mixture. The reaction was stirred overnight then quenched with saturated NaHCO₃, extracted into DCM (3 x 50 mL), washed with brine (100 mL) and dried with Na₂SO₄. The solvent was removed via rotary evaporation and the residue was purified using basified silica gel flash column chromatography, eluting with DCM/hexanes to afford a beige solid. Yield: 130 mg, 70%.

This compound has been reported previously.³⁸ ¹H NMR (400 MHz, CDCl₃) δ 8.67 (d, *J* = 6.4 Hz, 2H), 7.83 (d, *J* = 8.5 Hz, 2H), 7.46 (d, *J* = 6.2 Hz, 2H), 7.37 (d, *J* = 8.5 Hz, 2H).

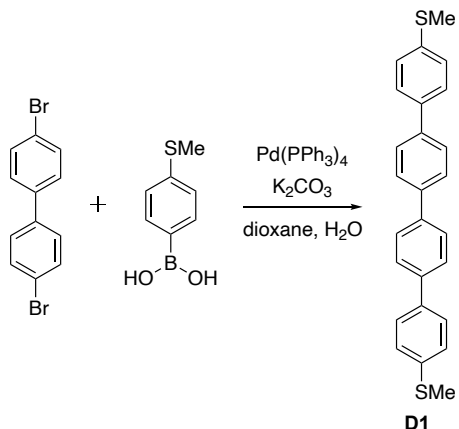


5. A 100 mL three-necked round bottom flask fitted with a reflux condenser and equipped with a Teflon coated stir bar under N₂ atmosphere was charged with 9-bromoanthracene (257 mg, 1 mmol), (4-thiomethoxyphenyl)boronic acid (193 mg, 1.15 mmol), K₂CO₃ (657 mg, 4.7 mmol), and Pd(PPh₃)₄ (40 mg, 0.035 mmol). A separate 50 mL round bottom flask equipped with a Teflon stir bar under N₂ atmosphere was charged with dioxane (8 mL), and water (2 mL) and sparged with N₂ for 20 min. The solution was then added to the mixture of solids resulting in a bright yellow cloudy solution. The reaction mixture was refluxed for 18 h. After cooling to room temperature, the solvent was removed via rotary evaporation. The solid residue was extracted with ethyl acetate (2 x 50 mL), washed with water (50 mL) and brine (50 mL), dried with Na₂SO₄ and the solvent was removed via rotary evaporation. The residue was purified using silica gel flash column chromatography, eluting with DCM/hexanes to afford a beige solid. Yield: 198 mg, 66%.
¹H NMR (500 MHz, CDCl₃) δ 8.50 (s, 1H), 8.11 – 7.99 (m, 2H), 7.69 (dd, *J* = 8.9, 1.0 Hz, 2H), 7.51 – 7.42 (m, 4H), 7.40 – 7.32 (m, 4H), 2.62 (s, 3H). ¹³C NMR (126 MHz, CDCl₃) δ 137.73, 136.38, 135.41, 131.72, 131.38, 130.28, 128.37, 126.74, 126.63, 126.33, 125.39, 125.12, 15.79.



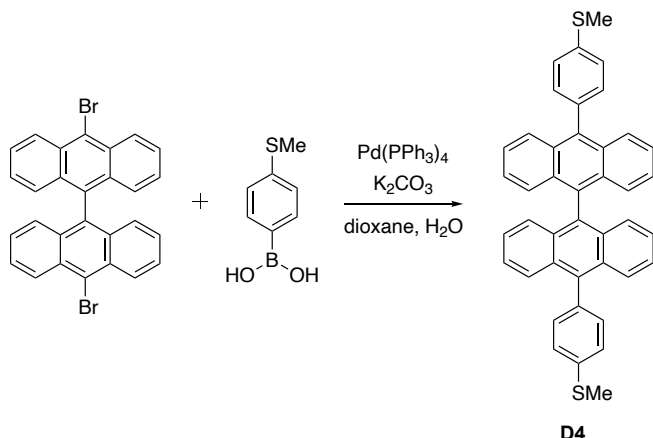
I4. A 25 mL round bottom flask equipped with a Teflon coated stir bar was charged with **5** (31 mg, 0.1 mmol) and dissolved in DCM (0.8 mL). 5 drops of TFA were added and N-iodosuccinamide (30 mg, 0.13 mmol) was added in portions. The suspension was allowed to stir for 18 h and then was quenched with saturated NaHCO₃, extracted with DCM (2 x 25 mL), washed with brine (50 mL) and dried with Na₂SO₄. The solvent was removed via rotary evaporation. The residue was purified using silica gel flash column chromatography, eluting with DCM/hexanes to afford a yellow solid. Yield: 21.6 mg, 50%.

¹H NMR (500 MHz, CDCl₃) δ 8.57 (d, *J* = 8.8 Hz, 2H), 7.70 – 7.60 (m, 2H), 7.57 (ddd, *J* = 8.9, 6.5, 1.2 Hz, 2H), 7.47 (d, *J* = 8.2 Hz, 2H), 7.37 (ddd, *J* = 8.8, 6.5, 1.2 Hz, 2H), 7.33 (d, *J* = 8.3 Hz, 2H), 2.62 (s, 3H). ¹³C NMR (126 MHz, CDCl₃) δ 138.50, 138.24, 134.96, 133.71, 133.52, 131.53, 131.09, 127.55, 127.49, 126.28, 125.64, 105.73, 15.70.



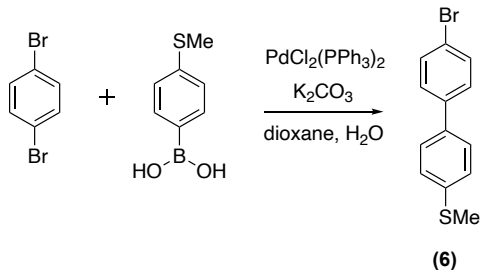
D1. A 100 mL three-necked round bottom flask fitted with a reflux condenser and equipped with a Teflon coated stir bar under N₂ atmosphere was charged with 4,4'-diiodobiphenyl (243 mg, 0.6 mmol), (4-thiomethoxyphenyl)boronic acid (242 mg, 1.44 mmol), K₂CO₃ (414 mg, 3 mmol), and Pd(PPh₃)₄ (42 mg, 0.04 mmol). A separate 50 mL round bottom flask equipped with a Teflon stir bar under N₂ atmosphere was charged with dioxane (12 mL) and water (2.5 mL) and sparged with N₂ for 20 min. The solution was then added to the mixture of solids resulting in a bright yellow cloudy solution. The reaction mixture was refluxed for 18 h. After cooling to room temperature the solution was filtered, and the resulting beige solid was washed with DCM, MeOH and acetone. Yield: 200 mg, 84%.

High-Res MS (ASAP+): calculated *m/z* for [M+H]⁺ 399.1241, found 399.1239.

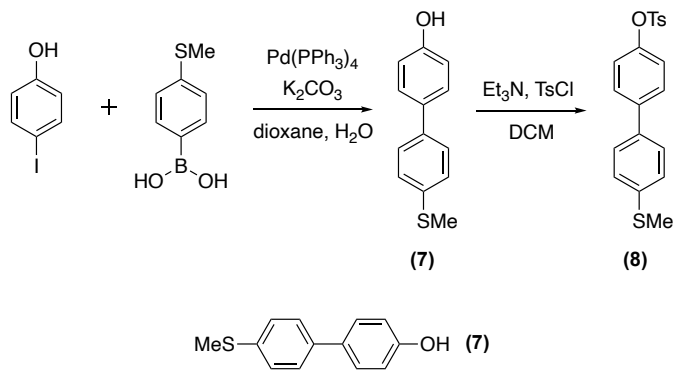


D4. A 100 mL three-necked round bottom flask fitted with a reflux condenser and equipped with a Teflon coated stir bar under N₂ atmosphere was charged with 10,10'-dibromo-9,9'-bianthryl (353 mg, 0.69 mmol), (4-thiomethoxyphenyl)boronic acid (278 mg, 1.66 mmol), K₂CO₃ (1.1 g, 8 mmol), and Pd(PPh₃)₄ (57 mg, 0.05 mmol). A separate 50 mL round bottom flask equipped with a Teflon stir bar under N₂ atmosphere was charged with dioxane (20 mL), and water (4 mL) and sparged with N₂ for 20 min. The solution was then added to the mixture of solids resulting in a bright yellow cloudy solution. The reaction mixture was refluxed for 36 h. After cooling to room temperature, the solvent was removed via rotary evaporation. The solid residue was extracted with DCM (2 x 100 mL), washed with water (100 mL) and brine (100 mL), dried with Na₂SO₄ and the solvent was removed via rotary evaporation. Recrystallization of the crude mixture in hot EtOH removed most impurities and afforded a pale yellow solid. Yield: 253 mg, 61%.

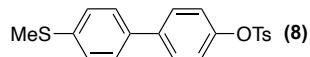
¹H NMR (500 MHz, CDCl₃) δ 7.85 (d, *J* = 8.8 Hz, 2H), 7.56 (s, 4H), 7.34 (ddd, *J* = 8.9, 6.3, 1.4 Hz, 2H), 7.23 (d, *J* = 8.7 Hz, 2H), 7.19 – 7.15 (m, 2H), 2.67 (s, 3H). ¹³C NMR (126 MHz, CDCl₃) δ 137.91, 137.24, 135.65, 133.46, 131.93, 131.38, 130.17, 127.16, 127.12, 126.39, 125.57, 125.29, 15.79.



6. A 100 mL three-necked round bottom flask fitted with a reflux condenser and equipped with a Teflon coated stir bar under N_2 atmosphere was charged with 1,4-dibromobenzene (1.42 g, 6 mmol), (4-thiomethoxyphenyl)boronic acid (672 mg, 4 mmol), K_2CO_3 (4.14 g, 30 mmol), and $\text{PdCl}_2(\text{PPh}_3)_2$ (127 mg, 0.1 mmol). A separate 100 mL round bottom flask equipped with a Teflon stir bar under N_2 atmosphere was charged with dioxane (24 mL), and water (12 mL) and sparged with N_2 for 20 min. The solution was then added to the mixture of solids resulting in a bright yellow cloudy solution. The reaction mixture was refluxed for 18 h. After cooling to room temperature, the solvent was removed via rotary evaporation. The solid residue was extracted with ethyl acetate (2 x 100 mL), washed with water (100 mL) and brine (100 mL), dried with Na_2SO_4 and the solvent was removed via rotary evaporation. The residue was purified using silica gel flash column chromatography, eluting with $\text{EtOAc}/\text{hexanes}$ to afford a white solid. Yield: 1g, 89%. This compound has been reported previously.³⁹ ^1H NMR (400 MHz, CDCl_3) δ 7.55 (d, $J = 8.6$ Hz, 2H), 7.48 (d, $J = 8.5$ Hz, 2H), 7.43 (d, $J = 8.6$ Hz, 2H), 7.32 (d, $J = 8.5$ Hz, 2H).



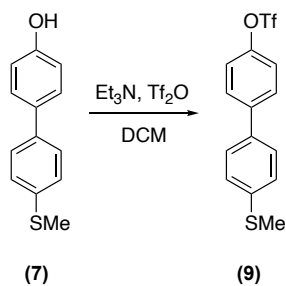
7. A 100 mL three-necked round bottom flask fitted with a reflux condenser and equipped with a Teflon coated stir bar under N_2 atmosphere was charged with 4-iodophenol (440 mg, 2 mmol), (4-thiomethoxyphenyl)boronic acid (370 mg, 2.2 mmol), K_2CO_3 (1.08 g, 7.8 mmol), and $\text{Pd}(\text{PPh}_3)_4$ (60 mg, 0.06 mmol). A separate 50 mL round bottom flask equipped with a Teflon stir bar under N_2 atmosphere was charged with dioxane (16 mL), and water (6 mL) and sparged with N_2 for 20 min. The solution was then added to the mixture of solids resulting in a bright yellow cloudy solution. The reaction mixture was refluxed for 18 h. After cooling to room temperature, the solvent was removed via rotary evaporation. The solid residue was dissolved in ethyl acetate (100 mL), washed with 0.5M HCl (50 mL), water (50 mL) and brine (50 mL), dried with Na_2SO_4 and the solvent was removed via rotary evaporation. The residue was purified using silica gel flash column chromatography, eluting with $\text{Et}_2\text{O}/\text{hexanes}$ to afford a white solid. Yield: 196 mg, 45%.
 ^1H NMR (500 MHz, CDCl_3) δ 7.48 (dd, $J = 8.4, 6.1$ Hz, 4H), 7.34 (d, $J = 8.4$ Hz, 2H), 6.92 (d, $J = 8.6$ Hz, 2H), 4.74 (s, 1H), 2.54 (s, 3H). ^{13}C NMR (126 MHz, CDCl_3) δ 155.01, 146.50, 137.70, 133.40, 128.11, 127.13, 127.08, 115.69, 16.07.



8. A 100 mL three-necked round bottom flask fitted with a reflux condenser and equipped with a Teflon coated stir bar under N_2 atmosphere was charged with **7** (32 mg, 0.15 mmol) and DCM (3

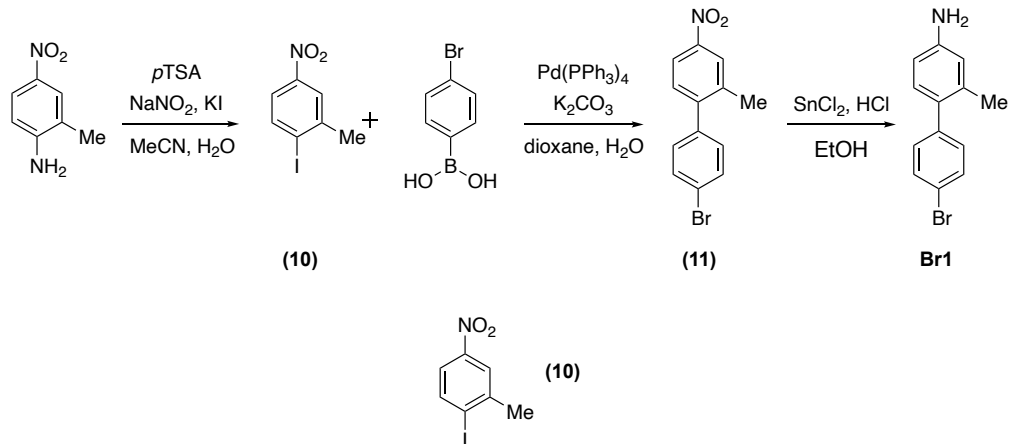
mL). Et₃N was added (0.03 mL, 0.22 mmol), followed by tosyl chloride (37 mg, 0.19 mmol). The solution was allowed to stir for 18 h and then diluted with DCM (50 mL), washed with water (50 mL) and brine (50 mL), dried with Na₂SO₄ and the solvent was removed via rotary evaporation. The residue was purified using silica gel flash column chromatography, eluting with EtOAc/hexanes to afford a white solid. Yield: 40 mg, 72%.

¹H NMR (500 MHz, CDCl₃) δ 7.74 (d, *J* = 8.4 Hz, 2H), 7.49 – 7.39 (m, 4H), 7.31 (dd, *J* = 10.7, 8.3 Hz, 4H), 7.03 (d, *J* = 8.7 Hz, 2H), 2.51 (s, 3H), 2.45 (s, 3H). ¹³C NMR (126 MHz, CDCl₃) δ 148.91, 145.39, 139.50, 138.28, 136.49, 132.48, 129.80, 128.57, 127.90, 127.38, 126.85, 122.73, 21.74, 15.76.



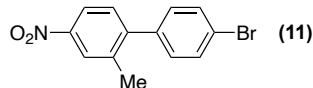
9. A 50 mL oven dried three-necked round bottom flask fitted with a reflux condenser and equipped with a Teflon coated stir bar under N₂ atmosphere was charged with 7 (136 mg, 0.63 mmol) and anhydrous DCM (5 mL). Anhydrous Et₃N was added (0.09 mL, 0.65 mmol), followed by triflic anhydride (0.12 mL, 0.71 mmol). The solution was allowed to stir for 18 h and was quenched with water, then diluted with DCM (50 mL), washed with water (50 mL) and brine (50 mL), dried with Na₂SO₄ and the solvent was removed via rotary evaporation. The residue was purified using silica gel flash column chromatography, eluting with DCM/hexanes to afford a white solid. Yield: 100 mg, 46%.

¹H NMR (500 MHz, CDCl₃) δ 7.62 (d, *J* = 8.8 Hz, 2H), 7.48 (d, *J* = 8.5 Hz, 2H), 7.38 – 7.31 (m, 4H), 2.53 (s, 3H). ¹⁹F NMR (471 MHz, CDCl₃) δ -71.87. ¹³C NMR (126 MHz, CDCl₃) δ 148.82, 141.04, 138.91, 135.90, 128.52, 127.48, 126.83, 121.70, 120.06, 15.66.



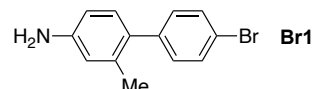
10. A 25 mL round bottom flask equipped with a Teflon coated stir bar was charged with 2-methyl-4-nitro-benzenamine (500 mg, 3.29 mmol) and dissolved in acetonitrile (25 mL) and water (2 mL). *p*-Toluenesulfonic acid monohydrate (1.9 g, 10 mmol) was added and the resulting suspension was allowed to stir for 5 minutes and placed in a room temperature water bath. A separate solution of NaNO₂ (460 mg, 6.7 mmol) and potassium iodide (1.38 g, 8.3 mmol) in water (3 mL) was added slowly, resulting in a viscous, dark brown mixture. The reaction was stirred overnight then quenched with saturated NaHCO₃, extracted into DCM (3 x 50 mL), washed with brine (100 mL) and dried with Na₂SO₄. The solvent was removed via rotary evaporation and the residue was purified using silica gel flash column chromatography, eluting with DCM/hexanes to afford a beige solid. Yield: 680 mg, 79%

This compound has been reported previously.⁴⁰ ¹H NMR (400 MHz, CDCl₃) δ 8.07 (d, *J* = 2.7 Hz, 1H), 8.00 (d, *J* = 8.5 Hz, 1H), 7.76 – 7.67 (m, 1H), 2.55 (s, 3H).



11. A 100 mL three-necked round bottom flask fitted with a reflux condenser and equipped with a Teflon coated stir bar under N₂ atmosphere was charged with **10** (263 mg, 1 mmol), 4-bromophenylboronic acid (201 mg, 1 mmol), K₂CO₃ (700 mg, 5.1 mmol), and Pd(PPh₃)₄ (30 mg, 0.03 mmol). A separate 50 mL round bottom flask equipped with a Teflon stir bar under N₂ atmosphere was charged with dioxane (8 mL), and water (2 mL) and sparged with N₂ for 20 min. The solution was then added to the mixture of solids resulting in a bright yellow cloudy solution. The reaction mixture was refluxed for 8 h. After cooling to room temperature, the solvent was removed via rotary evaporation. The solid residue was dissolved in ethyl acetate (50 mL), washed with water (50 mL) and brine (50 mL), dried with Na₂SO₄ and the solvent was removed via rotary evaporation. The residue was purified using silica gel flash column chromatography, eluting with DCM/hexanes to afford a white solid. Yield: 254 mg, 87%.

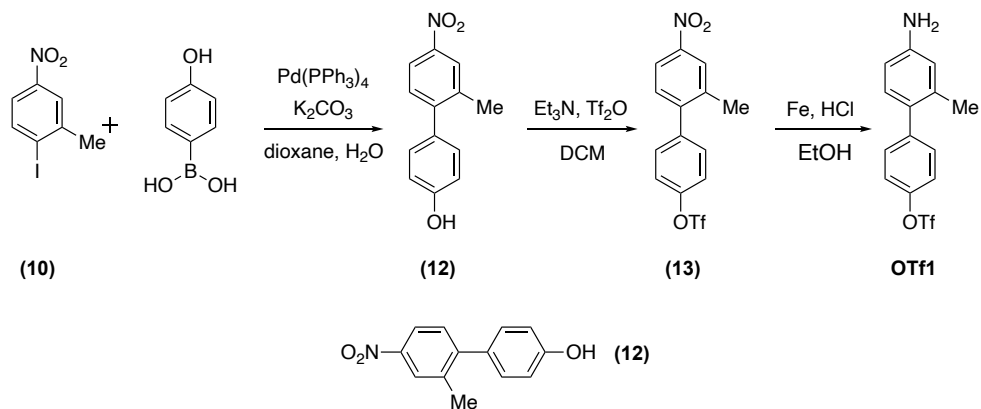
¹H NMR (400 MHz, CDCl₃) δ 8.15 (d, *J* = 2.4 Hz, 1H), 8.09 (dd, *J* = 8.3, 2.4 Hz, 1H), 7.60 (d, *J* = 8.4 Hz, 2H), 7.35 (d, *J* = 8.4 Hz, 1H), 7.18 (d, *J* = 8.4 Hz, 2H), 2.35 (s, 3H). ¹³C NMR (126 MHz, CDCl₃) δ 147.22, 138.60, 137.22, 131.71, 130.50, 130.37, 125.28, 122.38, 121.04, 20.59.



Br1. An oven-dried 50 mL three-neck round bottom flask fitted with a reflux condenser and equipped with a Teflon coated stir bar under N₂ atmosphere was charged with **17** (125 mg, 0.43 mmol), SnCl₂•2H₂O (600 mg, 2.6 mmol) and ethanol (8 mL). The solution was sparged with N₂ for 20 minutes. Concentrated aqueous HCl (1 mL) was then added and the solution was refluxed overnight. The mixture was cooled to room temperature and then poured into 10 mL of ice cold

water. The solution was basified by careful addition of 2 M aqueous NaOH until the pH reached ~10. The aqueous solution was then extracted with DCM (3 x 25 mL), washed with brine (50 mL) and dried with Na₂SO₄. The solvent was removed via rotary evaporation to afford a reddish brown oil. Yield: 112 mg, 99%

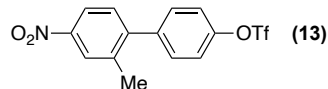
¹H NMR (500 MHz, DMSO) δ 7.54 (d, *J* = 8.5 Hz, 2H), 7.21 (d, *J* = 8.6 Hz, 2H), 6.87 (d, *J* = 8.0 Hz, 1H), 6.51 – 6.38 (m, 2H), 5.10 (s, 2H), 2.12 (s, 3H). ¹³C NMR (126 MHz, DMSO) δ 148.67, 141.64, 135.35, 131.72, 131.32, 130.65, 128.03, 119.50, 116.08, 112.28, 20.85.



12. A 100 mL three-necked round bottom flask fitted with a reflux condenser and equipped with a Teflon coated stir bar under N₂ atmosphere was charged with **10** (100 mg, 0.38 mmol), 4-hydroxyphenylboronic acid (68 mg, 0.5 mmol), K₂CO₃ (262 mg, 1.9 mmol), and Pd(PPh₃)₄ (12 mg, 0.01 mmol). A separate 50 mL round bottom flask equipped with a Teflon stir bar under N₂ atmosphere was charged with dioxane (6 mL), and water (2 mL) and sparged with N₂ for 20 min. The solution was then added to the mixture of solids resulting in a bright yellow cloudy solution. The reaction mixture was refluxed for 18 h. After cooling to room temperature, the solvent was removed via rotary evaporation. The solid residue was dissolved in DCM (50 mL), washed with water (50 mL) and brine (50 mL), dried with Na₂SO₄ and the solvent was removed via rotary evaporation.

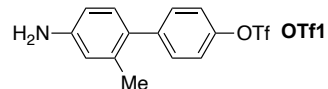
The residue was purified using silica gel flash column chromatography, eluting with EtOAc/hexanes to afford a white solid. Yield: 32 mg, 37%.

¹H NMR (400 MHz, CDCl₃) δ 8.13 (s, 1H), 8.07 (d, *J* = 8.5 Hz, 2H), 7.35 (d, *J* = 8.5 Hz, 1H), 7.20 (dd, *J* = 8.4, 1.5 Hz, 2H), 6.96 – 6.89 (m, 2H), 5.17 (s, 1H), 2.37 (s, 2H).



13. A 50 mL oven dried three-necked round bottom flask fitted with a reflux condenser and equipped with a Teflon coated stir bar under N₂ atmosphere was charged with **12** (31 mg, 0.14 mmol) and anhydrous DCM (2 mL). Anhydrous Et₃N was added (0.03 mL, 0.21 mmol), followed by triflic anhydride (0.30 mL, 0.18 mmol). The solution was allowed to stir for 18 h and was quenched with water, then diluted with DCM (30 mL), washed with water (30 mL) and brine (30 mL), dried with Na₂SO₄ and the solvent was removed via rotary evaporation. The residue was purified using silica gel flash column chromatography, eluting with EtOAc/hexanes to afford a white solid. Yield: 40 mg, 80%.

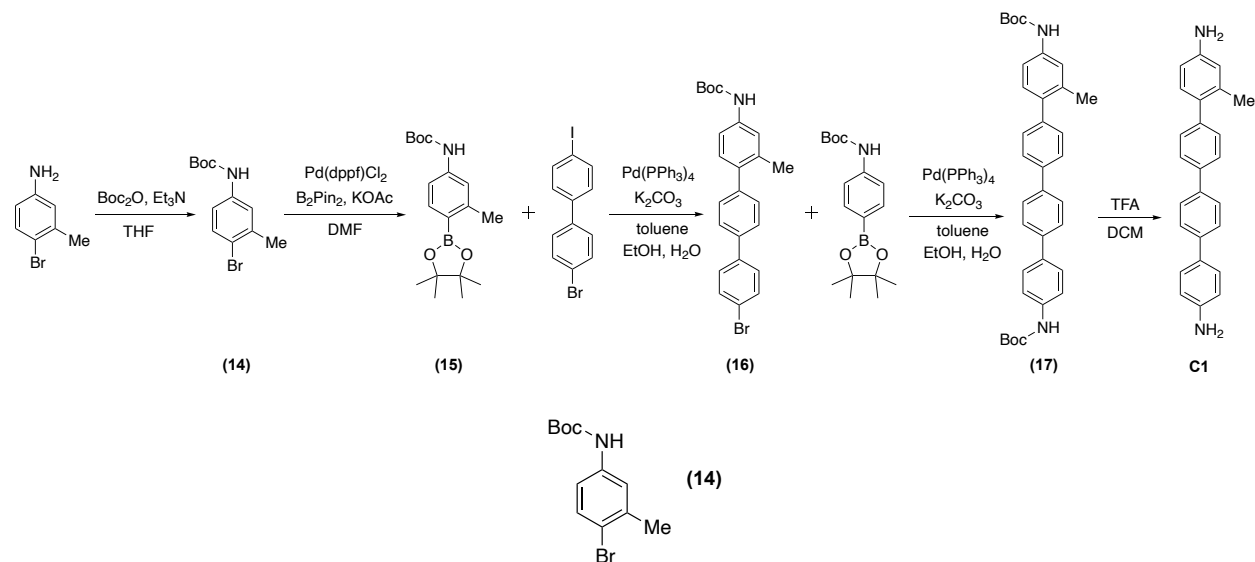
¹H NMR (500 MHz, CDCl₃) δ 7.35 (d, *J* = 8.8 Hz, 2H), 7.27 (d, *J* = 8.9 Hz, 2H), 7.00 (d, *J* = 8.0 Hz, 1H), 6.67 – 6.44 (m, 2H), 3.70 (s, 2H), 2.19 (s, 3H). ¹⁹F NMR (471 MHz, CDCl₃) δ -71.95. ¹³C NMR (126 MHz, CDCl₃) δ 148.11, 146.15, 142.51, 136.31, 131.15, 130.79, 130.42, 120.82, 120.09, 116.85, 112.70, 20.50.



OTf1. An oven-dried 25 mL three-neck round bottom flask fitted with a reflux condenser and equipped with a Teflon coated stir bar under N₂ atmosphere was charged with **20** (30 mg, 0.08 mmol) and ethanol (2.5 mL). The solution was sparged with N₂ for 20 minutes. Fe powder (27 mg,

0.5 mmol) was added. Concentrated aqueous HCl (1 mL) was then added slowly and the solution was refluxed overnight. The mixture was cooled to room temperature and then poured into 10 mL of ice cold water. The solution was basified by careful addition of 1M aqueous NaOH until the pH reached ~6. The aqueous solution was then extracted with DCM (3 x 25 mL), washed with brine (50 mL) and dried with Na₂SO₄. The solvent was removed via rotary evaporation to afford a reddish brown oil. Yield: 25 mg, 91%.

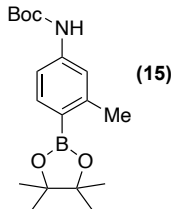
¹H NMR (500 MHz, CDCl₃) δ 7.62 (d, *J* = 8.8 Hz, 2H), 7.48 (d, *J* = 8.5 Hz, 2H), 7.38 – 7.31 (m, 4H), 2.53 (s, 3H). ¹⁹F NMR (471 MHz, CDCl₃) δ -71.87. ¹³C NMR (126 MHz, CDCl₃) δ 148.82, 141.04, 138.91, 135.90, 128.52, 127.48, 126.83, 121.70, 120.06, 15.66.



14. A 50 mL three-neck round bottom flask under N₂ atmosphere was charged with 4-bromo-3-methylaniline (1.93g, 10.4 mmol) and degassed THF (65). Triethylamine (2.5 mL, 18 mmol) was added, followed by di-tertbutyl-dicarbonate (3 mL, 13 mmol) and the reaction mixture was then refluxed for 18 h. The solvent was removed via rotary evaporation, and the residue was purified using silica gel flash column chromatography, eluting with Et₂O/hexanes. The resulting mixture of 292 and excess boc anhydride was then dissolved in DCM (100 mL) and imidazole (2.7 g,

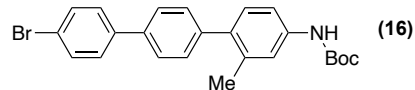
39mmol) was added. The solution was allowed to stir for 2 h then washed with 1% HCl w/w (2 x 100 mL), water (100 mL) and brine (100 mL) and dried with Na₂SO₄. The solvent was removed via rotary evaporation to afford a white solid. Yield: 2.1 g, 71%.

This compound has been reported previously.⁴¹ ¹H NMR (500 MHz, CDCl₃) δ 7.40 (d, *J* = 8.6 Hz, 1H), 7.32 (s, 1H), 7.02 (dd, *J* = 8.6, 2.7 Hz, 1H), 6.39 (s, 1H), 2.36 (s, 3H), 1.51 (s, 9H).



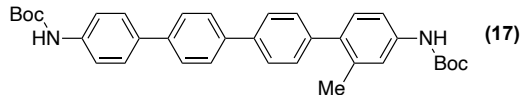
15. An oven-dried 25 mL three-neck round bottom flask fitted with a reflux condenser and equipped with a Teflon coated stir bar under N₂ atmosphere was charged with **14** (342 mg, 1.2 mmol), diboron pinacol ester (360 mg, 1.42 mmol), Pd(dppf)Cl₂ DCM adduct (26 mg, 0.03 mmol), potassium acetate (360 mg, 3.67 mmol) and dry degassed DMF (5 mL). The solution was stirred at 80 degrees for 18 h, allowed to cool to room temperature and partitioned between DCM (50 mL) and water (50 mL). The organic layer was washed with water (5 x 50 mL) and brine (2 x 50 mL) to remove the DMF, then dried with Na₂SO₄. The solvent was removed via rotary evaporation, and the residue was purified using silica gel flash column chromatography eluting with DCM/hexanes to afford a colorless oil that solidifies under vacuum to a fluffy white solid. Yield: 277 mg, 69%.

¹H NMR (500 MHz, CDCl₃) δ 7.68 (d, *J* = 8.1 Hz, 1H), 7.23 – 7.19 (m, 1H), 7.11 (dd, *J* = 8.2, 2.2 Hz, 1H), 6.47 (s, 1H), 2.51 (s, 3H), 1.51 (s, 9H), 1.32 (s, 12H). ¹³C NMR (126 MHz, CDCl₃) δ 152.45, 146.46, 140.60, 137.12, 119.08, 114.34, 83.23, 80.58, 28.34, 24.89, 22.36.



16. A 100 mL three-necked round bottom flask fitted with a reflux condenser and equipped with a Teflon coated stir bar under N₂ atmosphere was charged with 4-bromo-4'-iodobiphenyl (200 mg, .56 mmol), **15** (140 mg, 0.35 mmol), K₂CO₃ (350 mg, 2.5 mmol), and Pd(PPh₃)₄ (12 mg, 0.01 mmol). A separate 25 mL round bottom flask equipped with a Teflon stir bar under N₂ atmosphere was charged with toluene (8 mL), ethanol (2.5 mL) and water (2.5 mL) and sparged with N₂ for 20 min. The solution was then added to the mixture of solids resulting in a bright yellow cloudy solution. The reaction mixture was refluxed for 18 h. After cooling to room temperature, the solvent was removed via rotary evaporation. The solid residue was extracted with DCM (2 x 50 mL), washed with water (50 mL) and brine (50 mL), dried with Na₂SO₄ and the solvent was removed via rotary evaporation. The residue was purified using silica gel flash column chromatography, eluting with DCM/hexanes to afford a white solid. Yield: 146 mg, 95%.

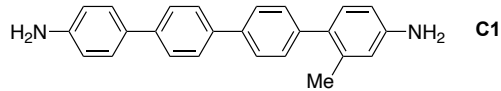
¹H NMR (500 MHz, DMSO) δ 9.33 (s, 1H), 7.72 – 7.66 (m, 2H), 7.65 (d, *J* = 3.8 Hz, 2H), 7.38 (d, *J* = 8.4 Hz, 1H), 7.31 (dd, *J* = 8.3, 2.2 Hz, 1H), 7.11 (d, *J* = 8.3 Hz, 1H), 2.21 (s, 3H), 1.46 (s, 9H). ¹³C NMR (126 MHz, DMSO) δ 153.27, 141.09, 139.46, 139.26, 137.48, 135.44, 134.94, 132.32, 130.23, 129.17, 127.07, 126.83, 121.34, 120.27, 116.42, 79.51, 28.61, 21.03.



17. A 50 mL three-necked round bottom flask fitted with a reflux condenser and equipped with a Teflon coated stir bar under N₂ atmosphere was charged with **16** (75 mg, 0.17 mmol), (4-tert-butoxycarbonylaminophenyl)boronic acid pinacol ester (65 mg, 0.2 mmol), K₂CO₃ (250 mg, 1.78 mmol), and Pd(PPh₃)₄ (6 mg, 0.005 mmol). A separate 25 mL round bottom flask equipped with

a Teflon stir bar under N₂ atmosphere was charged with toluene (8 mL), ethanol (2 mL) and water (2 mL) and sparged with N₂ for 20 min. The solution was then added to the mixture of solids resulting in a bright yellow cloudy solution. The reaction mixture was refluxed for 48 h. After cooling to room temperature, the solvent was removed via rotary evaporation. The solid residue was extracted with DCM (2 x 50 mL), washed with water (50 mL) and brine (50 mL), dried with Na₂SO₄ and the solvent was removed via rotary evaporation. The residue was purified using silica gel flash column chromatography, eluting with EtOAc/hexanes to afford a pale orange solid. Yield: 40 mg, 43%.

¹H NMR (500 MHz, CDCl₃) δ 7.76 – 7.65 (m, 6H), 7.62 (d, *J* = 8.6 Hz, 2H), 7.48 (d, *J* = 8.3 Hz, 2H), 7.41 (d, *J* = 8.3 Hz, 2H), 7.37 (s, 1H), 7.24 (s, 2H), 6.57 (s, 1H), 6.51 (s, 1H), 2.35 (s, 3H), 1.57 (s, 9H), 1.57 (s, 9H). ¹³C NMR (126 MHz, CDCl₃) δ 152.86, 152.79, 139.50, 139.40, 140.56, 138.96, 137.76, 137.43, 136.43, 136.29, 135.39, 130.40, 129.78, 127.51, 127.39, 127.11, 126.63, 120.4, 118.86, 116.14, 29.71, 28.37, 20.76.



C1. A 6 dram vial equipped with a Teflon coated stir bar was charged with **17** (15 mg, 0.03 mmol) and dissolved in DCM (2 mL). TFA was added (0.25 mL) and the solution was allowed to stir for 4 h then diluted with DCM (5 mL), washed with 2M NaOH (2 x 10 mL) and brine (10 mL) and dried with Na₂SO₄. The solvent was removed via rotary evaporation to afford a beige solid. Yield: 9 mg, 99%.

¹H NMR (400 MHz, DMSO) δ 7.80 – 7.61 (m, 6H), 7.43 (d, *J* = 7.9 Hz, 2H), 7.35 (d, *J* = 7.6 Hz, 2H), 6.94 (d, *J* = 7.9 Hz, 1H), 6.67 (d, *J* = 7.9 Hz, 2H), 6.49 (d, *J* = 13.1 Hz, 2H), 5.23 (s, 2H), 5.05 (s, 2H), 2.19 (s, 3H). ¹³C NMR (126 MHz, DMSO) δ 148.98, 148.40, 141.33, 140.00, 137.63,

137.51, 135.43, 131.79, 130.74, 130.12, 128.98, 127.51, 127.22, 126.37, 126.21, 116.14, 114.72,
High-Res MS (ESI+): calculated *m/z* for [M+H]⁺ 351.1685 found, 351.1880.

3.9 STM-BJ Method

Conductance measurements were made using a custom-built scanning tunneling microscope that has been described in detail before.²³ Conductance measurements were performed in dilute solutions (100 μM) of the molecules in either 1,2,4-trichlorobenzene (TCB), or propylene carbonate (PC) with 0.1 M tetrabutylammonium hexafluorophosphate (TBAPF₆) or tetrabutylammonium perchlorate (TBAP) as a supporting electrolyte.⁴² The insulated tips used with PC were created by driving a mechanically cut gold tip through Apiezon wax.⁴² One-dimensional (1D) conductance histograms are constructed using logarithmic bins (100/decade), and two-dimensional (2D) histograms use logarithmic bins along the conductance axis (100/decade) and linear bins (1000/nm) along the displacement axis. The junction length is determined by displacement profiling of the molecular conductance feature in the two-dimensional histograms.

3.10 SEM and EDX

Secondary electron images (SEI) were collected using a Zeiss Sigma VP scanning electron microscope (SEM) at an accelerating voltage of 5 kV. Energy dispersive X-ray spectra (EDX) were collected using an accelerating voltage of 12 kV and a Bruker XFlash 6|30 detector. Elemental compositions were approximated by integrating peaks in the EDX spectra using the

Bruker ESPRIT2 software. Reported compositions are the averages and standard deviations calculated for elemental compositions determined for 3-10 sites on the same sample region

3.11 Additional Data

The conductance data for iodides **I2** and **I3** is shown in both 1D and 2D histogram format. The dimer formed *in situ* is a good match for the *ex situ* synthesized dimer in both cases. For the amine analytes, when the concentration is sufficiently high, molecules will bind in parallel in the junction. This leads to the lower-G peak that is visible in both the **I2** and higher concentration **D2** traces (Figure 3.8b). Therefore, we show two concentrations of **D2** to demonstrate that both peaks in the **I2** histograms arise only from **D2**. For pyridine analytes, two peaks are often observed due to the different binding modes of pyridine, as can be seen in Figure 3.8i. Additionally, the conductance of **D3** is concentration dependent, hence the slightly different peak conductance values in Figure 3.8g.

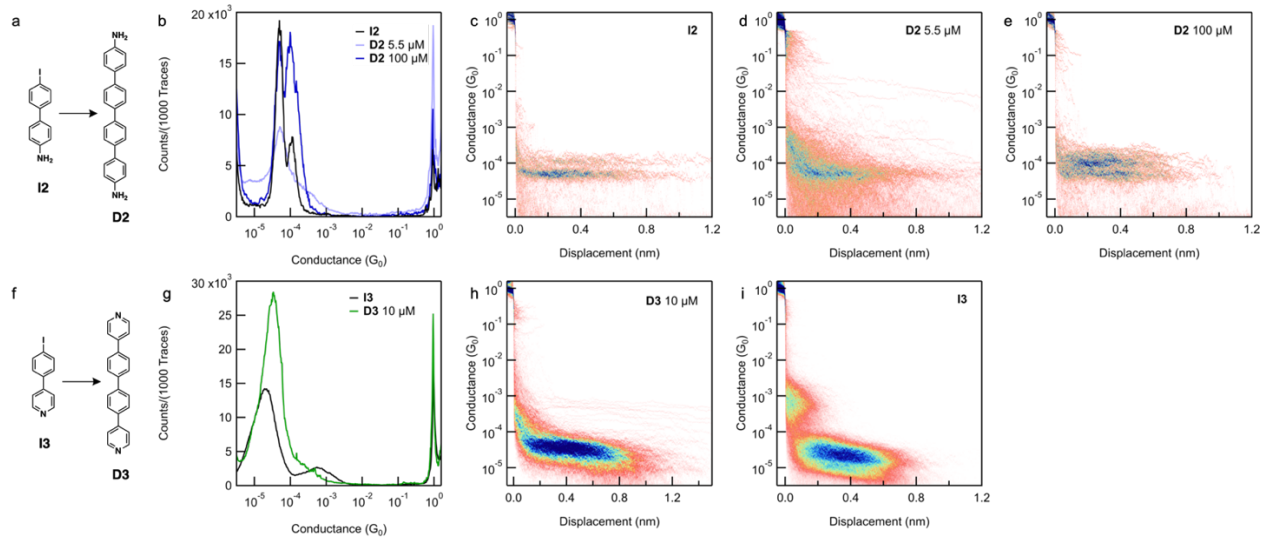


Figure 3.8 Conductance data for other aryl iodides studied. (a) Scheme of the reaction of **I2** to form **D2**. (b) 1D histogram overlay of a measurement of **I2** (black), in which dimer is visible, and ex situ synthesized **D2** (blue). Two concentrations of **D2** are shown to illustrate the peaks that arise from different concentrations. (c-e) 2D histograms corresponding to the traces in the 1D histogram in panel (b). (f) Scheme of the reaction of **I3** to form **D3**. (g) 1D histogram overlay of a measurement of **I3** (black), in which dimer is visible, and ex situ synthesized **D3** (green). (h-i) 2D histograms corresponding to the traces in the 1D histogram in panel (g).

We successfully dimerized iodide **I4**, which is a precursor more akin to what might be used in graphene nanoribbon synthesis. However, **D4** proved difficult to see via STM-BJ, likely due to

the high degree of twisting induced by the two adjacent anthracenes. We rely on MS and UV-vis data in this case to demonstrate the formation of homocoupled product.

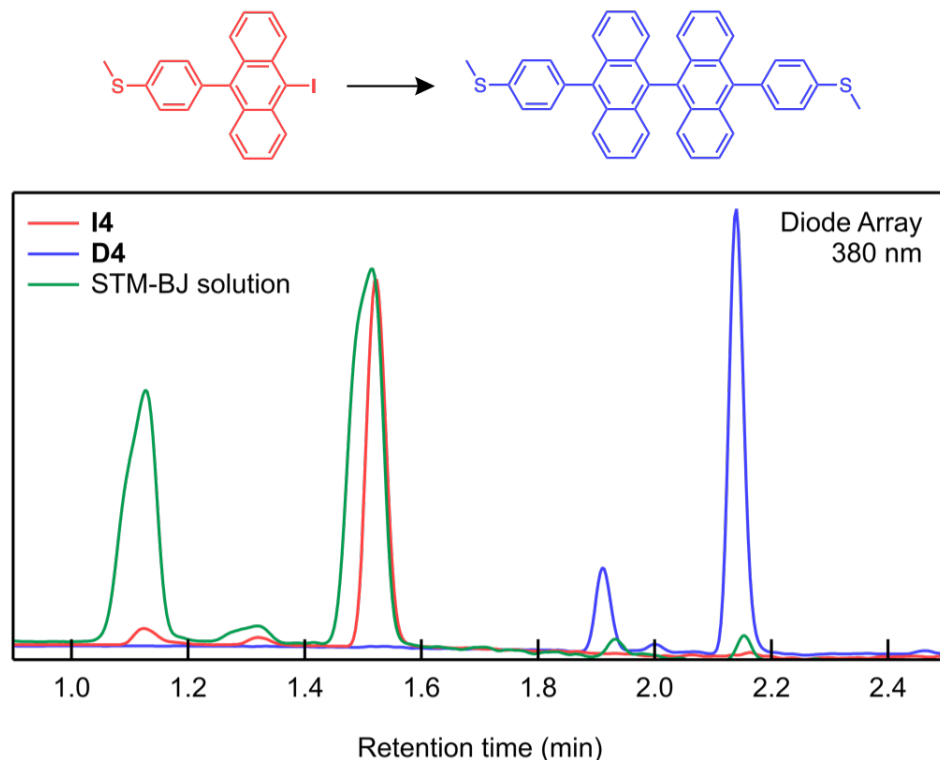


Figure 3.9 UV-vis data from the mass spectrometer confirming the *in situ* reaction of I4 to D4. The signature peaks of I4 and D4 are present in both standard and reaction spectra.

For the rest of the iodide series, we were able to confirm reaction via MS as well. Results for **I1**, **I2**, and **I3** are below.

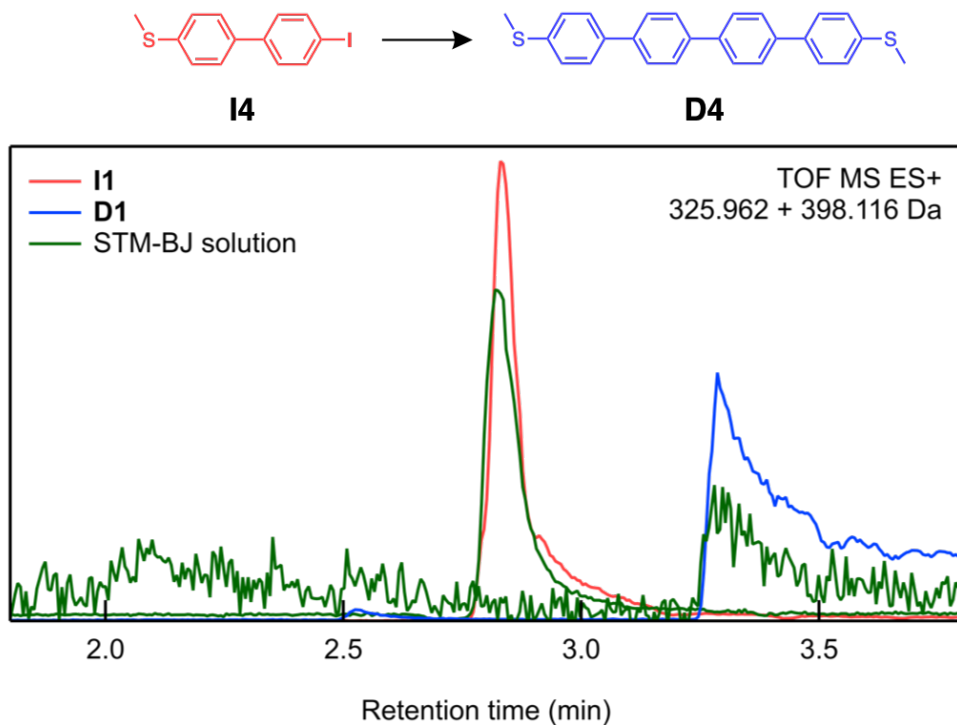


Figure 3.10 Mass spectra for the I1 standard (red), the D1 standard (blue), and the STM-BJ reaction (green). Both I1 and D1 are present in the STM-BJ reaction sample, demonstrating a successful *in situ* reaction. Note: D1 has low solubility and is difficult to detect, therefore to visualize it in the STM-BJ solution, the trace must be magnified significantly.

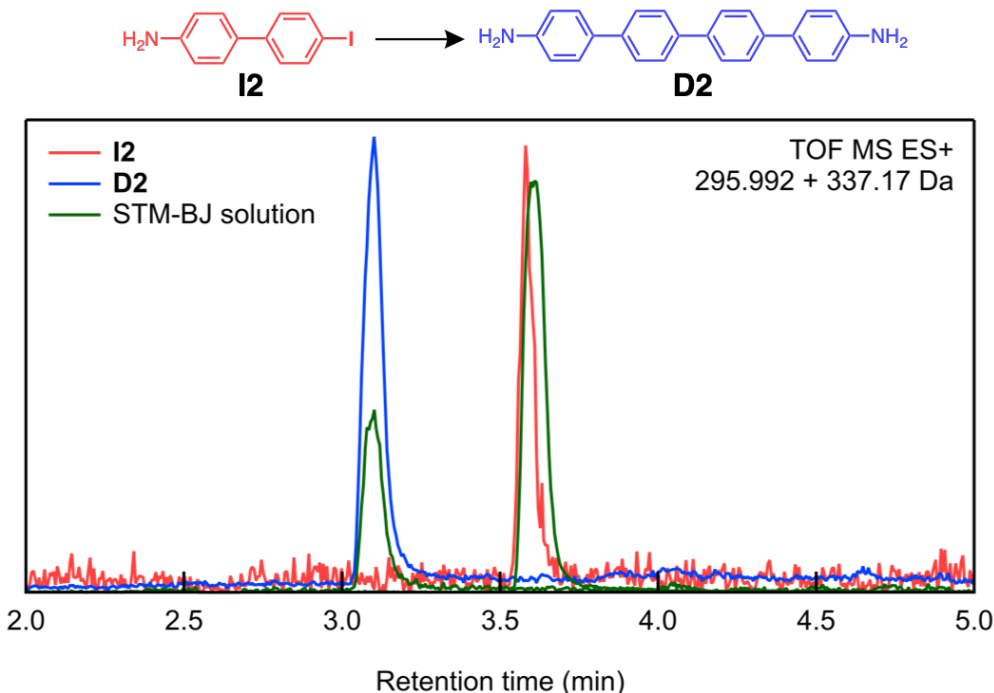


Figure 3.11 Mass spectra for the I2 standard (red), the D2 standard (blue), and the STM-BJ reaction sample (green). Both I2 and D2 are clearly present in the STM-BJ reaction sample, demonstrating a successful *in situ* reaction.

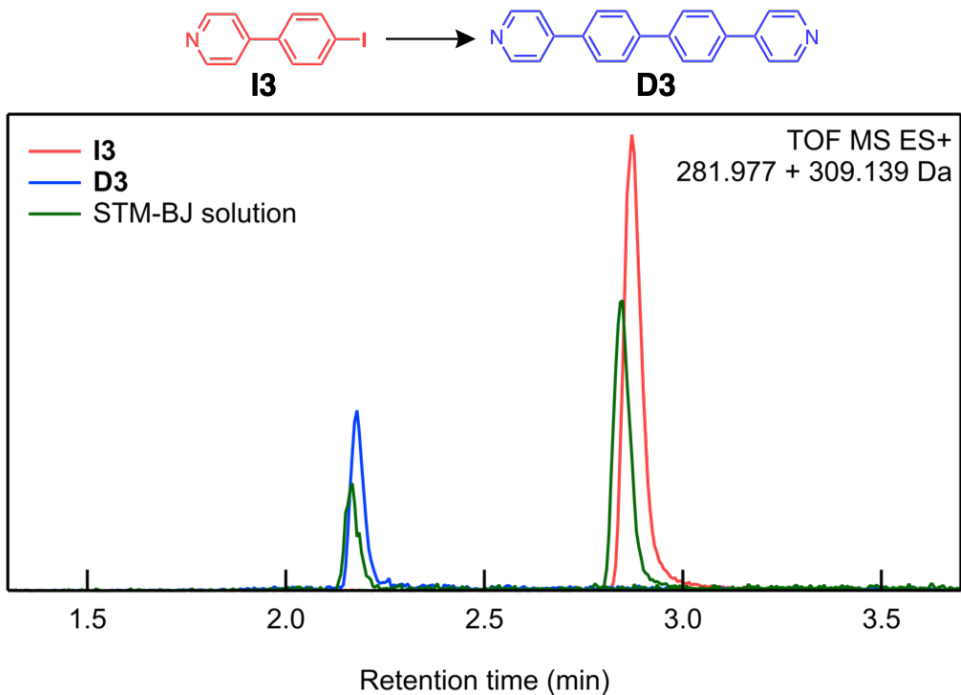


Figure 3.12 Mass spectra for the I3 standard (red), the D3 standard (blue), and the STM-BJ reaction sample (green). Both I3 and D3 are clearly present in the STM-BJ reaction sample, demonstrating a successful *in situ* reaction.

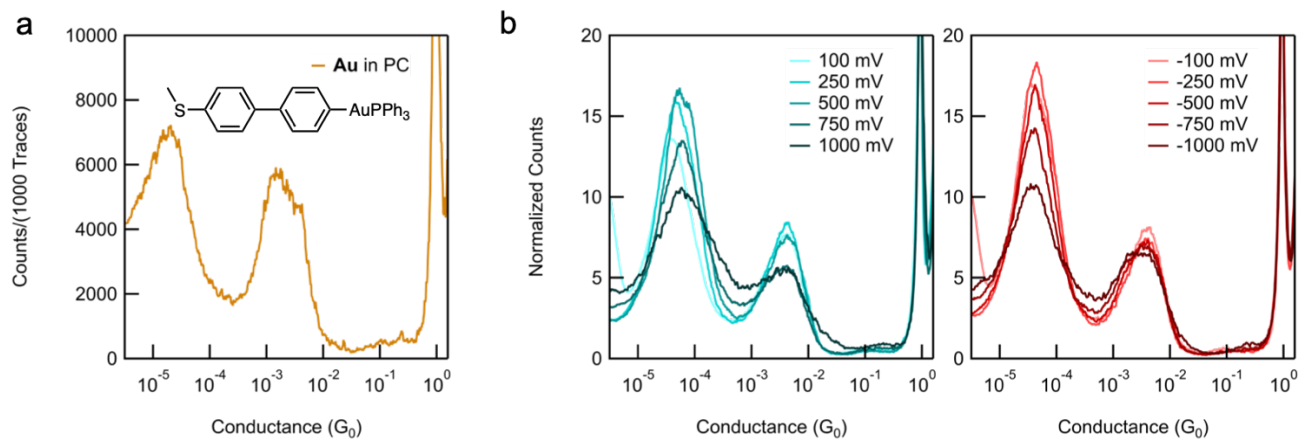


Figure 3.13 (a) Au measured in PC. Both monomer and dimer peaks are visible. (b) Au measured at all biases in TCB, with peak conductance values remaining constant.

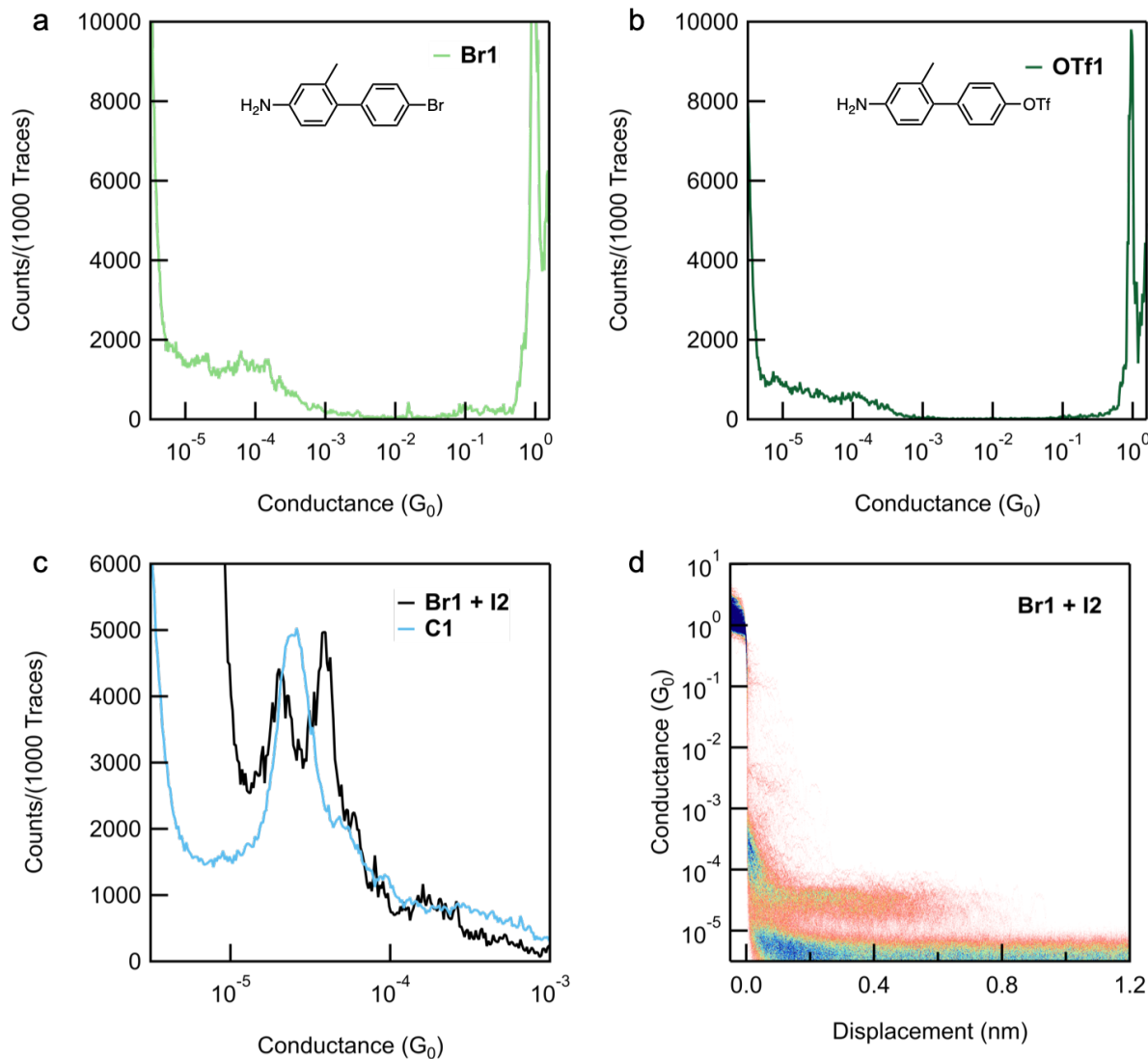


Figure 3.14 (a) **Br1** and (b) **OTf1** measured alone, to ensure they do not homocouple. No peaks are visible. (c) A set of 100 traces (black) that clearly shows two distinct peaks present in the cross-coupling experiment. **C1** is shown again (blue) to demonstrate its correlation with the emergent low-G peak. (d) The 2D histogram of **Br1 + I2**, visualizing the lower G peak arising from cross-coupling. As expected, the plateau length is the same as that of the homocoupling product.

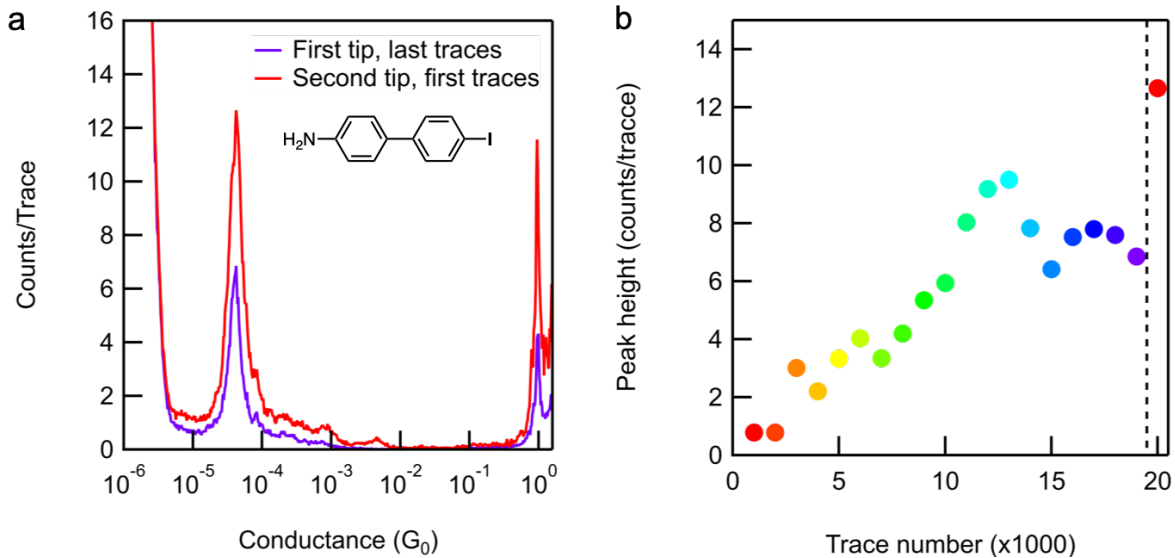


Figure 3.15 (a) The last set of traces (purple) after measuring I2 for 18,000 traces is compared to the first set of traces (red) after replacing the tip. There is a clear increase in counts, indicating the new, cleaner tip is able to pick up more dimer. (b) A plot of peak height versus trace number, to visualize the rise and fall of the counts in the first dataset, and the subsequent rise in counts immediately following replacing the tip.

As mentioned in Section 3.6, there is a possibility that TCB, as an aromatic solvent, is stacking along with the biphenyl analytes. This stacking could prevent surface migration of the dehalogenated species. This could explain the lack of reactivity in TCB, even though oxidative addition is observed. The same phenomenon would not be expected in PC, which is not aromatic.

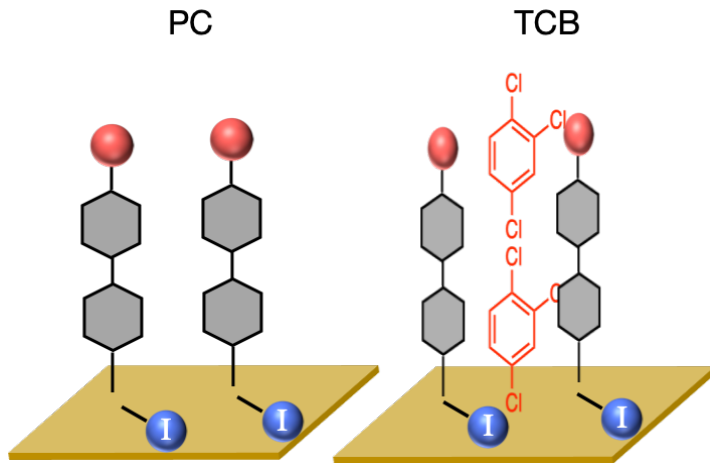


Figure 3.16 The left panel depicts the dehalogenated aryl groups without anything blocking them from migrating along the surface. On the right is a representation of how TCB (red) might be interacting with the biphenyl analytes (gray).

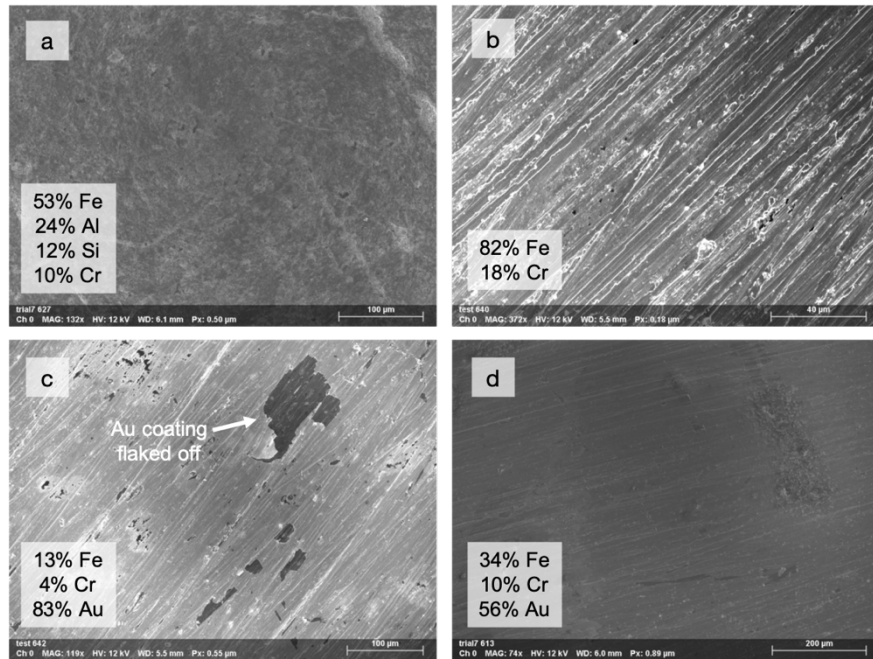


Figure 3.17 SEM images of the substrate with EDX-derived elemental compositions: (a) as purchased, (b) polished, (c) Au coated, and (d) after an experiment on the STM-BJ. As can be seen in (b), polishing the substrates makes them quite rough, which we believe to be essential to the *in situ* Ullmann coupling reactivity.

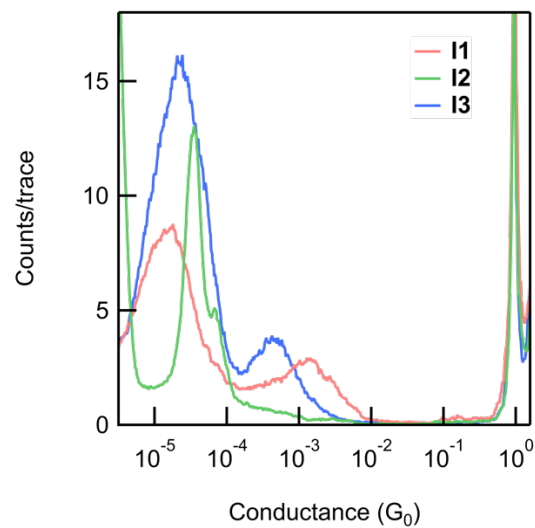


Figure 3.18 I1 (red), I2 (green), and I3 (blue) all measured in PC without supporting electrolyte. Dimer still readily forms in all cases. The role of the electrolyte is still incompletely understood.

3.12 NMR Spectra

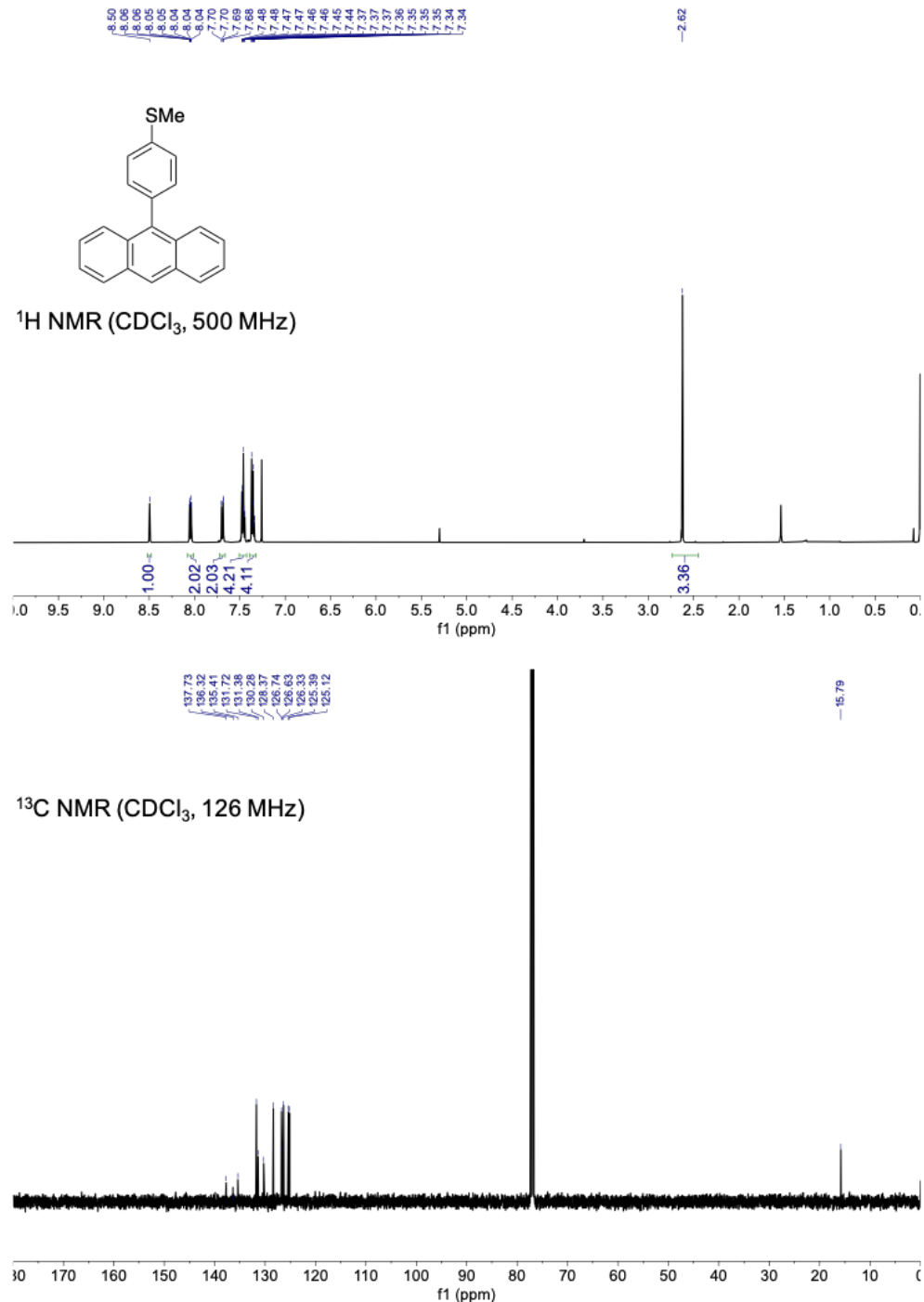


Figure 3.19 NMR spectra of compound 5.

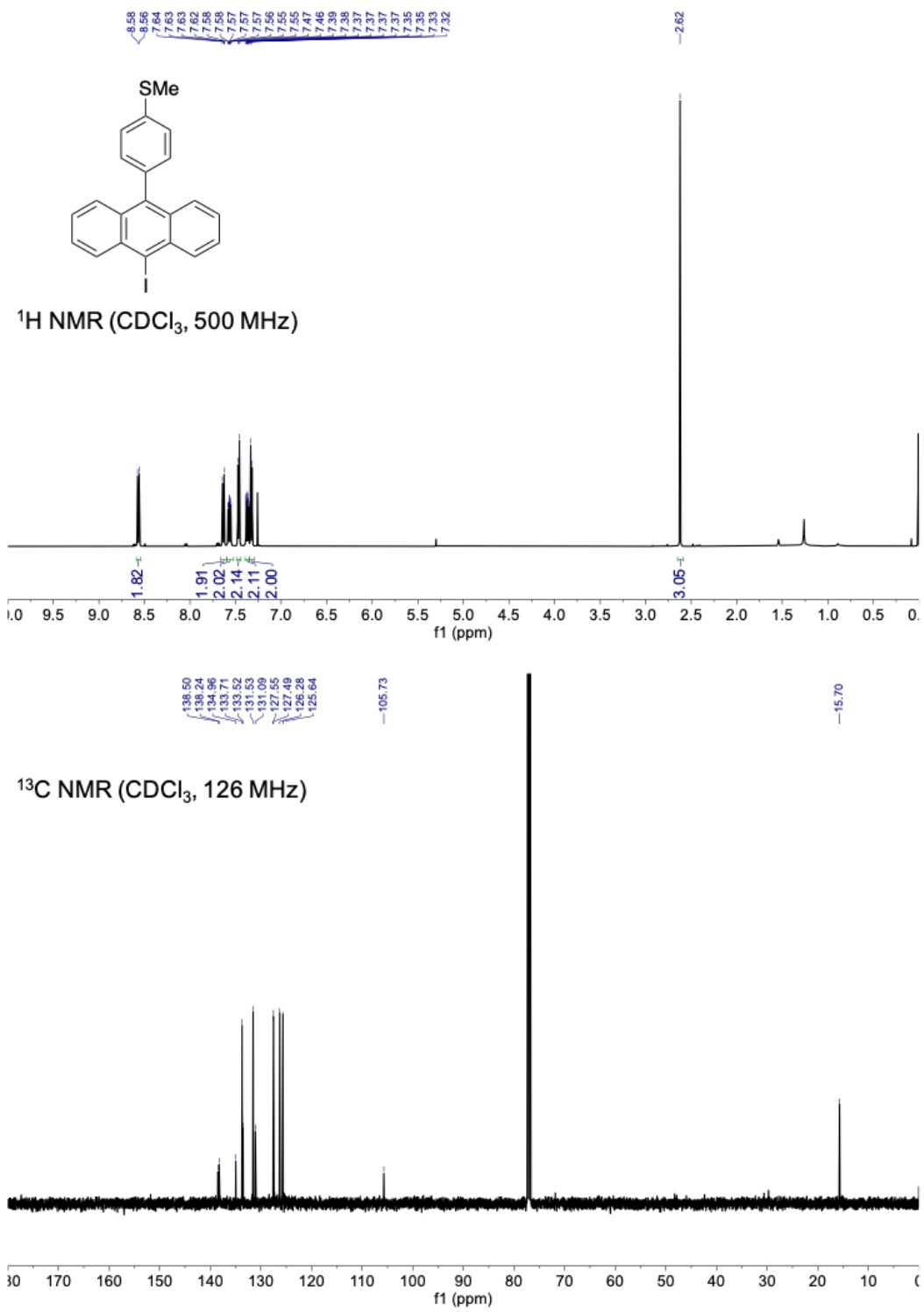


Figure 3.20 NMR spectra of compound I4.

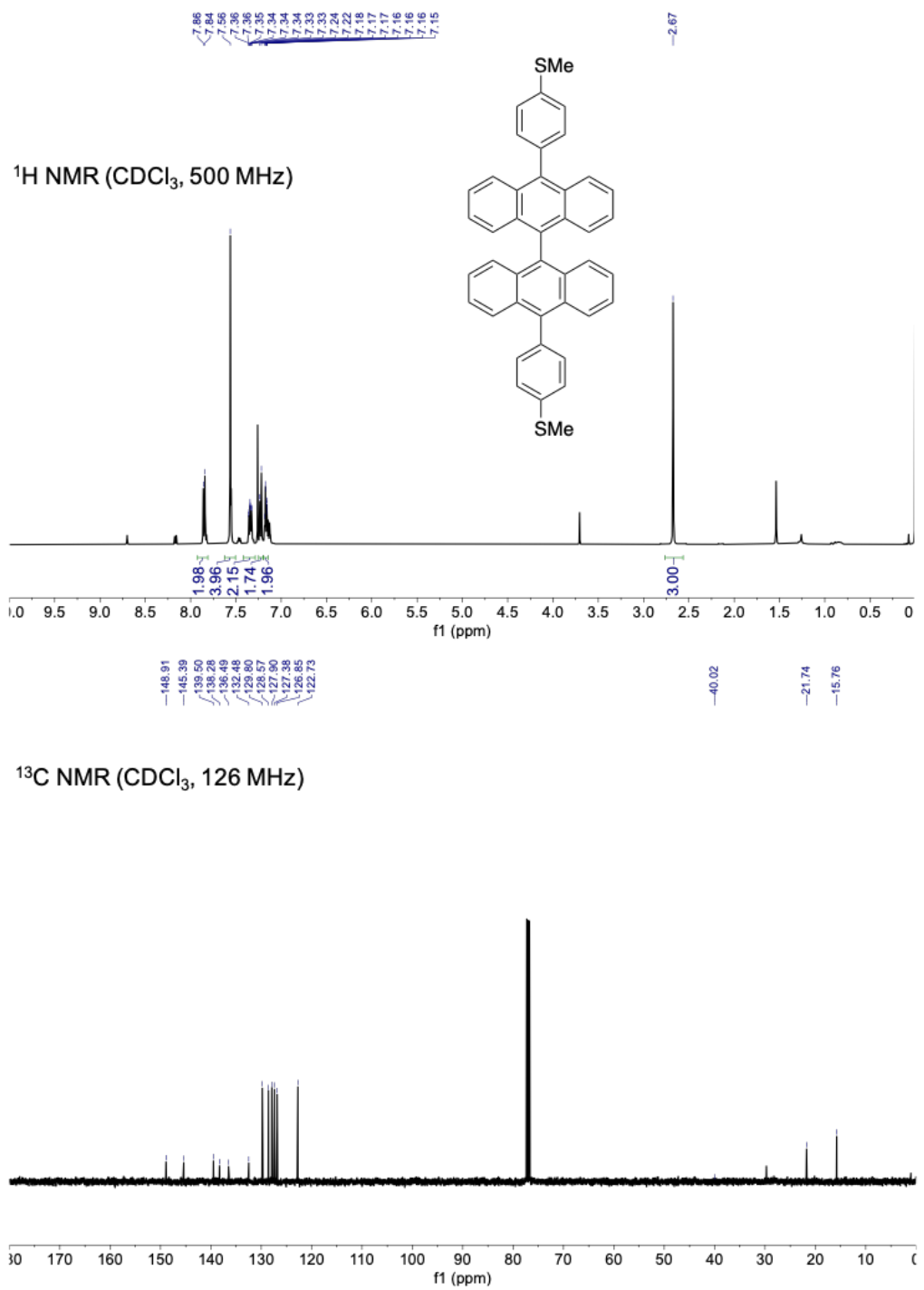


Figure 3.21 NMR Spectra of compound **D4**.

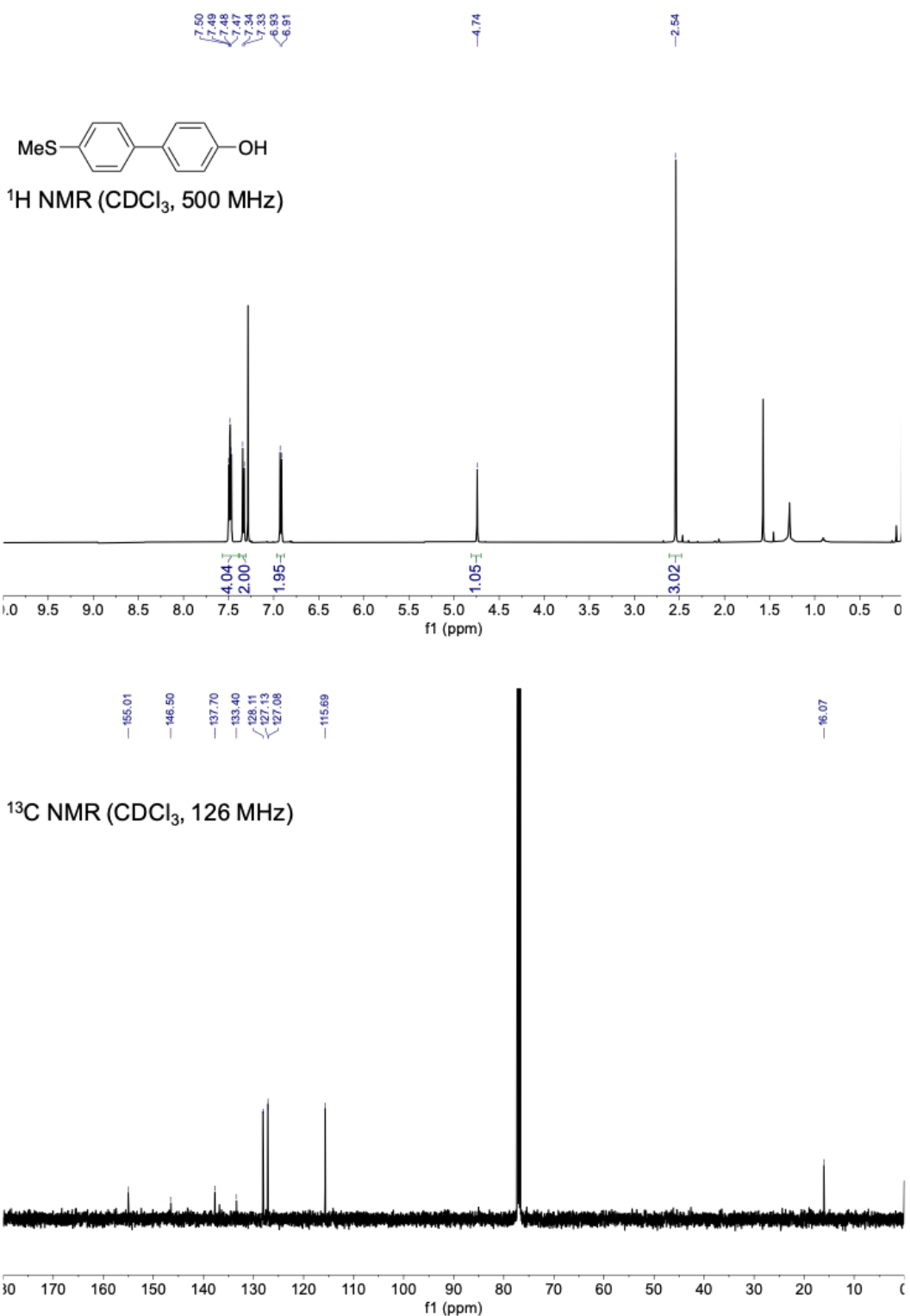


Figure 3.22 NMR spectra of compound 7.

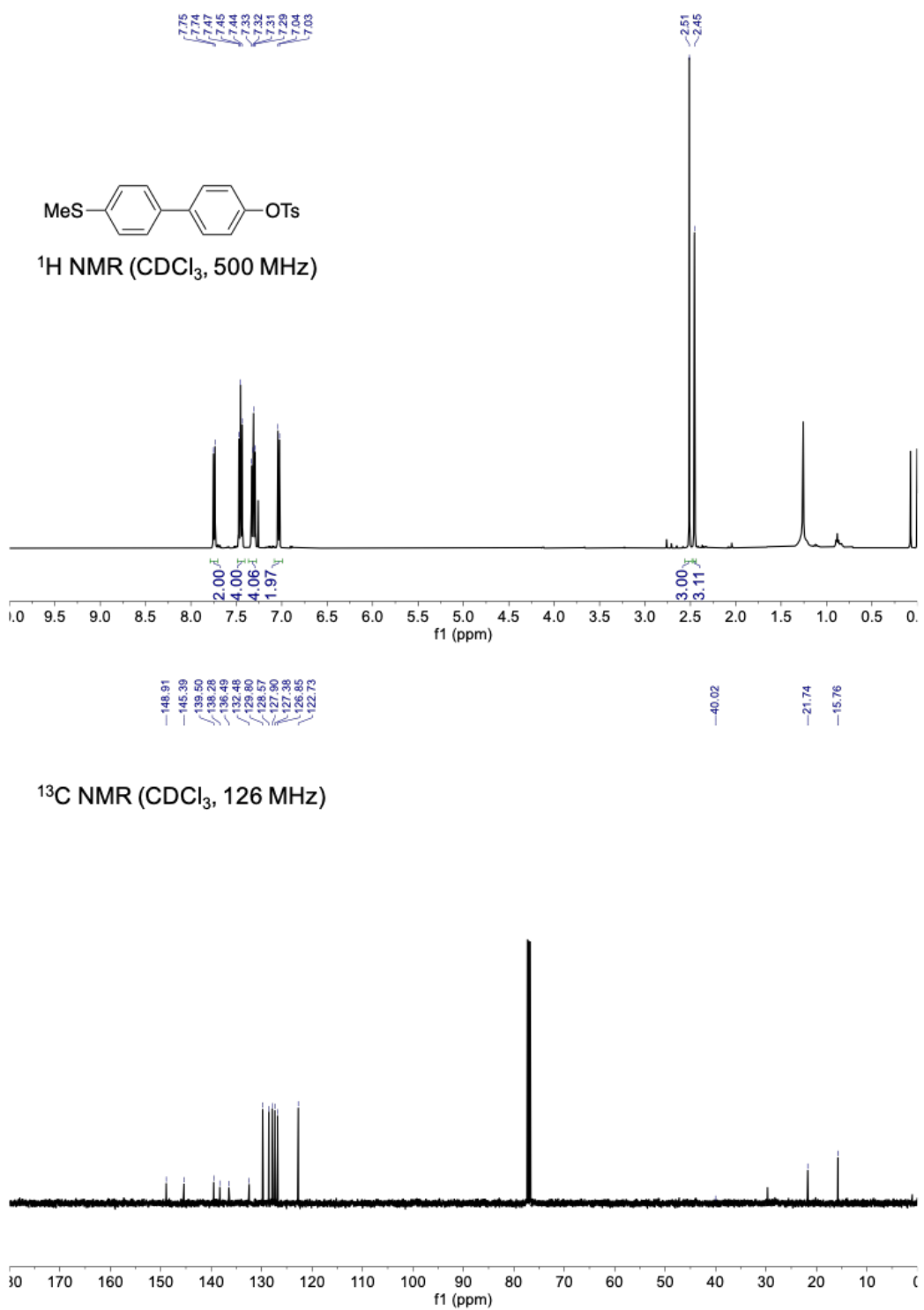


Figure 3.23 NMR spectra of compound 8.

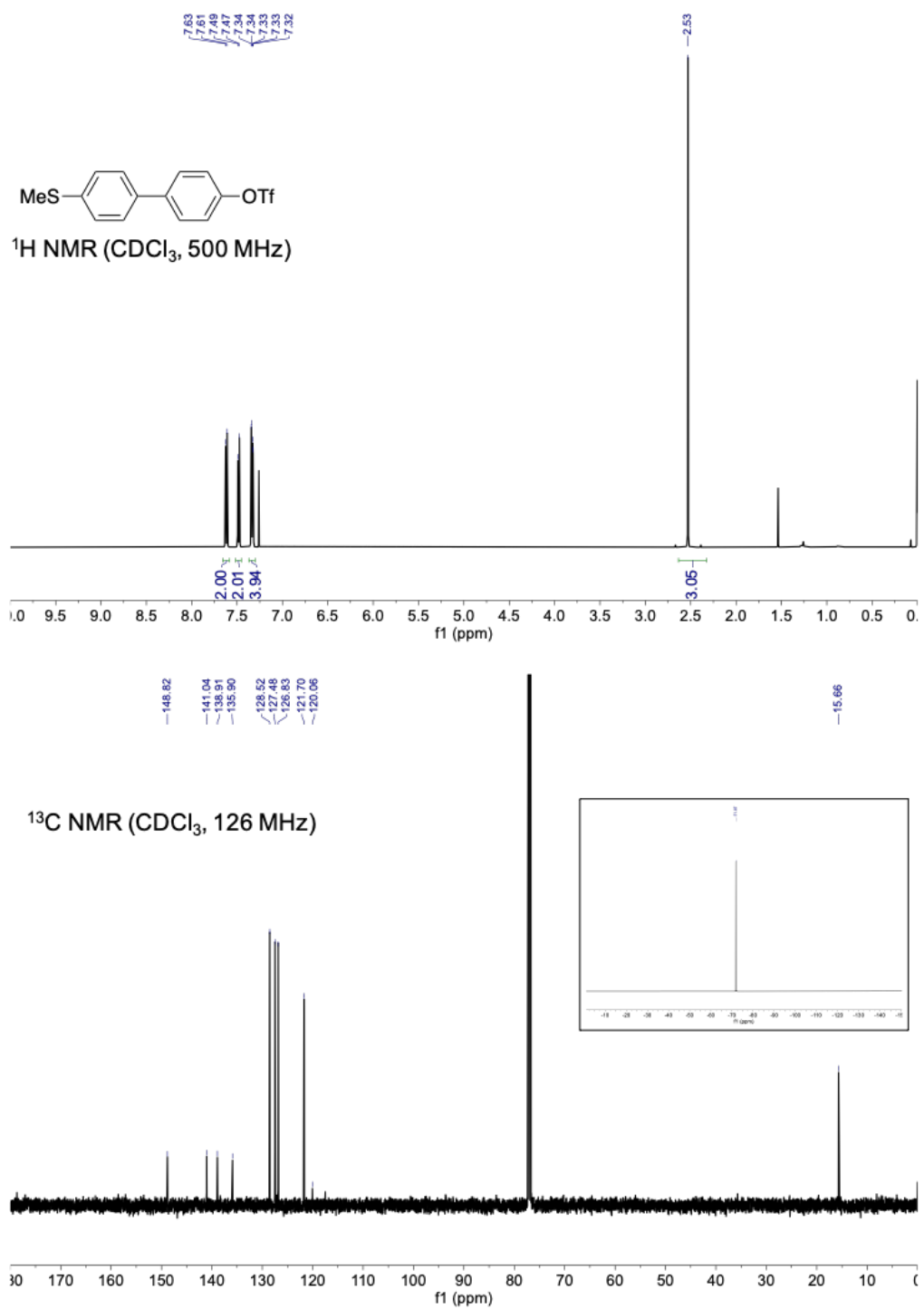


Figure 3.24 NMR spectra of compound 9.

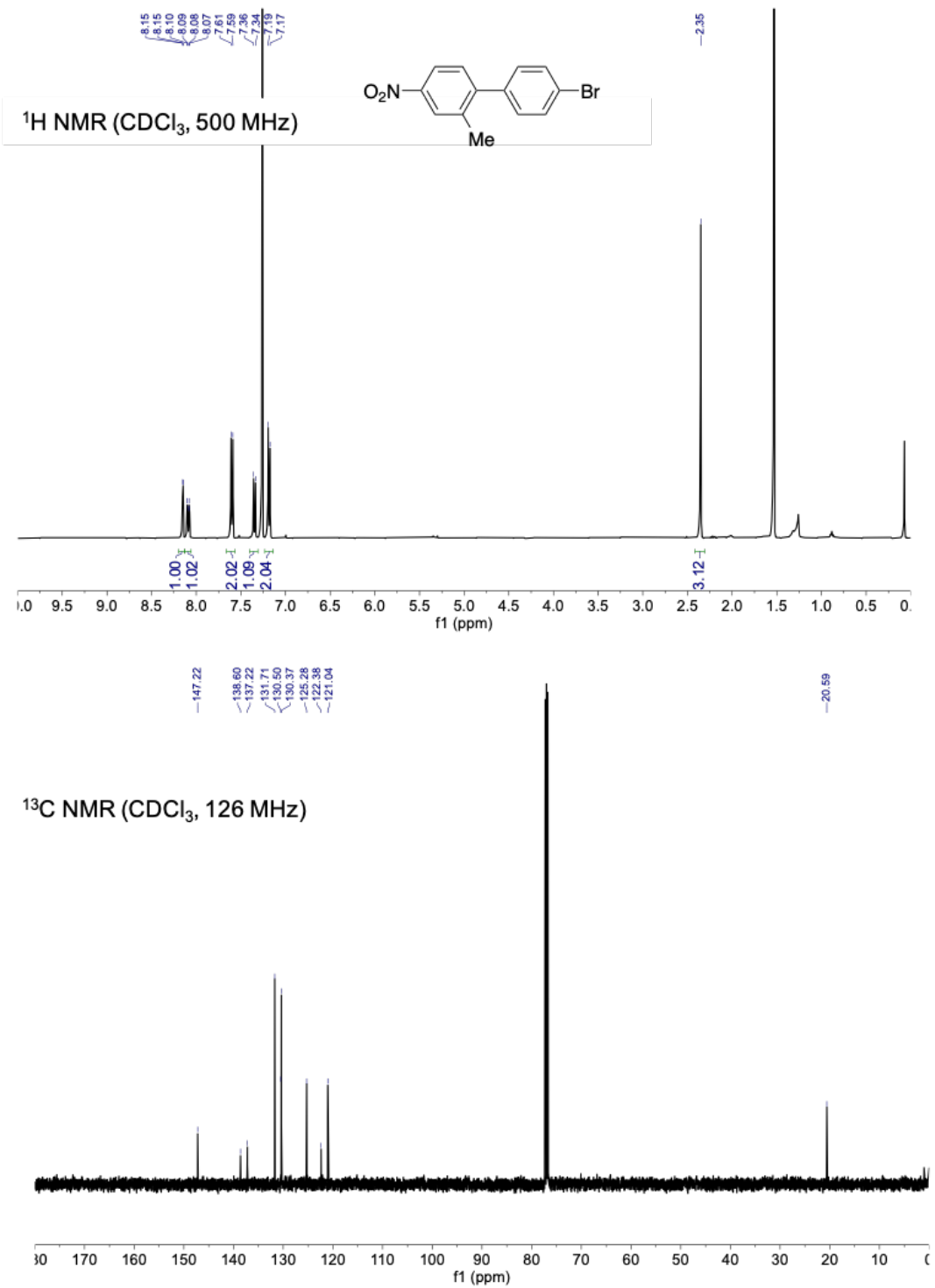


Figure 3.25 NMR spectra of compound **11**.

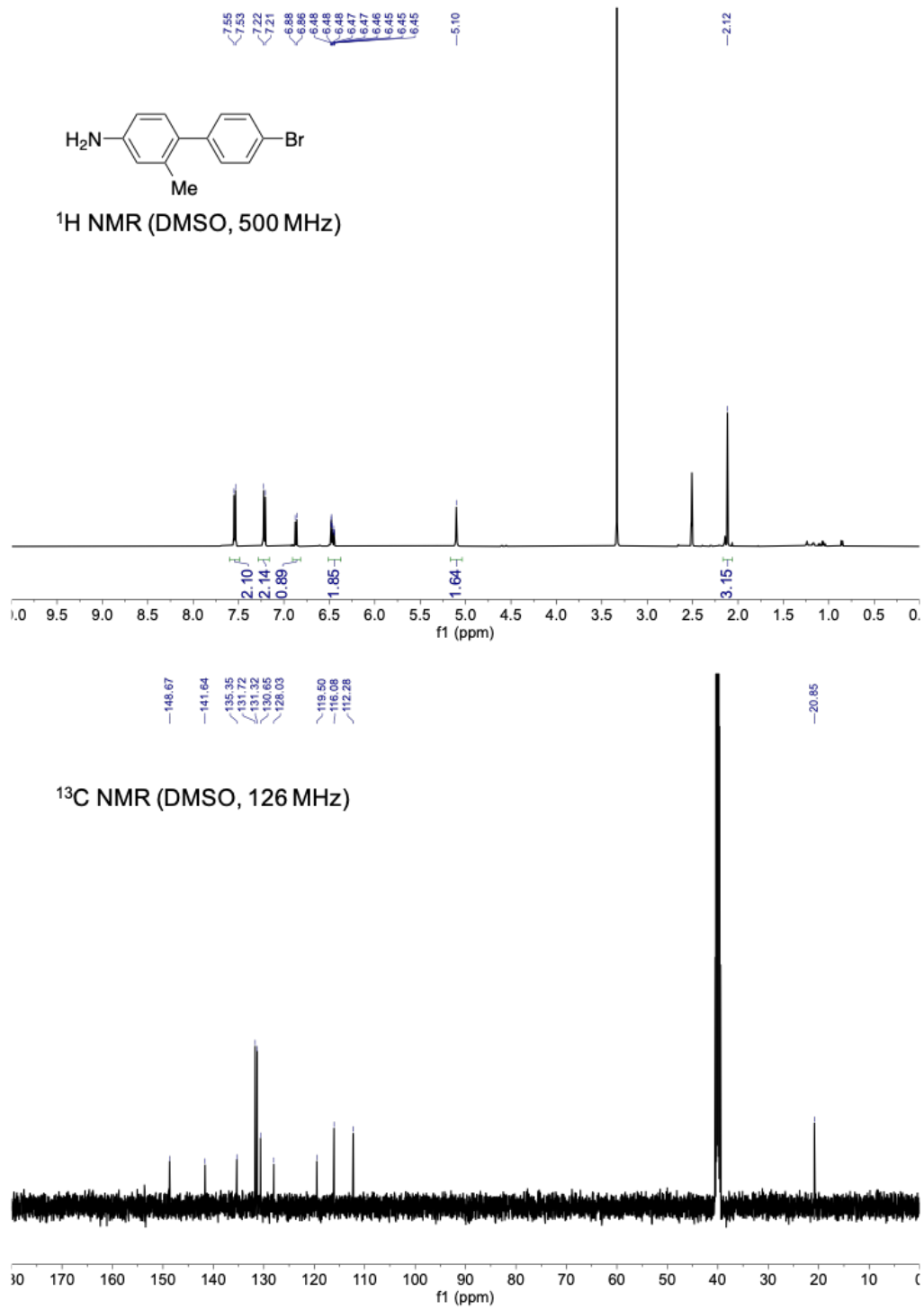


Figure 3.26 NMR spectra of compound **Br1**.

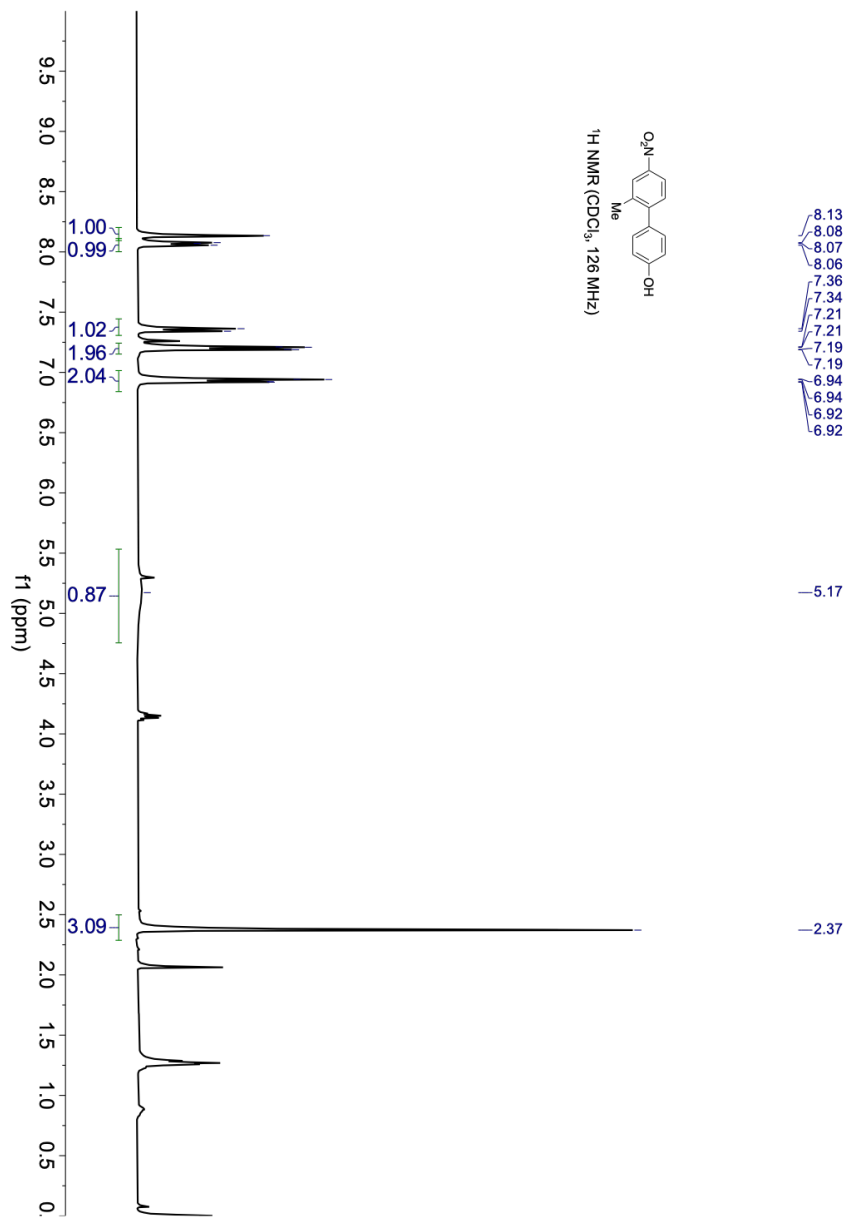


Figure 3.27 NMR spectrum of compound 12.

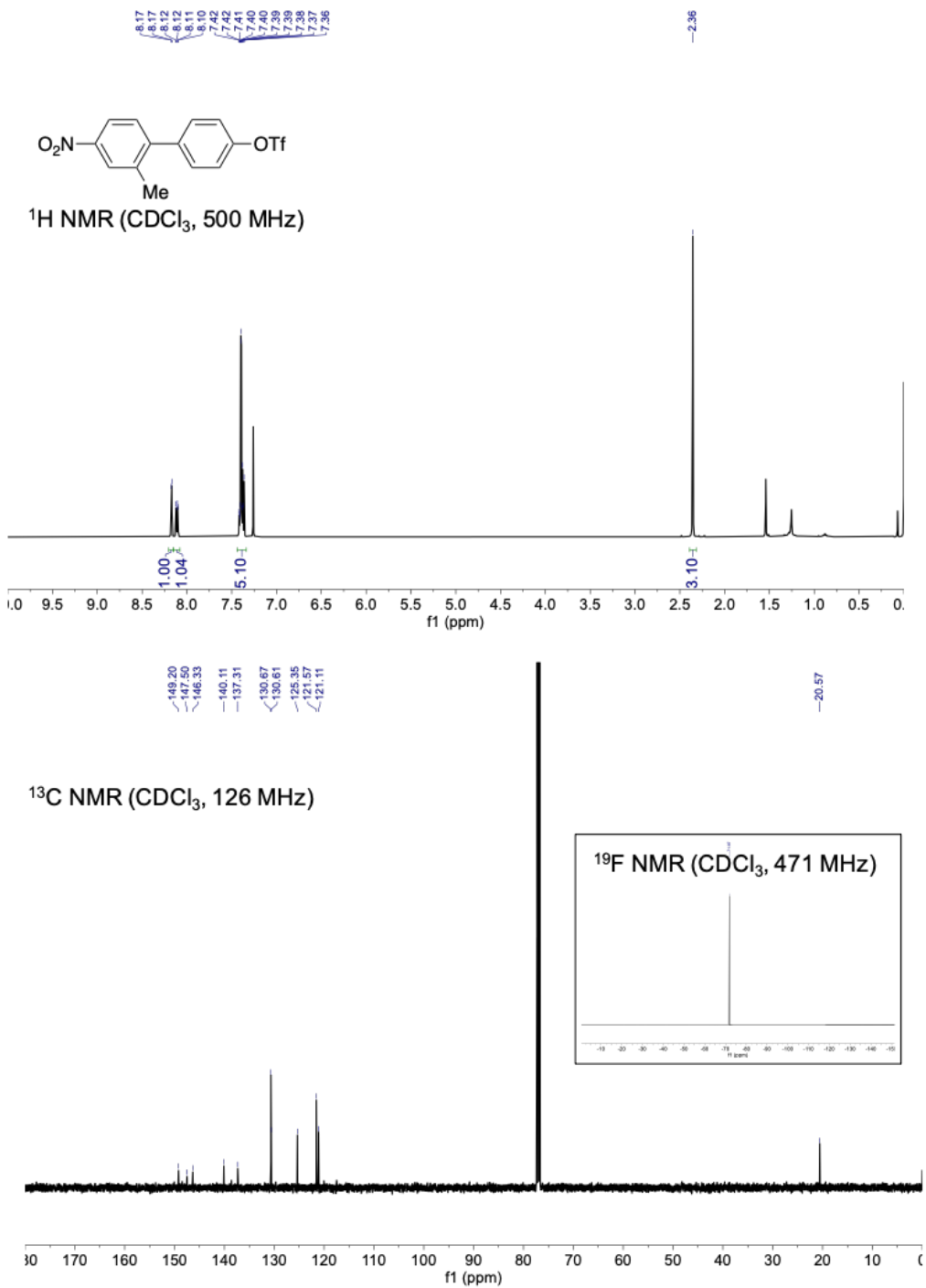


Figure 3.28 NMR spectra of compound **13**.

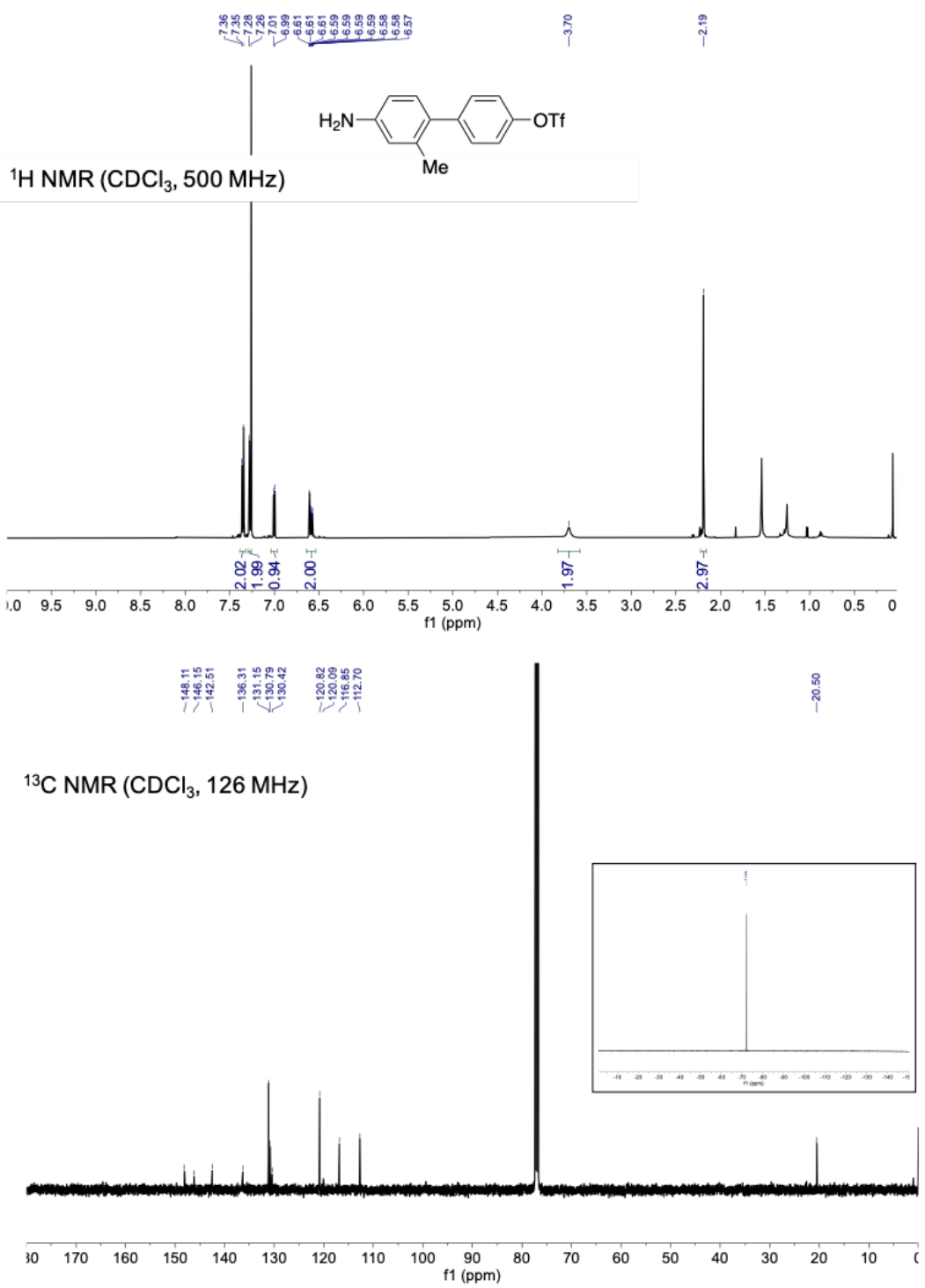


Figure 3.29 NMR spectra of compound **OTf1**.

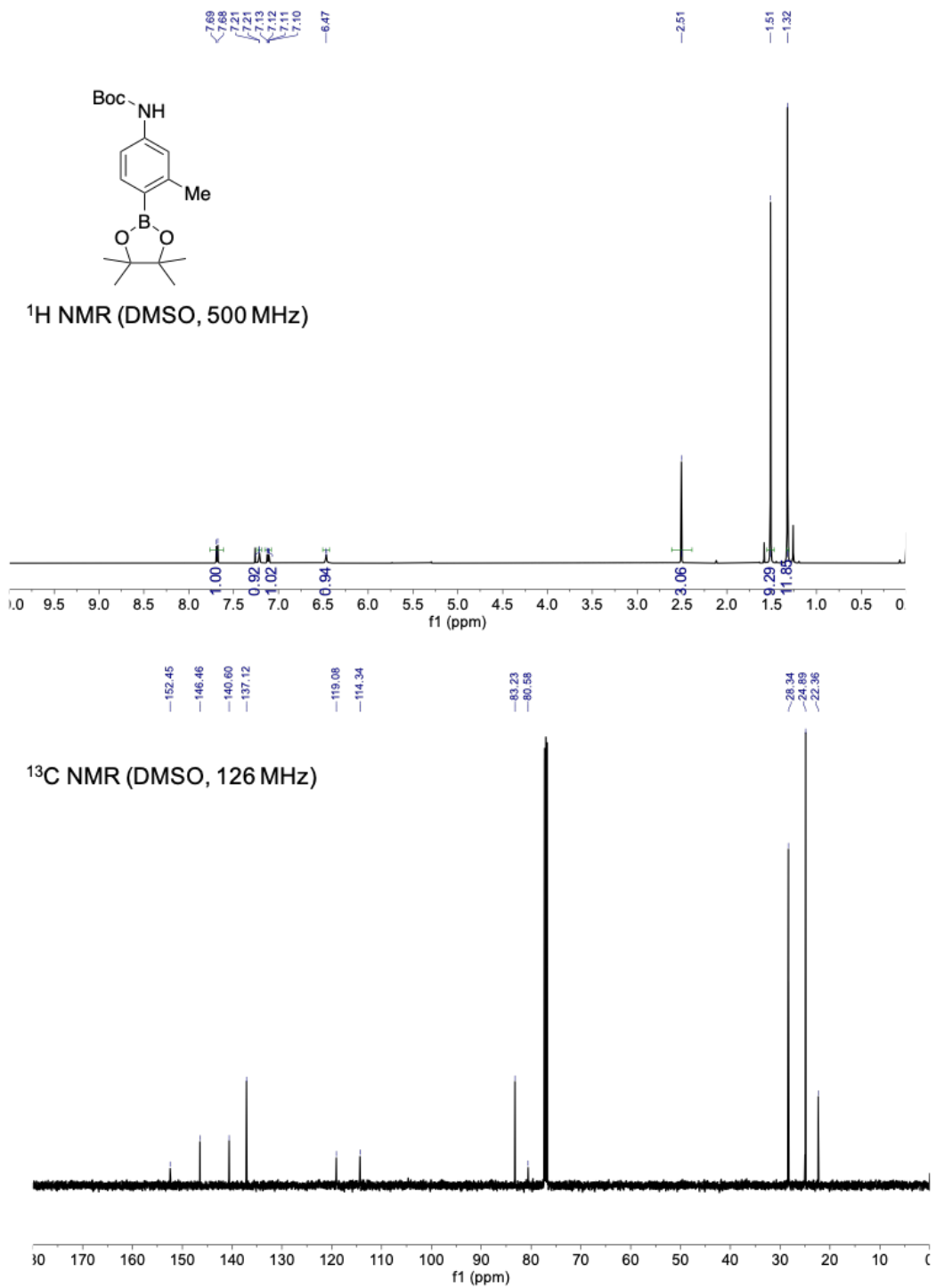


Figure 3.30 NMR spectra of compound **15**.

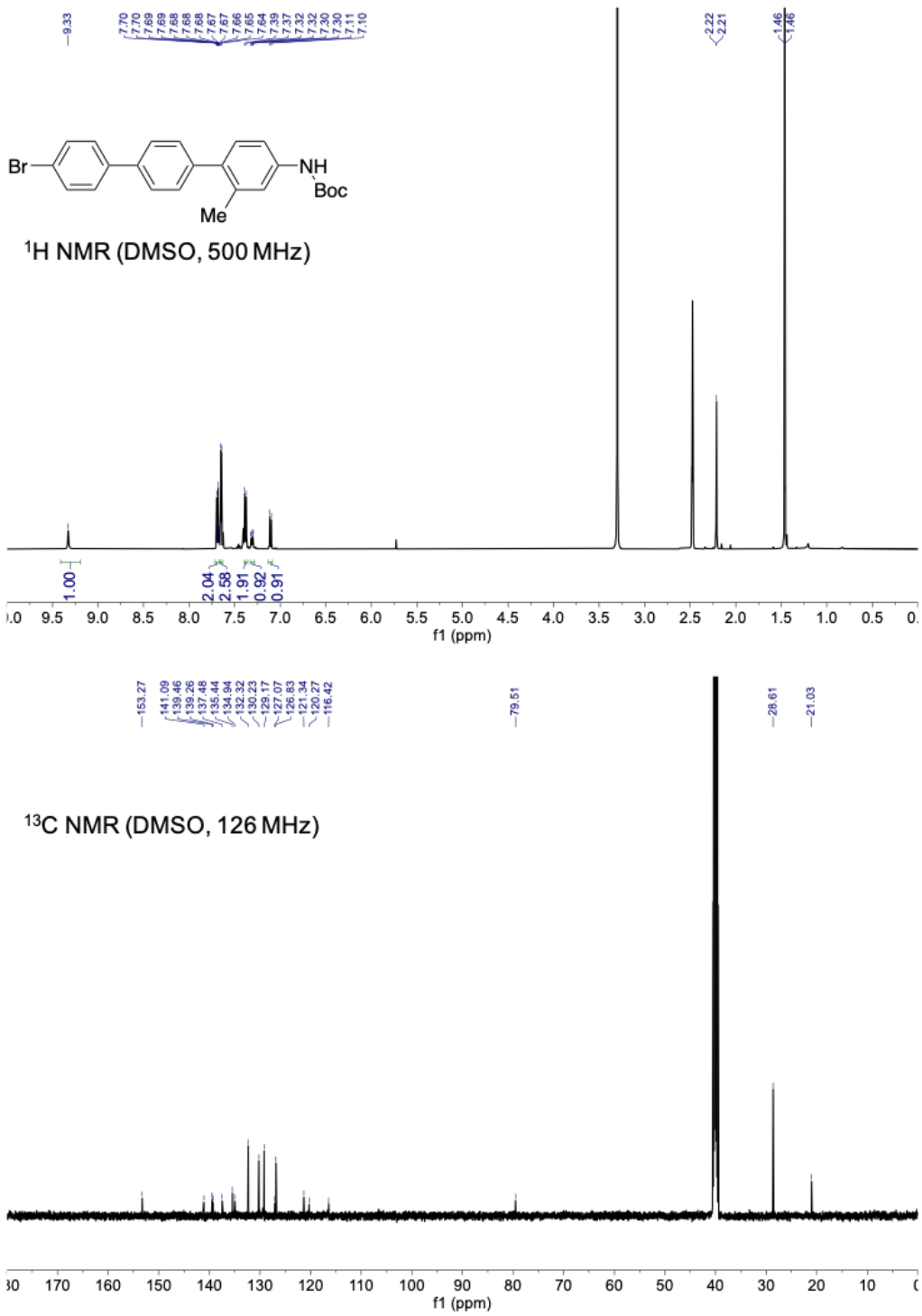


Figure 3.31 NMR spectra of compound **16**.

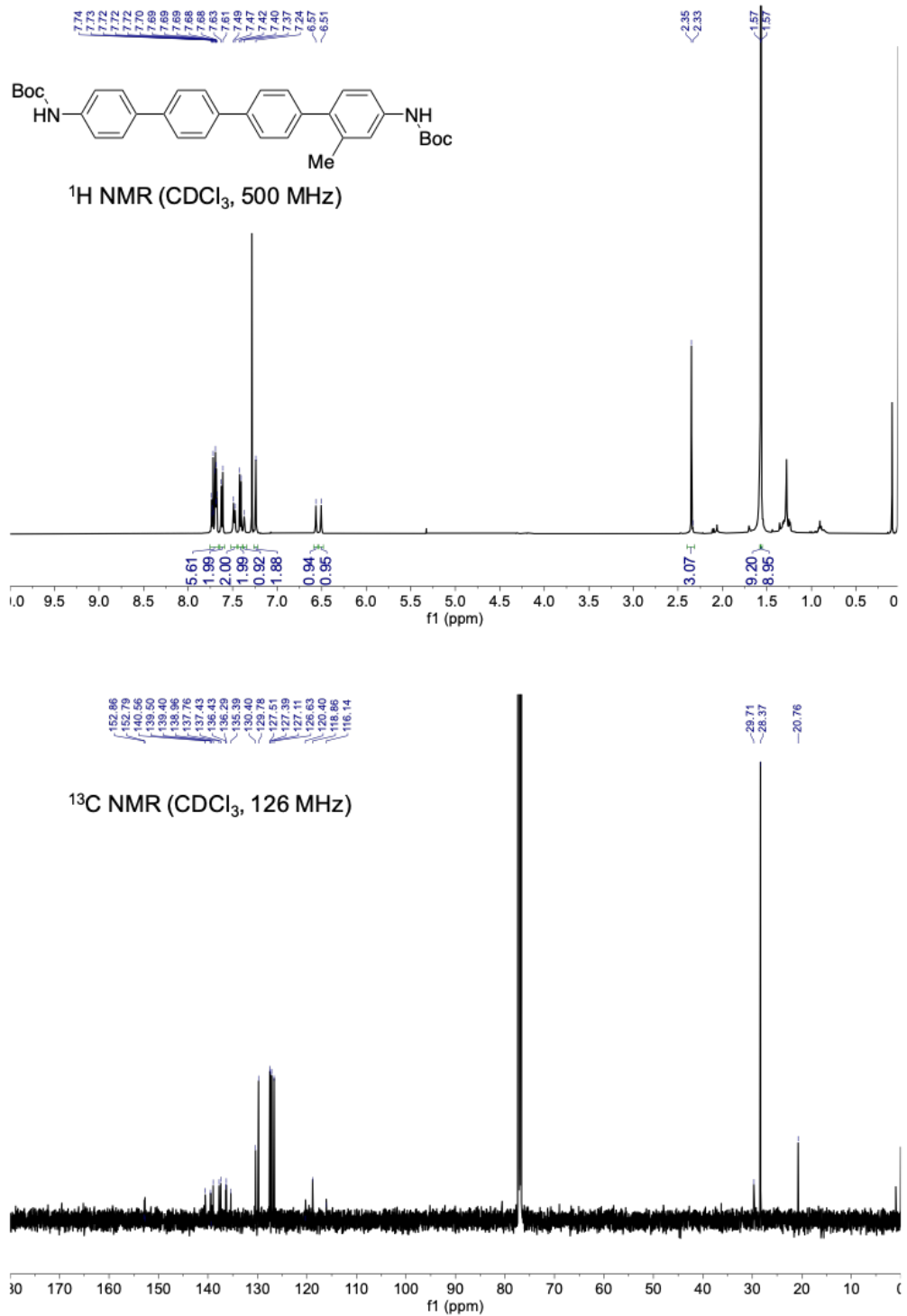


Figure 3.32 NMR spectra of compound **17**.

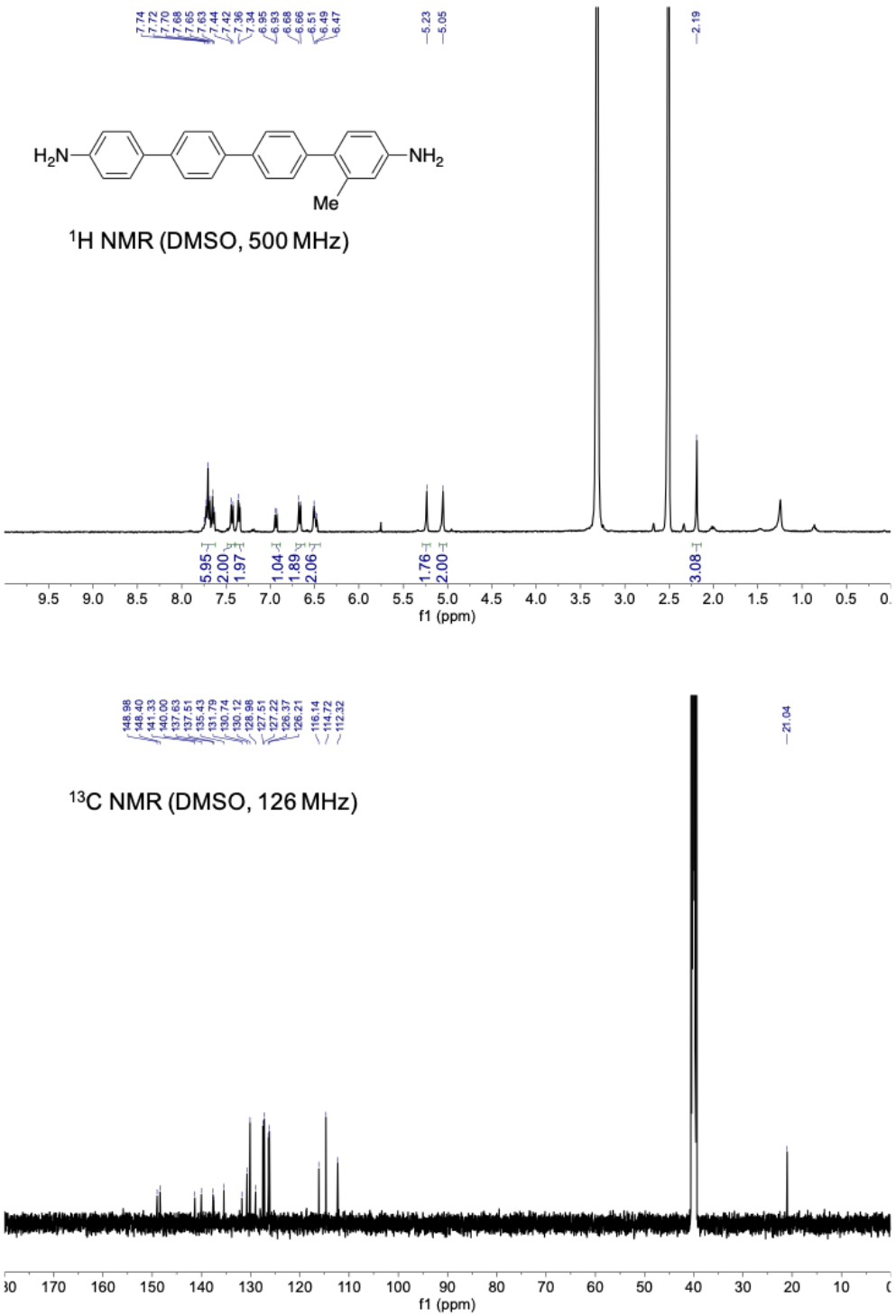


Figure 3.33 NMR spectra of compound C1.

3.13 References

- (1) Ullmann, F.; Bielecki, J. Ueber Synthesen in Der Biphenylreihe. *J. Ber. Dtsch. Chem. Ges.* **1901**, *34*, 2174–2185.
- (2) Isomura, Y.; Narushima, T.; Kawasaki, H.; Yonezawa, T.; Obora, Y. Surfactant-Free Single-Nano-Sized Colloidal Cu Nanoparticles for Use as an Active Catalyst in Ullmann-Coupling Reaction. *Chem. Commun.* **2012**, *48* (31), 3784–3786.
- (3) Yang, B.; Mao, Z.; Zhu, X.; Wan, Y. Functionalised Chitosan as a Green, Recyclable, Supported Catalyst for the Copper-Catalysed Ullmann C-N Coupling Reaction in Water. *Catal. Commun.* **2015**, *60*, 92–95.
- (4) Puthiaraj, P.; Ahn, W. S. Ullmann Coupling of Aryl Chlorides in Water Catalyzed by Palladium Nanoparticles Supported on Amine-Grafted Porous Aromatic Polymer. *Mol. Catal.* **2017**, *437*, 73–79.
- (5) Baqi, Y.; Muller, C. E. Rapid and Efficient Microwave-Assisted Copper(0)-Catalyzed Ullmann Coupling Reaction: General Access to Anilinoanthraquinone Derivatives. *Org. Lett.* **2007**, *9* (7), 1271–1274.
- (6) Baqi, Y.; Müller, C. E. Synthesis of Alkyl- and Aryl-Amino-Substituted Anthraquinone Derivatives by Microwave-Assisted Copper(0)-Catalyzed Ullmann Coupling Reactions. *Nat. Protoc.* **2010**, *5* (5), 945–953.
- (7) Li, Z.; Chen, Y.; Ye, P.; Jia, X.; Wu, X.; Wu, J.; Shi, Q.; Peng, A.; Huang, H. Microwave-Assisted Classic Ullmann C-C Coupling Polymerization for Acceptor-Acceptor Homopolymers. *Polymers (Basel)*. **2019**, *11* (11), 1–10.
- (8) Lindley, J.; Lorimer, J. P.; Mason, T. J. Enhancement of an Ullmann Coupling Reaction Induced by Ultrasound. *Ultrasonics* **1986**, *24* (5), 292–293.
- (9) Smith, K.; Jones, D. A Superior Synthesis of Diary1 Ethers by the Use of Ultrasound in the Ullmann Reaction. *J. Chem. Soc., Perkin Trans. I* **1992**, 407–408.
- (10) Karimi, B.; Esfahani, F. K. Unexpected Golden Ullmann Reaction Catalyzed by Au Nanoparticles Supported on Periodic Mesoporous Organosilica (PMO). *Chem. Commun.* **2011**, *47*, 10452–10454.

- (11) Monopoli, A.; Cotugno, P.; Palazzo, G.; Ditaranto, N.; Mariano, B.; Cioffi, N.; Ciminale, F.; Nacci, A. Ullmann Homocoupling Catalysed by Gold Nanoparticles in Water and Ionic Liquid. *Adv. Synth. Catal.* **2012**, *354*, 2777–2788.
- (12) Evano, G.; Blanchard, N.; Toumi, M. Copper-Mediated Coupling Reactions and Their Applications in Natural Products and Designed Biomolecules Synthesis. *Chem. Rev.* **2008**, *108* (8), 3054–3131.
- (13) Batra, A.; Cvetko, D.; Kladnik, G.; Adak, O.; Cardoso, C.; Ferretti, A.; Prezzi, D.; Molinari, E.; Morgante, A.; Venkataraman, L. Probing the Mechanism for Graphene Nanoribbon Formation on Gold Surfaces through X-Ray Spectroscopy. *Chem. Sci.* **2014**, *5*, 4419–4423.
- (14) Hla, S.; Bartels, L.; Meyer, G.; Rieder, K. Inducing All Steps of a Chemical Reaction with the Scanning Tunneling Microscope Tip: Towards Single Molecule Engineering. *Phys. Rev. Lett.* **2000**, *85* (13), 2777–2780.
- (15) Lackinger, M. Surface-Assisted Ullmann Coupling. *Chem. Commun.* **2017**, *53*, 7872–7885.
- (16) Zhou, X.; Wang, C.; Zhang, Y.; Cheng, F.; He, Y.; Shen, Q.; Shang, J.; Shao, X.; Ji, W.; Chen, W.; et al. Steering Surface Reaction Dynamics with a Self-Assembly Strategy: Ullmann Coupling on Metal Surfaces. *Angew. Chem., Int. Ed.* **2017**, *56*, 12852–12856.
- (17) Pham, T. A.; Song, F.; Nguyen, M.; Li, Z.; Studener, F.; Stöhr, M. Comparing Ullmann Coupling on Noble Metal Surfaces: On-Surface Polymerization of 1,3,6,8-Tetrabromopyrene on Cu(111)and Au(111). *Chem. Eur. J.* **2016**, *22*, 5937–5944.
- (18) Lahrood, A. R.; Bjo, J.; Heckl, W. M.; Lackinger, M. 1,3-Diiodobenzene on Cu(111) – an Exceptional Case of on-Surface Ullmann Coupling. *Chem. Commun.* **2015**, *51*, 13301–13304.
- (19) Basagni, A.; Ferrighi, L.; Cattelan, M.; Nicolas, L.; Handrup, K.; Vaghi, L.; Papagni, A.; Sedona, F.; Valentin, D. On-Surface Photo-Dissociation of C–Br Bonds : Towards Room Temperature Ullmann Coupling. *Chem. Commun.* **2015**, *51*, 12593–12596.
- (20) Lee, H. J.; Ho, W. Single-Bond Formation and Characterization with a Scanning Tunneling Microscope. *Science.* **1999**, *286*, 1719–1723.
- (21) de Oteyza, D. G.; Gorman, P.; Chen, Y.-C.; Wickenburg, S.; Riss, A.; Mowbray, D.; Etkin,

G.; Pedramrazi, Z.; Tsai, H.-Z.; Rubio, A.; et al. Direct Imaging of Covalent Bond Structure in Single-Molecule Chemical Reactions. *Science*. **2013**, *340*, 1434–1438.

- (22) Xu, B.; Tao, N. J. Measurement of Single-Molecule Resistance by Repeated Formation of Molecular Junctions. *Science*. **2003**, *301*, 1221–1223.
- (23) Venkataraman, L.; Klare, J. E.; Nuckolls, C.; Hybertsen, M. S.; Steigerwald, M. L. Dependence of Single-Molecule Junction Conductance on Molecular Conformation. *Nature* **2006**, *442*, 904–907.
- (24) Aragonès, A. C.; Haworth, N. L.; Darwish, N.; Ciampi, S.; Bloomfield, N. J.; Wallace, G. G.; Diez-perez, I.; Coote, M. L. Electrostatic Catalysis of a Diels – Alder Reaction. *Nature* **2016**, *531*, 88–91.
- (25) Zang, Y.; Stone, I.; Inkpen, M. S.; Ng, F.; Lambert, T. H.; Nuckolls, C.; Steigerwald, M. L.; Roy, X.; Venkataraman, L. In Situ Coupling of Single Molecules Driven by Gold-Catalyzed Electrooxidation. *Angew. Chem., Int. Ed.* **2019**, *58*, 16008–16012.
- (26) Starr, R. L.; Fu, T.; Doud, E. A.; Stone, I.; Roy, X.; Venkataraman, L. Gold–Carbon Contacts from Oxidative Addition of Aryl Iodides. *J. Am. Chem. Soc.* **2020**, *142* (15), 7128–7133.
- (27) Capozzi, B.; Xia, J.; Adak, O.; Dell, E. J.; Liu, Z.; Taylor, J. C.; Neaton, J. B.; Campos, L. M.; Venkataraman, L. Single-Molecule Diodes with High Rectification Ratios through Environmental Control. *Nat. Nanotechnol.* **2015**, *10*, 522–527.
- (28) Kamenetska, M.; Koentopp, M.; Whalley, A. C.; Park, Y. S.; Steigerwald, M. L.; Nuckolls, C.; Hybertsen, M. S.; Venkataraman, L. Formation and Evolution of Single-Molecule Junctions. *Phys. Rev. Lett.* **2009**, *102* (12), 2–5.
- (29) Weingarten, H. Mechanism of the Ullmann Condensation. *J. Org. Chem.* **1964**, *29* (5), 3624–3626.
- (30) Fernández, I.; Wolters, L. P.; Bickelhaupt, F. M. Controlling the Oxidative Addition of Aryl Halides to Au(I). *J. Comput. Chem.* **2014**, *35* (29), 2140–2145.
- (31) Bajo, S.; Laidlaw, G.; Kennedy, A. R.; Sproules, S.; Nelson, D. J. Oxidative Addition of Aryl Electrophiles to a Prototypical Nickel(0) Complex: Mechanism and

Structure/Reactivity Relationships. *Organometallics* **2017**, *36* (8), 1662–1672.

- (32) Labinger, J. A. Tutorial on Oxidative Addition. *Organometallics* **2015**, *34* (20), 4784–4795.
- (33) Xi, M.; Bent, B. E. Mechanisms of the Ullmann Coupling Reaction in Adsorbed Monolayers. *J Am Chem Soc* **1993**, *115*, 7426–7433.
- (34) Blake, M. M.; Nanayakkara, S. U.; Claridge, S. A.; Fernandez-Torres, L. C.; Sykes, E. C. H.; Weiss, P. S. Identifying Reactive Intermediates in the Ullmann Coupling Reaction by Scanning Tunneling Microscopy and Spectroscopy. *J. Phys. Chem. A* **2009**, *113* (47), 13167–13172.
- (35) Dong, L.; Liu, P. N.; Lin, N. Surface-Activated Coupling Reactions Confined on a Surface. *Acc. Chem. Res.* **2015**, *48* (10), 2765–2774.
- (36) Zhang, Y.; Starynowicz, P.; Christoffers, J. Fluorescent Bis(Oligophenylamino)Terephthalates. *European J. Org. Chem.* **2008**, No. 20, 3488–3495.
- (37) Lamothe, M.; Pauwels, P. J.; Belliard, K.; Schambel, P.; Halazy, S. Differentiation between Partial Agonists and Neutral 5-HT(1B) Antagonists by Chemical Modulation of 3-[3-(N,N-Dimethylamino)Propyl]-4-Hydroxy-N-[4-(Pyridin-4-Yl)Phenyl]Benzamide (GR-55562). *J. Med. Chem.* **1997**, *40* (22), 3542–3550.
- (38) Khlobystov, A. N.; Brett, M. T.; Blake, A. J.; Champness, N. R.; Gill, P. M. W.; O'Neill, D. P.; Teat, S. J.; Wilson, C.; Schröder, M. Stereoselective Association of Binuclear Metallacycles in Coordination Polymers. *J. Am. Chem. Soc.* **2003**, *125* (22), 6753–6761.
- (39) Doud, E. A.; Inkpen, M. S.; Lovat, G.; Montes, E.; Paley, D. W.; Steigerwald, M. L.; Vázquez, H.; Venkataraman, L.; Roy, X. In Situ Formation of N-Heterocyclic Carbene-Bound Single-Molecule Junctions. *J. Am. Chem. Soc.* **2018**, *140* (28), 8944–8949.
- (40) Bushnell, G. W.; Fischer, A.; Ibrahim, P. N. Formation of Aryliodine(III) Derivatives in the Nitration of Aryl Iodides in Acetic Anhydride. *J. Chem. Soc. Perkin Trans. 2* **1988**, No. 7, 1281–1285.
- (41) Lim, D. S. W.; Lew, T. T. S.; Zhang, Y. Direct Amidation of N-Boc- and N-Cbz-Protected Amines via Rhodium-Catalyzed Coupling of Arylboroxines and Carbamates. *Org. Lett.*

2015, *17* (24), 6054–6057.

- (42) Nagahara, L. A.; Thundat, T.; Lindsay, S. M. Preparation and Characterization of STM Tips for Electrochemical Studies. *Rev. Sci. Instrum.* **1989**, *60* (10), 3128–3130.

Chapter 4: Cyclopropenylidenes as Strong Carbene Anchoring Groups on Au Surfaces

4.1 Preface

This chapter is based on a manuscript entitled “Cyclopropenylidenes as Strong Carbene Anchoring Groups on Au Surface” by Evan A. Doud, Rachel L. Starr, Gregor Kladnik, Anastasia Voevodin, Enrique Montes, Narendra P. Arasu, Yaping Zang, Percy Zahl, Alberto Morgante, Latha Venkataraman, Héctor Vázquez, Dean Cvetko, Xavier Roy published in Journal of the American Chemical Society, 2020, 142 (47), 19902-19906.¹ Hector Vazquez and Enrique Montes at Institute of Physics, Czech Academy of Sciences performed the computational work. Percy Zahl from the Center for Functional Nanomaterials at Brookhaven National Laboratory performed the single molecule imaging using STM-AFM with assistance from Yaping Zang, a postdoctoral fellow at the time in Latha Venkataraman’s group at Columbia University. Latha Venkataraman, Giacomo Lovat, and Gregor Kladnik performed the NEXAFS measurements at the Elettra Synchotron Trieste in Italy. Dan Paley performed single crystal refinement. Evan Doud prepared the $\text{NiBr}_2(\text{PPh}_2)_2$ complex. Anastasia Voevodin synthesized the BAC molecules and assisted with sample preparation for STM-AFM imaging. I participated in the writing, editing, data analysis, and figure creation for this manuscript.

4.2 Introduction

In the previous two chapters we explored the binding and reactivity of aryl iodides in the single molecule junction. In this chapter, we transition to a new kind of linker for binding to gold:

cyclopropenylidene. This system is studied on a gold surface as opposed to in the single molecule junction, to better probe exactly how the cyclopropenylidene binds. We describe within a new class of linkers that holds promise over previously described carbene linkers, for both forming monolayers on metallic surfaces and in single molecule junctions.

Cyclopropenylidene, the smallest aromatic molecule displaying a carbene center, has received widespread theoretical and experimental interest due to its unique electronic structure, chemical reactivity and its existence in interstellar space.^{2–6} Cyclopropenylidene, however, is too unstable to be isolated as a free carbene. First reported as a stable crystalline solid by Bertrand and co-workers, bis(dialkylamino)cyclopropenylidenes (Figure 4.1a) consist of the cyclopropenylidene ring functionalized with two dialkylamino groups.^{3,4,7} The presence of these dialkylamino groups stabilizes the free carbene and, combined with the highly strained nature of the ring and the resulting small angle at the carbenic carbon, produce a molecule capable of remarkably strong σ-donation. Most experimental and theoretical investigations indicate that bis(dialkylamino)cyclopropenylidenes are in fact better σ-donors than the N-heterocyclic carbenes (NHCs) while having a smaller footprint.⁸ Carbenes have recently received intense attention due to their rich coordination chemistry^{9–11} and ability to form ultra-stable self-assembled monolayers on metal surfaces.^{12–17} While diazomethane derivatives have been used to assemble carbene molecules on Ru surfaces,¹⁷ most recent studies have focused on NHCs, prompting the question whether carbenes such as bis(dialkylamino)cyclopropenylidenes could strongly bind to metal surfaces.

In this work, we investigate for the first time the functionalization of metal surfaces with bis(diisopropylamino)cyclopropenylidene (BAC). Using density functional theory (DFT), we first present a detailed theoretical picture of the bonding energetics and geometry of BAC to a Au(111)

surface. We then develop a simple synthetic approach to deposit BAC on Au(111) surfaces in ultra-high vacuum (UHV), and use synchrotron radiation to probe the geometry of the carbenes on the surface through high-resolution X-ray photoelectron spectroscopy (XPS) and near-edge X-ray absorption fine structure (NEXAFS). To support these measurements, we image the surface-bound BACs using high-resolution scanning tunneling microscopy and atomic force microscopy (STM and AFM). Overall, our results indicate that cyclopropenylidenes are attractive anchoring groups to modify metal surfaces, and that they bind even more strongly than NHCs to Au surfaces without altering the surface structure. This work is the first demonstration of surface modification with a stable carbene other than NHC; more broadly it drives further exploration of various carbenes on metal surfaces.

4.3 Computational Studies of BAC Surface Binding

We first model the bonding of BAC to a Au(111) surface using atomistic DFT-based simulations with van der Waals interactions. We start by determining the orientation of the cyclopropenylidene ring relative to the Au(111) surface, which is modeled as three Au layers, each containing 36 atoms (see Section 4.8). For these simulations, the tilt angle (θ) of the ring relative to the surface normal is fixed and all other atoms, including the surface Au atoms, are fully relaxed. This is done by allowing the C atoms in the cyclopropenylidene ring to shift rigidly in any direction. The resulting energy profile is shown in Figure 4.1b. In the vertical orientation ($\theta = 0^\circ$), the binding energy is -1.34 eV, close to that of NHC on a Au(111) surface (-1.49 eV).¹⁶ The favored adsorption site for BAC is an atop site with a Au–C distance of 2.2 Å. As the molecule is tilted and θ increases, the binding energy increases due to the contributions from the Au–C dative

bond and the van der Waals interactions with the surface. The binding energy reaches a maximum at $\theta = 40^\circ$ (Figure 4.1b, c) and decreases for larger θ due to a reduction of the BAC–Au orbital overlap and steric repulsion between the isopropyl N-substituents and the surface. The calculated binding energy at $\theta = 40^\circ$ is -1.65 eV, larger than the reported value of -1.49 eV for MeNHC on Au(111).¹⁶

To quantify the steric role of the isopropyl N-substituents, we calculate the adsorption properties of a BAC molecule in which the isopropyl groups are replaced with H atoms (diaminocyclopropenylidenes, DAC). The binding energy is shown in Figure 4.1d as a function of tilt angle up to $\theta = 70^\circ$ (for $\theta > 70^\circ$, the Au contact atom is extracted from the surface and these geometries are thus excluded). Comparison with Figure 4.1b reveals that both BAC and DAC adopt roughly similar tilt angles on the Au(111) surface but the binding energy of BAC is significantly larger (by 0.2–0.4 eV) than that of DAC. When the tilt angle is large, however, the binding energy decreases more rapidly for BAC due to the increased steric repulsion with the surface. Similar to observations of NHCs bound to Au,¹⁸ we find that dispersive interactions between the surface and the cyclopropenylidene core and pendent isopropyl groups contribute significantly to the binding energy. These results suggest that the binding energy of cyclopropenylidenes to a Au substrate could be further increased by functionalizing the ring with amino groups bearing substituents that can strongly interact with the surface.

We also compare the binding energies of DAC and dihydroimidazol-2-ylidene (NHC) to understand the effect of the ring structure. Figure 4.1d presents the calculated binding energy of both model carbenes as a function of tilt angle. When $\theta = 0^\circ$, the binding energies of both molecules are similar and close to -1.10 eV. However, the DAC ring can sustain a stable geometry for larger θ whereas the NHC core cannot. This is seen even when calculated DAC or NHC rings are bound

to a single Au atom (Figure 4.5). These results suggest that cyclopropenylidene rings can form stronger and less constrained bonds to a Au(111) surface.

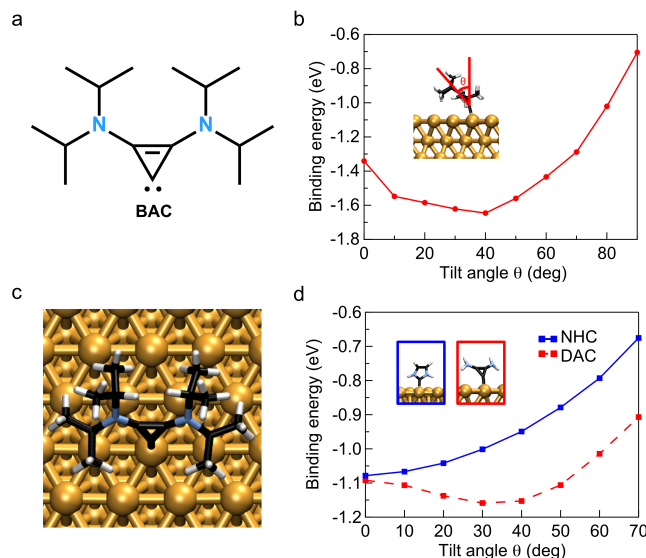


Figure 4.1 (a) Chemical structure of BAC. (b) Calculated binding energy of BAC as a function of tilt angle θ . (c) Structure of BAC absorbed on the Au(111) surface for $\theta = 40^\circ$. (d) Calculated binding energy of DAC and NHC cores on the Au(111) surface as a function of tilt angle θ .

4.4 Spectroscopic Analysis of Surface-Bound BACs

To validate these predictions and experimentally probe the binding of BAC to a Au surface, the BAC–CO₂ adduct was synthesized and used as a precursor that thermally decomposes in UHV to generate free BAC, which can be deposited from the gas phase onto the Au(111) surface (Figure 4.2a). We deposited BAC by thermal decomposition/sublimation of the BAC–CO₂ precursor on Au(111) surfaces and performed X-ray calculations of the C 1s core-electron binding energies for BAC on a Au surface (Figure 4.11). We performed XPS measurements on as-deposited and annealed monolayers.¹⁶ The XPS reveals the presence of C and N on the Au(111) surface and the absence of O, consistent with the BAC anchored to the surface without the CO₂ moiety (Figure

4.7). Moreover, the C 1s photoemission spectrum is well reproduced by DFT calculations of the C 1s core-electron binding energies for BAC on a Au surface (Figure 4.11). We performed X-ray polarization dependent NEXAFS measurements to determine the average orientation of the BAC ring relative to the Au(111) surface normal (Figure 4.2a). For this measurement, we focus on the N K-edge NEXAFS spectra because the C K-edge NEXAFS spectrum contains a complex fine structure with significant contribution from the isopropyl groups (Figure 4.12).

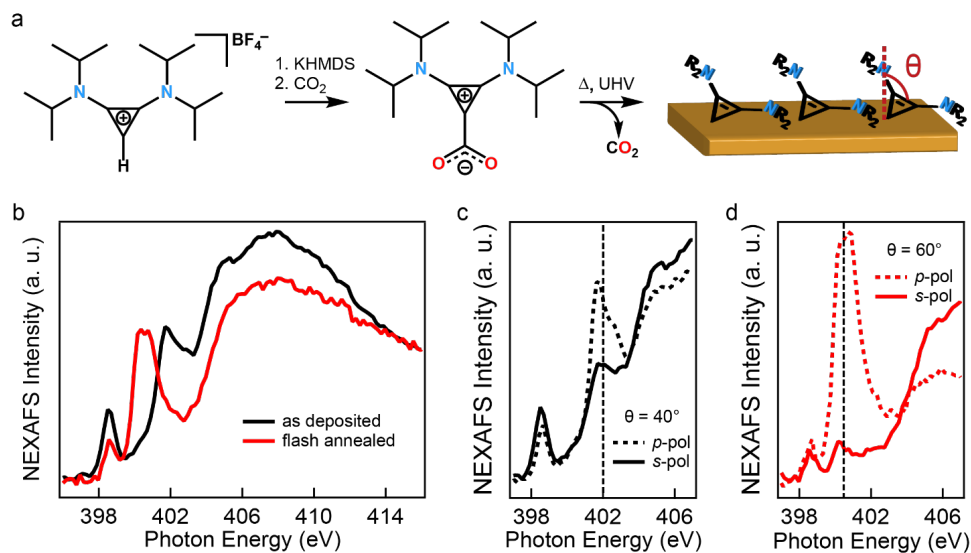


Figure 4.2 (a) Synthesis of BAC–CO₂ and subsequent vapor deposition onto Au(111). (b) Magic angle NEXAFS spectra collected at the N K-edge of the BAC deposited on the Au(111) substrate at 100 °C (black) and then annealed at 200 °C (red). (c, d) NEXAFS N K-edge spectra of the BAC deposited at 100 °C (c) and annealed at 200 °C (d) collected with the electric field of the incident photons perpendicular (p-pol) and parallel (s-pol) to the surface. The dashed vertical black line indicates the N 1s → π^* LUMO absorption peak in both (c) and (d).

We then examine the electronic structure of the unoccupied molecular orbitals in both the as-deposited and annealed films by comparing NEXAFS spectra in the magic angle configuration (Figure 4.2b). Under these specific conditions, the orientations of the molecules do not influence the NEXAFS signal.¹⁹ We notice a substantial change of the measured NEXAFS spectra between

the two films, with a shift of the main absorption peak from \sim 402 to \sim 400.5 eV after annealing at 200 °C. Note that the peak at \sim 398.5 eV, which grows with X-ray exposure, is likely due to molecular fragmentation caused by the beam and not an intrinsic property of the BAC. DFT-based half-core-hole calculations of the X-ray absorption spectra of the BAC molecule coupled to a Au dimer (Figure 4.13a) allow us to assign the absorption peaks at \sim 402 eV in the as deposited film and at \sim 400.5 eV in the annealed film to the same N 1s $\rightarrow \pi^*$ LUMO transition (Figure 4.13b). Of particular note, our DFT calculations reveal that the excitation energy of this transition strongly depends on the Au–C distance (Figure 4.13a). Although the observed energy difference is not fully reproduced by DFT, our calculations show a clear trend toward lower excitation energies with decreasing Au–C distances, indicating a stronger binding of the BAC to Au surface upon annealing. Annealing may enable molecular migration to undercoordinated Au sites, e.g., adatoms, enhancing electronic coupling.

We next measure NK-edge NEXAFS spectra of a BAC monolayer deposited on Au(111) at 100 °C with the incident photon electric field directed either perpendicular (s-polarization) or parallel (p-polarization) to the surface normal to determine the average molecular surface orientation.¹⁹ From the intensity difference of the N 1s $\rightarrow \pi^*$ LUMO transition absorption peaks (at \sim 402 eV) measured using *s*- and *p*-polarizations (Figure 4.2c), we calculate an average $\theta \sim 40^\circ$, consistent with our DFT calculations (Figure 4.1b). After annealing the sample to 200 °C, the linear dichroism of the N 1s $\rightarrow \pi^*$ LUMO transition (at \sim 400.5 eV) is enhanced (Figure 4.2d), resulting in $\theta \sim 60^\circ$. This average tilt angle is larger than DFT-based predictions, suggesting that annealing encourages BAC migration to undercoordinated Au sites, thus energetically favoring larger angles.

The orientation of NHCs on the surface is primarily determined by the N-substituents.¹⁶ For BAC, the increased distance between the N-substituted and the carbenic carbon allows for relaxation of the molecule onto the surface and thus a greater tilt angle θ . NHCs can pull adatoms from the Au(111) substrate, forming flat-lying bis(NHC) complexes with the adatom on the surface.^{16,20,21} These adatoms can be spectroscopically identified as satellite peaks in the XPS Au 4f spectrum.^{16,22} By contrast, we see no evidence for such adatom formation when BAC is deposited on Au(111). The XPS Au 4f spectrum has no satellite peaks indicative of adatom formation (Figure 4.7).²³

4.5 Imaging of Surface-Bound BACs

To support our spectroscopic and theoretical data, we imaged individual BAC molecules anchored to the Au surface with STM and AFM. Using the BAC–CO₂ precursor, we deposited a sub-monolayer of BAC on a Au(111) surface at ~5 K in ultrahigh vacuum. Figure 4.3a shows an STM image of the BACs affixed to the surface. Although a few dimers or clusters are visible, the molecules are generally well dispersed and separated with no preferred anchoring sites. We performed high resolution AFM imaging at 5 K of a single BAC using a CO-functionalized tip (Figure 4.3b). The BAC features two bright lobes attributed to the isopropyl groups. We simulated AFM images of the adsorbed molecule taken with a CO-functionalized tip using a probe particle model.²⁴ The simulation of the most stable geometry ($\theta = 40^\circ$) reproduces the main experimental observations (Figure 4.3c). The two bright features, separated by ~5 Å, result from the repulsion of the hydrogen atoms in the terminal methyl groups of the diisopropyl substituents furthest from the surface. The molecule measures ~10 Å across, the confirmed diameter of BAC bound to

reported metal-BAC complexes.²⁵ The three-membered ring is hidden underneath the bulky alkyl groups, expected for $\theta = 40^\circ$.

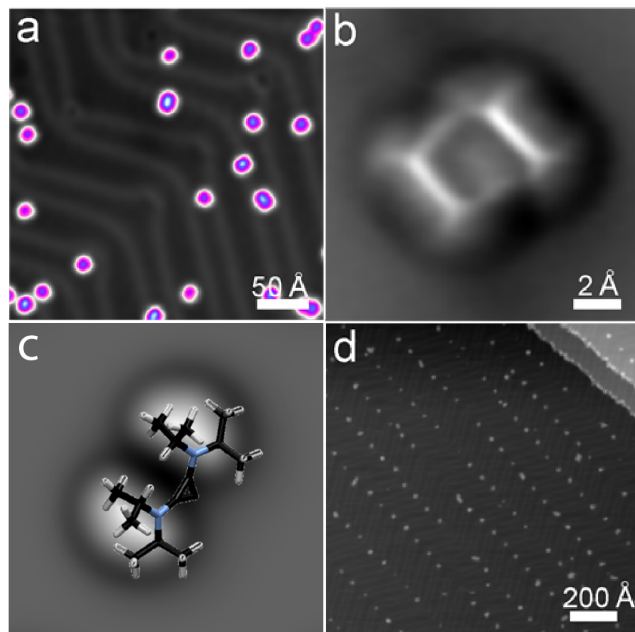


Figure 4.3 (a) STM image of BACs on the Au(111) surface (where the herring bone reconstruction is visible) (0.2 V, 50 pA). (b) High-resolution AFM image of a single BAC molecule. (c) Simulated AFM image for a single BAC. (d) STM image of the BAC molecules on the Au(111) surface after annealing to 110 °C for a few seconds (0.2 V, 50 pA).

The BAC-functionalized surface was heated at 110 °C for a few seconds and imaged again using STM to examine changes to the bound BACs. Figure 4.3d details the rearrangement of the molecules on the surface. At this temperature, the molecules are clearly mobile on the surface and relocate to the herringbone edges. The undercoordinated elbow sites of the herringbone structure are more favorable binding sites for BACs, corroborating the NEXAFS results.

4.6 Conclusion and Outlook

In summary, we have studied for the first time the functionalization of a Au surface with cyclopropenylidene carbenes. Our results indicate that BACs bind more strongly to the surface than NHCs, making them highly suitable as surface binding ligands. Compared to NHCs, BACs have a unique structure with the bulky substituents away from the carbenic carbon. High resolution X-ray absorption spectroscopy supported by DFT-based calculations and single molecule imaging reveal how this structure allows BACs to adopt tilted orientations that maximize their binding energy without Au-adatom formation. This work opens an exciting new area of investigation in the rapidly developing field of self-assembled carbene monolayers on surfaces.

4.7 Synthetic Details

BAC–CO₂ was synthesized following a previously reported literature procedure²⁶ starting from bis(diisopropylamino)cyclopropenium tetrafluoroborate [BAC][BF₄], also prepared via a literature procedure.⁴ Briefly, [BAC][BF₄] was deprotonated with potassium bis(trimethylsilyl)amide (KHMDS) in diethyl ether to form the free BAC. After removal of the solvent in vacuo, the free carbene was dissolved in hexanes and filtered. Carbon dioxide was bubbled through the hexanes solution to generate the adduct, BAC–CO₂, which precipitates from solution as a white solid. Unlike the free carbene, BAC–CO₂ is air stable, affording new opportunities as a precursor in various synthetic strategies.

4.8 Computational Details

Calculation of carbene molecules adsorbed on the Au(111) surface.

The adsorption properties and electronic structure of BAC and NHC molecules on the Au(111) surface were calculated using the SIESTA implementation of density functional theory (DFT).²⁷ The non-local vdW-DF functional of Dion et al. which includes van der Waals (vdW) interactions in the implementation of Román-Pérez and Soler^{28,29} was employed. The unit cell for calculations consists of three Au(111) layers, each containing 36 atoms, plus the molecule, and a vacuum gap of at least 10 Å (Figure 4.4). Molecular (gold) atoms were described using a double- ζ (single- ζ) polarized basis set. Reciprocal space was sampled using a $2 \times 2 \times 1$ Monkhorst pack grid and a realspace grid was defined with an equivalent cut-off energy of 250 Ry. The coordinates of molecular and Au surface atoms were relaxed until the Hellmann-Feynman forces acting on these atoms were smaller than 0.02 eV/Å. The tilt angle (θ) is fixed by constraining the relative position of the atoms in the cyclopropenylidene ring. The position of these atoms was kept fixed relative to each other, without restricting their displacement as a rigid unit. The tilt angle is defined as the angle between the plane of the cyclopropenylidene ring and the z axis. For the calculation of the binding energy, corrections to basis set superposition errors were taken into account. The binding energy for the fully unconstrained geometry is -1.72 eV, slightly higher than the geometries with constrained angle. The contribution of dispersion interactions to the binding energy was computed for the most S3 stable BAC geometry ($\theta = 40^\circ$) from the difference to a PBE calculation at the same geometry. We found a contribution of -1.40 eV to the total binding energy of -1.65 eV of BAC at $\theta = 40^\circ$. The binding energy of DAC at the same angle ($\theta = 40^\circ$) was calculated to be -1.16 eV, of which -0.93 eV corresponds to van der Waals interactions

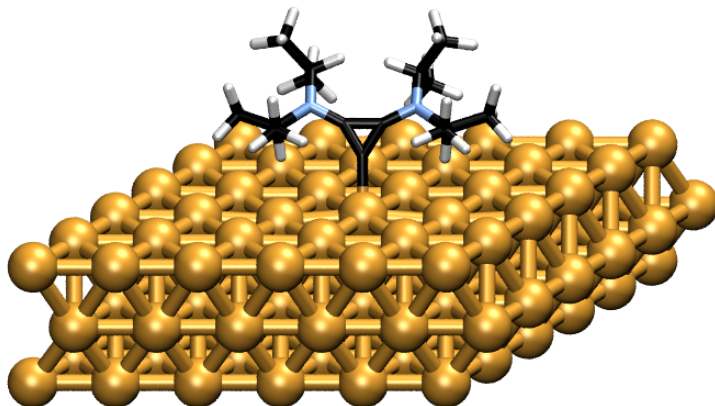


Figure 4.4 Unit cell used in the DFT calculations of the adsorbed molecule.

Calculation of isolated molecule and carbene-Au atom complexes.

The electronic properties of diaminocyclopropenylidene (DAC) and dihydroimidazol-2-ylidene (NHC) molecules as well as DAC-Au₁ and NHC-Au₁ complexes in the gas phase were calculated with Gaussian.³⁰ Exchange-correlation was approximated with the B3LYP functional. 6-31G* (LANL2DZ) basis sets were used to describe the Au atoms. The total energy of DAC-Au₁ and NHC-Au₁ complexes was calculated as a function of the angle between the C-Au bond and the carbene planes, as shown in Figure 4.5a for the DAC-Au₁ complex. This angle was constrained while all other degrees of freedom were optimized. Figure 4.5b shows the calculated energy profiles, with the energy at 0 degrees in each case set to zero for ease of comparison. While the most stable geometry of NHC-Au is found for 0 degrees, the lowest energy of the DAC-Au complex is obtained when the C-Au bond is tilted 24 degrees from the carbene plane. Thus, the possibility of DAC to bind at a tilted angle develops already with a single Au atom

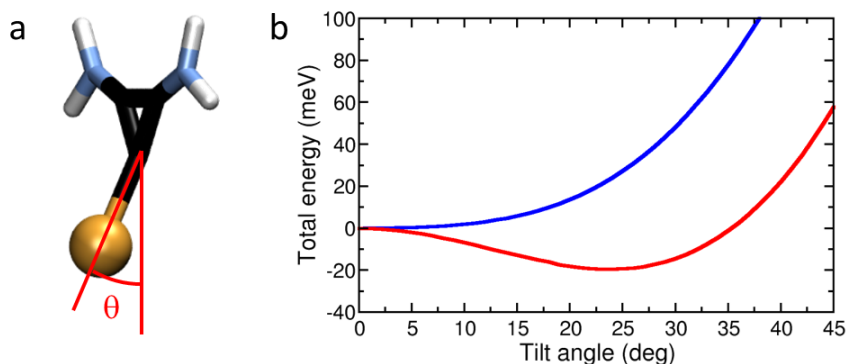


Figure 4.5 (a) Structure of the DAC -Au complex used in the calculations. (b) Energy of DAC - Au (red curve) and NHC-Au (blue curve) complexes as a function of tilt angle, relative to the value at 0 degrees.

To elucidate the origin of the out of plane binding in DAC but not in NHC, the electrostatic potential of isolated DAC and NHC molecules was calculated. Figure 4.6a shows the calculated electrostatic potential of DAC (top) and NHC (bottom) isolated molecules. Contour lines are plotted at 1, 10, and 20 eV. The position of the Au atom at its most stable conformation in Figure 4.6 is indicated by a cross. In Figure 4.6b, the three-dimensional electrostatic potential is represented in real-space projected onto an isosurface of the electron density (10^{-3} e/ \AA^3). Positive (negative) values of the potential, corresponding to blue (red) regions, indicate electron-deficient (electron-rich) regions of the molecule. The broader angular distribution in DAC compared to NHC evidences its ability to bond to Au in a tilted conformation.

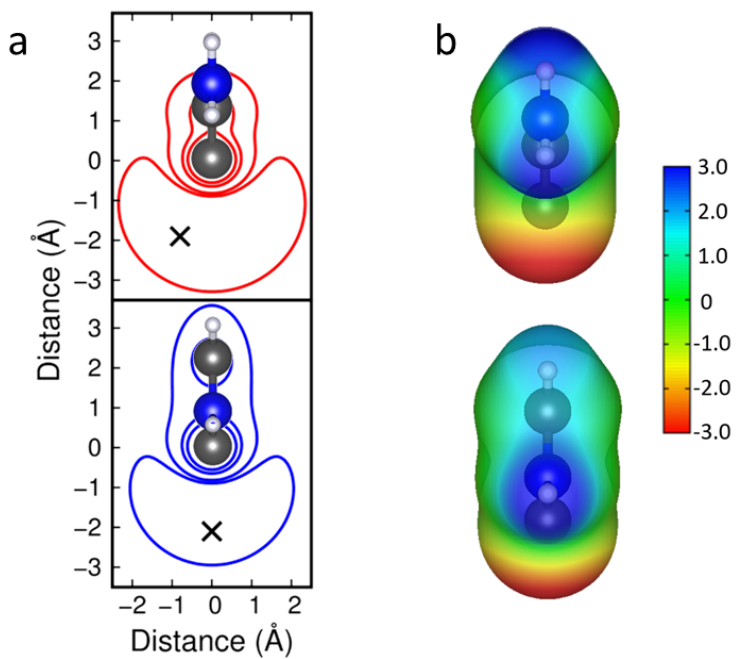


Figure 4.6 (a) Electrostatic potential contour lines of DAC and NHC. (b) Real-space representation for DAC (top) and NHC (bottom) of the electrostatic potential (in V) projected over the electron density isocontour ($10^{-3} \text{ e}/\text{\AA}^3$).

4.9 Details of XPS and NEXAFS Measurements

The X-ray photoemission (XPS) and absorption (NEXAFS) measurements were performed at the ALOISA beamline³¹ of the Elettra synchrotron. The Au(111) surface was prepared by cycles of Ar⁺ sputtering (1.5 keV) and thermal annealing up to ~750 K. Absence of surface contaminants was checked by XPS prior to molecule deposition. The BAC precursor was loaded into a pyrex cell and pumped down to high vacuum resulting in decarboxylation and sublimation of the carbene compounds for deposition. During the deposition the cell was heated to ~380 K and the sample chamber pressure reached 2×10^{-8} mbar. The temperature of the Au substrate was controlled during the deposition (as reported in the text) and then cooled down to ~200 K for the X-ray absorption measurement.

XPS spectra were taken at grazing incidence angle (4°) using a photon energy of 500 eV with the photon electric field aligned 4° off the surface normal. The emitted electrons were detected by a hemispherical electron analyzer in normal emission geometry, with overall energy resolution better than 220 meV. The binding energy scale has been calibrated using bulk spectral component of the Au 4f_{7/2} peak at 84.0 eV.²³

Figure 4.7 shows the XPS measurement of the BAC film deposited on Au(111) surface held at 370 K sample temperature. We detect no oxygen spectral features indicating that the CO₂ moiety in the precursor molecules is cleaved off leaving just the BAC molecule deposited on the substrate.

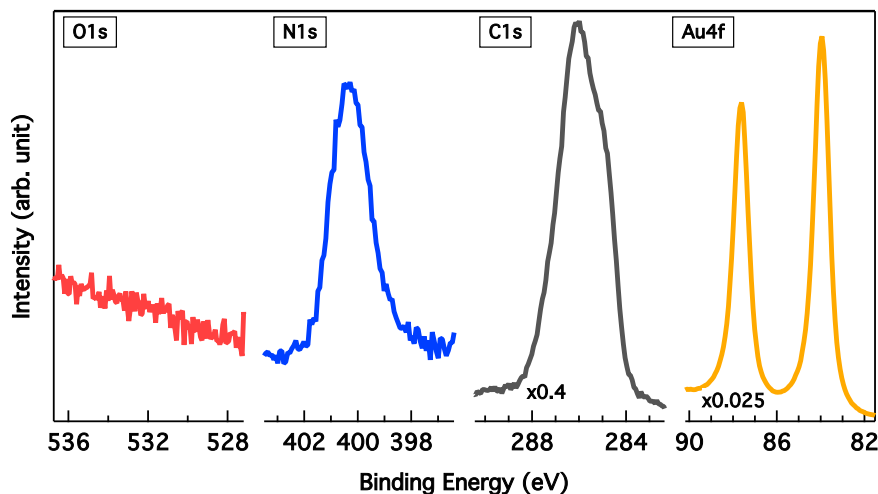


Figure 4.7 XPS measurement of the as-deposited BAC film at 370 K sample temperature. Lack of any oxygen signal indicates that CO₂ moiety is cleaved from the precursor molecules. Intensities of the C1s and Au4f spectral features are scaled as indicated for better comparison

The effect of temperature annealing the BAC film is further shown in Figure 4.8 and Figure 4.9. Some N1s and C1s signals are reduced after annealing to 430 K and 470 K, pointing to a partial desorption of the BAC. The C1s peak shape in the as deposited film displays two distinct

components at 285.2 and 286.0 eV, with the higher binding energy component likely due to bilayer formation where substrate screening of the core hole is less efficient. The C1s peak profile of the 430 K and 470 K annealed film demonstrates that predominantly the high binding energy component is reduced, whereas the low binding energy component is preserved. The slight increase of the Au4f signal upon temperature annealing also indicates that some of the BAC molecules desorb, leaving just the monolayer.

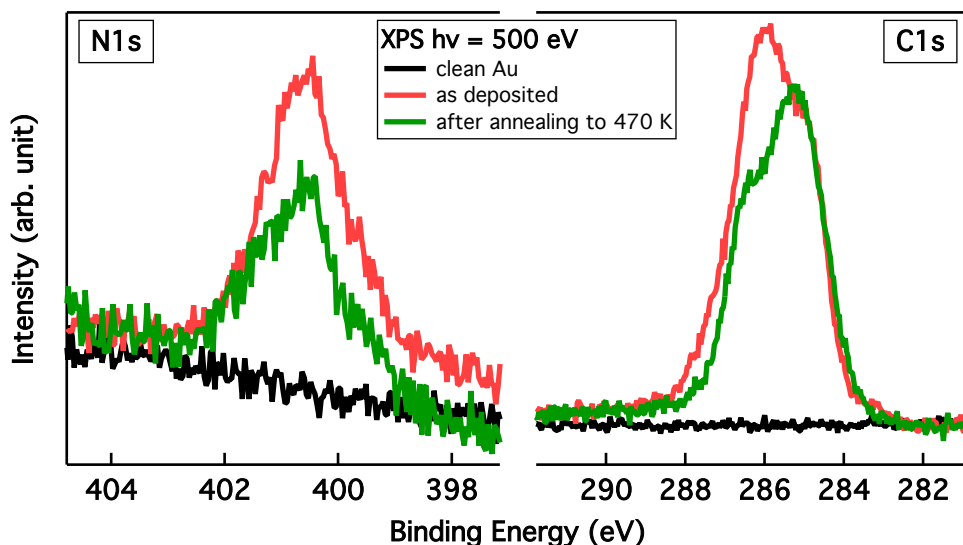


Figure 4.8 N1s and C1s XPS data of BAC film deposited on Au(111) (red) and after temperature annealing to 470 K (green). Changes in the C 1s peak shape indicate desorption of the second layer leaving just a single layer of BAC on Au. Clean gold substrate XPS scans are also shown (black) as a reference.

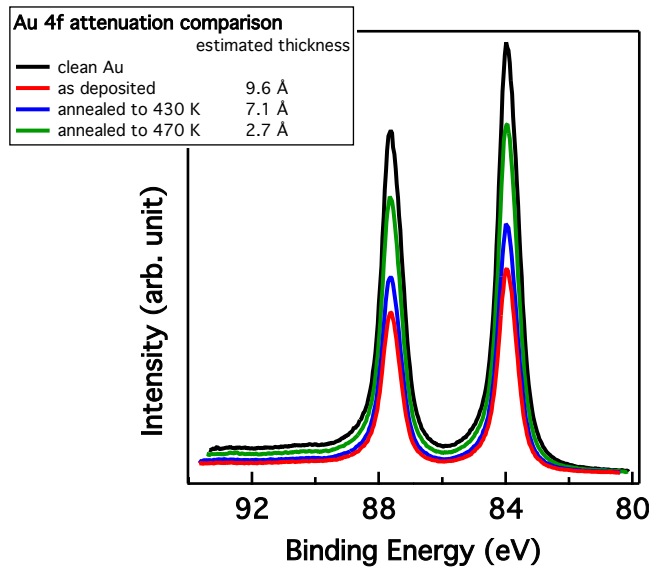


Figure 4.9 Comparison of Au 4f intensity attenuation due to different thicknesses of the BAC film remaining after temperature annealing the pristine (as deposited) film.

The NEXAFS N K-edge spectra were acquired in partial electron yield mode by a wide acceptance angle channeltron detector. A grid placed in front of the channeltron was polarized to -370 V, acting as a high-pass filter rejecting electrons with kinetic energies lower than 370 eV. The photon energy resolution was better than 150 meV. Polarization dependent NEXAFS spectra were taken in two polarizations, in *p*-polarization (photon electric field normal to the surface) and *s*-polarization (electric field parallel to the surface), to measure the molecular adsorption geometry.¹⁹ Magic angle NEXAFS spectra were measured with the surface normal at 55 degrees from the photon polarization.

4.10 Details of DFT Calculations of X-ray Photoemission and Absorption Spectra

We simulate the effect of gold adatoms or step edges by introducing a gold dimer as shown in Figure 4.10 and optimizing the geometry using density functional theory (DFT) with the B3LYP

functional and the double-zeta correlation-consistent basis set (cc-pVDZ) implemented in the NWChem computational chemistry package.³² The optimized geometry then served as input to GPAW, a DFT Python code based on the projector-augmented wave (PAW) method to calculate the core electron binding energies (CEBEs) as well as the X-ray absorption spectra (XAS).^{33–35}

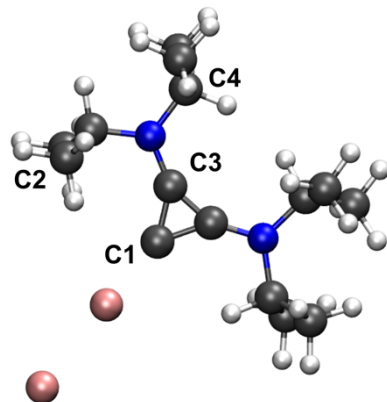


Figure 4.10 Optimized geometry of the BAC molecule with a gold dimer near the C1 carbene carbon.

We calculated the CEBEs of all inequivalent C1s sites with the PBE functional with a cell size of 25.6 Å and grid spacing of 0.2 Å using the delta Kohn-Sham scheme. The full core-hole PAW setups were created with GPAW and default parameter values. The inequivalent C1s sites are marked in Figure 4.10 and correspond to the carbene carbon (C1), aromatic carbons bound to nitrogen (C3), aliphatic carbons also bound to nitrogen (C4) and aliphatic carbons (C2) in the propyl groups. Figure 4.11a shows a comparison of the calculated C1s (blue) CEBEs with the measured XPS (green) after flashing the deposited film to 420K. The shape of the C1s peak changed significantly upon flashing to 430 K (compare with Figure 4.7) probably indicating desorption of the second layer. This is further corroborated by the DFT calculation of the C1s CEBEs. The calculated CEBEs were offset to match the measured XPS for better comparison and

the intensities were set to follow the expected stoichiometric ratios. The simulated peak shapes were obtained by gaussian convolution with FWHM = 0.4 eV.

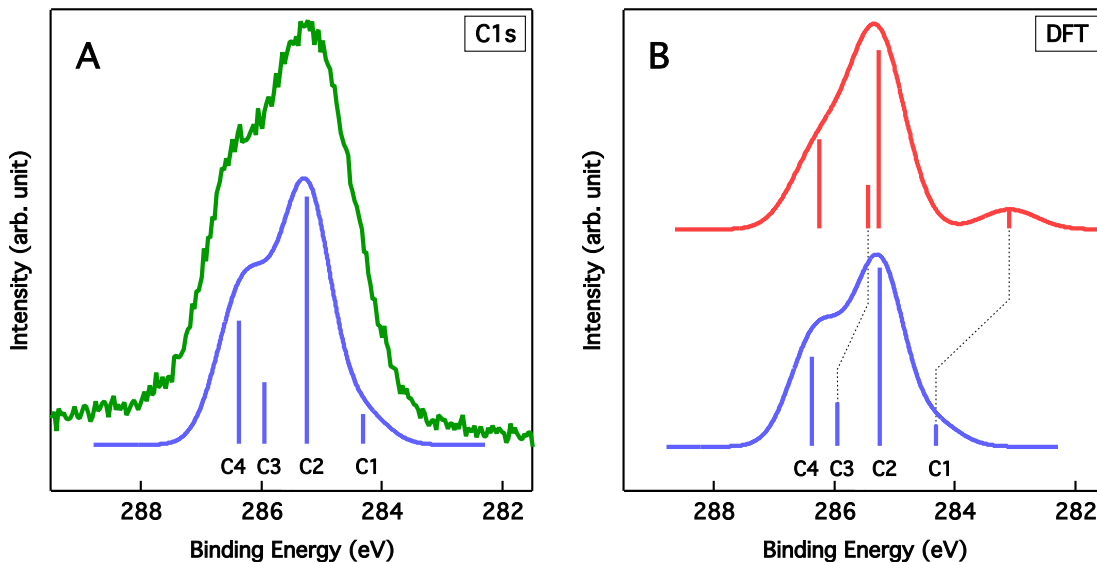


Figure 4.11 (a) Comparison of the measured C1s peak (green) with the calculated CEBEs, which are shifted to match the measured peak position. (b) Comparison of the calculated CEBEs for isolated BAC molecule (red) and the BAC molecule with a gold dimer placed near the carbene (C1) carbon.

The overall peak shape is well reproduced in the DFT calculation of the BAC molecule with an Au dimer. The effect of the Au dimer on the spectra are shown in the Figure 4.11b with the isolated BAC molecule CEBEs shown in red and the BAC with Au dimer CEBEs shown in blue. The calculated energies were offset to match the main (C2) component position belonging to the propyl group atoms presumably least prone to modification due to coupling with the Au dimer. The CEBEs of the peaks corresponding to the carbons closest to the Au dimer (C1 and C3) are found shifted towards higher binding energies relative to the positions of the other two peaks indicating a charge redistribution from the molecule's carbene core to the Au dimer.

X-ray absorption spectra (NEXAFS) were performed using the half core-hole transition potential method as implemented in GPAW. The calculation parameters were the same as for the CEBE calculations described above. The calculated NEXAFS spectra were obtained by gaussian convolution of the calculated transition intensities represented in the corresponding figures by sticks. We focus only on nitrogen K-edge NEXAFS spectra, since the measured carbon K-edge spectrum, Figure 4.12b, has a rich fine structure, due to the different initial states (C1-C4) where the majority of the signal stems from the aliphatic carbons. The contribution of the aromatic (and carbene) carbons is minimal and their effect on the measured absorption spectra is experimentally difficult to evaluate.

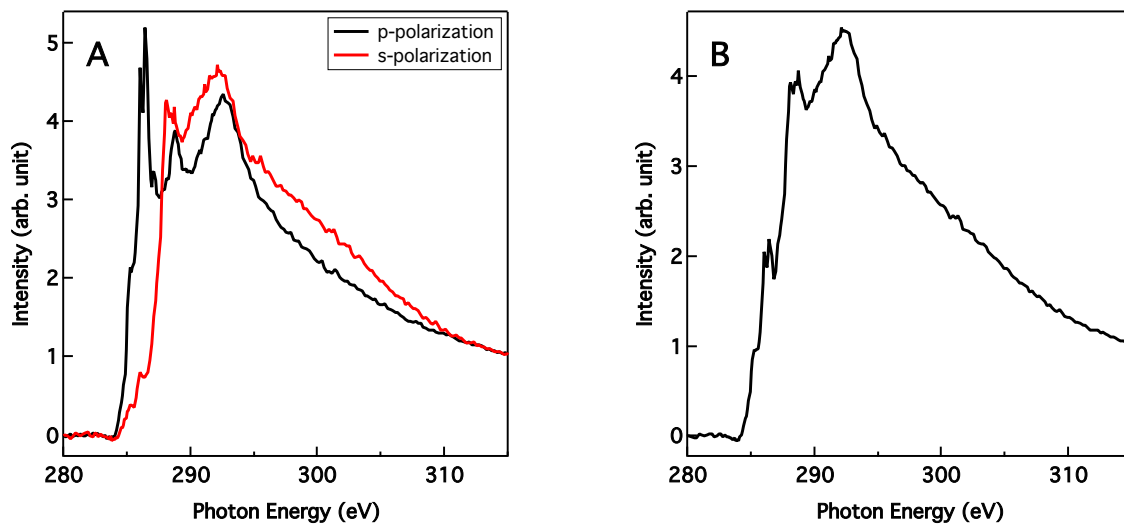


Figure 4.12 (a) Polarization dependent carbon K-edge NEXAFS of the flashed BAC film and (b) the corresponding magic angle NEXAFS.

Nitrogen K-edge spectra are easier to simulate since both N atoms in the molecule are equivalent. Moreover, the N atoms are directly bound to the aromatic (carbene) core indicating

that electronic structure changes localized on the aromatic core should manifest also in nitrogen related unoccupied orbitals. Additionally, as noted in the main text, the DFT calculations of the BAC geometry show that the aromatic carbons (C1 and C3) and the nitrogens lie almost in the same plane, which allows us to use the measured dichroism in the polarization dependent N K-edge NEXAFS to estimate the orientation of the aromatic (carbene) core of the molecule relative to the substrate plane.

We calculate NEXAFS in magic angle conditions, i.e. absorption spectra independent of the molecular orientation, since we are specifically interested in the unoccupied molecular states and the corresponding transition energies. Experimentally we observe a significant change in the absorption spectra, where it appears that the LUMO peak position shifts toward lower excitation energy upon flash annealing the deposited film to 430 K (see main text Figure 4.2b). We attribute this to reorganization of the BAC molecules on the Au substrate surface toward more reactive sites (Au adatoms, step edges). This is further corroborated by our DFT simulations where we investigate the effect of the distance between the gold dimer and the C1 (carbene) carbon on the simulated N K-edge NEXAFS, Figure 4.13.

In Figure 4.13a we compare the experimentally derived magic angle N K-edge NEXAFS data (top black and red traces) with the DFT calculated NEXAFS spectra for isolated BAC molecule and BAC molecule with a gold dimer positioned at different distances to the C1 (carbene) carbon. Of immediate note, the peak at \sim 398 eV in the measured spectra is attributed to synchrotron beam induced modification of the amino groups and is therefore not reproduced in the DFT calculations. The calculated NEXAFS spectra were obtained by gaussian convolution of the calculated transition intensities represented in the figure by sticks. The calculated absorption spectrum of isolated BAC molecule (yellow trace) reproduces the NEXAFS measured just after

deposition very well. The as deposited film is a multilayer, as established from the XPS data, therefore no features induced by molecule-substrate interactions are expected in the spectrum and is confirmed by the DFT calculation. The addition of a gold dimer induces some charge delocalization from the molecule to the gold dimer as indicated by the bubble plots shown in the Figure 4.13b. This further induces a transition energy shift of the LUMO orbital to lower energies, which reaches a minimum for a gold – carbon distance of about 2.0Å (red trace). This shift is indeed observed in the measured spectra, where after flashing to 430 K the NEXAFS changes significantly, with a shift of the peak at ~402 eV (black trace) to an energy of ~400.5 eV. Our DFT calculations show that this shift can be attributed to stronger Au substrate – BAC molecule interaction. Although the full -1.5 eV shift is not reproduced with our calculations, the trend is clear – stronger interaction, i.e. smaller distance between the C1 carbene carbon and the gold dimer, yields a larger shift of the LUMO excitation energy towards lower values.

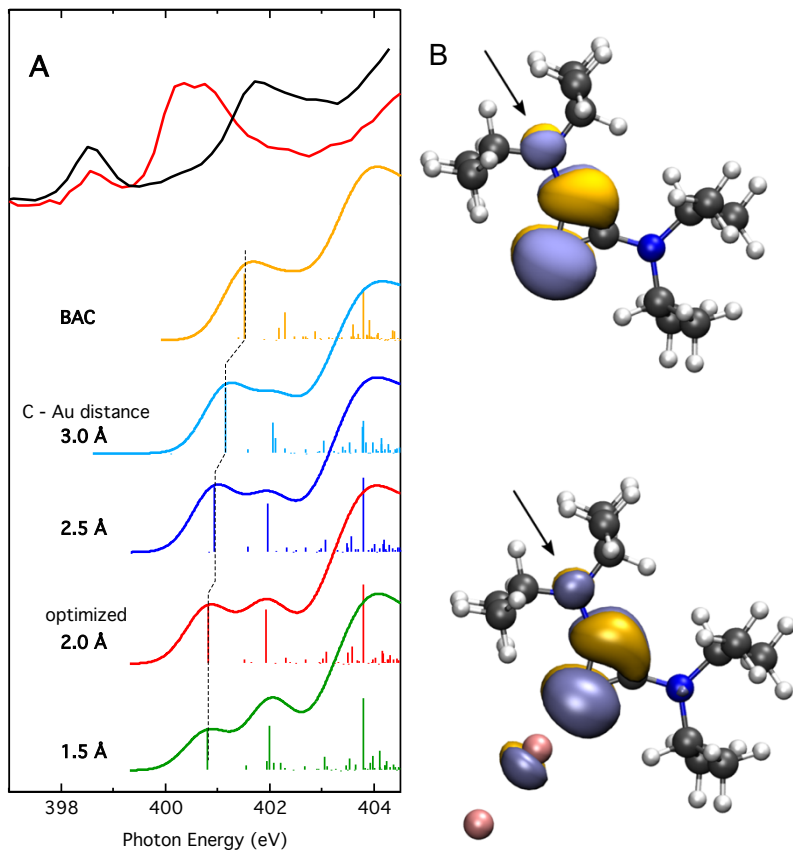


Figure 4.13 (a) Comparison of experimentally derived magic-angle N K-edge NEXAFS (top black after BAC deposition, top red after flash to 430 K) and DFT calculated NEXAFS spectra of isolated BAC molecule (yellow) and BAC molecule with a gold dimer at different distances from the C1 (carbene) carbon. (b) Bubble plot of the calculated “LUMO” with a half-core-hole on the nitrogen atom pointed on with an arrow for the isolated BAC molecule (top right) and the BAC molecule with a gold dimer (bottom right).

4.11 Scanning probe microscopy experiments

Measurements were performed with a Createc-based low-temperature (LT)-STM system custom upgraded (by the author P. Zahl) with NC-AFM capability and operated using the open source GXSM control software.^{36–38} Our Q-Plus sensor used for the STM/NC-AFM measurements has a 25 µm PtIr tip wire attached which was cut and sharpened by a focused ion beam (FIB)

milling following a final cleaning procedure in UHV using Ar⁺ sputtering from three directions before mounting on the SPM scanner.

Simulation of AFM images

AFM images were calculated using the probe particle model²⁴ for the BAC structure at θ = 40°. The parameters of the tip were chosen to simulate a CO-functionalized tip (lateral stiffness of 0.24 N/m). Images were generated by scanning the tip over BAC on a three-dimensional grid with a spacing of 0.1 Å. At each grid position of the vertical approach, the tip position was allowed to relax. An oscillation amplitude of 0.5-1 Å was used.

4.12 References

- (1) Doud, E. A.; Starr, R. L.; Kladnik, G.; Voevodin, A.; Montes, E.; Arasu, N. P.; Zang, Y.; Zahl, P.; Morgante, A.; Venkataraman, L.; et al. Cyclopropenylidenes as Strong Carbene Anchoring Groups on Au Surface. *J. Am. Chem. Soc.* **2020**, *142* (47), 19902–19906.
- (2) Kaiser, R. I. Experimental Investigation on the Formation of Carbon-Bearing Molecules in the Interstellar Medium via Neutral-Neutral Reactions. *Chem. Rev.* **2002**, *102* (5), 1309–1358.
- (3) Lavallo, V.; Canac, Y.; Donnadieu, B.; Schoeller, W. W.; Bertrand, G. Cyclopropenylidenes: From Interstellar Space to an Isolated Derivative in the Laboratory. *Science*. **2006**, *312* (5774), 722–724.
- (4) Lavallo, V.; Ishida, Y.; Donnadieu, B.; Bertrand, G. Isolation of Cyclopropenylidene-Lithium Adducts: The Weiss-Yoshida Reagent. *Angew. Chemie - Int. Ed.* **2006**, *45* (40), 6652–6655.
- (5) Schoeller, W. W.; Frey, G. D.; Bertrand, G. Tuning the Nucleophilicity in Cyclopropenylidenes. *Chem. - A Eur. J.* **2008**, *14* (15), 4711–4718.

- (6) Johnson, L. E.; DuPré, D. B. Topological and Orbital-Based Mechanisms of the Electronic Stabilization of Bis(Diisopropylamino)Cyclopropenylidene. *J. Phys. Chem. A* **2008**, *112* (32), 7448–7454.
- (7) Kinjo, R.; Ishida, Y.; Donnadieu, B.; Bertrand, G. Isolation of Bicyclopropenylidenes: Derivatives of the Smallest Member of the Fulvalene Family. *Angew. Chemie - Int. Ed.* **2009**, *48* (3), 517–520.
- (8) Kuchenbeiser, G.; Donnadieu, B.; Bertrand, G. Stable Bis(Diisopropylamino)Cyclopropenylidene (BAC) as Ligand for Transition Metal Complexes. *J. Organomet. Chem.* **2008**, *693* (5), 899–904.
- (9) Jazzar, R.; Soleilhavoup, M.; Bertrand, G. Cyclic (Alkyl)- And (Aryl)-(Amino)Carbene Coinage Metal Complexes and Their Applications. *Chem. Rev.* **2020**, *120* (9), 4141–4168.
- (10) Sau, S. C.; Hota, P. K.; Mandal, S. K.; Soleilhavoup, M.; Bertrand, G. Stable Abnormal N-Heterocyclic Carbenes and Their Applications. *Chem. Soc. Rev.* **2020**, *49* (4), 1233–1252.
- (11) Guisado-Barrios, G.; Soleilhavoup, M.; Bertrand, G. 1 H-1,2,3-Triazol-5-Ylidenes: Readily Available Mesoionic Carbenes. *Acc. Chem. Res.* **2018**, *51* (12), 3236–3244.
- (12) Crudden, C. M.; Horton, J. H.; Ebralidze, I. I.; Zenkina, O. V.; McLean, A. B.; Drevniok, B.; She, Z.; Kraatz, H. B.; Mosey, N. J.; Seki, T.; et al. Ultra Stable Self-Assembled Monolayers of N-Heterocyclic Carbenes on Gold. *Nat. Chem.* **2014**, *6* (5), 409–414.
- (13) Zhukhovitskiy, A. V.; MacLeod, M. J.; Johnson, J. A. Carbene Ligands in Surface Chemistry: From Stabilization of Discrete Elemental Allotropes to Modification of Nanoscale and Bulk Substrates. *Chem. Rev.* **2015**, *115* (20), 11503–11532.
- (14) Crudden, C. M.; Horton, J. H.; Narouz, M. R.; Li, Z.; Smith, C. A.; Munro, K.; Baddeley, C. J.; Larrea, C. R.; Drevniok, B.; Thanabalasingam, B.; et al. Simple Direct Formation of Self-Assembled N-Heterocyclic Carbene Monolayers on Gold and Their Application in Biosensing. *Nat. Commun.* **2016**, *7*, 12654.
- (15) Man, R. W. Y.; Li, C. H.; MacLean, M. W. A.; Zenkina, O. V.; Zamora, M. T.; Saunders, L. N.; Rousina-Webb, A.; Nambo, M.; Crudden, C. M. Ultrastable Gold Nanoparticles Modified by Bidentate N-Heterocyclic Carbene Ligands. *J. Am. Chem. Soc.* **2018**, *140* (5), 1576–1579.

- (16) Lovat, G.; Doud, E. A.; Lu, D.; Kladnik, G.; Inkpen, M. S.; Steigerwald, M. L.; Cvetko, D.; Hybertsen, M. S.; Morgante, A.; Roy, X.; et al. Determination of the Structure and Geometry of N-Heterocyclic Carbenes on Au(111) Using High-Resolution Spectroscopy. *Chem. Sci.* **2019**, *10* (3), 930–935.
- (17) Tulevski, G. S.; Myers, M. B.; Hybertsen, M. S.; Steigerwald, M. L.; Nuckolls, C. Formation of Catalytic Metal-Molecule Contacts. *Science*. **2005**, *309* (5734), 591–594.
- (18) Kim, H. K.; Hyla, A. S.; Winget, P.; Li, H.; Wyss, C. M.; Jordan, A. J.; Larrain, F. A.; Sadighi, J. P.; Fuentes-Hernandez, C.; Kippelen, B.; et al. Reduction of the Work Function of Gold by N-Heterocyclic Carbenes. *Chem. Mater.* **2017**, *29* (8), 3403–3411.
- (19) Stöhr, J. *NEXAFS Spectroscopy*; Springer: Heidelberg, 1992.
- (20) Wang, G.; Rühling, A.; Amirjalayer, S.; Knor, M.; Ernst, J. B.; Richter, C.; Gao, H. J.; Timmer, A.; Gao, H. Y.; Doltsinis, N. L.; et al. Ballbot-Type Motion of N-Heterocyclic Carbenes on Gold Surfaces. *Nat. Chem.* **2017**, *9*, 152–156.
- (21) Jiang, L.; Zhang, B.; Médard, G.; Seitsonen, A. P.; Haag, F.; Allegretti, F.; Reichert, J.; Kuster, B.; Barth, J. V.; Papageorgiou, A. C. N -Heterocyclic Carbenes on Close-Packed Coinage Metal Surfaces: Bis-Carbene Metal Adatom Bonding Scheme of Monolayer Films on Au, Ag and Cu. *Chem. Sci.* **2017**, *8* (12), 8301–8308.
- (22) Chaudhuri, A.; Lerotholi, T. J.; Jackson, D. C.; Woodruff, D. P.; Dhanak, V. Author Reply to: Comment on "Local Methylthiolate Adsorption Geometry on Au(111) from Photoemission Core-Level Shifts". *Phys. Rev. Lett.* **2009**, *103* (11), 119602.
- (23) Cossaro, A.; Floreano, L.; Verdini, A.; Casalis, L.; Morgante, A. Comment on "Local Methylthiolate Adsorption Geometry on Au(111) from Photoemission Core-Level Shifts." *Phys. Rev. Lett.* **2009**, *103* (11), 119601.
- (24) Hapala, P.; Kichin, G.; Wagner, C.; Tautz, F. S.; Temirov, R.; Jelínek, P. Mechanism of High-Resolution STM/AFM Imaging with Functionalized Tips. *Phys. Rev. B - Condens. Matter Mater. Phys.* **2014**, *90* (8), 085421.
- (25) Tamm, M.; Grzegorzewski, A.; Ekkehardt Hahn, F. Pentacarbonylchromium(0) and -Tungsten(0) Complexes with the Bis(Diisopropylamino) Cyclopropenylidene Ligand. *J. Organomet. Chem.* **1995**, *501* (1–2), 309–313.

- (26) Kuchenbeiser, G.; Soleilhavoup, M.; Donnadieu, B.; Bertrand, G. Reactivity of Cyclic (Alkyl)(Amino)Carbenes (CAACs) and Bis(Amino)Cyclopropenylidenes (BACs) with Heteroallenes: Comparisons with Their N-Heterocyclic Carbene (NHCs) Counterparts. *Chem. - An Asian J.* **2009**, *4* (11), 1745–1750.
- (27) Soler, J. M.; Artacho, E.; Gale, J. D.; García, A.; Junquera, J.; Ordejón, P.; Sánchez-Portal, D. The SIESTA Method for Ab Initio Order-N Materials Simulation. *J. Phys. Condens. Matter* **2002**, *14* (11), 2745–2779.
- (28) Dion, M.; Rydberg, H.; Schröder, E.; Langreth, D. C.; Lundqvist, B. I. Van Der Waals Density Functional for General Geometries. *Phys. Rev. Lett.* **2004**, *92* (24), 246401.
- (29) Román-Pérez, G.; Soler, J. M. Efficient Implementation of a van Der Waals Density Functional: Application to Double-Wall Carbon Nanotubes. *Phys. Rev. Lett.* **2009**, *103* (9), 096102.
- (30) Frisch, M. J.; Trucks, G. W.; Schlegel, H. B.; Scuseria, G. E.; Robb, M. A.; Cheeseman, J. R.; Scalmani, G.; Barone, V.; Petersson, G. A.; Nakatsuji, H.; et al. *Gaussian 16 Rev. A.03*; Wallingford, CT, 2016.
- (31) Floreano, L.; Naletto, G.; Cvetko, D.; Gotter, R.; Malvezzi, M.; Marassi, L.; Morgante, A.; Santaniello, A.; Verdini, A.; Tommasini, F.; et al. Performance of the Grating-Crystal Monochromator of the ALOISA Beamline at the Elettra Synchrotron. *Rev. Sci. Instrum.* **1999**, *70*, 3855–3864.
- (32) Valiev, M.; Bylaska, E. J.; Govind, N.; Kowalski, K.; Straatsma, T. P.; Van Dam, H. J. J.; Wang, D.; Nieplocha, J.; Apra, E.; Windus, T. L.; et al. NWChem: A Comprehensive and Scalable Open-Source Solution for Large Scale Molecular Simulations. *Comput. Phys. Commun.* **2010**, *181* (9), 1477–1489.
- (33) Bahn, S. R.; Jacobsen, K. W. An Object-Oriented Scripting Interface to a Legacy Electronic Structure Code. *Comput. Sci. Eng.* **2002**, *4* (3), 56–66.
- (34) Mortensen, J. J.; Hansen, L. B.; Jacobsen, K. W. Real-Space Grid Implementation of the Projector Augmented Wave Method. *Phys. Rev. B - Condens. Matter Mater. Phys.* **2005**, *71* (3), 035109.

- (35) Enkovaara, J.; Rostgaard, C.; Mortensen, J. J.; Chen, J.; Dułak, M.; Ferrighi, L.; Gavnholt, J.; Glinsvad, C.; Haikola, V.; Hansen, H. A.; et al. Electronic Structure Calculations with GPAW: A Real-Space Implementation of the Projector Augmented-Wave Method. *J. Phys. Condens. Matter* **2010**, *22* (25).
- (36) Zahl, P.; Wagner, T. GXSM - Smart & Customizable SPM Control. *Imaging Microsc.* **2015**, *1* (38–41).
- (37) Zahl, P.; Klust, A. GXSM Software Project Homepage.
- (38) Reineke, S.; Lindner, F.; Schwartz, G.; Seidler, N.; Walzer, K.; Lüssem, B.; Leo, K. White Organic Light-Emitting Diodes with Fluorescent Tube Efficiency. *Nature* **2009**, *459* (7244), 234–238.

Chapter 5: Conclusions and Outlook

5.1 Summary

Through this work, we have explored a range of binding and reactivity at the single molecule scale. Although the STM was, until recently, primarily used as an imaging tool or towards molecular electronics applications, this and related work opens the door for its use in both informing and executing synthetic chemistry.

Chapter 1 introduces reactivity in the STM-BJ by first detailing the history of STM-driven and -imaged reactions. The focus then shifts towards reactions in the STM-BJ, which can be triggered by a variety of stimuli. Some recent examples demonstrated that the STM-BJ allows for studying a scope of reactions beyond traditional solution-based or surface chemistry. Some reactions can even be promoted one molecule at a time. The benefits of this method are detailed, as well as the significant challenges inherent to this technique. This chapter provides an overview of progress in the field of STM-BJ-driven reaction chemistry and how it fits into nanoscale materials synthesis.

We then transition into the original PhD research, beginning with a study on the binding of aryl iodides in the single molecule junction. Two modes of binding are found, which correspond to the molecule binding to the gold electrode with (datively) and without (covalently) the iodide. This is some of the first experimental evidence of these two binding modes, which have previously only been suggested in the literature or examined computationally. A series of gold analogs corroborates the covalent binding mode, as well as DFT calculations. We lastly demonstrate that the covalent binding mode, proceeding through an oxidative addition-like process, can be favored

over the dative binding mode by applying a certain bias. Therefore, this system presents a new and facile route towards highly conducting, covalent gold-carbon junctions.

With our improved understanding of aryl iodide binding and dehalogenation, we next study the reactivity of the aryl iodides in the junction after the dehalogenation step, namely their dimerization or Ullmann coupling. Although this project is still in progress, many notable observations have been made regarding the reactivity and mechanism, the latter being particularly difficult to probe in the STM-BJ. We demonstrate that biphenyl-based systems with a variety of linkers undergo this Ullmann coupling-like dimerization with no exogenous chemicals or stimuli, at room temperature open to the ambient atmosphere. We validate our original oxidative addition mechanistic hypothesis, and take advantage of different halide proclivities towards oxidative addition to perform a cross-coupling. Many other reaction criteria in this system are still being studied, however the progress made so far lends crucial insight into the mechanism of the Ullmann coupling, which is still debated and has proven difficult to study in solution or on surfaces.

The last research section relates to a different type of linker, exploring the binding of cyclopropenylidene carbenes on gold surfaces. Using a combination of computational and experimental surface analysis techniques, we find that the amine-functionalized cyclopropenylidenes bind more strongly to the gold surface than N-heterocyclic carbenes, which are considered to be strong binders to gold. The unique structure of the cyclopropenylidene allows for the functional groups to point away from the carbonic carbon, therefore permitting the cyclopropenylidene to adopt a tilted orientation which maximizing the binding energy without forming an Au-adatom. With an improved understanding cyclopropenylidene binding, these strong binders are promising for the field of self-assembled monolayers.

5.2 Future Work

Each of the research areas described has many possible directions to explore. Because the Ullmann coupling project is still underway, most of our future planning has focused on the Ullmann-related questions yet to explore. Some of the aspects of the reaction included in Chapter 3, for example, warrant further study, including the roles of the electrolyte and surface roughness. Though we have made many interesting observations, the exact causation is still not entirely understood. Further experiments would likely prove to be revealing, including a more systematic study of both the electrolyte and the surface. The identity, size, and amount of the electrolyte could be varied, and the resulting effects of reactivity studied. Additionally, the surface roughness could be more systematically modified with different methods of gold deposition, changing the underlying surfaces, or more rigorous surface analysis techniques.

Moreover, the aforementioned attempts to quantify the reaction efficiency, or amount of dimer formed, would be extremely helpful for this and future projects. Preliminary fluorescence experiments are promising, as the molecules in this study are quite fluorescent and distinguishable. This technique also holds potential to be generalizable for other reaction systems studied in the junction. Other possible routes for quantification might include HPLC or NMR, if molecules are sufficient soluble.

Concurrently, computational work examining the reaction pathway, transition states, activation energies, and dipoles of this system is underway and also holds immense promise for validating some of our experimental findings. Specifically, we hope that computations can clarify some electric field effects, as we have seen some conflicting experimental observations. Future

computational work might probe the mechanism further by varying the halide or by having more than one analyte molecule in the system.

There are many other concepts that we have considered but have not been described within, such as determining and quantifying the electric field, scaling the system up to a flow cell-like setup, or expanding the substrate scope to perform other cross-couplings or even different types of reactions. Further mechanistic details can be probed both experimentally and computationally as well, which would be very informative considering the challenges of *in situ* mechanistic studies.

5.3 Concluding Remarks

This body of PhD research is at the intersection of many areas of chemistry, including physical, organic, inorganic, and computational, as well as physics and engineering. The field of molecular electronics holds many possibilities for collaborative experimentation, learning, and brainstorming, which will continue well beyond these projects. Working together, scientists from different fields have an immense opportunity in junction reactivity studies to deeply probe and understand chemical processes like never before. I hope my work has made a dent in this understanding, and that others will build upon it to continue the quest towards a fundamental understanding of reaction chemistry.